Stoomkraken: van voedingsanalyse tot fabrieksoptimalisatie

Steam Cracking: from Feedstock Analysis to Plant Optimization

Thomas Dijkmans

UNIVERSITEIT
GENT

Promotoren:

prof. dr. ir. Guy B. Marin

Laboratorium voor Chemische Technologie

Vakgroep Chemische Proceskunde en Technische Chemie

Universiteit Gent

prof. dr. Ir. Kevin M. Van Geem

Laboratorium voor Chemische Technologie

Vakgroep Chemische Proceskunde en Technische Chemie

Universiteit Gent

Decaan: Prof. dr. ir. Rik Van de Walle

Rector: Prof. dr. Anne De Paepe

EXAMENCOMMISSIE

Leescommissie

Prof. dr. ir. Kevin Van Geem [promotor]

Vakgroep Chemische proceskunde en Chemische Technologie

Faculteit Ingenieurswetenschappen en Architectuur

Ugent

Prof. dr. Frederic Lynen

Vakgroep Organische Chemie

Faculteit Wetenschappen

Universiteit Gent

Prof. Tiziano Faravelli

Dipartimento di Chimica, Materiali e Ingegneria Chimica

Politecnico di Milano

Dr. Ir. Arno Oprins

Technology & Innovation, STC Geleen

SABIC Geleen

Andere leden

Prof. dr. ir. Guy B. Marin [promotor]

Laboratorium voor Chemische Technologie

Vakgroep Chemische Proceskunde en Technische Chemie

Universiteit Gent

Prof. dr. Marie-Françoise Reyniers

Laboratorium voor Chemische Technologie

Vakgroep Chemische Proceskunde en Technische Chemie

Universiteit Gent

Prof. dr. ir. Geraldine Heynderickx

Laboratorium voor Chemische Technologie

Vakgroep Chemische Proceskunde en Technische Chemie

Universiteit Gent

Prof. dr. ir. Luc Taerwe [voorzitter]

Vakgroep Bouwkundige Constructies

Universiteit Gent

Voor mijn vrouw, kinderen en ouders

Acknowledgements

In de eerste plaats wil ik mijn promotoren, prof. Marin en prof. Van Geem bedanken om mij bij te staan. Dankzij hun hulp heb ik dit doctoraat tot een goed einde kunnen brengen.

Graag wil ik ook mijn dank betuigen aan mijn thesisstudenten Joris Derouck, Steven Vandermeersch, Ive Van Goethem, Robin Strumane en Willem Raes die rechtstreeks of onrechtstreeks tot dit werk hebben bijgedragen. Zonder jullie was dit werk nooit geworden tot wat het nu is.

Het experimentele werk bracht natuurlijk de nodige technische problemen met zich en dus graag zou ik Michaël, Hans, Erwin, Bert en alle andere technici willen bedanken om met mij deze problemen van de baan te helpen.

Graag wil ik ook mijn vele collega's van het LCT bedanken die mij 4 jaar lang hebben moeten aanhoren. Meer specifiek wil ik Steven, Carl, Nick en Ruben bedanken om mij gezelschap te houden gedurende mijn doctoraat en voor hun waardevolle inbreng. Verder wil ik Aäron, Andres, Amit, David, Ezgi, Gonzalo, Hans-Heinrich, Hassan, Jelena, Kaustav, Kostas, Maria, Marko, Mike, Panos, Natalia, Pieter, Ruben en Yu bedanken voor de nodige ontspanning tijdens de koffiepauze.

Als laatste wil ik mijn familie bedanken om mij te blijven steunen doorheen deze vier jaren. Meer specifiek wil ik mijn vrouw Melissa bedanken die met mij de goede en de slechte tijden van mijn doctoraat heeft mogen delen of ze het nu wou of niet. Verder wil ik mijn ouders bedanken voor de jarenlange steun doorheen mijn studietraject. Zonder jullie bijdrage was ik hier nu nooit geweest. Als laatste wil ik mijn twee jonge dochters Emma en Amylia bedankten. Jullie toverden altijd een glimlach op mijn gezicht als ik thuiskwam, hoe goed of hoe slecht mijn dag ook geweest was.

Thomas Dijkmans
Gent 2014

Contents

Notation

Roman symbols

A	Pre-exponential factor	(mol,s,m^3)
$\tilde{A}$	Single-event pre-exponential factor	(mol,s,m^3)
$a_1 - a_7$	NASA polynomial coefficients	(-)
Ac	Acceleration factor	(-)
C	Concentration	$(mol.m^{-3})$
CIP	Coil inlet pressure	(Pa)
CIT	Coil inlet temperature	(K)
COP	Coil outlet pressure	(Pa)
COT	Coil outlet temperature	(K)
c_p	Constant pressure molar heat capacity	$(J.mol^{-1}.K^{-1})$
c_v	Constant volume molar heat capacity	$(J.mol^{-1}.K^{-1})$
$\overline{c_v}$	Mixture average constant volume molar heat capacity	$(J.mol^{-1}.K^{-1})$
d_c	Thickness of the cokes	(m)
d_h	Hydraulic diameter	(m)
d_i	Inner tube diameter	(m)
d_o	Outer tube diameter	(m)
d_w	Thickness of the wall	(m)
E_a	Activation energy	(J)

f	Fanning friction factor	(-)
F	Molar flow of component	(mol.s^{-1})
ΔG_k	Reaction Gibbs free energy	(J.mol^{-1})
g^0	Standard Gibbs free energy of formation	(-)
ΔH_k	Reaction enthalpy	(J.mol^{-1})
h	Height	(m)
ΔH_{vap}	Vaporization enthalpy	(J.mol^{-1})
h^0	Standard enthalpy of formation	(J.mol^{-1})
k	Rate coefficient	(mol,s,m^3)
K_{ceq}	Equilibrium coefficient	(mol,m³)
LHV	Lower heating value	(J.kg^{-1})
M	Molar mass	(kg.mol^{-1})
$\dot{m}$	Hydrocarbon mass flow rate	(kg.s^{-1})
M_{eff}	Molecularity	(mol.m^{-3})
n_e	Number of single events	(-)
n_o	Number of objectives	(-)
n_r	Number of reactions	(-)
n_s	Number of species	(-)
Nu	Nusselt number: $Nu = \dfrac{\alpha \ d_i}{\lambda_g}$	(-)
N_x	Numbers of atoms x	(-)
O_i	Objective i	(-)

P	Price	($)
P/E	Propene of ethene ratio	$(wt.wt^{-1})$
p_{atm}	Atmospheric pressure	(Pa)
Pr	Prandtl number: $Pr = \frac{\mu c_p}{\lambda_g}$	(-)
p_t	Total pressure	(Pa)
q	Heat flux to process gas	$(W.m^{-2})$
Q	Heat input	$(J.kg^{-1})$
r	Reaction rate	$(mol.m^{-3}.s^{-1})$
R	Universal gas constant	$(J.mol^{-1}.K^{-1})$
$r^0_{c,max}$	Maximum initial coking rate	$(kg.m^{-2}.s^{-1})$
Re	Reynolds number: $Re = \frac{v d_i \rho}{\mu}$	(-)
RF	Relative response factor	(-)
RL	Runlength	(days)
R_{s1}	First dimension resolution	(-)
R_{s2}	Second dimension resolution	(-)
R_{s2D}	Two-dimensional resolution	(-)
S	Shannon entropy	(-)
s^0	Standard entropy of formation	$(J.mol^{-1}.K^{-1})$
T	Temperature	(K)
t	Time	(s)
T_b	Boiling point	(K)

t_r	Retention time	(s)
U	Overall heat transfer coefficient	$(W.m^{-2}.K^{-1})$
u	Standard free energy of formation	$(J.mol^{-1})$
v	Velocity	$(m.s^{-1})$
V	Peak volume	(-)
w	Mass fraction of component i	(-)
x	Steam quality	(%)
Y	Mole fraction of component i	(-)
z	Axial position in reactor	(m)

Greek Symbols

α	Convection coefficient	$(W.m^{-2})$
α_i	Enhanced molecular reaction coefficient	(-)
Δ	Difference	(-)
δ	Steam dilution	$(kg.kg^{-1})$
ζ	Reduced inverse viscosity	$(Pa^{-1}.s^{-1})$
λ	Conductivity coefficient	$(W.m^{-2}.K^{-1})$
μ	Dynamic viscosity	(Pa.s)
ν	Stoichiometric coefficient (Reactant = negative, Product = positive) = $v" + v'$	(-)
v'	Forward stochiometric coefficient (negative)	(-)

v''	Backward stochiometric coefficient (positive)	(-)
ρ	Density	$(kg.m^{-3})$
ϕ	Wilke coefficient	(-)
Ω	Cross-sectional surface area	(m²)
ω	Circumference	(m)
ω_{A1}	Peak width of component A in the first dimension	(s)
ω_{A2}	Peak width of component A in the second dimension	(s)

Sub- and superscripts

0	Low pressure limit
∞	High pressure limit
aro	Aromatic
B	Backward reaction
boil	Boiling point
c	Cokes
C	Carbon
cr	Critical
f	Forward reaction
FID	FID channel
g	Gas phase
H	Hydrogen

i	Inner
i,j,y,z,k	Component number or reaction number
o	Outer
r	Reduced
ref	Reference reaction
req	Requested
S	Sulfur
SCD	SCD channel
St	Internal standard
TB	Third body
w	Wall

Acronyms

AED	Atom emission detector
API	American petroleum institute
CFD	Computational fluid dynamics
CPU	Central processing unit
DA	Diaromatics
DASPK	Differential-algebraic solver using preconditioned Krylov methods
DN	Dinaphthenes
EA	Element analyzer

FID	Flame ionization detector
FPD	Flame photometric detector
FT-ICR-MS	Fourier transform ion cyclotron resonance mass spectrometry
GC	Gas chromatography
$GC \times GC$	Comprehensive two-dimensional gas chromatography
GPU	Graphical processing unit
ΔGAV_i^0	Group Additive Value of kinetic parameter, referred to the value of the reference reaction
I	Isoparaffins
ISAT	In-situ tabulation
LC	Liquid chromatography
LSODA	Livermore solver for ordinary differential equations, with automatic method switching for stiff and non-stiff problems.
LSODE	Livermore solver for ordinary differential equations
LSODES	Livermore solver for ordinary differential equations with general sparse Jacobian matrices.
MA	Monoaromatics
MN	Mononaphthenes
MS	Mass spectrometry
NA	Naphthenoaromatics
NCD	Nitrogen chemiluminescence detector
NDA	Naphthenodiaromatics

NIMBUS	Non-differentiable interactive multi-objective bundle-based optimization system
NTrA	Naphthenotriaromatics
ODE	Ordinary differential equation
OPEX	Operating expenses
P	Paraffins
PAH	Polycyclic aromatic hydrocarbons
PASH	Polycyclic sulfur containing hydrocarbons
pFPD	Pulsed flame photometric detector
PINA	n-Paraffins, isoparaffins, naphthenes and aromatics
PIONA	n-Paraffins, isoparaffins, olefins, naphthenes and aromatics
PNA	Paraffins, naphthenes and aromatics
QSSA	Quasi steady state assumption
RADAU5	Implicit Runge-Kutta method of RADAU type of order 5
SARA	Saturates, aromatics, resins and asphaltenes
SCD	Sulfur chemiluminescence detector
SFC	Supercritical fluid chromatography
SIC	Selected ion chromatogram
SPE	Solid phase extraction
TCD	Thermal conductivity detector
TIC	Total ion chromatogram
TLE	Transfer line exchanger
TN	Trinaphthenes

TOF-MS   Time of flight mass spectrometry

TrA   Triaromatics

VGO   Vacuum gas oil

VODE   Variable-coefficient Ordinary Differential Equation solver, with fixed-leading-coefficient implementation.

Samenvatting

Stoomkraken van koolwaterstoffen blijft nog steeds een van de meest belangrijke maar ook meest energieverbruikende processen in de petrochemische industrie. In dit proces worden koolwaterstoffen uit aardolie fracties, zoals ethaan, propaan, nafta en gasolie, omgezet in lichte olefines en aromaten voor de petrochemische industrie. Door de uitputting van de voorraad aardolie en de bijhorende prijsstijging van lichte oliefracties zoals nafta, staan stoomkrakers vandaag voor de uitdaging om ofwel steeds zwaardere fracties afkomstig van aardolie te kraken zoals (vacuüm)gasolie, of lichtere voedingen uit schaliegas, zoals ethaan te gebruiken. Door de lage winstmarges van de huidige stoomkrakers is het van groot belang dat er accurate simulatiemodellen voor handen zijn de processen in het bijzonder voor deze zwaardere voedingen. Zulke modellen kunnen gebruikt worden om de performantie van het proces naar een ongekend niveau van efficiëntie te brengen en zo het energieverbruik te verminderen en de winst te maximaliseren. Deze modellen combineren fundamentele inzichten in de samenstelling van de voeding, de product samenstelling, de radicalaire en moleculaire reacties en transportfenomenen. Verder zijn deze modellen onvervangbaar voor de ontwikkeling, optimalisatie en real-time controle van moderne processen. Dit omdat de modellen toelaten om de productsamenstelling te voorspellen voor een brede waaier aan procescondities en voedingen.

Het doel van dit werk was bovendien om een computationeel efficiënt en fundamenteel simulatiemodel te ontwikkelen. Dit model moet in staat zijn om niet alleen accuraat de productsamenstelling te voorspellen maar moet ook bruikbaar zijn voor de optimalisatie van het

proces. Daarbij horend moeten de technieken voor een gedetailleerde analyse van de voeding verbeterd worden zodat een meer gedetailleerde voedingssamenstelling bepaald kan worden die gebruikt kan worden door deze fundamentele modellen.

In het eerste deel van dit proefschrift en meer precies in Hoofdstuk 2, 3 en 4 wordt het gebruik van $GC \times GC$ als een analytisch hulpmiddel voor het verkrijgen van een gedetailleerde samenstelling van een brede waaier aan voedingen besproken. $GC \times GC$ werd gekoppeld aan een reeks van verschillende (selectieve) detectoren die niet alleen toelaten om de zuivere koolwaterstoffen maar ook zwavelhoudende, stikstofhoudende en een aantal zuurstofhoudende koolwaterstoffen te kwantificeren. De techniek laat toe om tot op een koolstofgetal van 46 een benaderende moleculaire samenstelling van een staal te verkrijgen. Deze benaderende moleculaire samenstelling verdeelt het staal in verschillende chemische families en op koolstofgetal. 20 verschillende chemische families werden waargenomen waarvan 11 koolwaterstoffamilies (n-paraffines, isoparaffines, mononaftenen, dinaftenen, monoaromaten, naftenoaromaten, diaromaten, naftenodiaromaten, triaromaten, naftenotriaromaten en tetra-aromaten), 3 zwavelhoudende families (thiolen/sulfiden, benzothiofenen en dibenzothiofenen) en 6 stikstofhoudende families (pyridines, anilines, quinolines, indolen, acridines en carbazolen). De ontwikkelde techniek laat toe om een kwantitatieve analyse uit te voeren van de meeste aardoliefracties met uitzondering van de hele zware vacuümgasolies en het vacuümresidu. De techniek werd toegepast om de gedetailleerde samenstelling van atmosferische gasolies en vacuümgasolies te bepalen maar ook van schalieolie.

Het verkrijgen van zulke gedetailleerde samenstellingen gebruikmakende van analytische technieken, zoals $GC \times GC$, is niet gemakkelijk, foutgevoelig en zeer tijdrovend. Dit maakt deze technieken nagenoeg onbruikbaar in een industriële omgeving. Mathematische methodes die een gedetailleerde voedingssamenstelling kunnen reconstrueren op basis van een beperkte set van macroscopische eigenschappen, zoals gemiddelde dichtheid, kookspuntcurve en groep-type analyses, kunnen hiervoor een alternatief bieden. Om hier op in te spelen beschrijft Hoofdstuk 5 de uitbreiden van een bestaand voedingsreconstructieprogramma genaamd SIMCO. SIMCO wordt in Hoofdstuk 5 uitgebreid naar vacuümgasolies en zwavelhoudende koolwaterstoffen. De bestaande methode is gebaseerd op de maximalisatie van de Shannon entropie. Deze methode bepaalt de concentratie van elke molecule of pseudo-component in een vooraf gedefinieerde bibliotheek van componenten door de entropie objectieffunctie the maximaliseren rekening houdende met een aantal randvoorwaarden die vastgelegd zijn door de opgegeven macroscopische eigenschappen. Hierdoor kan deze methode zeker eenvoudig uitgebreid worden door een uitbreiding van de bestaande bibliotheek met nieuwe componenten en een uitbreiding van de macroscopische eigenschappen die in rekening gebracht kunnen worden. Hoofdstuk 5 beschrijft niet enkel de uitbreiding van de bibliotheek tot op een koolstofgetal van 45 maar ook de toevoeging van drie verschillende structurele klassen van zwavelhoudende componenten. Bovendien worden er extra commerciële indices gedefinieerd zoals elementair zwavelgehalte, aromatisch zwavelgehalte en een gedetailleerde groepsanalyse om de reconstructie van zwavelhoudende koolwaterstoffen te verbeteren. Er wordt aangetoond dat het nodig is om een PINA analyse, kookspuntcurve, elementanalyse (CHS), dichtheid en aromatisch zwavelgehalte op te geven om de gedetailleerde samenstelling van gasolies te voorspellen.

In Hoofdstuk 6 wordt een fundamenteel reactormodel genaamd COILSIM1D besproken. COILSIM1D is in staat de productsamenstelling van een waaier aan voedingen (ethaan tot gasolies) te voorspellen in de radiatiesectie van een stoomkraker. COILSIM1D combineert een radicalair, microkinetisch model (CRACKSIM) met de vergelijkingen van een propstroomreactor. Het microkinetisch model bestaat uit twee deelnetwerken. Aan de ene kant is er het β netwerk en aan de andere kant het monomoleculaire μ netwerk. Deze onderverdeling is een gevolg van de μ hypothese. Deze hypothese stelt dat monomoleculaire reacties overheersen voor radicalen met meer dan 5 koolstofatomen (μ radicalen). Op deze radicalen kan verder nog de Quasi-stationaire toestandshypothese worden toegepast waardoor de concentratie van deze radicalen analytisch kan berekend worden en deze radicalen kunnen geëlimineerd worden uit het finale stelsel van modelvergelijkingen.

In het tweede deel van Hoofdstuk 6 worden de modelvergelijkingen voor een 1-dimensionale propstroomreactor beschreven samen met de procedure om het resulterende, stijve stelsel van differentiaalvergelijking op te lossen. Deze procedure omvat een op maat gemaakte numeriek algoritme om the stijfheid van de differentiaalvergelijkingen te verminderen maar ook de beschrijving van en algoritme dat toelaat om in plaats van een temperatuur-, druk- of warmteprofiel, twee kraakscherpte indices op te geven zoals de uitlaattemperatuur en de uitlaatdruk.

In het laatste deel van Hoofdstuk 6 wordt de computationele efficiëntie van COILSIM1D onderzocht en door verbeteringen aan onder andere de berekening van de viscositeit wordt de totale simulatietijd met een factor 3 gereduceerd.

In Hoofdstuk 7 wordt het fundamentele reactormodel COILSIM1D uitgebreid zo dat het buiten de buizen in de radiatiesectie ook de warmtewisselaar na de radiatiesectie (TLE) kan simuleren. Deze TLE koelt de productstroom snel af zodat er geen krakingsreacties meer kunnen optreden. Zowel de vergelijkingen voor de binnenste en de buitenste buis worden besproken en een oplossingsmethode wordt voorgesteld. Het model is gevalideerd met twee verschillende, industriële TLE's: één voor een propaanfornuis en één voor een naftafornuis. De gesimuleerde data is in lijn met de (beperkte) industriële data. Het model wordt ook gebruikt om een aantal veelvuldig gebruikte veronderstellingen over TLE's in de literatuur te valideren. Er wordt aangetoond dat de convectieve warmteweerstand in de buitenste buis verwaarloosd kan worden maar dat reacties in de binnenste buis toch nog een belangrijke rol spelen. Reactie gebeurt voornamelijk in het begin van de TLE waar de temperatuur nog hoog is. Afhankelijk van de benodigde precisie van de productsamenstelling kan het dus belangrijk zijn om reacties mee te nemen in de TLE.

Hoofdstuk 8 koppelt het ontwikkelde simulatiemodel met een optimalisatie-algoritme voor meerdere objectieven NSGA-II-a-JG. Deze combinatie wordt gebruikt voor de optimalisatie met meerdere objectieven van de stoomkraakfornuizen voor verschillende voedingen. Twee verschillende combinaties van objectieffuncties werden gekozen om de brutowinst of de brutowinst per eenheid te representeren. De combinaties van objectieffuncties werden vergeleken met elkaar maar ook met de optimalisatie naar één enkele objectieffunctie zijnde brutowinst of brutowinst per eenheid. De objectieven representatief voor zowel brutowinst als de brutowinst per eenheid zijn: de totale productie van etheen en propeen, exploitatiekosten en initiële,

maximale cokevormingssnelheid. Deze combinatie van objectieven werd gebruikt om de optimalisatie naar meerdere objectieven van verschillende voedingen, het co-kraken van ethaan en propaan en het effect van cokesvorming in de reactor te bestuderen.

In Hoofdstuk 9 worden enkele technieken om de computationele efficiëntie van het simulatiemodel te verbeteren. Twee wiskundige technieken, met name tabuleren en het gebruik van een analytische Jacobiaan in plaats van een eindige-differentie Jacobiaan, en één computationele techniek, met name het gebruik van de grafische kaart om deel van de berekeningen uit te voeren, werden bestudeerd. Combineren van de analytische Jacobiaan met berekeningen door de grafische kaart resulteerde in het snelste algoritme dat tot 120 keer sneller was dan het oorspronkelijke algoritme.

Summary

Steam cracking of hydrocarbons remains one of the most important but also most energy intensive processes in the petrochemical industry. In this process hydrocarbons coming from crude oil fractions, such as ethane, propane, naphtha and gas oils, are cracked into the base chemicals of the petrochemical industry, e.g. light olefins and aromatics. With the depletion of the crude oil reserves and the corresponding price increase of light oil fractions such as naphtha steam crackers now face the challenge of either cracking increasingly heavier feedstocks, such as gas oils and vacuum gas oils coming from lower quality crude oils, or move to lighter feedstocks, such as ethane coming from the shale gas production.

Due to the narrow profit margins at which these steam crackers operate it is of extreme importance that accurate simulation models are available, even for these heavier feedstocks. These models can be used to raise the performance of the steam cracker to unprecedented levels of efficiency and thus reduce overall energy consumption and maximize profit. They should also incorporate fundamental insights in feed and product composition, the controlling chemical reactions and transport phenomena. Furthermore these models are indispensable for state-of-the-art process design, optimization and real-time control, since they enable predictive reactor simulations over a wide range of process conditions and for a wide range of feedstocks.

The objective of this work was to develop a computational efficient fundamental simulation model which in addition to yield prediction can also be used for optimization of the steam cracker. Furthermore, techniques for the detailed analysis of a feedstock have been improved and

developed to obtain a more detailed feedstock composition required by these types of fundamental models.

In the first part of this thesis, namely Chapter 2, 3 and 4, the use of $GC \times GC$ as an analytical tool to obtain the detailed composition of a broad range of hydrocarbon samples is investigated. $GC \times GC$ was coupled to an array of different (selective) detectors allowing not only for the quantification of pure hydrocarbons but also sulfur containing hydrocarbons, nitrogen containing hydrocarbons and some oxygenates. The technique was usable up to a maximum carbon number of 46 and was able to get a near-molecular composition of the sample based on the chemical family and carbon number of the components. 20 different chemical families were observed of which 11 hydrocarbon families (n-paraffins, isoparaffins, mononaphthenes, dinaphthenes, monoaromatics, naphthenoaromatics, diaromatics, naphthenodiaromatics, triaromatics, naphthenotriaromatics, and tetra-aromatics), 3 sulfur containing hydrocarbon families (thiols/sulfides, benzothiophenes and dibenzothiophenes) and 6 nitrogen containing hydrocarbon families (pyridines, anilines, quinolines, indoles, acridines and carbazoles). The developed analytical method allows the quantitative analysis of most crude oil fraction with the exception of very heavy vacuum gas oils and vacuum residue and has been applied to determine the detailed composition of atmospheric and vacuum gas oils as well as shale oil.

Obtaining detailed compositional information using analytical techniques such as $GC \times GC$ is, however, not straightforward and often time-consuming. In an industrial environment these techniques are often not feasible and fast computational methods that can reconstruct the detailed

composition of a feedstock based on a limited set of macroscopic properties, such as average density, distillation data and group-type analyses, become useful. To this extend Chapter 5 describes the extension of an existing feedstock reconstruction program called SIMCO towards vacuum gas oils and sulfur containing hydrocarbons. The existing method is based upon the maximization of Shannon entropy. This method determines the abundances of each molecule or pseudo-component in a pre-defined library of components by maximizing the entropy objective function subject to a number of constraints that are determined by the available macroscopic properties. As such this method can easily be extended by extending the existing library with new components and extending the macroscopic properties being taken into account by the algorithm. Chapter 5 not only describes the extension of the library up to a carbon number of 45 but also the addition of three new structural classes of sulfur components. Furthermore additional commercial indices such as elemental sulfur, aromatic sulfur and a detailed group type analysis are studied to improve the reconstruction of the sulfur containing hydrocarbons. It was shown that the combination of a PINA analysis, boiling point curve, elemental analysis (CHS), density and aromatic sulfur was able to accurately predict not only the detailed composition related to pure hydrocarbons but also sulfur containing hydrocarbons of different gas oil fractions.

In Chapter 6 the fundamental reactor model called COILSIM1D is presented. COILSIM1D is able to predict the yields of a wide variety of feedstocks (ethane up to gas oils) inside the radiant coil of a steam cracking unit. It combines a free-radical based microkinetic model (CRACKSIM) with a 1D plug flow reactor model. Chapter 6 both describes the microkinetic model which is divided into two sub-network namely the β network and the monomolecular μ network. This

division is caused by the μ hypothesis which states that monomolecular reactions dominate for radicals with more than 5 carbon atoms (μ radicals) apart from some exceptions. The quasi-steady state assumption can furthermore be used to analytically calculate the concentration of these μ radicals and thus these μ radicals can be eliminated from the final set of model equations.

In the second part of Chapter 6 the model equations for a 1D plug flow reactor are described and a procedure to solve the resulting stiff differential equations is presented. This procedure includes a specialized numerical procedure to overcome the stiffness of the resulting differential equations but also the description of the shooting method which allows, instead of specifying the temperature, pressure or heat flux profile, for two severity indices such as the coil outlet temperature and coil outlet pressure to be used.

In the last part of Chapter 6 the computational efficiency of COILSIM1D is investigated and improvements to the calculations of the viscosity are made, by either using the graphical processing unit or tabulation, decreasing the final simulation time up to a factor of 3.

In Chapter 7 the fundamental reactor model COILSIM1D is further extended so that in addition to the radiant coil it can also simulate the transfer line exchanger of a steam cracking unit which quickly cools the effluent to below cracking temperatures. Both the governing equations for the inner and outer tube are discussed and a solution method for these equations is presented. The model is validated using two different industrial TLE's, one for a propane furnace and one for a naphtha furnace and the simulated data matches the industrial data. The model is used to test some common assumptions made in literature, such as neglecting the outer tube convective heat transfer and neglecting reactions in the inner tube. It is shown that, depending on the needed

accuracy of the simulation, reactions cannot be neglected but the outer tube convective resistance can safely be neglected. Significant reactions still occurred in the beginning of the TLE were the temperature was high enough and depending on the required accuracy of the final yields reactions in the TLE cannot be neglected.

Chapter 8 applied the developed simulation model COILSIM1D and couples it to a multi-objective optimization algorithm, namely the elitist non-dominant sorting genetic algorithm with adapted jumping gene operator (NSGA-II-aJG). The combination is used to study the multi-objective optimization of steam cracking furnaces for a wide array of feedstocks. Two different combinations of objectives, chosen to be representative for either gross profit or gross profit per unit, are compared with each other and with the single objective optimizations toward gross profit and gross profit per unit. The objective set, combining total production of ethene and propene, running costs and initial maximum coking rate, was shown to be representative for both gross profit and gross profit per unit and was used to study the multi-objective optimization of different feedstocks, the co-cracking of ethane and propane and the effect of the formation of cokes inside the reactor.

In Chapter 9 techniques to increase the computational efficiency of the simulation engine are presented. Two mathematical techniques, namely tabulation and using an analytical Jacobian instead of a finite differences Jacobian, and one computational technique, namely using the graphical processing unit to handle part of the calculations, are presented. It is shown that a

combination of the analytical Jacobian together with GPU calculations showed the best results and an acceleration factor up to 120 can be obtained.

Glossary

Ab Initio	Latin term for "from first principles". It refers to the fact that the results are obtained by applying the established laws of nature without assumptions, special models or experimental input. Ab initio methods determine the energy of a molecule or transition state by solving the Schrödinger equation.
API gravity	American Petroleum institute gravity (API) is a measure of how heavy or light a petroleum liquid is compared to water. If its API gravity is greater than 10, it is lighter and floats on water; if less than 10, it is heavier and sinks.
Arrhenius activation energy	The coefficient E_a describing the temperature dependency of the rate coefficient $k = A \exp(-E_a/RT)$ with A the temperature independent pre-exponential factor.
Arrhenius pre-exponential factor	See Arrhenius activation energy.
Central processing unit	The hardware within a computer that carries out the instructions of a computer program by performing the basic arithmetical, logical, and input/output operations of the system
COILSIM1D	Fundamental reactor model developed at the Laboratory for Chemical Technology of the Ghent University

Comprehensive two-dimensional gas chromatography	Advanced analytical technique that provides two-dimensional separation by combining two different analytical columns connected with an interface, called the modulator, that ensures that the entire sample is comprehensively subjected to both separations.11
CRACKSIM	Single-event microkinetic model developed at the Laboratory for Chemical Technology of the University of Ghent
Enthalpy	The enthalpy H is a thermodynamic quantity and is calculated from the internal energy U as $H = U + pV$, with p the pressure and V the volume of the system
Entropy	The entropy S is a thermodynamic property that is related to the disorder of the system. A system with a larger number of states that can be occupied, will therefore have a higher entropy.
Feedstock reconstruction method	Method that permits deriving the detailed composition of a complex feedstock (or in fact any other mixture) from limited macroscopic information.
Gas condensate	A low-density mixture of hydrocarbons that are present as gaseous components in raw natural gas and are extracted therefrom by condensation
Graphical processing unit	A specialized electronic circuit designed to rapidly manipulate and alter memory to accelerate the creation of images

Gross profit	The difference between revenue and the cost of making a product or providing a service, before deducting overhead, payroll, taxation, and interest payments over a certain time period.
Gross profit per unit	The difference between revenue and the cost of making a product or providing a service, before deducting overhead, payroll, taxation, and interest payments expressed per unit sold
Group additivity method	A group additivity method is a technique that allows to predict properties from molecular structures. For example, within Benson's group additivity method a property can be written as a sum of contributions arising from its constituent groups.
Group contribution method	See group additivity method.
Homologous series of components	A series of components, e.g. hydrocarbons, with the same core structure, but with increasing chain or side-chain length.
Lumping	Grouping of species which are generally isomers or homologous species with similar reactivity in order to reduce the total number of species in a kinetic model.
NSGA-II-aJG	Elitist non-dominant sorting genetic algorithm with adapted jumping gene operator
Operating expenses	Ongoing cost for running a product, business, or system
Oxygenate	Hydrocarbon that contains oxygen as part of their chemical structure

Pareto optimality	State of allocation of resources in which it is impossible to make any one individual better off without making at least one individual worse off.
PIONA	An analysis method that divides crude oil components according to their groups (n-paraffins, isoparaffins, olefins; naphthenes and aromatics)
PNA	An analysis method that divides crude oil components according to their groups (paraffins, naphthenes and aromatics)
Profit margin	The difference between the cost of producing a product and the sales price for that product.
Pyrolysis	The uncatalysed decomposition of organic components resulting from exposure to high temperature, in the absence of molecular oxygen.
Quasi-steady state approximation	Mathematical expression that expresses that the time rate of change of the concentration of all quasi-steady state species is equal to zero.
Reaction family	A class of reactions that are characterized by the same pattern of electron rearrangement steps.
SARA	Saturate, Aromatic, Resin and Asphaltene (SARA) is an analysis method that divides crude oil components according to their polarizability and polarity.

Single-event microkinetic model	A kinetic model that consists of elementary reactions and accounts for all energetically equivalent reaction paths, i.e. Single-events, to determine each reaction rate.
Single-event pre-exponential factor	The pre-exponential factor excluding the number of single-events of the reaction
Steam cracking	A petrochemical process in which saturated hydrocarbons are converted into small unsaturated hydrocarbons by exposure to high temperature in the presence of steam.
Steam quality	Mass fraction of steam in a saturated water mixture

Chapter 1: Introduction and outline

1.1 Introduction

Steam cracking of hydrocarbons is one of the most important processes in the petrochemical industry. In this process hydrocarbons coming from fossil origin, such as ethane, propane, or the crude oil fractions naphtha and gas oil, are cracked into the base chemicals of the petrochemical industry, i.e. light olefins and aromatics. The chemicals produced by steam cracking are used in downstream units, e.g. polyethene and polypropene plants, to produce more valuable final products, e.g. polyethene, or intermediate products, e.g. ethene oxide, ethene glycol, etc.

The most important product of a steam cracker is ethene which is a key building block in the petrochemical industry. In recent years, the world has witnessed the largest ethene capacity expansion, with capacity growing at a compound annual growth rate of 4% between 2007 and 2012, to reach a total production capacity of 156 million tonnes ethene per year in 2012 as depicted on Figure 1.1. The bulk of the new capacity has come from the Gulf Cooperation Council (GCC) countries and China which have an average annual growth rate of nearly 15% and 14% respectively. In 2012 alone the GCC countries added an additional ethene capacity of 2.1 million tonnes per year which is 47% of the total additions of that year.
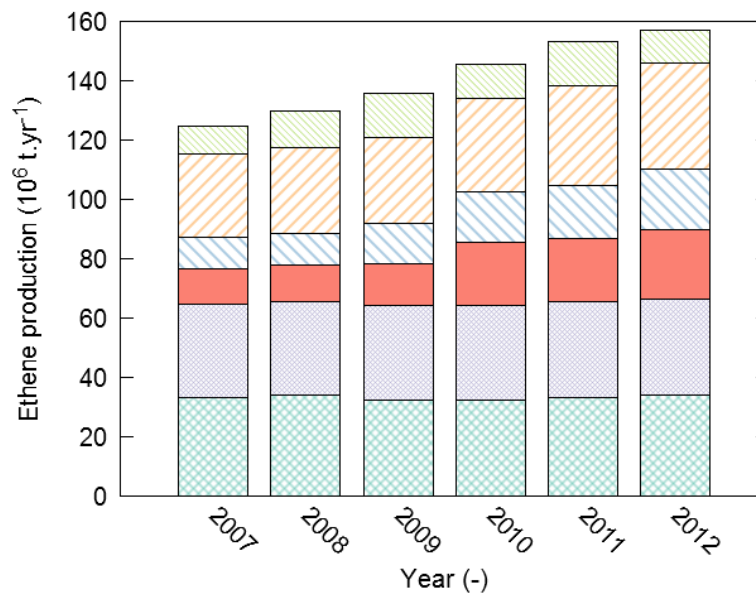
Figure 1.1: Development of global ethene capacity by region: ⬚ **North-America;** ⬚ **Europe;** ⬚ **GCC countries;** ⬚ **China;** ⬚ **Rest of Asia;** ⬚ **Rest of the world**

(Baker, 2012)

The production of ethene relies heavily on the supply of crude oil and gas. The global consumption of crude oil continues to increase as it is in addition to natural gas and coal currently the most important starting material for the production of electricity, fuels and chemicals (Newell & Iler, 2013).

It is however expected that conventional crude oil production and conversion will decline as worldwide reserves deplete and prices of crude oil keep rising. As shown in Table 1.1, it is estimated that heavy oil, extra heavy oil and bitumen make up about 70% of the remaining global oil resources.

Table 1.1: Approximate world oil reserves (Alboudwarej et al., 2006)

Conventional oil (~40°API)	**30 %**
Heavy oil (less than 22.3°API),	15 %
Extra heavy oil (less than 10°API))	25 %
Oil sand and bitumen	30 %

To keep up with the rise in demand of ethene and propene new plants will have to be able to crack increasingly heavier feedstocks such as gas oils and vacuum gas oils. The cracking behavior of these fractions differs from that of the conventional feeds. This is mainly related to the difference in composition between the lighter and the heavier cuts. VGO's for example, contain significant amounts of di-, tri- and poly-aromatic compounds that are not present in light fractions (Van Geem et al., 2008). These heavier feedstocks bring additional problems such as fouling of tubes in the convection section and downstream units (Ngan et al., 2003).

With the rise of shale gas another alternative for the production of ethene besides crude oil is available. Figure 1.2 shows that over the past years the shale gas production in the US has increased dramatically. From 2000 to 2012 the production capacity of shale gas has increased more than 100 fold and by 2016 the development of shale gas exploration in the US is expected to increase natural gas liquids production by more than 40%. Wet shale gas consists of 75% methane, 16% ethane, 5% propane and 1% butane, pentane, hexane and other gases (Foster, 2013).
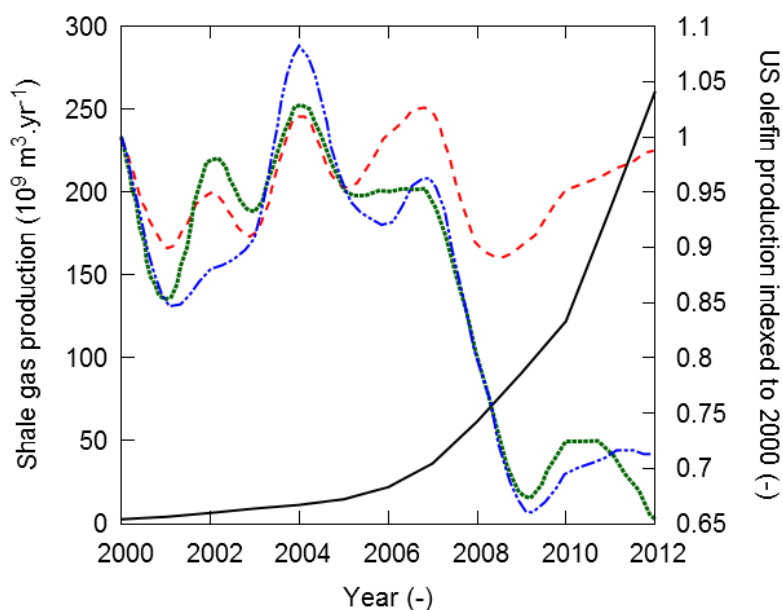
Figure 1.2: Shale gas, ethene, propene and butadiene production from 2000 to 2012 ("What Shall We Do with All Our New Natural Gas?," 2012; Bruijnincx & Weckhuysen, 2013): ━━ **Shale gas production (left axis);** ━ ━ ━ **Ethene production (right axis);** ▪▪▪▪▪ **Propene production (right axis);** ━▪▪ **butadiene production (right axis)**

Figure 1.2 also shows the indexed (to the year 2000) production capacity of ethene, propene and butadiene. It shows a gradual increase of all three of these products until the energy crisis of 2008 where the production capacity dropped dramatically. After 2008 the shale gas production increases and the production capacity of ethene follows that trend as more and more crackers use cheap ethane as a feedstock. However when cracking ethane only 5 kg of propene and 5 kg of C4- olefins are produced per 100 kg of ethene. When naphtha is cracked about 40 kg of propene and 25 kg of C4- olefins is produced per 100 kg of ethene. Propene and butadiene are other key building blocks in the petrochemical industry and ethane cracking thus produces only a limited amount of these other key building blocks besides ethene. This effect is also visible in Figure 1.2 as although the ethene production recovers after 2008, propene and butadiene production remains

at an all-time low for the past 12 years. As a consequence the butadiene prices have been very unstable as can be seen in Figure 1.3.
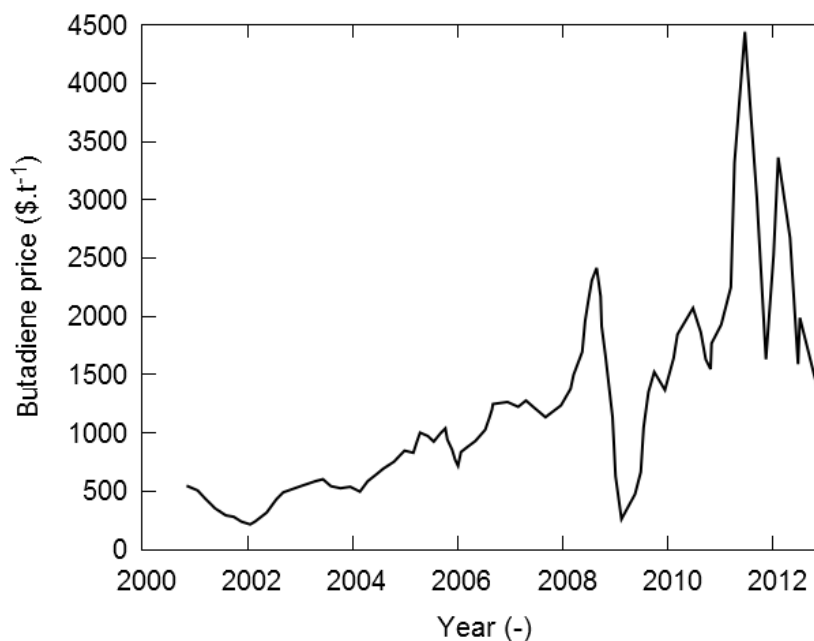
Figure 1.3: Butadiene price evolution over time (Hodges, 2013)

With the increase in production of shale gas on-purpose production routes for these key chemicals such as propene have also gained momentum (Ding & Hua, 2013). For propene shale gas production offers a solution as it can be produced by propane dehydrogenation. Large propane dehydrogenation plants are now being built or have been announced, for instance by Petrologistics and Dow Chemical (Bruijnincx & Weckhuysen, 2013). However significant efforts are still required for the on-purpose production of butadiene and aromatics and the occasional high price of these products are very beneficial for current naphtha crackers (Foster, 2013).

This implies that two alternative routes are available for ethene producers: either use light feedstocks resulting in a decrease in the production of other key chemicals such as butadiene or, alternatively, use heavier crude oil fractions. The latter requires major adjustments to the

installations so that they can handle the additional fouling problems these feedstocks impose on the equipment. Moreover, these heavy feedstocks have a different cracking behavior than the lighter feedstocks and current simulations models will need to be adjusted to be able to predict product yields and to determine optimal process variables as well as identify any possible issues that a certain feedstock might impose on the equipment.

From a research point of view these heavy feedstocks also provide new challenges. Current analytical techniques are unable to provide the necessary level of detail in the feedstock composition needed for fundamental process models and are often too time consuming to be used in an industrial environment. New techniques are thus needed that can supply this detailed feedstock composition in a reasonable amount of time.

Furthermore the current kinetic models only deal with lighter feedstocks such as ethane, propane and naphtha and need to be extended to deal with these heavier feedstocks. However the computational burden of these extended models should remain limited in order to be able to use these models to determine optimal process variables needed and to keep a plant using these feedstocks profitable. This chapter will explain the followed approach in this work and give an overview of the techniques that are currently available in literature.

1.2 Fundamental modeling strategy

The main goal of advanced process models is to relate properties of the feedstock with the desired product specifications and the necessary process variables. Furthermore these product specifications are often derived from the main objective that all industrial processes have, namely making profit while respecting the environmental constraints. In this respect the product slate is

often not fixed but is optimized in such a way that profit is maximized taking into account the plant's operating window. An advanced process model thus needs to be able to account for all the needs of industry (e.g. profit, environmental impact,…) and translate these needs into the optimal process variables and product specifications.

In the present work a fundamental model has been developed and improved which is not only able to simulate the steam cracking process for a wide variety of feedstocks but can also be used to optimize the steam cracking process. Figure 1.4 gives an overview of the fundamental modeling approach. It essentially consists of combining a microkinetic model with a reactor model (1D, 2D or 3D) that uses the detailed feedstock composition to calculate the detailed product composition by integrating the continuity, energy and momentum equations The resulting differential equations can be integrated using the appropriate numerical solvers and are able to simulate reactors at different scales (industrial, pilot, bench)
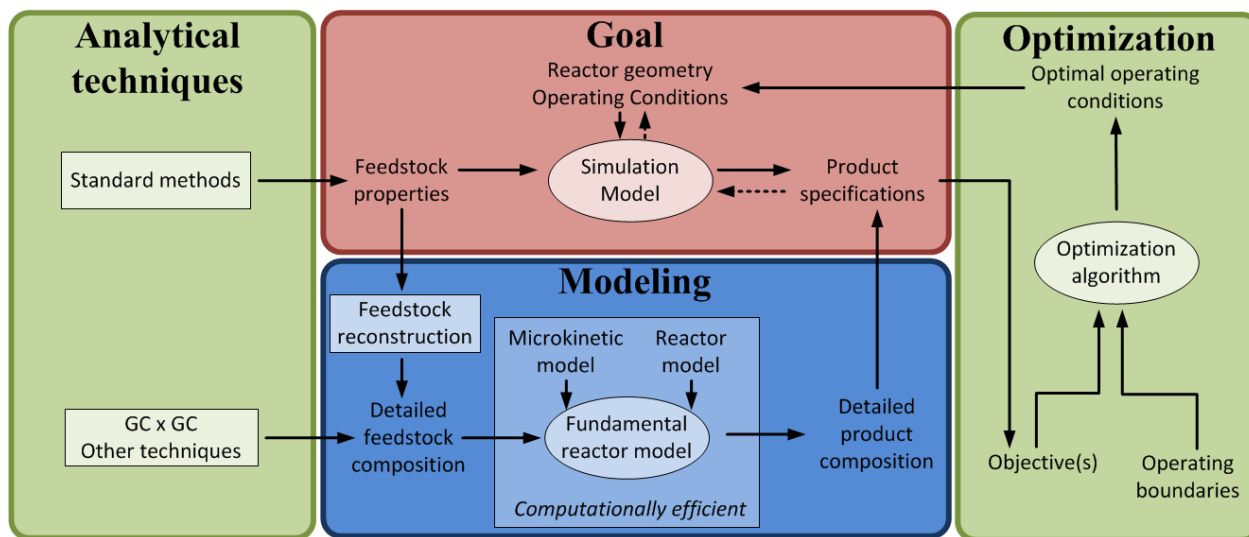
Figure 1.4: Fundamental modeling approach used in this work (based upon Pyl (2013))

The development of such a fundamental model is very challenging and requires a wide variety of tools and strategies that will be described in more detail in this chapter.

At the heart of this modeling approach lies the fundamental reactor model which combines both a microkinetic model and a reactor model. This fundamental reactor model transforms the detailed feedstock composition into a detailed product composition and thus connects the feedstock with the product. The fundamental reactor model combines a microkinetic model, containing the reactions between all the chemical species, with a reactor model which accounts for the transport phenomena.

1.2.1 **Kinetic model**

Since the pioneer work of Rice (Rice, 1931; Rice & Herzfeld, 1934; Kossiakoff & Rice, 1943) it is well known that gas phase pyrolysis proceeds through a free radical mechanism which is inherently characterized by a vast number of species and reactions which dramatically increases as the molar mass of the feed molecule(s) increases. Therefore many research groups have

developed tools, such as NETGEN (Broadbelt et al., 1994, 1996), RMG (Susnow et al., 1997; Matheu et al., 2001; Van Geem et al., 2006; Harper et al., 2011), REACTION (Blurock, 1995, 2004a, 2004b; Moreac et al., 2006), RING (Rangarajan et al., 2012a, 2012b), COMGEN (Ratkiewicz & Truong, 2002), MECHGEN (Németh et al., 2002), KING (Di Maio & Lignola, 1992), RAIN (Fontain et al., 1987; Fontain & Reitsam, 1991), CASB (Porollo et al., 1997), GRACE (Yoneda, 1979), RNG (Karaba et al., 2013) and Genesys (Vandewiele et al., 2012) that can automatically generate these complex mechanisms and can also determine reaction rate coefficients and thermodynamic data in a systematic way. As the molar mass of the reactant(s) increases the complexity of the reacting mixture increases and these network generation tools need to limit the number of species and reactions in the final kinetic model. This can be done with different reduction techniques such as lumping or applying the quasi steady state approximation (QSSA). Tools that implement such strategies are EXGAS (Bounaceur et al., 2002; Buda et al., 2005; Glaude et al., 2010), MAMA/MAMOX (Pierucci et al., 2005; Mehl et al., 2008), MOLEC (Chevalier et al., 1990; Muharam & Warnatz, 2007) and PRIM (Clymans & Froment, 1984; Hillewaert et al., 1988; Van Geem et al., 2008).

Although validated model assumptions are imposed to limit the number of species in the final kinetic model, the number of species considered can be very extensive. Due to the ever-growing computational power of personal computers but also high-performance computers these kinetic models continue to grow. Figure 1.5 shows an overview of the number of reactions as a function of the number of species for a wide range of kinetic models developed over the past 2 decades for pyrolysis, combustion and oxidation. It is clear that over the years the size of the kinetic models has grown significantly both in number of species as in number of reactions but the trend seems

to be that the number of reactions is approximately 5.5 times the number of species (black line in

Figure 1.5).
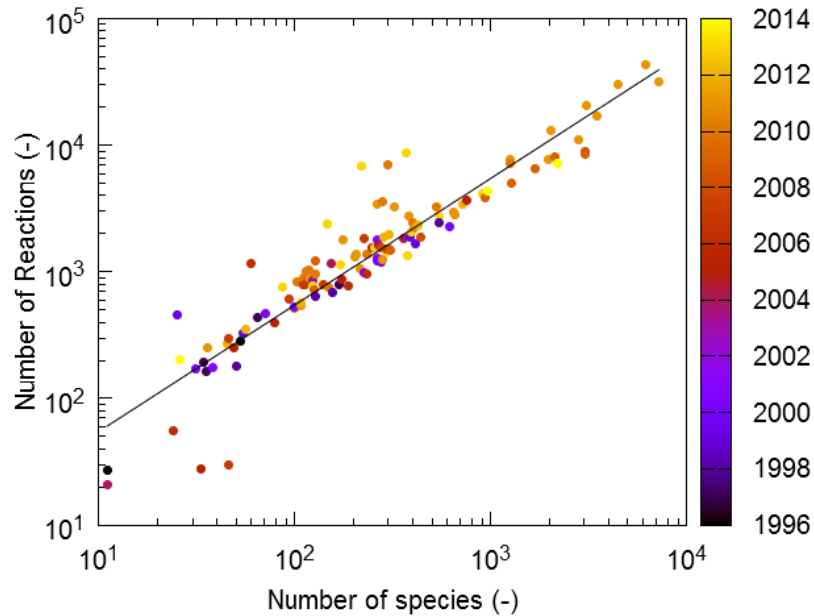
Figure 1.5: Evolution of the size of different kinetic models for pyrolysis, combustion and oxidation over the

past 2 decades (after Lu and Law (2009))

Due to the ever increasing size of kinetic models the computational load increases drastically.

Although it is true that the computational power has increased over time, it is clear that

computational efficiency is crucial for both kinetic model and reactor model. Speed becomes

especially important when the fundamental simulation model is used for online optimization of a

running plant (Pierucci et al., 1996) or when more complex reactor geometries using CFD are

simulated.

1.2.2 **Reactor model**

Steam cracking is a non-isothermal, non-adiabatic and non-isobaric process. Due to the high velocities and thus high Reynolds numbers of the cracked gas inside the inner tube it is often assumed that no radial gradients are present inside the inner tube (Gal & Lakatos, 2008), except for the temperature in a very thin film close to the wall in which all resistance to heat transfer is located (Froment et al., 2011). Thus most of the time the tubular reactor inside a furnace is modeled as a one-dimensional plug flow reactor in which no thermal gradients are assumed. The steam cracking process is often modeled using these assumption (Ranjan et al., 2012; Karaba et al., 2013) and two major tools, SPYRO® (Dente et al., 1979; Ranzi et al., 1983; van Goethem et al., 2001) and COILSIM1D (Van Geem et al., 2008), have been developed using the model equations for a one-dimensional plug flow reactor.

These models however fail to predict the radial temperature profile that can exist inside the tubes. This radial temperature profile can have a significant effect on the calculated reactant concentrations and more in particular on those of the gas-phase radicals at the internal wall of the reactor tubes. Efforts have been made to develop more complex models which take into account these radial effects (Sundaram & Froment, 1980; Van Geem et al., 2004).

However nowadays there is an increasing interest in the use of new 3-dimensional reactor geometries in the field of steam cracking. These 3D reactor geometries offer increased heat transfer and thus a lower external wall temperature at the price of an increased pressure drop. It is clear that these 3D reactor geometries cannot be modeled by simple 1D or 2D reactor model equations and that more complex simulations are needed. Several CFD studies regarding 3D reactor geometries are available in literature (Lan et al., 2007; Hu et al., 2011a; Hu et al., 2011b)

but only few incorporate a kinetic model that properly accounts for the free-radical chemistry (De Saegher et al., 1996; Detemmerman & Froment, 1998; Schietekat et al., 2014) to allow a trustworthy prediction of the effect of reactor configuration on product yields. Moreover the kinetic model needs to be reduced to keep the final simulation time within reasonable boundaries. For example Schietekat et al. (2014) reduced the full single-event microkinetic CRACKSIM model to its relevant core for propane cracking. The final network consisted of only 203 reactions between 13 molecules and 13 radicals.

1.2.3 Computational efficiency

It is clear that as the complexity of the reactor model increases the complexity of the used kinetic model seems to decrease to finish the simulation in a reasonable time. Computational improvements in both the kinetic model as in solving the reactor model equations could allow to increase complexity. Several attempts have been made to improve the computational efficiency of the algorithms and several different techniques are available in literature. These techniques can roughly be divided into three different categories namely chemical techniques, mathematical techniques and computational techniques.

The chemical techniques requires some chemical knowledge of the process being studied and include reduction techniques (Bhattacharjee et al., 2003; Law, 2007; He et al., 2011; Andreis et al., 2013) but also techniques such as the quasi steady state assumption (Turanyi et al., 1993; Lu et al., 2001; Zhang et al., 2013) which keep the size of the mechanism and thus the number of equations that needs to be solved limited. The term limited is however severely dependent on the complexity of the reactor model that is being used.

The mathematical techniques focus on speeding up both the integrator (e.g. different types of solvers) and/or function evaluations (e.g. by approximating computationally expensive functions) by improvement of the adopted algorithms. They include techniques such as tabulation which replaces variables that are otherwise difficult to calculate, e.g. reaction rates, by tabulated values and calculate them using interpolation techniques (Pope, 1997; Hiremath & Pope, 2013; Ren et al., 2013) but also replacing the finite difference Jacobian with an analytical expression for the Jacobian (Perini et al., 2012).

The computational techniques maximize the algorithm's efficiency on state-of-the-art computer hardware. Such computational techniques include using CPU\GPU hybrid calculations (Shi et al., 2011; Zhang et al., 2011; Shi et al., 2012).

1.3 Analytical techniques

The fundamental modeling approach requires that a detailed feedstock composition is supplied to the algorithm. The amount of detail in the analysis of the feedstock needs to be on the same level as the amount of detail used in the kinetic model. When a single event microkinetic model is used a (near-) molecular composition of the feedstock is thus required (Alvarez et al., 2014).

For lighter feedstocks such as naphtha a wide variety of techniques is available which can supply this near-molecular composition (Vendeuvre et al., 2005; Adam et al., 2008b; ASTM-D6730, 2011; Pyl et al., 2011; Omais et al., 2012; ASTM-D5134, 2013). However for heavier fractions the detailed structural characterization remains limited due to the complexity of the fractions and the limitations of the analytical technique (Merdrignac & Espinat, 2007). High boiling point fractions contain a significant number of isomers and organic compounds which can drastically

increase with the cut point. These fractions present a broad range of polarities and can contain paraffinic, aromatic or hetero-atomic molecules making the analysis of these fractions extremely difficult.

Nevertheless several techniques have been developed that can supply a near-molecular composition. Comprehensive two-dimensional gas chromatography (GC × GC) is one of the latest developments in analytical separation techniques. Compared to conventional gas chromatography GC × GC offers an enhanced peak capacity and higher sensitivity. In addition the ordered retention of structurally related compounds is very useful (Van Geem et al., 2010). Many studies underline the benefit of GC × GC and the technique has already been coupled to a wide variety of detectors. For example GC × GC – FID (Dallüge et al., 2003; Wang & Zhang, 2007; Adam et al., 2008a; Dutriez et al., 2009; Dutriez et al., 2010; Van Geem et al., 2010; van der Westhuizen et al., 2011), is often used to obtain detailed compositional information of samples ranging from naphtha's up to vacuum gas oils. For high boiling fractions, e.g. kerosene's and heavier, a distinction between different chemical groups and by carbon number is often made as the sheer number of possible isomers makes it impossible to differentiate on a molecular level. The compositional information obtained by these techniques drives the level of detail of even the most complex kinetic models to new levels. Information about other compounds besides hydrocarbons can even be obtained by augmenting the device with different detectors. For example GC × GC – SCD (Hua et al., 2003; Hua et al., 2004; Ruiz-Guerrero et al., 2006; Yang & Wang, 2010; Mahe et al., 2011) is used to obtain compositional information about the sulfur compounds present in crude oil derived fractions while GC × GC – NCD (Adam et al., 2007;

Adam et al., 2009; Lissitsyna et al., 2013) is used to obtain compositional information of nitrogen compounds in crude oil fractions.

GC × GC – TOF-MS (Adam et al., 2007; Adam et al., 2008a; Van Geem et al., 2010; van der Westhuizen et al., 2011) is another combination and can be used to obtain both qualitative information (identification of unknown peaks) as quantitative information about crude oil derived fractions.

Another technique that rivals the compositional information that can be obtained with GC × GC is Fourier transform ion cyclotron resonance mass spectrometry or FT-ICR MS (Kekalainen et al., 2009; Bae et al., 2010; Shi et al., 2010; Cengceng et al., 2012). The advantage of this technique is that it can identify the elemental composition, double bond equivalents, rings plus double bonds to carbon, and the carbon number, based on ultra-high-resolution and accurate mass measurements (Fernandez-Lima et al., 2009). The disadvantage of FTICR-MS is the formidable cost of the device which prohibits its widespread availability and routine use (Lei et al., 2011).

1.4 Feedstock reconstruction

Obtaining the detailed feedstock composition based on analytical techniques can be expensive and is prone to errors. Consequently, chemical engineers often resort to average macroscopic properties of these mixtures, e.g. average molar mass, average density, distillation data, or global group-type analyses (e.g. SARA, PNA, PIONA, etc.) to characterize these mixtures (Riazi, 2005). Several of these indices may correlate well with certain compositional characteristics and are therefore widely used as fast, simple and often inexpensive means to characterize and distinguish process feedstocks (Pyl, 2013). However, as shown in Figure 1.4, a detailed feedstock

composition is required for the kinetic model in the fundamental modeling approach and only these properties do not suffice.

Various so-called feedstock reconstruction techniques have been developed as a cheap and fast alternative for the detailed feedstock analysis. These methods can reconstruct a detailed composition of a complex mixture based on a limited number of average properties. Two different types of methods can be distinguished in literature. The difference in the methods can be found in the way that they select a single detailed composition out of all theoretical possible compositions that match the supplied macroscopic properties. The first type determines a detailed molecular composition by optimizing a specific objective function in addition to the constraints that are derived from the macroscopic properties while a second type uses a large experimental database to construct correlations between the macroscopic properties of the samples in the database and the detailed composition of the samples in the database. These correlations can then be used on unknown samples for which the database is representative.

The objective functions chosen in the first type of methods can be derived from theoretical concepts such as Gibbs free energy (Ha et al., 2005) or Shannon entropy (Hudebine & Verstraete, 2004; Van Geem et al., 2007) or can be a user-defined cost function (Albahri, 2005; Androulakis et al., 2005). To optimize these functions under the given constraints a set of compounds is needed for which the mole fractions can be adjusted in the optimization algorithm. This set of molecules can either be generated a priori (library compounds) (Allen & Liguras, 1991; Albahri, 2005; Van Geem et al., 2007; Pyl et al., 2010) or before optimization an algorithm can generate a set of molecules that needs to be considered. In the latter case this set can be generated using

either group contribution methods (Jaffe et al., 2005) or stochastic methods (Campbell & Klein, 1997; Hudebine & Verstraete, 2004; Ha et al., 2005).

For the second type of methods correlations can be either based on artificial neural networks (Joo et al., 2001) or some sort of empirical correlations (Dente et al., 1979). In both cases a large experimental database is needed. The need for this database limits the application range of these methods. A priori determination is needed to tell whether a specific feedstock falls into the application range of the database. This is often done based on non-physicochemical criteria or user involvement making these types of methods error prone, non-transparent and non-extendible. These methods are however considerably faster that methods using an objective function (Pyl et al., 2010).

1.5 Optimization

To sustain or improve margins against global market trends (such as increasing feedstock prices) most of the steam crackers nowadays have to push the operation closer to actual constraints and as close as possible to optimal conditions, leading to increased profitability (Ghashghaee & Karimzadeh, 2011). Due to these low profit margins, e.g. Figure 1.6, optimization of a steam cracking reactor can be very beneficial (Keyvanloo et al., 2012) and thus the optimization of the pyrolysis process has drawn continuing attention from researchers and a wide range of different types of optimization approaches have been considered.

7
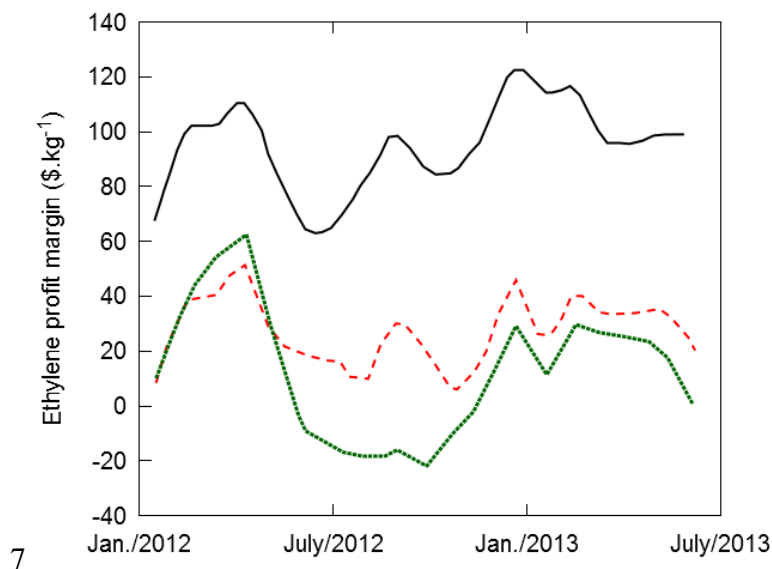
Figure 1.6: Evolution of the ethene profit margin between January 2012 and July 2013 for different feedstocks

(Lippe, 2013): ▬▬Ethane and propane; ▬ ▬ Naphtha; ▪▪▪▪▪ Gas oil
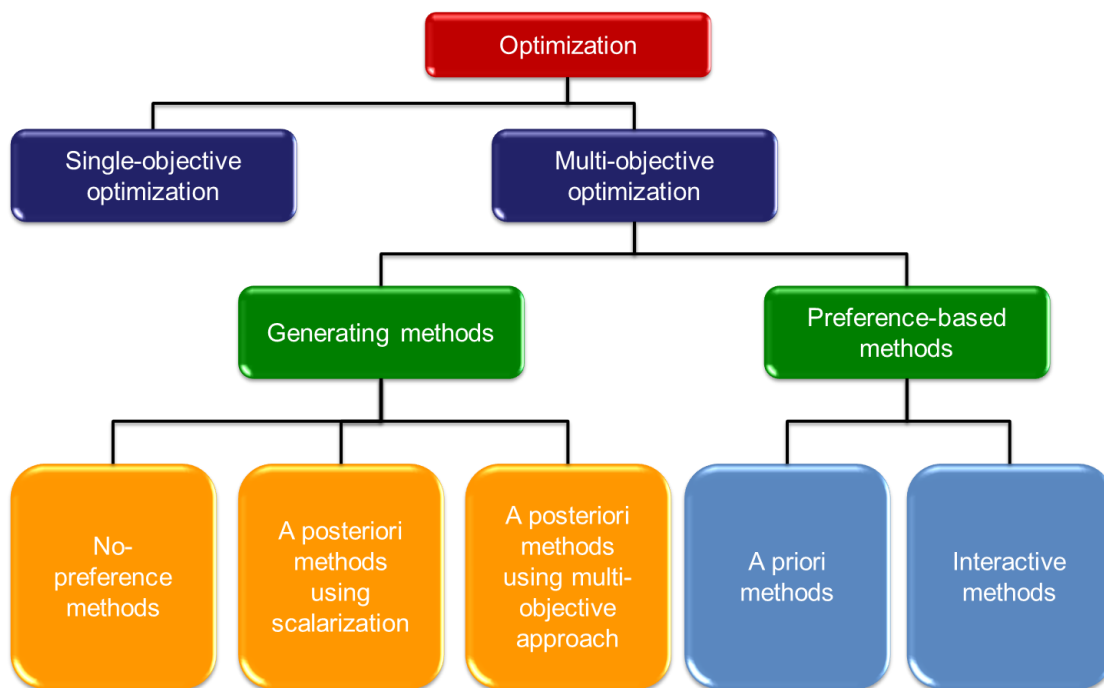
Figure 1.7: Overview of the different optimization techniques (after Rangaiah (2009))

Many methods are available for solving optimization problems. Figure 1.7 shows an overview of the different optimization techniques available and often used in chemical engineering.

Optimization can be done either using a single objective or multiple (conflicting) objectives. In case of the latter Pareto-optimal solutions are obtained. Figure 1.8 explains the concept of Pareto Optimality. First a Pareto-optimal solution is a point in the variable space where one objective cannot be improved, by changing the variables, without worsening at least one of the other objectives or a point where a so-called Pareto-improvement is not possible. On Figure 1.8 possible Pareto improvements from point A are depicted by green arrows as both objectives improve. The red arrows are not Pareto improvements as either objective 1 or objective 2 is worse off. Pareto-optimal solutions are depicted by the black line in Figure 1.8. In these points no Pareto-improvements within the objective space are possible and the black line is called the Pareto front.
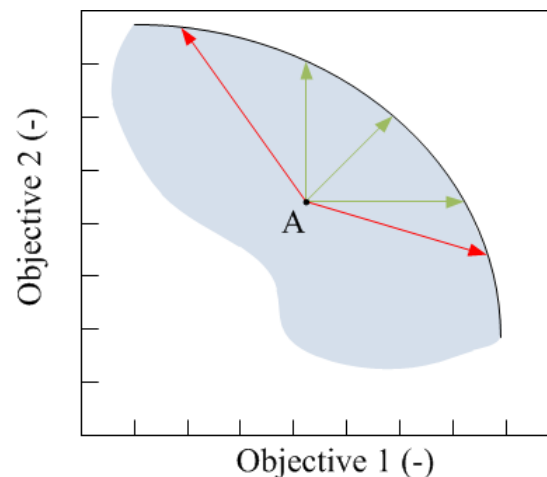
Figure 1.8: Concept of Pareto optimality: Blue area = Objective space, Green arrows = Pareto improvement, Red arrow = no Pareto improvement, Black line = Pareto front

Even for multi-objective optimization many methods transform these multiple objectives into a single objective by combining the objectives in a scalar function (Rangaiah, 2009). This scalar function can be defined in multiple ways resulting in the different methods depicted in Figure 1.7. Multi-objective optimization methods can roughly be divided into two categories namely the generating methods and the preference-based methods. The generating methods generate one or more Pareto-optimal solutions without any interference from the user. The obtained Pareto-optimal solutions are supplied to the user after the algorithm is finished. After optimization the user can select the preferred solution out of the set of Pareto-optimal solutions. The preference-based methods require input from the user at some stage(s) of the algorithm to account for the preference of the user regarding current and future solutions.

The generating methods are further divided into three subgroups: no-preference methods, a posteriori methods using the scalarization approach and a posteriori methods using the multi-objective approach. The no-preference based methods will generate a single Pareto-optimal solution without any relative priority of objectives whatsoever. An example of a no-preference method is the method of global criterion (Costa & Pereira, 2010) were the scalar function is of the form:

$$F = \sum_{i=1}^{n_o} \left\| f_i(x) - z^{ideal} \right\| \tag{1.1}$$

To avoid scaling effects the functions $f_i(x)$ can also be normalized in a uniform space.

The a posteriori methods using scalarization try to rank their objectives either based on a scalar function combining all objectives. By changing this scalar function multiple Pareto-optimal solutions can be generated. The a posteriori method using a multi-objective approach ranks the

objectives based on population based methods such as non-dominated sorting. A well-known

example of an a posteriori method using scalarization is linear scalarization (Ramos et al., 2013):

$$F = \sum_{i=1}^{n_o} w_i f_i(x) \tag{1.2}$$

where the weights of the objectives are the parameters for the scalarization. By changing these

weights different points of the Pareto front can be found.

Methods using the multi-objective approach can be based on genetic algorithms (Khosla et al.,

2007; Nabavi et al., 2009, 2011; Keyvanloo et al., 2012), differential evolution algorithms (Wang

& Tang, 2013), swarm algorithms (Li et al., 2007) and simulated annealing (Sankararao & Yoo,

2011). The methods applied in these algorithms are much more complex and fall outside the

scope of this introduction.

The preference based methods are further divided into two groups; the a priori methods and the

interactive methods. In the former method the preferences of the user are included in the initial

formulation of a suitable single objective problem. An example of this method is the value

function method where a scalar function, supplied by the user, is used to rank the different

objectives (Liu et al., 2010).

$$F = G\big(f_1(x), f_2(x), \dots, f_n(x)\big) \tag{1.3}$$

The optimization problem is thus transformed into a single objective optimization problem for the

function G.

The interactive methods on the other hand require user input during the algorithm to rank the

different possible solutions. An example is the NIMBUS method (Hakanen et al., 2005) where at

each iteration the user looks at the current set of objectives and tells the algorithm which

objectives can be decreased, which objectives are satisfactory and which objectives can be increased to generate a new set of objectives in the next iteration. Both methods only return a single optimal solution.

Although almost all of these methods transform the multiple objectives into a single objective (with exception of the a posteriori multi-objective approach) the resulting single objective optimization is not always straightforward to solve and may require complex single-objective optimization algorithms.

For the optimization of the steam cracking process the most used methods are either a priori methods or a posteriori methods using the multi-objective approach. In the former case a value function reflecting the total profit is often chosen to optimize the problem. For example Berreni and Wang (2011) tried to maximize yearly profit for a propane furnace by changing the external wall temperatures and the steam dilution. This was done by dynamic optimization over the run length of the reactor and accounting for the cokes that builds up in the reactor over the course of time. They reported a significant gain in profit (around 100.000 $ per year) as compared to the base case. They also reported an improvement in the run length of the reactor.

Instead of optimizing a single furnace optimization of an entire steam cracking plant (multiple furnaces) has also been done. In case of plant optimization additional degrees of freedom, e.g. different furnaces can use different feedstocks, and constraints, e.g. two furnaces cannot be decoked at the same time, become important. These additional degrees of freedom and constraints are not necessarily real constraints, e.g. the number of feedstocks used, and thus mixed integer nonlinear programming techniques need to be applied. For example Guo et al. (2014) studied the economic performance of ethene olefin plants. An optimization of an

industrial plant with five different furnaces using three different feedstocks, e.g. ethane, naphtha and light diesel, was studied. Process variables such as flow rates, feedstock choice and cleanup time were varied to maximize the profit over time.

In addition to optimizing multiple furnaces several authors use the multi-objective approach on a single furnace (Li et al., 2007; Gao et al., 2008; Nabavi et al., 2009; Wang & Tang, 2013). For example Nabavi et al. (2009) studied both bi- and tri-objective optimization with objectives like the yield of ethene, the yield of propene, ethene production, heat duty and run length of a furnaces while varying process variables like flow rate, outlet pressure, outlet temperature, steam dilution and inlet temperature. In this study they used a kinetic model of LPG thermal cracking including coke formation reactions that was developed by Towfighi et al. (2006). They showed tri-objective optimization of the LPG thermal cracker is desirable to find a wider range of optimal solutions compared to those by bi-objective or single-objective optimization. The best process variables could be chosen from the Pareto-optimal solutions based on user's preferences, demand for products, process operability, safety analyses, etc.

Common to all of the above mentioned optimization studies is the limited validity range of the used kinetic model, which makes generalization of the obtained results not trivial. Free-radical based kinetic models are considered, but only when light gaseous feedstocks are cracked, where the product spectrum is not that complex and optimization is not that challenging. For heavier naphtha feedstocks optimization is a lot more important and challenging because of the lower profit margins and complex product spectrum.

1.6 Outline

The development and validation of a fundamental model requires the combination and use of a wide scale of techniques and modeling approaches as shown in Figure 1.4 In this Ph.D. all these topics will be addressed, basically going from feed to product and from molecular scale to process scale.

In Chapter 2 to 4 the focus is on novel analytical techniques and their applications. In Chapter 2 the use of GC × GC for the detailed analysis of heavy hydrocarbon feedstocks, e.g. VGO's, is discussed. In this chapter the GC×GC, equipped with a flame ionization detector (FID), allows for a quantitative analysis of vacuum gas oils in 11 different chemical families namely n-paraffins, isoparaffins, mononaphthenes, dinaphthenes, monoaromatics, naphthenoaromatics, diaromatics, naphthenodiaromatics, triaromatics, naphthenotriaromatics, and tetra-aromatics. Thanks to the use of a metal capillary column the maximum carbon number of the method is drastically increased without decreasing the separating power of the technique and the maximum carbon number that can be observed is raised up to 46 which allows the quantitative analysis of most crude oil fraction with the exception of very heavy vacuum gas oils and vacuum residue.

In Chapter 3 the GC×GC method is further extended to incorporate the analysis of sulfur containing hydrocarbons next to the pure hydrocarbons. To this purpose the GC × GC was coupled to both an FID and a sulfur chemiluminescence detector (SCD) to accurately quantify both the hydrocarbons and the sulfur containing hydrocarbons in a feedstock but potentially also in the cracking effluent. With the ability to see sulfur containing hydrocarbons three additional groups could be differentiated: thiols/sulfides, benzothiophenes and dibenzothiophenes. The

procedure presented in Chapter 3 is applied to three different gas oils containing a different amount of sulfur containing compounds.

Chapter 4 takes a step further and adds, in addition to the already present FID and SCD, a nitrogen chemiluminescence detector (NCD) to the GC × GC device. In addition to the sulfur containing and pure hydrocarbons, nitrogen containing hydrocarbons can now also be differentiated. The technique presented in Chapter 4 is applied to obtain compositional information of a shale oil.

Next to the use of analytical methods to obtain a detailed feedstock composition a numerical method is also presented and extended. Chapter 5 extends a previously implemented feedstock reconstruction method (Pyl et al., 2010). This method is based on the maximization of Shannon entropy and an extension of the library allows to extend the feedstock reconstruction from kerosene's up to vacuum gas oils. Chapter 5 further extends this Shannon entropy maximization method to include the reconstruction of sulfur containing compounds. The library is extended with three different structural classes of sulfur containing compounds and different macroscopic properties related to sulfur are tested in order to increase the accuracy of the reconstructed composition.

Chapter 6 presents the fundamental reactor model called COILSIM1D used throughout this work. COILSIM1D is able to predict the yields of a wide variety of feedstocks (ethane up to gas oils) inside the radiant coil of a steam cracking unit. It combines a free-radical based microkinetic model (CRACKSIM) with the equations of a 1D plug flow reactor model. Chapter 6 addresses the governing equations of this model as well as the numerical method to integrate the resulting differential equations. The computational efficiency of COILSIM1D is also addressed in this

chapter and improvements in the calculations of the viscosity are made to decrease the simulation times.

In Chapter 7 COILSIM1D is extended so that in addition to the radiant coil it can also simulate the transfer line exchanger of a steam cracking unit which quickly cools the effluent to below cracking temperatures. Both the governing equations for the inner and outer tube are discussed and a solution method for these equations is presented. The model is used to simulate two different industrial TLE's: one for a propane furnace and one for a naphtha furnace and the results seem to match the limited industrial validation data. Significant reactions can still occur in the beginning of the TLE depending on the type of furnace. Hence, depending on the required accuracy of the final yields reactions in the TLE cannot always be neglected.

In Chapter 8 multi-objective optimization of steam cracking furnaces is studied using the COILSIM1D described in Chapter 6. Based on some example cases the effect of the objective functions, the used feedstock, start of run conditions or end of run conditions and co-cracking on the optimal process variables is studied.

Finally further optimization of the computational efficiency of simulations of reactive mixtures with detailed chemistry is studied in Chapter 9. Different techniques to increase the computational efficiency of the simulation engine are studied. Two mathematical techniques, namely tabulation and using an analytical expression for the Jacobian instead of a finite differences Jacobian, and one computational technique, namely using a GPU to accelerate the calculations, are studied and combined. A combination of the analytical Jacobian together with GPU calculations showed the best results and an acceleration factor up to 120 is obtained.

In Chapter 10 the general conclusions are presented.

1.7 References

Adam, F., Bertoncini, F., Brodusch, N., Durand, E., Thiébaut, D., Espinat, D., & Hennion, M.-C. (2007). New benchmark for basic and neutral nitrogen compounds speciation in middle distillates using comprehensive two-dimensional gas chromatography. Journal of Chromatography A, 1148, 55-64.

Adam, F., Bertoncini, F., Coupard, V., Charon, N., Thiébaut, D., Espinat, D., & Hennion, M.-C. (2008a). Using comprehensive two-dimensional gas chromatography for the analysis of oxygenates in middle distillates: I. Determination of the nature of biodiesels blend in diesel fuel. Journal of Chromatography A, 1186, 236-244.

Adam, F., Bertoncini, F., Dartiguelongue, C., Marchand, K., Thiébaut, D., & Hennion, M.-C. (2009). Comprehensive two-dimensional gas chromatography for basic and neutral nitrogen speciation in middle distillates. Fuel, 88, 938-946.

Adam, F., Vendeuvre, C., Bertoncini, F., Thiebaut, D., Espinat, D., & Hennion, M. C. (2008b). Comprehensive two-dimensional gas chromatography for enhanced analysis of naphthas: New column combination involving permethylated cyclodextrin in the second dimension. Journal of Chromatography A, 1178, 171-177.

Albahri, T. A. (2005). Molecularly explicit characterization model (MECM) for light petroleum fractions. Industrial & Engineering Chemistry Research, 44, 9286-9298.

Alboudwarej, H., Felix, J., & Taylor, S. (2006). Highlighting Heavy Oil Oilfield Review, 18, 34-53.

Allen, D. T., & Liguras, D. (1991). Structural Models Of Catalytic Cracking Chemistry - A Case-Study Of A Group Contribution Approach To Lumped Kinetic Modeling: Van Nostrand, R.

Alvarez, A., Castañeda, L. C., & Ancheyta, J. (2014). On the application of petroleum feedstock modeling techniques for developing molecule-based models of hydrocarbon conversion processes. Catalysis Today, 220–222, 198-207.

Andreis, G. S. L., Vaz, F. A., & De Bortoli, A. L. (2013). Bioethanol combustion based on a reduced kinetic mechanism. Journal of Mathematical Chemistry, 51, 1584-1598.

Androulakis, I. P., Weisel, M. D., Hsu, C. S., Qian, K. N., Green, L. A., Farrell, J. T., & Nakakita, K. (2005). An integrated approach for creating model diesel fuels. Energy & Fuels, 19, 111-119.

ASTM-D5134, 2013, Standard Test Method for Detailed Analysis of Petroleum Naphthas through n-Nonane by Capillary Gas Chromatography.ASTM International, West Conshohocken, PA, 2003, DOI: 10.1520/D5134

ASTM-D6730, 2011, Standard Test Method for Determination of Individual Components in Spark Ignition Engine Fuels by 100–Metre Capillary (with Precolumn) High-Resolution Gas Chromatography.ASTM International, West Conshohocken, PA, 2003, DOI:10.1520/D6730-01R11

Bae, E., Na, J.-G., Chung, S. H., Kim, H. S., & Kim, S. (2010). Identification of about 30 000 Chemical Components in Shale Oils by Electrospray Ionization (ESI) and Atmospheric Pressure Photoionization (APPI) Coupled with 15 T Fourier Transform Ion Cyclotron

Resonance Mass Spectrometry (FT-ICR MS) and a Comparison to Conventional Oil. *Energy & Fuels, 24*, 2563-2569.

Baker, J. (2012). GPCA: Ethylene continues expansion in 2012. http://www.icis.com/resources/news/2012/11/22/9617145/gpca-ethylene-continues-expansion-in-2012/

Berreni, M., & Wang, M. (2011). Modelling and dynamic optimization of thermal cracking of propane for ethylene manufacturing. *Computers & Chemical Engineering, 35*, 2876-2885.

Bhattacharjee, B., Schwer, D. A., Barton, P. I., & Green, W. H. (2003). Optimally-reduced kinetic models: reaction elimination in large-scale kinetic mechanisms. *Combustion and Flame, 135*, 191-208.

Blurock, E. S. (1995). Reaction - System For Modeleling Chemical Reactions. *Journal of Chemical Information and Computer Sciences, 35*, 607-616.

Blurock, E. S. (2004a). Detailed mechanism generation. 1. Generalized reactive properties as reaction class substructures. *Journal of Chemical Information and Computer Sciences, 44*, 1336-1347.

Blurock, E. S. (2004b). Detailed mechanism generation. 2. Aldehydes, ketones, and olefins. *Journal of Chemical Information and Computer Sciences, 44*, 1348-1357.

Bounaceur, R., Warth, V., Marquaire, P. M., Scacchi, G., Domine, F., Dessort, D., Pradier, B., & Brevert, O. (2002). Modeling of hydrocarbons pyrolysis at low temperature. Automatic generation of free radicals mechanisms. *Journal of Analytical and Applied Pyrolysis, 64*, 103-122.

Broadbelt, L. J., Stark, S. M., & Klein, M. T. (1994). Computer-generated pyrolysis modeling - On the fly generation of species, reactions and rates. *Industrial & Engineering Chemistry Research, 33*, 790-799.

Broadbelt, L. J., Stark, S. M., & Klein, M. T. (1996). Computer generated reaction modelling: Decomposition and encoding algorithms for determining species uniqueness. *Computers & Chemical Engineering, 20*, 113-129.

Bruijnincx, P. C. A., & Weckhuysen, B. M. (2013). Shale Gas Revolution: An Opportunity for the Production of Biobased Chemicals? *Angewandte Chemie International Edition, 52*, 11980-11987.

Buda, F., Bounaceur, R., Warth, V., Glaude, P., Fournet, R., & Battin-Leclerc, F. (2005). Progress toward a unified detailed kinetic model for the autoignition of alkanes from C-4 to C-10 between 600 and 1200 K. *Combustion and Flame, 142*, 170-186.

Campbell, D. M., & Klein, M. T. (1997). Construction of a molecular representation of a complex feedstock by Monte Carlo and quadrature methods. *Applied Catalysis a-General, 160*, 41-54.

Cengceng, G., Shuyuan, L. I., Yue, M. A., Changtao, Y. U. E., Jilai, H. E., & Wenzhi, S. (2012). Analysis and identification of oxygen compounds in Longkou shale oil and Shenmu coal tar. *Oil Shale, 29*, 322-333.

Chevalier, C., Warnatz, J., & Melenk, H. (1990). Automatic Generation of Reaction-Mechanisms for the Description of the Oxidation of Higher Hydrocarbons. *Berichte Der Bunsen-Gesellschaft-Physical Chemistry Chemical Physics, 94*, 1362-1367.

Clymans, P. J., & Froment, G. F. (1984). Computer-generation of reaction paths and rate-equations in the thermal-cracking of normal and branched paraffins. Computers & Chemical Engineering, 8, 137-142.

Costa, N. R., & Pereira, Z. L. (2010). Multiple response optimization: a global criterion-based method. Journal of Chemometrics, 24, 333-342.

Dallüge, J., Beens, J., & Brinkman, U. A. T. (2003). Comprehensive two-dimensional gas chromatography: a powerful and versatile analytical tool. Journal of Chromatography A, 1000, 69-108.

De Saegher, J. J., Detemmerman, T., & Froment, G. F. (1996). Three dimensional simulation of high severity internally finned cracking coils for olefins production. Revue De L Institut Francais Du Petrole, 51, 245-260.

Dente, M., Ranzi, E., & Goossens, A. G. (1979). Detailed prediction of olefin yields from hydrocarbon pyrolysis through a fundamental simulation model (SPYRO). Computers & Chemical Engineering, 3, 61-75.

Detemmerman, T., & Froment, F. (1998). Three dimensional coupled simulation of furnaces and reactor tubes for the thermal cracking of hydrocarbons. Revue De L Institut Francais Du Petrole, 53, 181-194.

Di Maio, F. P., & Lignola, P. G. (1992). KING, a Kinetic Network Generator. Chemical Engineering Science, 47, 2713-2718.

Ding, J., & Hua, W. (2013). Game Changers of the C3 Value Chain: Gas, Coal, and Biotechnologies. Chemical Engineering & Technology, 36, 83-90.

Dutriez, T., Courtiade, M., Thiebaut, D., Dulot, H., Bertoncini, F., Vial, J., & Hennion, M. C. (2009). High-temperature two-dimensional gas chromatography of hydrocarbons up to nC(60) for analysis of vacuum gas oils. Journal of Chromatography A, 1216, 2905-2912.

Dutriez, T., Courtiade, M., Thiebaut, D., Dulot, H., & Hennion, M. C. (2010). Improved hydrocarbons analysis of heavy petroleum fractions by high temperature comprehensive two-dimensional gas chromatography. Fuel, 89, 2338-2345.

Fernandez-Lima, F. A., Becker, C., McKenna, A. M., Rodgers, R. P., Marshall, A. G., & Russell, D. H. (2009). Petroleum Crude Oil Characterization by IMS-MS and FTICR MS. Analytical Chemistry, 81, 9941-9947.

Fontain, E., Bauer, J., & Ugi, I. (1987). Computer Assisted Bilateral Generation of Reaction Networks from Educts and Products. Chemistry Letters, 16, 37-40.

Fontain, E., & Reitsam, K. (1991). The generation of reaction networks with RAIN. 1. The reaction generator. Journal of Chemical Information and Computer Sciences, 31, 96-101.

Foster, J. (2013). Can shale gas save the naphtha crackers? http://www.platts.com/IM.Platts.Content/InsightAnalysis/IndustrySolutionPapers/ShaleGasReport13.pdf

Froment, G. F., Bischoff, K. B., & De Wilde, J. (2011). Chemical reactor analysis and design (3th edition): Wiley.

Gal, T., & Lakatos, B. G. (2008). Thermal cracking of recycled hydrocarbon gas-mixtures for re-pyrolysis: Operational analysis of some industrial furnaces. Applied Thermal Engineering, 28, 218-225.

Gao, X. D., Chen, B. Z., He, X. R., Qiu, T., Li, J. C., Wang, C. M., & Zhang, L. J. (2008). Multi-objective optimization for the periodic operation of the naphtha pyrolysis process using a

new parallel hybrid algorithm combining NSGA-II with SQP. Computers & Chemical Engineering, 32, 2801-2811.

Ghashghaee, M., & Karimzadeh, R. (2011). Multivariable optimization of thermal cracking severity. Chemical Engineering Research and Design, 89, 1067-1077.

Glaude, P. A., Herbinet, O., Bax, S., Biet, J., Warth, V., & Battin-Leclerc, F. (2010). Modeling of the oxidation of methyl esters-Validation for methyl hexanoate, methyl heptanoate, and methyl decanoate in a jet-stirred reactor. Combustion and Flame, 157, 2035-2050.

Guo, H., Lin, J., Yang, Y., & Liu, Y. (2014). Effect of minerals on the self-heating retorting of oil shale: Self-heating effect and shale-oil production. Fuel, 118, 186-193.

Ha, Z. Y., Ring, Z., & Liu, S. J. (2005). Derivation of molecular representations of middle distillates. Energy & Fuels, 19, 2378-2393.

Hakanen, J., Miettinen, K., Mäkelä, M. M., & Manninen, J. (2005). On interactive multiobjective optimization with NIMBUS® in chemical process design. Journal of Multi-Criteria Decision Analysis, 13, 125-134.

Harper, M. R., Van Geem, K. M., Pyl, S. P., Marin, G. B., & Green, W. H. (2011). Comprehensive reaction mechanism for n-butanol pyrolysis and combustion. Combustion and Flame, 158, 16-41.

He, K. Y., Androulakis, I. P., & Ierapetritou, M. G. (2011). Numerical Investigation of Homogeneous Charge Compression Ignition (HCCI) Combustion with Detailed Chemical Kinetics Using On-the-Fly Reduction. Energy & Fuels, 25, 3369-3376.

Hillewaert, L. P., Dierickx, J. L., & Froment, G. F. (1988). Computer-Generation of Reaction Schemes and Rate-Equations for Thermal Cracking. AIChE Journal, 34, 17-24.

Hiremath, V., & Pope, S. B. (2013). A study of the rate-controlled constrained-equilibrium dimension reduction method and its different implementations. Combustion Theory and Modelling, 17, 260-293.

Hodges, P. (2013). Butadiene price collapse sends warning on H2 demand. http://www.icis.com/blogs/chemicals-and-the-economy/2013/07/butadiene-prices-down-64-from-peak-as-demand-destruction-continues/sthash.ixjMkjAL.dp

Hu, G. H., Wang, H. G., & Qian, F. (2011a). Numerical simulation on flow, combustion and heat transfer of ethylene cracking furnaces. Chemical Engineering Science, 66, 1600-1611.

Hu, G. H., Wang, H. G., Qian, F., Zhang, Y., Li, J. L., Van Geem, K. M., & Marin, G. B. (2011b). Comprehensive CFD Simulation of Product Yields and Coking Rates for a Floor- and Wall-Fired Naphtha Cracking Furnace. Industrial & Engineering Chemistry Research, 50, 13672-13685.

Hua, R. X., Li, Y. Y., Liu, W., Zheng, J. C., Wei, H. B., Wang, J. H., Lu, X., Kong, H. W., & Xu, G. W. (2003). Determination of sulfur-containing compounds in diesel oils by comprehensive two-dimensional gas chromatography with a sulfur chemiluminescence detector. Journal of Chromatography A, 1019, 101-109.

Hua, R. X., Wang, J. H., Kong, H. W., Liu, J., Lu, X., & Xu, G. W. (2004). Analysis of sulfur-containing compounds in crude oils by comprehensive two-dimensional gas chromatography with sulfur chemiluminescence detection. Journal of Separation Science, 27, 691-698.

Hudebine, D., & Verstraete, J. J. (2004). Molecular reconstruction of LCO gasoils from overall petroleum analyses. Chemical Engineering Science, 59, 4755-4763.

Jaffe, S. B., Freund, H., & Olmstead, W. N. (2005). Extension of structure-oriented lumping to vacuum residua. Industrial & Engineering Chemistry Research, 44, 9840-9852.

Joo, E., Park, S., & Lee, M. (2001). Pyrolysis reaction mechanism for industrial naphtha cracking furnaces. Industrial & Engineering Chemistry Research, 40, 2409-2415.

Karaba, A., Zamostny, P., Lederer, J., & Belohlav, Z. (2013). Generalized Model of Hydrocarbons Pyrolysis Using Automated Reactions Network Generation. Industrial & Engineering Chemistry Research, 52, 15407-15416.

Kekalainen, T., Pakarinen, J. M. H., Wickstrom, K., & Vainiotalo, P. (2009). Compositional Study of Polar Species in Untreated and Hydrotreated Gas Oil Samples by Electrospray Ionization Fourier Transform Ion Cyclotron Resonance Mass Spectrometry (ESI FTICR-MS). Energy & Fuels, 23, 6055-6061.

Keyvanloo, K., Sedighi, M., & Towfighi, J. (2012). Genetic algorithm model development for prediction of main products in thermal cracking of naphtha: Comparison with kinetic modeling. Chemical Engineering Journal, 209, 255-262.

Khosla, D. K., Gupta, S. K., & Saraf, D. N. (2007). Multi-objective optimization of fuel oil blending using the jumping gene adaptation of genetic algorithm. Fuel Processing Technology, 88, 51-63.

Kossiakoff, A., & Rice, F. O. (1943). Thermal Decomposition of Hydrocarbons, Resonance Stabilization and Isomerization of Free Radicals. Journal of the American Chemical Society, 65, 590-595.

Lan, X., Gao, J., Xu, C., & Zhang, H. (2007). Numerical simulation of transfer and reaction processes in ethylene furnaces. Chemical Engineering Research & Design, 85, 1565-1579.

Law, C. K. (2007). Combustion at a crossroads: Status and prospects. Proceedings of the Combustion Institute, 31, 1-29.

Lei, Z., Huhman, D. V., & Sumner, L. W. (2011). Mass Spectrometry Strategies in Metabolomics. Journal of Biological Chemistry, 286, 25435-25442.

Li, C. F., Zhu, Q. X., & Geng, Z. Q. (2007). Multi-objective particle swarm optimization hybrid algorithm: An application on industrial cracking furnace. Industrial & Engineering Chemistry Research, 46, 3602-3609.

Lippe, D. (2013). Ethylene production prospects clouded by first-half turnarounds. Oil & Gas Journal, 111, 102-111.

Lissitsyna, K., Huertas, S., Quintero, L. C., & Polo, L. M. (2013). Novel simple method for quantitation of nitrogen compounds in middle distillates using solid phase extraction and comprehensive two-dimensional gas chromatography. Fuel, 104, 752-757.

Liu, C. W., Zhang, J., Xu, Q., & Li, K. Y. (2010). Cyclic scheduling for best profitability of industrial cracking furnace system. Computers & Chemical Engineering, 34, 544-554.

Lu, T. F., Ju, Y. G., & Law, C. K. (2001). Complex CSP for chemistry reduction and analysis. Combustion and Flame, 126, 1445-1455.

Lu, T. F., & Law, C. K. (2009). Toward accommodating realistic fuel chemistry in large-scale computations. Progress in Energy and Combustion Science, 35, 192-215.

Mahe, L., Dutriez, T., Courtiade, M., Thiebaut, D., Dulot, H., & Bertoncini, F. (2011). Global approach for the selection of high temperature comprehensive two-dimensional gas chromatography experimental conditions and quantitative analysis in regards to sulfur-

containing compounds in heavy petroleum cuts. Journal of Chromatography A, 1218, 534-544.

Matheu, D. M., Lada, T. A., Green, W. H., Dean, A. M., & Grenda, J. M. (2001). Rate-based screening of pressure-dependent reaction networks. Computer Physics Communications, 138, 237-249.

Mehl, M., Vanhove, G., Pitz, W. J., & Ranzi, E. (2008). Oxidation and combustion of the n-hexene isomers: A wide range kinetic modeling study. Combustion and Flame, 155, 756-772.

Merdrignac, I., & Espinat, D. (2007). Physicochemical characterization of petroleum fractions: the state of the art. Oil & Gas Science and Technology-Revue D Ifp Energies Nouvelles, 62, 7-32.

Moreac, G., Blurock, E. S., & Mauss, F. (2006). Automatic generation of a detailed mechanism for the oxidation of n-decane. Combustion Science and Technology, 178, 2025-2038.

Muharam, Y., & Warnatz, J. (2007). Kinetic modelling of the oxidation of large aliphatic hydrocarbons using an automatic mechanism generation. Physical Chemistry Chemical Physics, 9, 4218-4229.

Nabavi, S. R., Rangaiah, G. P., Niaei, A., & Salari, D. (2009). Multiobjective Optimization of an Industrial LPG Thermal Cracker using a First Principles Model. Industrial & Engineering Chemistry Research, 48, 9523-9533.

Nabavi, S. R., Rangaiah, G. P., Niaei, A., & Salari, D. (2011). Design Optimization of an LPG Thermal Cracker for Multiple Objectives. International Journal of Chemical Reactor Engineering, 9, 1-34.

Németh, A., Vidóczy, T., Héberger, K., Kúti, Z., & Wágner, J. (2002). MECHGEN: Computer Aided Generation and Reduction of Reaction Mechanisms. Journal of Chemical Information and Computer Sciences, 42, 208-214.

Newell, R. G., & Iler, S. (2013). The Global Energy Outlook: National Bureau of Economic Research.

Ngan, D. Y. K., Chan, P. Y. J., & Baumgartner, A. J. (2003). Thermal cracking of crude oil and crude oil fractions containing pitch in an ethylene furnace. Patent 6632351

Omais, B., Courtiade, M., Charon, N., Roullet, C., Ponthus, J., & Thiebaut, D. (2012). Using gas chromatography to characterize a direct coal liquefaction naphtha. Journal of Chromatography A, 1226, 61-70.

Perini, F., Galligani, E., & Reitz, R. D. (2012). An Analytical Jacobian Approach to Sparse Reaction Kinetics for Computationally Efficient Combustion Modeling with Large Reaction Mechanisms. Energy & Fuels, 26, 4804-4822.

Pierucci, S., Brandani, P., Ranzi, E., & Sogaro, A. (1996). An industrial application of an on-line data reconciliation and optimization problem. Computers & Chemical Engineering, 20, 1539-1544.

Pierucci, S., Ranzi, E., Dente, M., & Barendregt, S. (2005). A kinetic generator of hydrocarbon pyrolysis mechanisms. L. Puigjaner & A. Espuna (Eds.), European Symposium on Computer-Aided Process Engineering (Vol. 20, pp. 241-246).

Pope, S. B. (1997). Computationally efficient implementation of combustion chemistry using in situ adaptive tabulation. Combustion Theory and Modelling, 1, 41-63.

Porollo, A. A., Lushnikov, D. E., Pivina, T. S., & Ivshin, V. P. (1997). Computer representation and generation of possible pathways for thermal decomposition reactions of organic compounds. Journal of Molecular Structure*, 391, 117-124.

Pyl, S. P. (2013). Sustainable Production of Light Olefins: from Fossil to Renewable Resources. Ugent.

Pyl, S. P., Schietekat, C. M., Reyniers, M. F., Abhari, R., Marin, G. B., & Van Geem, K. M. (2011). Biomass to olefins: Cracking of renewable naphtha. Chemical Engineering Journal*, 176, 178-187.

Pyl, S. P., Van Geem, K. M., Reyniers, M. F., & Marin, G. B. (2010). Molecular Reconstruction of Complex Hydrocarbon Mixtures: An Application of Principal Component Analysis. AIChE Journal*, 56, 3174-3188.

Ramos, M. A., Gómez, J. M., & Reneaume, J.-M. (2013). Simultaneous Optimal Design and Control of an Extractive Distillation System for the Production of Fuel Grade Ethanol Using a Mathematical Program with Complementarity Constraints. Industrial & Engineering Chemistry Research*, 53, 752-764.

Rangaiah, G. P. (2009). Multi-objective optimization: Techniques and Applications in Chemical Engineering (Vol. 1): World Scientific Publishing.

Rangarajan, S., Bhan, A., & Daoutidis, P. (2012a). Language-oriented rule-based reaction network generation and analysis: Applications of RING. Computers & Chemical Engineering*, 46, 141-152.

Rangarajan, S., Bhan, A., & Daoutidis, P. (2012b). Language-oriented rule-based reaction network generation and analysis: Description of RING. Computers & Chemical Engineering*, 45, 114-123.

Ranjan, P., Kannan, P., Al Shoaibi, A., & Srinivasakannan, C. (2012). Modeling of Ethane Thermal Cracking Kinetics in a Pyrocracker. Chemical Engineering & Technology*, 35, 1093-1097.

Ranzi, E., Dente, M., Plerucci, S., & Biardi, G. (1983). Initial product distributions from pyrolysis of normal and branched paraffins. Industrial & Engineering Chemistry Fundamentals*, 22, 132-139.

Ratkiewicz, A., & Truong, T. N. (2002). Application of Chemical Graph Theory for Automated Mechanism Generation. Journal of Chemical Information and Computer Sciences*, 43, 36-44.

Ren, Z. Y., Goldin, G. M., Hiremath, V., & Pope, S. B. (2013). Simulations of a turbulent non-premixed flame using combined dimension reduction and tabulation for combustion chemistry. Fuel*, 105, 636-644.

Riazi, M. R. (2005). Characterization of petroleum fractions: ASTM International.

Rice, F. O. (1931). The Thermal Decomposition of Organic Compounds from the Standpoint of Free Radicals. I. Saturated Hydrocarbons. Journal of the American Chemical Society*, 53, 1959-1972.

Rice, F. O., & Herzfeld, K. F. (1934). The Thermal Decomposition of Organic Compounds from the Standpoint of Free Radicals. VI. The Mechanism of Some Chain Reactions. Journal of the American Chemical Society*, 56, 284-289.

Ruiz-Guerrero, R., Vendeuvre, C., Thiebaut, D., Bertoncini, F., & Espinat, D. (2006). Comparison of comprehensive two-dimensional gas chromatography coupled with sulfur-

chemiluminescence detector to standard methods for speciation of sulfur-containing compounds in middle distillates. Journal of Chromatographic Science, 44, 566-573.

Sankararao, B., & Yoo, C. K. (2011). Development of a Robust Multiobjective Simulated Annealing Algorithm for Solving Multiobjective Optimization Problems. Industrial & Engineering Chemistry Research, 50, 6728-6742.

Schietekat, C. M., Van Cauwenberge, D. J., Van Geem, K. M., & Marin, G. B. (2014). Computational fluid dynamics-based design of finned steam cracking reactors. AIChE Journal, 60, 794-808.

Shi, Q., Yan, Y., Wu, X., Li, S., Chung, K. H., Zhao, S., & Xu, C. (2010). Identification of Dihydroxy Aromatic Compounds in a Low-Temperature Pyrolysis Coal Tar by Gas Chromatography−Mass Spectrometry (GC−MS) and Fourier Transform Ion Cyclotron Resonance Mass Spectrometry (FT-ICR MS). Energy & Fuels, 24, 5533-5538.

Shi, Y., Green Jr, W. H., Wong, H.-W., & Oluwole, O. O. (2011). Redesigning combustion modeling algorithms for the Graphics Processing Unit (GPU): Chemical kinetic rate evaluation and ordinary differential equation integration. Combustion and Flame, 158, 836-847.

Shi, Y., Green, W. H., Wong, H. W., & Oluwole, O. O. (2012). Accelerating multi-dimensional combustion simulations using GPU and hybrid explicit/implicit ODE integration. Combustion and Flame, 159, 2388-2397.

Sundaram, K. M., & Froment, G. F. (1980). Two dimensional model for the simulation of tubular reactors for thermal cracking. Chemical Engineering Science, 35, 364-371.

Susnow, R. G., Dean, A. M., Green, W. H., Peczak, P., & Broadbelt, L. J. (1997). Rate-based construction of kinetic models for complex systems. Journal of Physical Chemistry A, 101, 3731-3740.

Towfighi, J., Niaei, A., Karimzadeh, R., & Saedi, G. (2006). Systematics and modelling representations of LPG thermal cracking for olefin production. Korean Journal of Chemical Engineering, 23, 8-16.

Turanyi, T., Tomlin, A. S., & Pilling, M. J. (1993). On the error of the quasi-steady-state approximation. Journal of Physical Chemistry, 97, 163-172.

van der Westhuizen, R., Ajam, M., De Coning, P., Beens, J., de Villiers, A., & Sandra, P. (2011). Comprehensive two-dimensional gas chromatography for the analysis of synthetic and crude-derived jet fuels. Journal of Chromatography A, 1218, 4478-4486.

Van Geem, K. M., Heynderickx, G. J., & Marin, G. B. (2004). Effect of radial temperature profiles on yields in steam cracking. AIChE Journal, 50, 173-183.

Van Geem, K. M., Hudebine, D., Reyniers, M. F., Wahl, F., Verstraete, J. J., & Marin, G. B. (2007). Molecular reconstruction of naphtha steam cracking feedstocks based on commercial indices. Computers & Chemical Engineering, 31, 1020-1034.

Van Geem, K. M., Pyl, S. P., Reyniers, M. F., Vercammen, J., Beens, J., & Marin, G. B. (2010). On-line analysis of complex hydrocarbon mixtures using comprehensive two-dimensional gas chromatography. Journal of Chromatography A, 1217, 6623-6633.

Van Geem, K. M., Reyniers, M. F., & Marin, G. B. (2008). Challenges of modeling steam cracking of heavy feedstocks. Oil & Gas Science and Technology-Revue De L Institut Francais Du Petrole, 63, 79-94.

Van Geem, K. M., Reyniers, M. F., Marin, G. B., Song, J., Green, W. H., & Matheu, D. M. (2006). Automatic reaction network generation using RMG for steam cracking of n-hexane. AIChE Journal, 52, 718-730.

van Goethem, M. W. M., Kleinendorst, F. I., van Leeuwen, C., & van Velzen, N. (2001). Equation-based SPYRO® model and solver for the simulation of the steam cracking process. Computers & Chemical Engineering, 25, 905-911.

Vandewiele, N. M., Van Geem, K. M., Reyniers, M. F., & Marin, G. B. (2012). Genesys: Kinetic model construction using chemo-informatics. Chemical Engineering Journal, 207, 526-538.

Vendeuvre, C., Bertoncini, F., Espinat, D., Thiébaut, D., & Hennion, M.-C. (2005). Multidimensional gas chromatography for the detailed PIONA analysis of heavy naphta: Hyphenation of an olefin trap to comprehensive two-dimensional gas chromatography. Journal of Chromatography A, 1090, 116-125.

Wang, F. C. Y., & Zhang, L. (2007). Chemical composition of group II lubricant oil studied by high-resolution gas chromatography and comprehensive two-dimensional gas chromatography. Energy & Fuels, 21, 3477-3483.

Wang, X., & Tang, L. (2013). Multi-objective Operation Optimization of Naphtha Pyrolysis Process using a Parallel Differential Evolution. Industrial & Engineering Chemistry Research, 14415–14428.

What Shall We Do with All Our New Natural Gas? (2012). http://www.advisorperspectives.com/commentaries/aci_40512.php

Yang, Y. T., & Wang, Z. (2010). Determination of Sulfur-containing Compounds in Straight Run Diesel Oil by Comprehensive Two Dimensional Gas Chromatography. Chinese Journal of Analytical Chemistry, 38, 1805-1808.

Yoneda, Y. (1979). Chemogram, a Computer-Program Package for Chemical Logic .3. Estimation of the Thermodynamic Properties of Organic-Compounds in the Ideal-Gas State .1. Acyclic Compounds and Cyclic-Compounds with a Ring of Cyclopentane, Cyclohexane, Benzene, or Naphthalene. Bulletin of the Chemical Society of Japan, 52, 1297-1314.

Zhang, S. L., Androulakis, I. P., & Ierapetritou, M. G. (2013). A hybrid kinetic mechanism reduction scheme based on the on-the-fly reduction and quasi-steady-state approximation. Chemical Engineering Science, 93, 150-162.

Zhang, Y., Vouzis, P., & Sahinidis, N. V. (2011). GPU simulations for risk assessment in CO2 geologic sequestration. Computers & Chemical Engineering, 35, 1631-1644.

Chapter 2: Detailed characterization of heavy petroleum fractions

2.1 Introduction

In Chapter 1 it was shown, e.g. Figure 1.4, that the application of microkinetic models requires a "molecular" composition of the feedstock. This molecular composition of the feedstock can be translated in a molecular composition of a product and its corresponding product specifications using the microkinetic model.

However, the characterization of these heavy petroleum fractions has been and continues to be one of the main challenges of analytical chemists. Fractions such as atmospheric and vacuum gas oils can easily contain over one million different compounds. Due to the sheer number of compounds these fractions are often characterized using global characteristics such as simulated distillation, elementary and/or structural analysis (Dutriez et al., 2010a). Such techniques only give a limited amount of information although there are currently a wide range of methods available in literature which can obtain "near-molecular" compositions of these heavy fractions. Obviously it is extremely challenging for these analytical techniques to handle the sheer number of compounds present in the feedstock. A first analytical method which is capable of obtaining this near-molecular composition is Fourier transform ion cyclotron resonance mass spectrometry (FT-ICR-MS). FT-ICR-MS can be used with different ionization modes and allows for unprecedented molecular identification of these fractions (Fu et al., 2006; Fernandez-Lima et al., 2009; Liu et al., 2011). The technique can identify the elemental composition, double bond

equivalents (rings plus double bonds to carbon) and carbon number of the compounds present in the mixture, based on ultra-high-resolution and accurate mass measurements (Fernandez-Lima et al., 2009) without prior separation. Isomers with a different elemental composition can thus be resolved based on minute differences in the m/z ratio which can be observed due to the high resolution of FT-ICR-MS.

When ions have identical elemental compositions, some other physical property must be exploited to differentiate between these isomers. Often the differences in fragmentation patterns between these isomers is significant enough to resolve the different isomers and thus a near-molecular composition is obtained (Polfer et al., 2006). One of the main disadvantages of FT-ICR-MS is however the formidable cost of the device which prohibits its widespread availability and routine use (Lei et al., 2011).

Cheaper techniques can be found in the field of chromatography. Techniques such as liquid chromatography (Herod et al., 2007; Oro & Lucy, 2011), supercritical fluid chromatography (Andersson et al., 1992; Andersson et al., 1993) and gas chromatography (Zhao et al., 2014) have been used in the past to characterize a broad range of crude oil fractions. These techniques are unable to separate the large number of compounds in gas oils and vacuum gas oils and thus cannot obtain a near-molecular composition for these fractions (Dallüge et al., 2003).

Nowadays two-dimensional techniques, such comprehensive two-dimensional gas chromatography (GC × GC), are often used for the analysis of these increasingly complex crude oil derived fractions (Wang & Zhang, 2007; Adam et al., 2008a; Adam et al., 2008b; Aguiar et al., 2010; Dutriez et al., 2010b; Van Geem et al., 2010; van der Westhuizen et al., 2011). Due to the additional dimension these techniques have a significant higher peak capacity compared to conventional one-dimensional techniques (van der Westhuizen et al., 2011) and allow to obtain a

near-molecular composition of these fractions. Moreover $GC \times GC$ is significantly cheaper compared to FT-ICR-MS and thus more widely applied for routine analysis.

In this chapter a $GC \times GC$ method is applied for the analysis of heavy petroleum fractions and more specifically vacuum gas oils. The method gives a very detailed quantification based on both chemical family and carbon number. A differentiation in 11 different types of groups is made namely: n-paraffins, isoparaffins, mononaphthenes, dinaphthenes, monoaromatics, naphthenoaromatics, diaromatics, naphthenodiaromatics, triaromatics, naphthenotriaromatics and tetra-aromatics while the carbon number can range from 6 up to 46. The experimental procedure is tested using a Polywax655 sample consisting of polyethene with a narrow mass distribution and a number average molar mass of 655 g/mol and three vacuum gas oils obtained from different refineries.

2.2 Experimental

2.2.1 Samples and chemicals

Hydrogen, helium, nitrogen and air were provided at a minimum purity of 99.99% (Air Liquide, Belgium). Polywax655 was obtained from Restek. It consists of pure polyethene with a narrow mass distribution and a number average molar mass of 655 g/mol. Carbon disulfide and benzene were also purchased from Sigma-Aldrich with a minimum purity of 99.9% and 99.0% respectively. VGO A was supplied by the Total refinery (Antwerp, Belgium), VGO B by the ExxonMobil refinery (Antwerp, Belgium) and VGO C by the Shell refinery (Rotterdam, The Netherlands). An overview of the physical and chemical properties of VGO A, B and C can be found in Table 2.1. The elemental composition of the VGO's was determined using a Flash EA2000 (Interscience, Belgium) equipped with a TCD. The density was determined using a

DA-100M density meter from Mettler Toledo and the ASTM-D1160 boiling point curve was determined using a B/R 1100 ASTM-D1160 vacuum distillation apparatus from the B/R instrument corporation.

Before injection, 20 mg of Polywax was weighed and put inside a glass vial and dissolved in 7.5 ml of benzene. Prior to injection the vacuum gas oils were diluted (1v/5v) in carbon disulfide. A different solvent was used for Polywax as it did not dissolve completely in carbon disulfide.

Table 2.1: Physical and chemical properties of the vacuum gas oils

	VGO A	VGO B	VGO C
Elemental analysis (wt%)			
Carbon	87.4 ± 0.3	87.4 ± 0.3	87.1 ± 0.3
Hydrogen	12.5 ± 0.2	12.4 ± 0.2	12.4 ± 0.2
Sulfur	0.14 ± 0.02	0.25 ± 0.02	0.4 ± 0.02
Density (kg.m^{-3})	0.862	0.891	0.886
ASTM-D1160 (K)			
0%	400	469	400
5%	527	589	550
10%	548	616	573
20%	575	651	601
30%	592	674	618
40%	609	693	634
50%	622	713	652
60%	634	732	666
70%	646	750	681
80%	661	765	701
90%	675	782	726
95%	688	797	751
100%	740	820	821

2.2.2 HT-GC $\times$ GC experiments

All experiments were carried out using a Thermo Scientific TRACE GC×GC (Interscience, Belgium). A schematic overview of the setup is given in Figure 2.2**.**
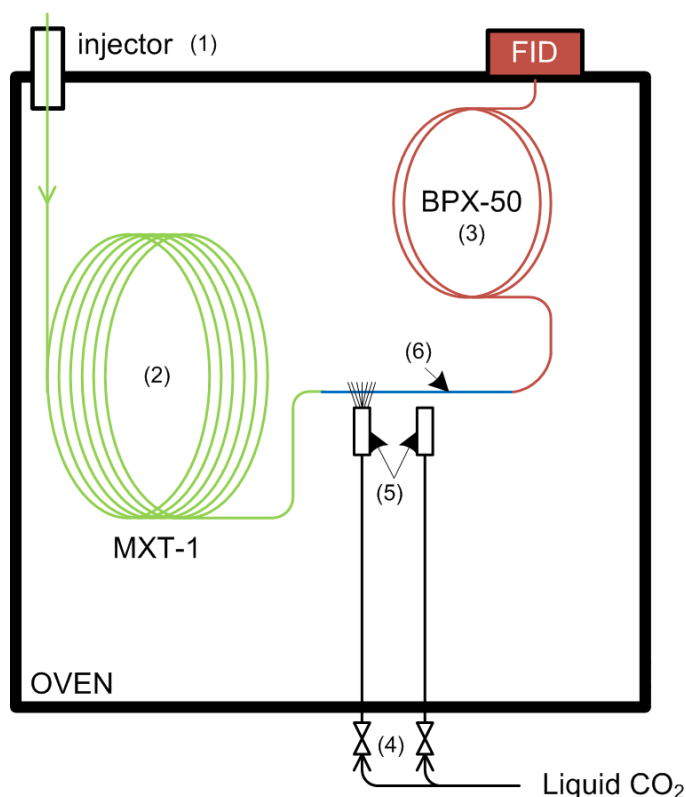
Figure 2.2: Schematic overview of the GC × GC - FID setup (1: cold-on column injector, 2: 1st dimension column, 3: 2nd dimension column, 4: solenoid valves, 5: two-jet cryogenic CO2 modulator, 6: a piece of deactivated column) after Pyl et al. (2011)

The device was equipped with a dual stage cryogenic liquid CO_2 modulator and a flame ionization detector (FID). H_2, air and N_2 (make-up gas) flow rates were respectively 35, 350 and 35 ml.min^{-1}. The detector temperature was set at 643 K and the data acquisition rate was 100 Hz. The GC × GC was equipped with a cold-on column injector. This cold-on column injector was air cooled to about 10 K below oven temperature and was connected to a retention gap (MXT®-guard column 0.30 m × 0.53 mm ID). The retention gap was connected to the first dimension column by means of an MXT connector from Restek. The first and second column were connected by a piece of deactivated fused silica column via SilTite metal ferrules from SGE. The column set consisted of a non-polar first dimension column (MXT-1, Restek,

60 m × 0.25 mm, 0.25 µm) and a mid-polar second dimension column (BPX-50, SGE, 2 m ×

0.25 mm, 0.25 µm) placed in the same oven. Helium was used as a carrier gas with a constant

flow rate of 2.1 ml.min^{-1} at the outlet of the column. The flow rate was chosen based on the

procedure developed by Beens et al. (2005) so that both columns operate near their optimum

conditions. The GC system was operated in temperature programmed conditions. The oven

temperature started at 313 K and was heated to 643 K at a rate of 3 K.min^{-1} where it is held for 10

min. The maximum temperature of the oven was limited by the second dimension column which

had a maximum operating temperature of 643 K. 2D modulation was carried out on the piece of

deactivated fused silica column in between the first and second dimension column. The

modulation period was optimized to be as low as possible to ensure maximal separation in the

first dimension without causing wrap-around. Four different modulation times were evaluated in

the range between 6 and 10 seconds, which resulted in a modulation time of 8 seconds being the

optimal one for the used column combination and samples.

Injection was carried out with a 0.5 µl on-column syringe from SGE and 0.2 µl of sample was

injected into the retention gap.

2.2.3 Quantification methodology

Data acquisition was performed using Thermo Scientific's Chrom-Card data system. The raw

data was exported to a cdf file and imported into GCImage (Zoex, USA). GCImage performed

the contour plotting, retention time measurement, peak fitting and blob integration (Reichenbach

et al., 2005). Each peak, or so called blob, was identified by both a group and a carbon number.

The different groups used in the identifications of the sample are n-paraffins, isoparaffins,

mononaphthenes, dinaphthenes, monoaromatics, naphthenoaromatics, diaromatics,

naphthenodiaromatics, triaromatics, naphthenotriaromatics and tetra-aromatics. The peak name,

1D retention time, 2D retention time and peak volume were exported as a csv file that was used for future processing. The mass fraction of each component can be calculated based on the blob volume. This can be done by internal normalization (Beens et al., 1998):

$$w_i = \frac{RF_i . V_i}{\sum_j RF_j . V_j} \tag{2.1}$$

Where w_i is the mass fraction of component i, RF_i is the relative response factor for component i and V_i is the peak volume of component i. It has been demonstrated that various isomeric hydrocarbons, produce only slightly different relative FID responses, and hence that a fair approximation of the relative response factor may be written as (Beens et al., 1998):

$$RF_i = \frac{M_i}{M_{CH4} . N_{C,i}} \tag{2.2}$$

Where M_i is the molar mass of component i, M_{CH4} is the molar mass of the reference component which in this case is methane and $N_{C,i}$ is the number of carbon atoms in component i. After identification and quantification, the composition of the sample can be used to calculate the elemental composition:

$$w_C = \sum_{i=1}^{n} w_i \frac{M_C . N_{C,i}}{M_i} \tag{2.3}$$

$$w_H = \sum_{i=1}^{n} w_i \frac{M_H . N_{H,i}}{M_i} \tag{2.4}$$

Where M_C and M_H are the molar mass of carbon and hydrogen respectively and $N_{H,i}$ is the number of hydrogen atoms in component i. Based on the data in the csv file a boiling point curve similar to the ASTM-D2887 (ASTM-D2887, 2013) can be constructed as the retention times of the paraffins can clearly be distinguished in the chromatogram. The boiling point (T_b) of a component can be calculated as:

$$T_{b,i} = T_{b,n} + \frac{t_{r,i}^{1D} - t_{r,n}^{1D}}{t_{r,n+1}^{1D} - t_{r,n}^{1D}}\left(T_{b,n+1} - T_{b,n}\right) \tag{2.5}$$

Where the subscript n stands for the n-paraffin closest to but with a lower retention time than component i while the subscript n+1 stands for the n-paraffin closest to but with a higher retention time than component I, t_R^{1D} stands for the first dimension retention time of the component and T_b stands for the boiling point of the component. The cumulative mass fraction curve is obtained by ordering the peaks or blobs by boiling point and the corresponding summation of the mass fractions.

2.3 Results and discussion

2.3.1 Establishing the maximum carbon number of the method

To establish the maximum carbon number of the method a Polywax 655 reference mixture dissolved in benzene was injected. Polywax polyethenes are fully saturated homopolymers of ethene that exhibit a high degree of linearity and crystallinity. These synthetic waxes have narrow molar mass distributions with a typical polydispersity of 1.08 and are often used to calibrate SIMDIST methods. Polywax 655 has an approximate carbon range between 20 and 100 (Wang & Firor, 2005) and therefore ideal for the intended purposes. Figure 2.3 shows the $GC \times GC$ chromatogram of the Polywax sample. It is clear that only part of the Polywax 655 sample is visible on the chromatogram as the highest carbon number after 125 minutes is only 46. At around 115 minutes or a carbon number of 42 the second dimension retention time starts to increase rapidly with increasing carbon number. At this point the oven has reached its maximum temperature of 643 K and is operating at isothermal conditions. The chromatogram also clearly shows the major solvent peak of benzene. Besides the benzene peak also a smaller peak is visible which could be a contaminant in benzene (purity of 99%) such as methylcyclopentadiene. At a

temperature of 643 K in the GC oven, i.e. near the end of the analysis, the thermal stability of these heavy hydrocarbons inside the GC column is questionable (Schwartz et al., 1987). However Hernandez-Baez et al. (2012) showed that for n-tetracontane (C40) even long exposure (20 minutes and longer) at 643 K only results in conversion well below 1%, hence, the maximum carbon number of compounds that can be quantified with the method is established at 46. Since a cold-on column injector is used, the minimum carbon number that can accurately be measured depends on the boiling point of the used solvent. Compounds with a lower boiling point than the solvent will undergo the so called "reverse solvent effect" resulting into broad and poorly separated peaks (Poole, 2012). Since carbon disulfide, which has a boiling point of 319 K, is used for the unknown samples the minimum possible carbon number will be 6 as hexane has a boiling point of 342 K.
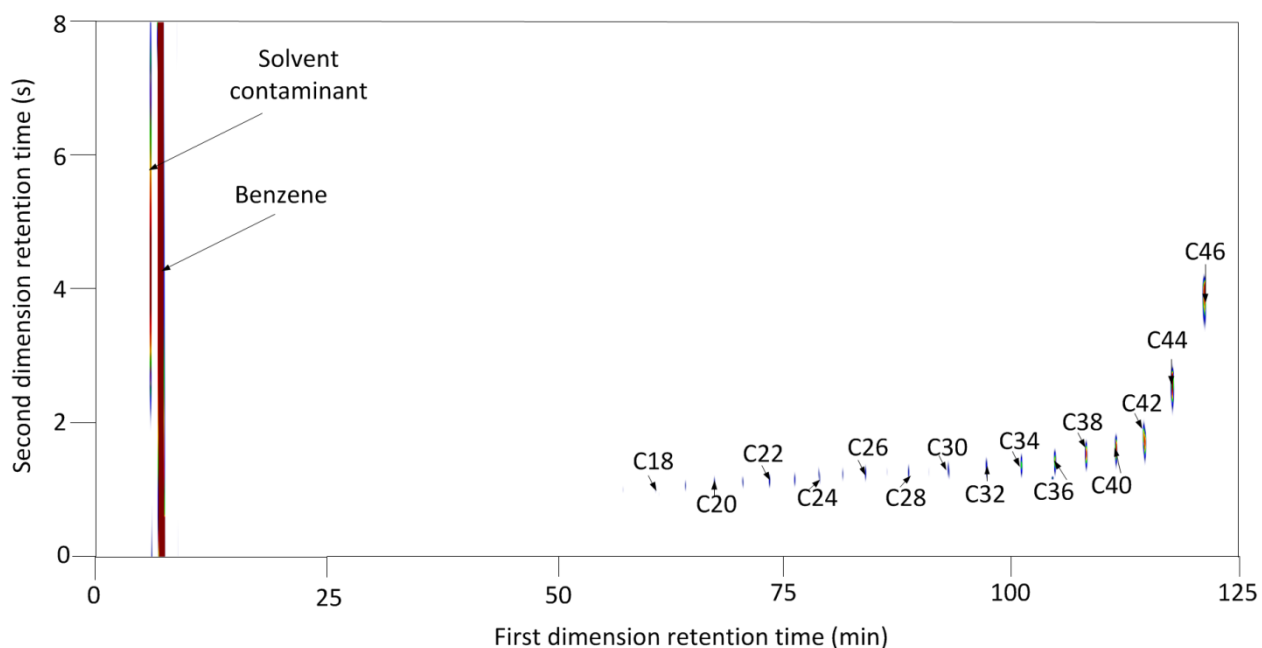
Figure 2.3: GC × GC-FID chromatogram of the polywax sample dissolved in benzene

2.3.2 Validation and reproducibility of the method

To test the repeatability of the method two repeatability tests were carried out. In the first test the injection of Polywax 655 was repeated 3 times. Although only part of the sample (up to C46) elutes, the quantification of this part should be repeatable. More specifically the part of the sample not eluting from the column, and that thus stays in the retention gap due to its high boiling point (842 K), should remain the same. Since next to the solvent benzene only n-paraffins are present in the Polywax 655 mixture the separation between the compounds is very good. The latter is confirmed by the 2D resolution, as defined by Dutriez et al. (2009):

$$Rs_{2D} = \sqrt{Rs_1^2 + Rs_2^2} = 2.\sqrt{\frac{(\Delta t_{r1})^2}{(\omega_{A1} + \omega_{B1})^2} + \frac{(\Delta t_{r2})^2}{(\omega_{A2} + \omega_{B2})^2}} \tag{2.6}$$

with Rs_1 the resolution in the first dimension of the chromatogram, R_{s2} the resolution in the second dimension of the chromatogram, Δt_{r1} the difference in retention time between compound A and B in the first dimension, Δt_{r2} the difference in retention time between compound A and B in the second dimension, ω_{A1} the peak width of compound A in the first dimension, ω_{A2} the peak width of compound A in the second dimension, ω_{B1} the peak width of compound B in the first dimension and ω_{B2} the peak width of compound B in the second dimension. Baseline separation is obtained when the resolution is at least 1.5. Applying Equation 2.6 results in a 2D resolution of at least 5 for any combination of peaks which assures baseline separation of the peaks. Table 2.2 shows the average value and the absolute and relative standard deviation of the GC × GC analysis of Polywax 655. The results in Table 2.2 are normalized to 100% although it was clear from Section 2.3.1 that not all compounds are visible on the chromatogram. From Table 2.2 it is clear that the repeatability of the method is good as the standard deviation for all compounds is within 5% of the measured values.

Table 2.2: Average mass fraction (wt%), absolute (wt%) and relative standard deviation (%) for the

normalized results of the GC × GC analysis of Polywax 655 (three repeat injections)

Name	Average (wt%)	Rel. deviation (%)	Name	Average (wt%)	Rel. deviation (%)
Tridecane	0.06±0.01	0.27	Hexacosane	1.58±0.05	3.36
Tetradecane	0.17±0.01	2.89	Heptacosane	1.20±0.06	4.68
Pentadecane	0.18±0.01	4.86	Octacosane	2.12±0.06	2.60
Hexadecane	0.45±0.01	1.25	Nonacosane	0.88±0.03	3.98
Heptadecane	0.36±0.01	3.90	Triacontane	2.38±0.04	1.57
Octadecane	0.81±0.03	3.33	Dotriacontane	2.93±0.07	2.51
Nonadecane	1.09±0.04	3.59	Tetratriacontane	4.18±0.09	2.23
Eicosane	1.13±0.05	4.38	Hexatriacontane	4.62±0.22	4.78
Heneicosane	1.50±0.07	4.52	Octatriacontane	6.76±0.12	1.84
Docosane	1.44±0.02	1.18	Tetracontane	8.45±0.33	3.95
Tricosane	1.09±0.05	4.35	Dotetracontane	12.79±0.20	1.53
Tetracosane	2.19±0.07	3.11	Tetratetracontane	17.95±0.25	1.38
Pentacosane	1.48±0.03	1.71	Hexatetracontane	22.21±0.90	4.05

In real VGO's significant peak overlap can occur due to the sheer number of compounds present in the sample. Many of these overlapping compounds, however, are from the same group making peak overlap of these compounds less of an issue. Note that overlap between different groups and different carbon numbers can still occur near the borders of these groups. To verify the effect of this overlap on the repeatability of the method, VGO A was injected three times. Figure 2.4 shows the GC × GC chromatogram of one of the injections of VGO A using a cold-on column injector. On the chromatogram the different group types that can be differentiated are shown. These include 11 different groups namely n-paraffins, isoparaffins, mononaphthenes, dinaphthenes, monoaromatics, naphthenoaromatics, diaromatics, naphthenodiaromatics, triaromatics, naphthenotriaromatics, and tetra-aromatics. In addition to the groups a carbon number can be assigned. The carbon number is assigned using the so called "roof tile" structure or ascending bands of isomeric compounds (Van Geem et al., 2010) combined with the position

of some of the important compounds inside each group (e.g. naphthalene for the diaromatics) to

obtain a starting point. This information allows to determine a very detailed group type analysis.

A detailed group type analysis of VGO A is shown in Table 2.3. Table 2.3 shows the average and

standard deviation of three repeat analysis of VGO A. Based on Table 2.3 it is clear that even

with peak overlap between different groups the repeatability of the method is good. The relative

deviation is higher than was the case for Polywax 655 but still does not exceed 8% for groups of

which the total mass fraction is at least 0.5wt%. If the total mass fraction is lower than 0.5 wt%

the overlap between other groups and the experimental error can cause the relative deviation to be

higher but the absolute deviation stays below 1000 ppmw.
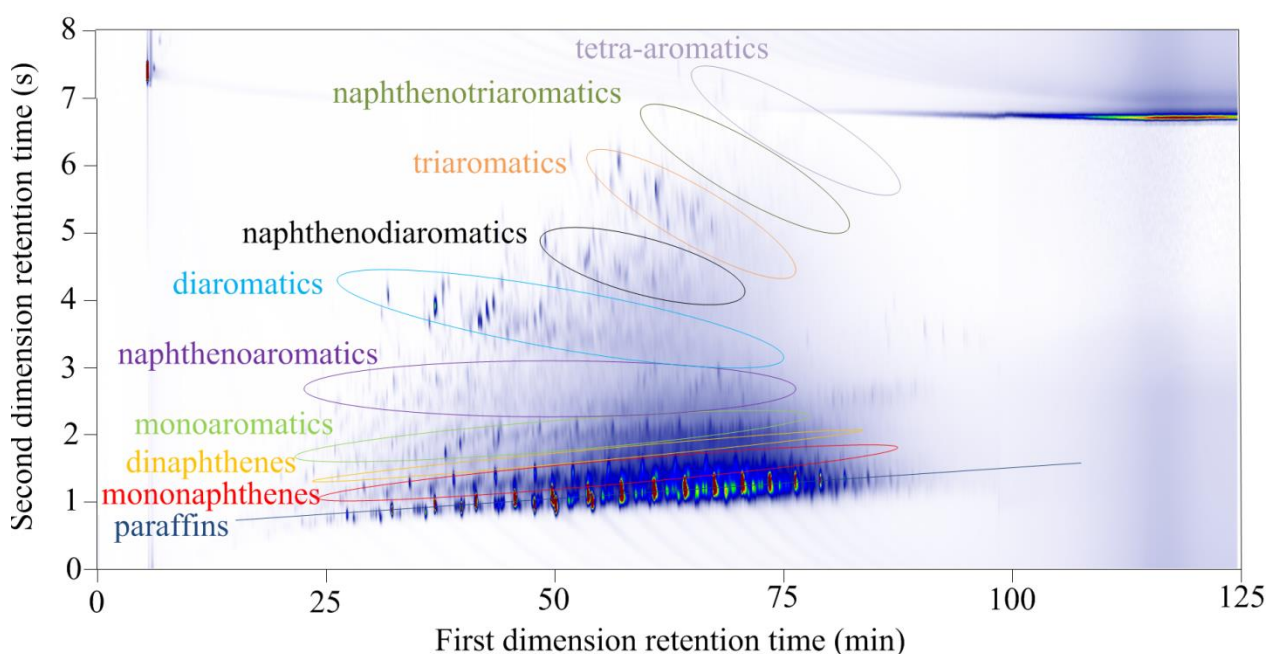
Figure 2.4: GC × GC - FID chromatogram of VGO A

To further validate the method Equations 2.3, 2.4 and 2.5 are used to calculate the elemental

composition and the boiling point curve of VGO A. Equations 2.3 and 2.4 yield 87.1 wt % of

carbon and 12.9 wt% of hydrogen respectively. Compared to the values in Table 2.1 these values

are within the error margins of the elemental analyzer and can thus be used for comparison with

those determined by GC × GC analysis. However Table 2.1 shows that next to pure hydrocarbons, sulfur containing hydrocarbons are also present. These sulfur containing hydrocarbons cannot be differentiated from the existing hydrocarbon matrix and are thus not visible by the current method. This could however be solved by using selective detectors as will be demonstrated in Chapter 3 and Chapter 4.

The boiling point curve calculated using Equation 2.5, i.e. ASTM-D2887, is compared with a boiling point curve obtained using the ASTM-D1160 method (ASTM-D1160, 2013). Since both methods obtain a different type of boiling point curve, i.e. ASTM-D1160 vs. ASTM-D2887, they were converted to the respective true boiling point curves using common conversion methods (Riazi, 2005). Figure 2.5 shows both the true boiling point curve obtained by the ASTM-D1160 method and obtained by using Equation 2.5. Both curves agree well although there are some deviations at the start and the end of the boiling point curves. In these regions the experimental error but also the conversion error is large (Riazi, 2005). Similar conclusions could be drawn for the analysis of VGO B and VGO C and their final detailed group type analysis can be found in Appendix A.

Table 2.3: Detailed group type analysis of VGO A (3 repeat injections) in wt%: P=n-paraffins, I=isoparaffins, MN=mononaphthenes, DN=dinaphthenes, MA=monoaromatics, NA=naphthenoaromatics, DA=diaromatics, NDA=naphthenodiaromatics, TrA=Triaromatics, NTrA=naphthenotriaromatics, TeA=Tetra-aromatics

#C	P	I	MN	DN	MA	NA	DA	NDA	TrA	NTrA	TeA	Total
10	n.d.	n.d.	n.d.	n.d.	n.d.	0.01 ± 0.01	n.d.	n.d.	n.d.	n.d.	n.d.	0.08 ± 0.04
11	0.04 ± 0.01	0.03 ± 0.01	0.13 ± 0.01	0.13 ± 0.01	0.05 ± 0.01	0.11 ± 0.01	0.08 ± 0.02	n.d.	n.d.	n.d.	n.d.	0.54 ± 0.09
12	0.12 ± 0.02	0.08 ± 0.02	0.26 ± 0.02	0.27 ± 0.03	0.11 ± 0.01	0.22 ± 0.01	0.44 ± 0.02	n.d.	n.d.	n.d.	n.d.	1.53 ± 0.09
13	0.22 ± 0.01	0.25 ± 0.05	0.5 ± 0.01	n.d.	n.d.	0.42 ± 0.02	0.87 ± 0.01	n.d.	n.d.	n.d.	n.d.	2.8 ± 0.07
14	n.d.	n.d.	0.84 ± 0.02	0.27 ± 0.01	0.3 ± 0.01	0.68 ± 0.01	0.84 ± 0.01	n.d.	n.d.	n.d.	n.d.	4.28 ± 0.02
15	0.63 ± 0.03	n.d.	0.9 ± 0.05	0.4 ± 0.1	0.6 ± 0.04	n.d.	0.78 ± 0.02	0.76 ± 0.02	0.26 ± 0.01	n.d.	n.d.	5.8 ± 0.1
16	1.02 ± 0.01	0.76 ± 0.04	1.06 ± 0.01	0.3 ± 0.1	1.29 ± 0.03	0.88 ± 0.04	1.26 ± 0.06	0.88 ± 0.02	0.57 ± 0.03	n.d.	n.d.	8.2 ± 0.1
17	1.12 ± 0.04	1.2 ± 0.05	1.32 ± 0.02	n.d.	0.73 ± 0.01	1.1 ± 0.05	0.8 ± 0.04	1.05 ± 0.03	0.68 ± 0.02	n.d.	0.06 ± 0.02	8.6 ± 0.1
18	1.8 ± 0.02	1.6 ± 0.08	1.23 ± 0.03	n.d.	1.1 ± 0.05	1.49 ± 0.01	0.72 ± 0.04	1 ± 0.05	0.7 ± 0.02	0.12 ± 0.01	0.05 ± 0.01	9.8 ± 0.2
19	1.95 ± 0.03	2.03 ± 0.07	1.98 ± 0.03	n.d.	1.06 ± 0.01	n.d.	0.68 ± 0.02	1 ± 0.04	0.52 ± 0.02	0.2 ± 0.02	n.d.	11.16 ± 0.06
20	1.6 ± 0.05	1.38 ± 0.03	1.74 ± 0.02	n.d.	1.32 ± 0.03	n.d.	0.9 ± 0.05	0.72 ± 0.01	0.57 ± 0.03	0.15 ± 0.05	n.d.	8.5 ± 0.1
21	1.82 ± 0.07	1.71 ± 0.03	1.8 ± 0.03	n.d.	2.03 ± 0.07	n.d.	0.58 ± 0.02	0.54 ± 0.03	0.1 ± 0.02	n.d.	n.d.	8.75 ± 0.07
22	1.2 ± 0.05	1.5 ± 0.05	1.58 ± 0.02	n.d.	1.8 ± 0.05	n.d.	0.34 ± 0.01	n.d.	0.1 ± 0.02	n.d.	n.d.	6.6 ± 0.03
23	1.38 ± 0.03	2 ± 0.04	1.16 ± 0.04	n.d.	1.92 ± 0.06	n.d.	n.d.	n.d.	n.d.	n.d.	n.d.	6.9 ± 0.02
24	1.25 ± 0.05	1.83 ± 0.03	0.7 ± 0.02	n.d.	1.5 ± 0.05	n.d.	n.d.	n.d.	n.d.	n.d.	n.d.	5.37 ± 0.03
25	1 ± 0.05	1.36 ± 0.04	n.d.	n.d.	1.47 ± 0.03	n.d.	n.d.	n.d.	n.d.	n.d.	n.d.	3.84 ± 0.06
26	0.5 ± 0.02	1.15 ± 0.05	n.d.	n.d.	1.02 ± 0.02	n.d.	n.d.	n.d.	n.d.	n.d.	n.d.	2.73 ± 0.03
27	0.22 ± 0.01	0.84 ± 0.03	n.d.	n.d.	n.d.	n.d.	n.d.	n.d.	n.d.	n.d.	n.d.	1.06 ± 0.02
28	n.d.	0.72 ± 0.03	n.d.	n.d.	n.d.	n.d.	n.d.	n.d.	n.d.	n.d.	n.d.	0.9 ± 0.03
29	0.07 ± 0.07	0.46 ± 0.02	n.d.	n.d.	n.d.	n.d.	n.d.	n.d.	n.d.	n.d.	n.d.	0.54 ± 0.09
30	0.08 ± 0.08	0.4 ± 0.1	n.d.	n.d.	n.d.	n.d.	n.d.	n.d.	n.d.	n.d.	n.d.	0.56 ± 0.07
31	0.08 ± 0.04	0.27 ± 0.03	n.d.	n.d.	n.d.	n.d.	n.d.	n.d.	n.d.	n.d.	n.d.	0.35 ± 0.07
32	n.d.	0.25 ± 0.05	n.d.	n.d.	n.d.	n.d.	n.d.	n.d.	n.d.	n.d.	n.d.	0.3 ± 0.05
Total	17.00 ± 0.2	21.20 ± 0.2	15.39 ± 0.03	2.2 ± 0.2	16.80 ± 0.1	7.40 ± 0.1	8.43 ± 0.03	6.40 ± 0.08	3.92 ± 0.04	0.60 ± 0.06	0.14 ± 0.01	100
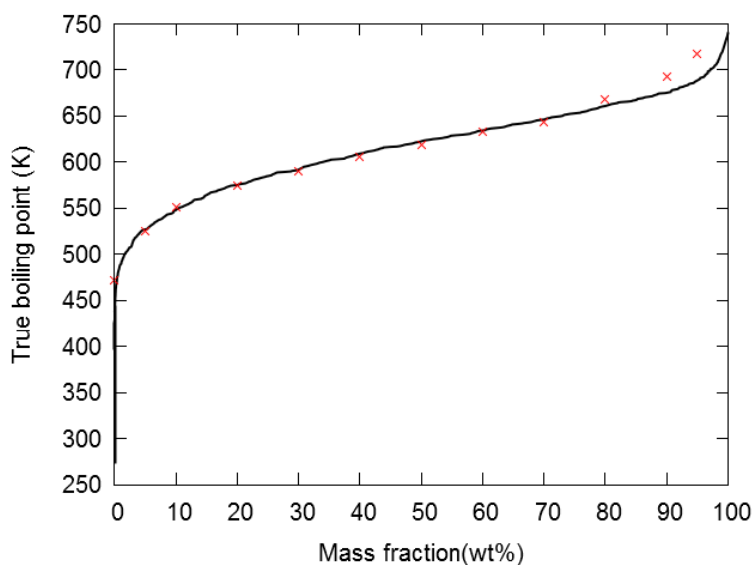
Figure 2.5: True boiling point curve obtained using ASTM-D1160 ($\times$) and calculated from Equation 2.5 using the GC $\times$ GC chromatogram (▬) and after conversion to the true boiling point curve using common conversion methods (Riazi, 2005)

2.4 Conclusions

The increasing complexity of detailed kinetic models dictates improvements to the current analytical techniques to obtain a near-molecular composition of fractions as complex as atmospheric and vacuum gas oils. These fractions can easily contain over one million different compounds and the characterization of these fractions remains difficult. In this chapter an analytical technique which is able to obtain the required near-molecular composition of these fractions was tested. The method used high-temperature comprehensive two dimensional gas chromatography to obtain a detailed group type analysis of the vacuum gas oils. A distribution into 11 different groups is made namely n-paraffins, isoparaffins, mononaphthenes, dinaphthenes, monoaromatics, naphthenoaromatics, diaromatics, naphthenodiaromatics, triaromatics, naphthenotriaromatics, and tetra-aromatics and for each group a distribution according the carbon number is obtained. The carbon number can range from 6 up to 46. The method gives consistent

results with a relative standard deviation lower than 8% as long as there is more than 5000 ppmw

of the specific (pseudo-)component. For compounds with lower values the absolute error does not

exceed 1000 ppmw. The calculated elemental composition and boiling point curve based on the

$GC \times GC$ analysis agrees well with the values determined using other experimental methods. A

major shortcoming of the method is its inability to differentiate hetero-atom containing

hydrocarbons such as sulfur containing hydrocarbons but a selective detector, such as a sulfur or

nitrogen chemiluminescence detector can solve this issue.

2.5 References

Adam, F., Bertoncini, F., Coupard, V., Charon, N., Thiébaut, D., Espinat, D., & Hennion, M.-C. (2008a). Using comprehensive two-dimensional gas chromatography for the analysis of oxygenates in middle distillates: I. Determination of the nature of biodiesels blend in diesel fuel. Journal of Chromatography A, 1186, 236-244.

Adam, F., Bertoncini, F., Thiebaut, D., Hennion, M. C., Lahoutifard, N., & Addinall, A. (2008b). Comprehensive 2D GC for achieving nitrogen speciation in middle distillates. LC-GC North America, 21, 39.

Aguiar, A., Silva, A. I., Azevedo, D. A., & Neto, F. R. A. (2010). Application of comprehensive two-dimensional gas chromatography coupled to time-of-flight mass spectrometry to biomarker characterization in Brazilian oils. Fuel, 89, 2760-2768.

Andersson, P. E., Demirbüker, M., & Blomberg, L. G. (1992). Quantitative hydrocarbon group analysis of gasoline and diesel fuel by supercritical fluid chromatography. Journal of Chromatography A, 595, 301-311.

Andersson, P. E., Demirbüker, M., & Blomberg, L. G. (1993). Characterization of fuels by multi-dimensional supercritical fluid chromatography and supercritical fluid chromatography—mass spectrometry. Journal of Chromatography A, 641, 347-355.

ASTM-D1160, 2013, Standard Test Method for Distillation of Petroleum Products at Reduced Pressure.ASTM International, West Conshohocken, PA, 2003, DOI:10.1520/D1160

ASTM-D2887, 2013, Standard Test Method for Boiling Range Distribution of Petroleum Fractions by Gas Chromatography.ASTM International, West Conshohocken, PA, 2003, DOI:10.1520/D2887

Beens, J., Boelens, H., Tijssen, R., & Blomberg, J. (1998). Quantitative Aspects of Comprehensive Two-Dimensional Gas Chromatography (GC×GC). Journal of High Resolution Chromatography, 21, 47-54.

Beens, J., Janssen, H.-G., Adahchour, M., & Brinkman, U. A. T. (2005). Flow regime at ambient outlet pressure and its influence in comprehensive two-dimensional gas chromatography. Journal of Chromatography A, 1086, 141-150.

Dallüge, J., Beens, J., & Brinkman, U. A. T. (2003). Comprehensive two-dimensional gas chromatography: a powerful and versatile analytical tool. Journal of Chromatography A, 1000, 69-108.

Dutriez, T., Courtiade, M., Thiébaut, D., Dulot, H., Bertoncini, F., & Hennion, M.-C. (2010a). Extended characterization of a vacuum gas oil by offline LC-high-temperature comprehensive two-dimensional gas chromatography. Journal of Separation Science, 33, 1787-1796.

Dutriez, T., Courtiade, M., Thiebaut, D., Dulot, H., Bertoncini, F., Vial, J., & Hennion, M. C. (2009). High-temperature two-dimensional gas chromatography of hydrocarbons up to nC(60) for analysis of vacuum gas oils. Journal of Chromatography A, 1216, 2905-2912.

Dutriez, T., Courtiade, M., Thiebaut, D., Dulot, H., & Hennion, M. C. (2010b). Improved hydrocarbons analysis of heavy petroleum fractions by high temperature comprehensive two-dimensional gas chromatography. Fuel, 89, 2338-2345.

Fernandez-Lima, F. A., Becker, C., McKenna, A. M., Rodgers, R. P., Marshall, A. G., & Russell, D. H. (2009). Petroleum Crude Oil Characterization by IMS-MS and FTICR MS. Analytical Chemistry, 81, 9941-9947.

Fu, J., Klein, G. C., Smith, D. F., Kim, S., Rodgers, R. P., Hendrickson, C. L., & Marshall, A. G. (2006). Comprehensive Compositional Analysis of Hydrotreated and Untreated Nitrogen-Concentrated Fractions from Syncrude Oil by Electron Ionization, Field Desorption Ionization, and Electrospray Ionization Ultrahigh-Resolution FT-ICR Mass Spectrometry. Energy & Fuels, 20, 1235-1241.

Hernandez-Baez, D. M., Tohidi, B., Chapoy, A., Bounaceur, R., & Reid, A. (2012). Establishing the Maximum Carbon Number for Reliable Quantitative Gas Chromatographic Analysis of Heavy Ends Hydrocarbons. Part 1: Low-Conversion Thermal Cracking Modeling. Energy & Fuels, 26, 2600-2610.

Herod, A. A., Bartle, K. D., & Kandiyoti, R. (2007). Characterization of heavy hydrocarbons by chromatographic and mass spectrometric methods: An overview. Energy & Fuels, 21, 2176-2203.

Lei, Z., Huhman, D. V., & Sumner, L. W. (2011). Mass Spectrometry Strategies in Metabolomics. Journal of Biological Chemistry, 286, 25435-25442.

Liu, P., Shi, Q., Pan, N., Zhang, Y., Chung, K. H., Zhao, S., & Xu, C. (2011). Distribution of Sulfides and Thiophenic Compounds in VGO Subfractions: Characterized by Positive-Ion Electrospray Fourier Transform Ion Cyclotron Resonance Mass Spectrometry. Energy & Fuels, 25, 3014-3020.

Oro, N. E., & Lucy, C. A. (2011). High performance liquid chromatographic separations of gas oil samples and their hydrotreated products using commercial normal phases. Journal of Chromatography A, 1218, 7788-7795.

Polfer, N. C., Valle, J. J., Moore, D. T., Oomens, J., Eyler, J. R., & Bendiak, B. (2006). Differentiation of isomers by wavelength-tunable infrared multiple-photon dissociation-mass spectrometry: Application to glucose-containing disaccharides. Analytical Chemistry, 78, 670-679.

Poole, C. (2012). Gas chromatography (First edition): Elsevier.

Pyl, S. P., Schietekat, C. M., Reyniers, M. F., Abhari, R., Marin, G. B., & Van Geem, K. M. (2011). Biomass to olefins: Cracking of renewable naphtha. Chemical Engineering Journal*, 176*, 178-187.

Reichenbach, S. E., Kottapalli, V., Ni, M. T., & Visvanathan, A. (2005). Computer language for identifying chemicals with comprehensive two-dimensional gas chromatography and mass spectrometry. Journal of Chromatography A*, 1071*, 263-269.

Riazi, M. R. (2005). Characterization of petroleum fractions: ASTM International.

Schwartz, H. E., Brownlee, R. G., Boduszynski, M. M., & Su, F. (1987). Simulated distillation of high-boiling petroleum fractions by capillary supercritical fluid chromatography and vacuum thermal gravimetric analysis. Analytical Chemistry*, 59*, 1393-1401.

van der Westhuizen, R., Ajam, M., De Coning, P., Beens, J., de Villiers, A., & Sandra, P. (2011). Comprehensive two-dimensional gas chromatography for the analysis of synthetic and crude-derived jet fuels. Journal of Chromatography A*, 1218*, 4478-4486.

Van Geem, K. M., Pyl, S. P., Reyniers, M. F., Vercammen, J., Beens, J., & Marin, G. B. (2010). On-line analysis of complex hydrocarbon mixtures using comprehensive two-dimensional gas chromatography. Journal of Chromatography A*, 1217*, 6623-6633.

Wang, C., & Firor, R. (2005). High-Temperature Simulated Distillation System Based on the 6890N GC: Agilent Technologies.

Wang, F. C. Y., & Zhang, L. (2007). Chemical composition of group II lubricant oil studied by high-resolution gas chromatography and comprehensive two-dimensional gas chromatography. Energy & Fuels*, 21*, 3477-3483.

Zhao, Y., Hong, B., Fan, Y. Q., Wen, M., & Han, X. (2014). Accurate analysis of polycyclic aromatic hydrocarbons (PAHs) and alkylated PAHs homologs in crude oil for improving the gas chromatography/mass spectrometry performance. Ecotoxicology and Environmental Safety*, 100*, 242-250.

Chapter 3: Combined analysis of PAH/PASH in hydrocarbon matrices using GC × GC

3.1 Abstract

A new gas chromatographic method has been developed which is able to quantify polycyclic aromatic hydrocarbons (PAH) and polycyclic aromatic sulfur containing hydrocarbons (PASH) up to 4 rings. The method combines the power of both a flame ionization detector (FID) and a sulfur chemiluminescence detector (SCD) in series on a single comprehensive two-dimensional GC (GC × GC) and provides mass fractions of compounds separated by carbon number n ($C_nH_xS_y$) and class. In addition to PAH and PASH separation the method is extended towards non- and mono-aromatic (sulfur containing) compounds (paraffins, naphthenes, monoaromatics, thiols, sulfides, disulfides and thiophenes). The 95% confidence interval is doubled when a single injection technique is used instead of a more accurate double injection technique. A flexible correction procedure which combines the advantages of the two dimensional separation of GC × GC and its ability to easily define overlapping groups between the FID and the SCD chromatograms is applied. The method is validated using theoretical reference mixtures and is applied on three commercial gas oils with sulfur content from 0.16 wt% up to 1.34 wt%. The repeatability is good with an average of 3.4% which is in the same range as the much more expensive FT-ICR-MS technique.

Keywords: GC × GC, Sulfur chemiluminescence detector, sulfur, gas oil, polycyclic aromatic compounds, polycyclic aromatic sulfur containing compounds

3.2 Introduction

Crude oil is a complex mixture containing a wide variety of compounds such as alkanes, naphthenes, olefins, monoaromatics and Polycyclic Aromatic Hydrocarbons (PAH). In addition to these hydrocarbons crude oil consists of a significant fraction of heteroatom containing compounds, with sulfur being the principal hetero-element present in crude oils (Liu et al., 2010). Despite the low content of sulfur in light fractions, e.g. naphtha, sulfur can represent up to 6 wt% of the total elemental content in heavier fractions, e.g. vacuum gas oils (Dutriez et al., 2009). Sulfur containing compounds found in crude oils include thiols, sulfides, thiophenes, benzothiophenes, dibenzothiophenes and homologues. Benzothiophenes, dibenzothiophenes and higher sulfur containing ring systems are often called Polycyclic Aromatic Sulfur containing Hydrocarbons (PASH). These sulfur compounds can induce air pollution in the form of sulfur oxides (SO_x) during combustion, promote corrosion and bad odor in fuels, as well as poison the catalyst (Mahe et al., 2011). Detailed information on the distribution and the type of sulfur containing compounds in middle distillates is essential for improving desulfurization technology (Hua et al., 2003). Also for steam cracking small quantities of sulfur compounds can drastically influence coke formation (Reyniers & Froment, 1995; Wang et al., 2008), and accurate quantification of the type and quantity of the sulfur containing compounds is crucial.

Several standardized methods for the detection of PAH have been developed. ASTM-D6591 is a method to determine the aromatic hydrocarbon types in middle distillates by high performance liquid chromatography with a refractive index detector (ASTM-D6591, 2011). ASTM-D6379 also uses high performance liquid chromatography with a refractive index detector but is used for aviation fuels and petroleum distillates (ASTM-D6379, 2011). ASTM-D5186 is a method for the determination of the aromatic content and polynuclear aromatic content of diesel fuels and

aviation turbine fuels by supercritical fluid chromatography (ASTM-D5186, 2009). ASTM-D2425 is a test method for different hydrocarbon types in middle distillates by mass spectrometry (ASTM-D2425, 2009). One of the main weaknesses of all the above methods is that they incorrectly quantify the amount of PAH when sulfur containing compounds are present (ASTM-D2425, 2009; ASTM-D5186, 2009; ASTM-D6379, 2011; ASTM-D6591, 2011). Quantifying sulfur compounds is very laborious and time consuming due to the complexity of sulfur compound isomers and the matrix consisting of an excess of hydrocarbons with similar properties. Standard methods for the quantification of the total amount of sulfur e.g. ASTM-D2622 (2010) and ASTM-D5453 (2012), or specific sulfur compounds, e.g. ASTM-D5504 (2012), have been developed but no standard method is currently available that can quantify the sulfur containing hydrocarbons separately to the authors' knowledge. The latter also implies that there is no standard method available which could quantify both PAH and sulfur containing hydrocarbons simultaneously. Next to ASTM methods gas chromatography-mass spectrometry (GC-MS) methods have been developed for the detection and quantification of sulfur containing hydrocarbons. However this technique is not purely selective towards sulfur compounds (Kelly L.C., 2010) because the hydrocarbon matrix fragmentation pattern will often interfere due to orders of magnitude differences in concentrations between these chemical structures (Stumpf et al., 1998). One of these methods is Robinson's method (Robinson, 1971), a mass spectrometric procedure, which can determine up to 21 compound types in aromatic petroleum fractions including different types of PAH and PASH. It has been reported that this method fails when thiols and sulfides are present since these compounds tend to be distributed along the saturated types (Robinson, 1971). To solve some of these problems sulfur selective detectors are widely applied because they allow a straightforward quantification of sulfur containing hydrocarbons.

Several types of sulfur detectors exist such as the Sulfur Chemiluminescence Detector (SCD) (Xu et al., 1995; Lee & Ubanyionwu, 2008), the Atomic Emission Detector (AED) (Stumpf et al., 1998; Pang et al., 2010; Moustafa & Andersson, 2011) and the Flame Photometric Detector (FPD) (Schulz et al., 1999). The main advantage of SCD and AED detectors is that the response is more or less linear and equimolar to the amount of sulfur (Adlard, 1995), which bypasses the need for calibration of these detectors. On the contrary the response of the FPD detector is nonlinear, not equimolar (Adlard, 1995; Del Río et al., 2011) and has a limited dynamic range making calibration very time consuming. In addition the FPD exhibits quenching of the sulfur response from co-eluting hydrocarbons, which increases the detection limit. The newest generation FPD, the so-called pulsed flame photometric detector (pFPD), allows to overcome the reduced sensitivity and equimolar response but still exhibits quenching of the sulfur response, a non-linear increase of the signal with the concentration (Del Río et al., 2011) and a limited dynamic range. With the rise of GC × GC all these selective detectors can nowadays be coupled to two-dimensional (2D) techniques such as GC × GC - MS (Ong et al., 2003; Ávila et al., 2012; Pena-Abaurrea et al., 2012; Ventura et al., 2012; Rathsack & Otto, 2014), GC × GC - FPD (Chin et al., 2010), GC × GC - pFPD (Zeigler et al., 2012), GC × GC - AED (van Stee et al., 2003), and GC × GC - SCD (Hua et al., 2003; Hua et al., 2004; Ruiz-Guerrero et al., 2006; Mahe et al., 2011; Dutriez et al., 2013) but all the previously mentioned advantages and disadvantages still hold. The acquisition rate of the AED detector is also too slow to be used quantitatively in GC × GC - AED (van Stee et al., 2003) without artificially increasing peak width in the second dimension and thus decreasing the resolution.

The SCD has also been successfully coupled to other comprehensive techniques such as LC-GC-FID-SCD (Beens & Tijssen, 1997), TLC-GC-FID-SCD (Bacaud et al., 2002) and

SFC-GC × GC-SCD (Dutriez et al., 2013) to identify various sulfur containing compounds in hydrotreated gas oils (Bacaud et al., 2002). Obviously when using selective detectors only information about the sulfur compounds is obtained and no information regarding both the PAH and the PASH distribution is obtained separately.

Next to chromatographic techniques purely spectroscopic techniques such as FTICR-MS are also available (Liu et al., 2010; Liu et al., 2011; Ávila et al., 2012). The advantage of the latter is that it can identify the elemental composition, double bond equivalents (rings plus double bonds to carbon), and carbon number, based on ultra-high-resolution and accurate mass measurements (Fernandez-Lima et al., 2009). However, a disadvantage of FTICR-MS is its high cost which prohibits its widespread availability and routine use (Lei et al., 2011).

To overcome the limitations of the currently available methods for analyzing sulfur containing fractions a new characterization method which gives quantitative information about the PAH and PASH distribution per carbon atom needs to be developed. The method proposed in this work combines the sensitivity and straight forward calibration of a FID and a SCD with the increased separation power of a GC × GC. Quantitative information about the content of PAH and PASH compounds can be obtained in a single run or two separate runs. The GC × GC results in structured ordering of peaks in the 2D chromatogram without wrap around, i.e. the roof-tile effect, if modulation time, column length and carrier gas flow rate are properly selected (Van Geem et al., 2010). The method also allows to determine the elemental composition and validation of other analytical techniques e.g. elemental analysis.

3.3 Experimental

3.3.1 Samples and chemicals

Analytical gases (helium, nitrogen, hydrogen and air) were provided at a minimum purity of 99.99% (Air Liquide, Belgium). Heptane, decane, dodecane, hexadecane, toluene, styrene, naphthalene, bromobenzene and 1,2-benzodiphenylene sulfide were purchased from Sigma-Aldrich with a minimum purity of 99%. Phenanthrene, fluoranthene, 1pentanethiol, thiophenes, benzothiophene, 3methylbenzothiophene, dibenzothiophenes and 3chlorothiophene were purchased from Sigma-Aldrich with a minimum purity of 98% and 1decanethiol was purchased from Sigma-Aldrich with a minimum purity of 96%.

Gas oils A, B and C were supplied by the Total refinery in Antwerp, Belgium. The elemental composition of gas oils A, B and C was determined using a Flash EA2000 (Interscience, Belgium) equipped with both a TCD and FPD detector. For sulfur concentrations larger than 5000 ppm the TCD detector was used while for sulfur concentrations lower than 5000 ppm the FPD detector was used. The elemental composition is based on three repeat analyses of each of the gas oils and can be found in Table 3.1. The uncertainty on the amount of sulfur detected with this method is within vendor specifications.

Table 3.1: Measured elemental (C, H & S) composition of the three gas oils by FLASH 2000 elemental

analyzer and using the GC × GC composition

	Elemental analyzer			GC × GC		
	Carbon (wt%)	Hydrogen (wt%)	Sulfur (wt%)	Carbon (wt%)	Hydrogen (wt%)	Sulfur (wt%)
Gas oil A	85.6 ± 0.3	13.0 ± 0.2	1.34 ± 0.02	85.3	13.4	1.30
Gas oil B	85.7 ± 0.3	13.4 ± 0.2	0.84 ± 0.02	85.4	13.7	0.83
Gas oil C	86.5 ± 0.3	13.3 ± 0.2	0.16 ± 0.01	86.2	13.6	0.16

3.3.2 Sample preparation

In order to validate the method three synthetic test mixtures containing typical PAH (toluene, styrene, naphthalene, phenanthrene, fluoranthene) and PASH (benzothiophene, 2-methyl benzothiophene, dibenzothiophene, 1,2-benzodiphenylene sulfide) compounds as well as some other typical hydrocarbon (decane, dodecane, hexadecane) and sulfur containing compounds (1-pentanethiol, 1-decanethiol) were prepared and dissolved in heptane. The composition of the test mixtures can be found in Table 3.2. Test mixtures 1 and 2 are representative for the hydrocarbons, PAH and sulfur containing hydrocarbons found in fossil derived fractions from crude and shale oils. Test mixture 1 contains a large amount of sulfur typical for an untreated crude oil fraction, while test mixture 2 contains a low amount of sulfur representative for a mildly hydrotreated fraction. Test mixture 3 is a mixture containing very few compounds (heptane, 3-chlorothiophene, phenanthrene and dibenzothiophenes) at realistic concentration levels for phenanthrene and dibenzothiophene.

Before analysis of the gas oil samples 3-chlorothiophene and bromobenzene were added as internal standards. For the FID analysis the samples contain around 2 wt% of bromobenzene while for the SCD analysis the samples contain around 400 ppmw of 3-chlorothiophene.

Table 3.2. Composition of the test mixtures

Compounds	Mass fraction Mixture 1 (wt%)	Mass fraction Mixture2 (wt%)	Mass fraction Mixture3 (wt%)	1D retention time (min)
Hydrocarbons				
Heptane	Rest	Rest	Rest	7.1
Toluene	1.10	0.00	0.00	8.7
Styrene	1.39	3.19	0.00	13.7
Bromobenzene	0.00	6.13	0.00	15.8
Decane	0.00	2.67	0.00	20.3
Naphthalene	1.26	3.87	0.00	28.1
Dodecane	1.14	2.83	0.00	29.7
Hexadecane	1.37	3.05	0.00	46.8
Phenanthrene	1.07	2.37	2.07	52.3
Fluoranthene	0.61	1.40	0.00	61.5
Sulfur containing				
Thiophene	1.40	0.25	0.00	5.7
1-pentanethiol	1.31	0.20	0.00	10.4
3-chlorothiophene	1.93	0.34	2.87	11.9
Benzothiophene	1.03	0.31	0.00	27.9
2-methylbenzothiophene	1.66	0.27	0.00	33.6
1-decanethiol	1.03	0.20	0.00	35.2
Dibenzothiophene	0.93	0.29	0.31	51.2
1,2-benzodiphenylene sulfide	0.26	0	0.00	70.5

3.3.3 GC × GC - SCD/FID analysis

All experiments were carried out using a Thermo Scientific TRACE GC × GC (Interscience, Belgium), see Figure 3.1. For modulation the device is equipped with a dual stage cryogenic liquid CO_2 modulator. The device is equipped with both a FID and a SCD which are in series to each other with the FID being the first detector. This allows analyzing a sample both on the FID and the SCD in a single run. However, the single run technique requires that at least two internal standards are used, one for the hydrocarbon compounds and one for the sulfur compounds, because of the large difference in concentration between hydrocarbons (wt% level) and sulfur

compounds (ppm level) in crude oil fractions. In addition, to ensure reasonable sensitivity on both detectors an optimal split flow rate and a detector range need to be determined. In our case these optimal conditions corresponded to a maximal sensitivity on the SCD without exceeding the linear range of the FID detector. The results of analyzing under these conditions is compared with the scenario in which each of the detectors is used under its own optimal conditions, i.e. maximal sensitivity either on the FID or on the SCD. The optimal split flow rate for the FID detector was found to be 50 ml.min^{-1} at a FID detector range of 10 while the optimal split flow rate for the SCD was found to be 10 ml.min^{-1} where the FID detector range was set at 100. The suboptimal split flow rate for both the FID and the SCD detector was found to be 50 ml.min^{-1} at a FID detector range of 10. Different concentrations of sulfur could, of course, influence these optimal conditions. For the FID H_2, air and N_2 (make-up gas) flow rates were respectively 35, 350 and 35 ml.min^{-1}. The FID temperature was set at 523 K and its acquisition rate was 100 Hz. The SCD consisted of the 355 Sulfur Chemiluminescence Detector from Agilent and was coupled to the FID using an adapter supplied by Agilent. For the SCD the H_2 and air flow rates were set at 45 and 5 ml.min^{-1}, respectively, while the burner temperature was set at 1073 K. The acquisition rate of the SCD was set at 100 Hz. The split/splitless injector temperature was set at 523 K. The column set consisted of a non-polar first dimension column (Rtx-1 PONA, Restek, 50 m × 0.25 mm × 0.5 μm) and a mid-polar second dimension column (BPX-50, SGE, 2 m × 0.15 m, 0.15 μm) placed in the same oven. The first and the second column were connected to each other with a piece of deactivated fused silica column by means of a SilTite™ metal ferrule from SGE. 2D modulation was carried out on a piece of deactivated column. The modulation period was optimized to be as low as possible to ensure maximal separation in the first dimension without causing wrap-around. Four different modulation times were evaluated in the range between 5 and

8 seconds, which resulted in a modulation time of 6 seconds being the optimal one for the used column combination and samples.
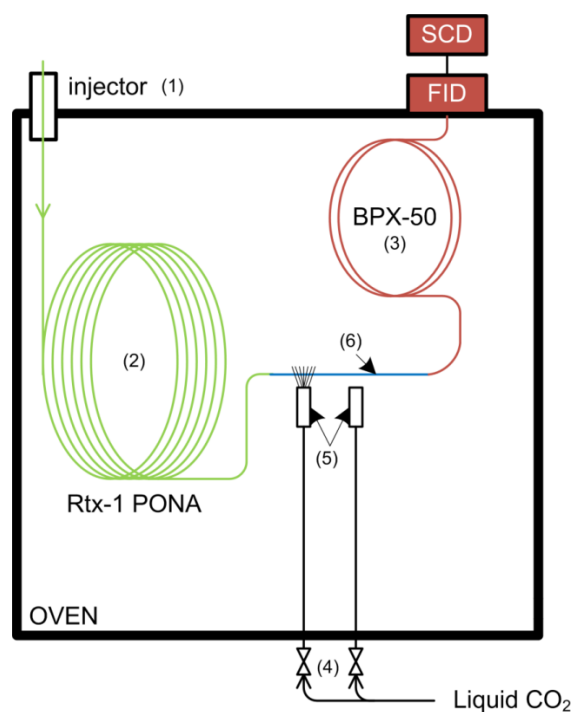
Figure 3.1: Schematic overview of the GC × GC - FID/SCD setup (1: split/splitless injector, 2: 1st dimension column, 3: 2nd dimension column, 4: solenoid valves, 5: two-jet cryogenic CO2 modulator, 6: a piece of deactivated column)

Helium was used as a carrier gas with a constant flow rate of 2.1 ml.min^{-1} at the outlet of the column. The flow rate was chosen based on the calculations of Beens et al. (2005) so that both columns operate near their optimum conditions. The GC system was operated under programmed temperature conditions. The oven program starts at 313 K and goes up to 573 K at a rate of 3K/min. The temperature is held constant at 573 K for 10 min.

To validate the proposed quantification method peak overlap was forced for test mixture 3 between dibenzothiophene and phenanthrene while keeping the internal standard (3-chlorothiophene) separated. Alternative conditions for this forced overlap were obtained. In this

case the oven temperature went from 323 K to 573 K at a rate of 120 K/min. The temperature

was then held constant at 573 K for 10 min. The carrier gas flow rate was set at 5.0 ml.min^{-1}. The

conditions for the GC × GC for the different operation modes are summarized in Table 3.3.

Table 3.3: Overview of the GC × GC conditions

Detector	Gas oils and Test mixture 2			Test mixture 1	Test mixture 3
	FID/SCD sub optimized	FID	SCD	FID and SCD	FID and SCD

Injection
  Temperature
  Split flow
	523 K
	50 ml.min^{-1}
		523 K
		50 ml.min^{-1}
			523 K
			10 ml.min^{-1}
				523 K
				50 ml.min^{-1}
					523 K
					150 ml.min^{-1}

Carrier gas	2.1 ml.min^{-1}	2.1 ml.min^{-1}	2.1 ml.min^{-1}	2.1 ml.min^{-1}	5.0 ml.min^{-1}
Oven program	313 to 573K at 3K/min 10 min at 573K	313 to 573K at 3K/min 10 min at 573K	313 to 573K at 3K/min 10 min at 573K	313 to 573K at 3K/min 10 min at 573K	313 to 573K at 120K/min 10 min at 573K
Modulation time	6 s	6 s	6 s	6 s	6s

Detection
  FID
    Temperature
    Range
    Acquisition rate
  SCD
    Temperature
    Acquisition rate
	523 K
	10
	100 Hz
	
	1073 K
	100 Hz
		523 K
		10
		100 Hz
		
		1073 K
		100 Hz
			523 K
			10
			100 Hz
			
			1073 K
			100 Hz
				523 K
				10
				100 Hz
				
				1073 K
				100 Hz
					523 K
					10
					100 Hz
					
					1073 K
					100 Hz

3.4 Quantification methodology

3.4.1 Data acquisition

Data acquisition was performed using Thermo Scientific's Chrom-Card data system. The raw data was exported to a cdf file and imported into GCImage (Zoex, USA). GCImage performed the contour plotting, retention time measurement, peak fitting and blob integration (Reichenbach et al., 2005). Each peak (or blob) was tentatively identified by both a group and a carbon number. The peak name, 1D retention time, 2D retention time and peak volume were exported as a csv file that was used for further processing.

3.4.2 Quantification using the FID chromatogram

The initial mass fraction of a compound i on the FID ($w_{i,FID}$) channel can be calculated using the mass fraction of the internal standard (bromobenzene), w_{st}:

$$w_{i,FID} = \frac{RF_{i,FID} . V_{i,FID}}{RF_{st,FID} . V_{st,FID}} . w_{st,FID} \tag{3.1}$$

where $RF_{i,FID}$ is the relative response factor for compound i on the FID, $V_{i,FID}$ is the peak volume of compound i on the FID, $RF_{st,FID}$ is the relative response factor of the internal standard on the FID and $V_{st,FID}$ is the peak volume of the internal standard on the FID. Beens et al.(Beens et al., 1998) demonstrated that FID response factors for isomers of hydrocarbons differ only marginally, and hence that it is a fair approximation to write the relative response factor with respect to methane as (Beens et al., 1998):

$$RF_{i,FID} = \frac{M_i}{M_{CH4} . N_{C,i}} \tag{3.2}$$

where M_i is the molar mass of compound i, $N_{c,i}$ is the carbon number of compound i and M_{ch4} is the molar mass of methane.

In this article Equation 3.2 is used both for pure hydrocarbons and for sulfur containing compounds. This approximation removes the need to calibrate for each compound present in the mixture and will be validated using the test mixture. However, individual response factors for the two internal standards 3-chlorothiophene and bromobenzene were determined experimentally because the method of Beens et al. (1998) has not been verified for halogen atom-containing molecules. Calibration showed that the relative response factors of 3-chlorothiophene and bromobenzene are 1.94 and 1.87 respectively, which differs from the values obtained using the method of Beens et al. (1998), 1.85 and 1.63, respectively.

3.4.3 Quantification of the SCD chromatogram

For the SCD chromatogram a similar method as in the case of the FID chromatogram can be adopted. Since the response of the SCD detector is linear and equimolar to the amount of sulfur (Mahe et al., 2011) the following formula can be written:

$$w_{i,SCD} = \frac{V_{i,SCD}}{V_{st,SCD}} \cdot w_{st,SCD} \cdot \frac{M_i}{N_{S,i} \cdot M_{st}} \tag{3.3}$$

where $N_{s,i}$ is the number of sulfur atoms in compound i and M_{st} the molar mass of sulfur standard. In case of the SCD detector 3-chlorothiophene is used as an internal standard. Again the assumption of a linear, equimolar response of the detector towards the amount of sulfur removes the need for calibration. These assumptions will be extensively validated using the test mixtures in Section 3.5.1.

3.4.4 Quantification procedure

Due to the complex nature of any gas oil sample peak overlap on the GC × GC – FID chromatogram is unavoidable between hydrocarbon compounds and sulfur compounds. The large

difference in concentrations makes it almost impossible to differentiate between the sulfur compounds and overlapping hydrocarbon compounds. For this reason the initially calculated FID mass fractions by Equation 3.1 need to be corrected using the mass fractions of the sulfur compounds obtained from the SCD chromatogram using Equation 3.3. Therefore on the FID chromatogram all peaks are identified as purely hydrocarbon compounds and there is no differentiation between sulfur compounds and overlapping hydrocarbon compounds. Obviously this will result in an overestimation of the mass fractions of certain hydrocarbon compounds if they overlap with certain sulfur compounds. For example it can be seen in Figure 3.3 that there is potential overlap between diaromatics and benzothiophenes, which causes an overestimation of diaromatics due to the addition of benzothiophenes if only the GC × GC – FID chromatogram would be used. This overestimation inside a hydrocarbon group y is equal to:

$$w_{y,FID,overestimation} = \frac{RF_{y,FID}.V_{z,FID}}{RF_{st,FID}.V_{st,FID}}.w_{st,FID} \qquad (3.4)$$

with z being the identified sulfur compound. The latter also implies that the sulfur compound z is underestimated by this procedure using only information from the FID chromatogram by:

$$w_{z,FID,underestimation} = \frac{RF_{z,FID}.V_{z,FID}}{RF_{st,FID}.V_{st,FID}}.w_{st,FID} = w_{z,SCD} \qquad (3.5)$$

where $w_{z,SCD}$ is the mass fraction of sulfur compound z on the SCD. It is clear that both the underestimation and the overestimation are strongly dependent on the amount of sulfur compounds present in the mixture. An increase in sulfur compounds would result in a near linear increase of $V_{z,FID}$ and thus in a near linear increase in the overestimation and the underestimation of the pure and sulfur containing hydrocarbons, respectively. This underestimation is equal to the amount for the group z calculated using the SCD ($w_{z,SCD}$) chromatogram since no sulfur was

assumed in the FID chromatogram. Elimination of $V_{z,FID}$ from Equation 3.4 by incorporating

Equation 3.5 and Equation 3.3 leads to the following correction formula:

$$w_{y,FID,overestimation} = \frac{RF_{y,FID}}{RF_{z,FID}} \cdot w_{z,SCD} = \frac{RF_{y,FID}}{RF_{z,FID}} \cdot \frac{V_{z,SCD}}{V_{st,SCD}} \cdot w_{st,SCD} \cdot N_{S,z} \cdot \frac{M_{st}}{M_z} \tag{3.6}$$

Equation 3.6 can as such be used to recalculate the mass fractions of the hydrocarbon groups

determined using the FID chromatogram. Obviously the latter requires that the detected amount

of the sulfur compounds z is equal on both the FID and the SCD and thus that Equation 3.2 is

valid for both pure and sulfur containing hydrocarbons which will be validated by a standard

mixture.

3.5 Results and discussion

3.5.1 Response factor evaluation and methodology validation

For the optimized conditions of each injector three repeat analyses of test mixture 1 have been

carried out. The composition of Test mixture 1 is chosen in such a way that it gives a high

response on the FID for both pure and sulfur containing hydrocarbons. Hence, the mass fraction

of the compounds can be accurately determined because none of the compounds is near or below

the quantification limit of the used method. In Test mixture 2 some of the sulfur compounds are

below the quantification limit on the FID channel which is around 0.25 wt%. Figure 3.2 presents

the FID chromatogram of text mixture 1 and shows that all the different compounds are properly

separated. This is confirmed by the 2D resolution, as defined by Dutriez et al. (2009):

$$Rs_{2D} = \sqrt{Rs_1^2 + Rs_2^2} = 2. \sqrt{\frac{(\Delta t_{r1})^2}{(\omega_{A1} + \omega_{B1})^2} + \frac{(\Delta t_{r2})^2}{(\omega_{A2} + \omega_{B2})^2}} \tag{3.7}$$

With Rs_1 the resolution in the first dimension of the chromatogram, R_{s2} the resolution in the

second dimension of the chromatogram, Δt_{r1} the difference in retention time between compound

A and B in the first dimension, Δt_{r2} the difference in retention time between compound A and B in the second dimension, ω_{A1} the peak width of compound A in the first dimension, ω_{A2} the peak width of compound A in the second dimension, ω_{B1} the peak width of compound B in the first dimension and ω_{B2} the peak width of compound B in the second dimension. Baseline separation is obtained when the resolution is at least 1.5. Applying Equation 3.7 results in a 2D resolution of at least 3 for any combination of peaks (see Table 3.4) which assures baseline separation of the peaks.
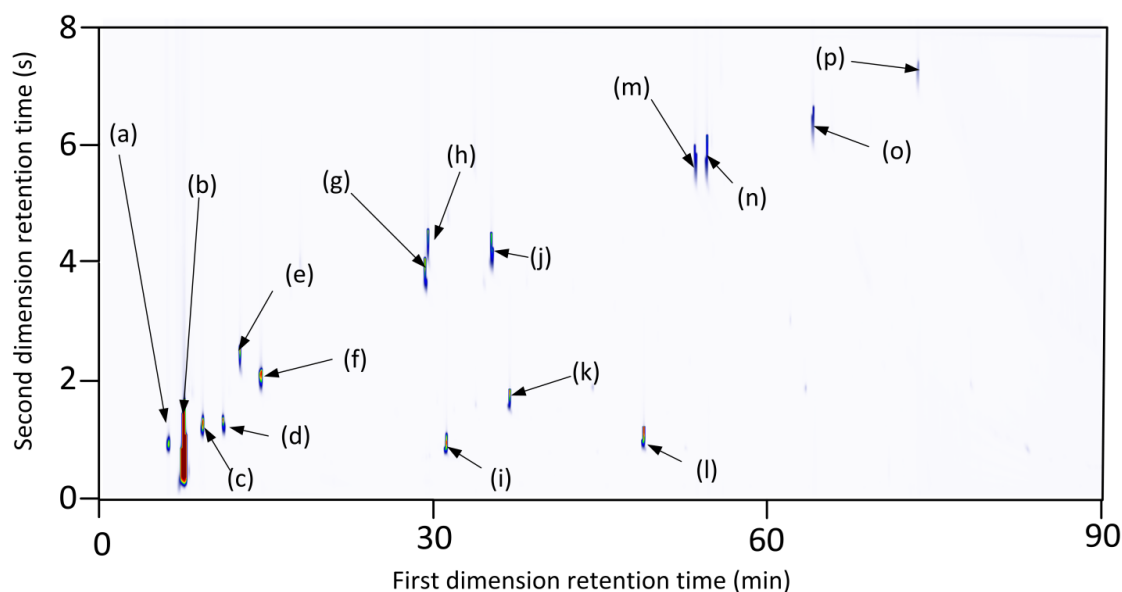
Figure 3.2. GC × GC – FID chromatogram of test mixture 1: (a) thiophene, (b) heptane, (c) toluene, (d) 1-pentanethiol, (e) 3-chlorothiophene, (f) styrene, (g) naphthalene, (h) benzothiophene, (i) dodecane, (j) 2-methylbenzothiophene, (k) 1-decanethiol, (l) hexadecane, (m) dibenzothiophene, (n) phenanthrene, (o) fluoranthene, (p) 1,2- benzodiphenylene sulfide

To evaluate the accuracy of the calculation of the response factors according to Equation 3.2 and assuming equimolarity on the SCD a first quantification of test mixture 1 was carried out using theoretically derived response factors. Table 3.4 gives an overview of the obtained results using the methodologies discussed in Section 3.3.3. The relative error between the results quantified

using the FID and the real values (based on sample preparations) vary from 1% until 4.5%. No significant differences can be observed between pure hydrocarbon compounds and sulfur containing compounds. The repeatability is good and the boundaries of the 95% confidence interval deviate for most compounds less than 6% with an average value of 3.7%. Only fluoranthene and 1,2-benzodiphenylene sulfide have repeatability which is higher than 6%. Fluoranthene and 1,2-benzodiphenylene sulfide are the heaviest compounds in the mixture and the increased value could be due to discrimination effects in the split/splitless injector (Dutriez et al., 2009). For these compounds a different injector such as an on-column injector could be beneficial (Bailey, 2005). However, due to the limited boiling point range of the studied gas oils, the fact that none of these compounds were found in the gas oils and that maximal sensitivity of a detector can easily be achieved by changing the split flow rate, the split/splitless injector was preferred for all injections.

On the SCD the introduced relative error compared to the real mass fractions by using equimolarity is overall lower than the error on the FID. The relative error is for most of the compounds below 1% with the exception of the error of thiophene which is 1.51%. The increase is related to the low boiling point (357 K) of thiophene. Due to the low boiling point when using cryogenic CO_2 modulation compounds with a boiling point below 360K cannot be trapped, and hence the peak is smeared out over the second dimension. The higher signal to noise ratio for the unmodulated peak gives rise to an increase of the uncertainty on the measured mass fraction.

Table 3.4. Average quantified mass fractions, 95% confidence interval (% relative to total amount) and relative error with respect to the real mass fractions of three

repeat injections on both the FID and the SCD for test mixture 1

	FID				SCD			
	Mass fraction (wt%)	95% confidence interval (%)	Error (%)	Min. 2D res.	Mass fraction (wt%)	95% confidence interval (%)	Error (%)	Min. 2D res
Hydrocarbons								
Toluene	1.14±0.06	5.26	3.92	15.7	-	-	-	-
Styrene	1.45±0.02	1.38	4.50	16.1	-	-	-	-
Naphthalene	1.23±0.03	2.44	-2.14	3.6	-	-	-	-
Dodecane	1.15±0.04	3.48	1.18	58.8	-	-	-	-
Hexadecane	1.44±0.01	0.69	4.55	121.2	-	-	-	-
Phenanthrene	1.03±0.03	2.91	-3.78	4.3	-	-	-	-
Fluoranthene	0.60±0.06	10.00	-1.72	17.9	-	-	-	-
Sulfur containing								
Thiophene	1.39±0.04	2.88	-1.18	4.6	1.42±0.02	1.39	1.51	5.6
1-pentanethiol	1.27±0.04	3.15	-3.28	15.7	1.27±0.01	1.08	-0.77	15.6
3-chlorothiophene*	1.93	-	-	16.1	1.93	-	-	15.6
Benzothiophene	1.01±0.03	2.97	-1.22	3.6	1.04±0.03	3.01	0.99	28.3
2-methylbenzothiophene	1.62±0.03	1.85	-2.54	54.3	1.67±0.02	1.39	0.37	28.3
1-decanethiol	1.07±0.06	5.61	4.05	58.8	1.03±0.03	2.86	0.23	35.8
Dibenzothiophene	0.90±0.02	2.22	-3.32	4.3	0.94±0.03	3.00	0.62	5.3
1,2-benzodiphenylene sulfide	0.27±0.02	7.41	-3.35	10.5	0.26±0.03	9.64	0.42	5.3

* Internal standard

Table 3.4 further shows that the repeatability between SCD injections is good because the boundaries of the 95% confidence interval deviate less than 3% with an average value of 2.1%. 1,2-benzodiphenylene sulfide has again a higher deviation which is less than 10%. The difference between the quantification of sulfur compounds on both the FID and the SCD detector is also smaller than 5%. The error using the linear equimolar response of the SCD injector is also similar to the values mentioned by Adlard (1995). Most of the calculated response factors for the SCD are within 5% although Adlard reports deviations up to 43% for some light sulfur compounds (e.g. methanethiol) and up to 13 % for heavier compounds sulfur compounds (e.g. dibenzothiophenes).Taking everything into account the total error of the method is estimated to be around 6% with the exception of the heaviest compounds fluoranthene and 1,2-benzodiphenylene sulfide where the error is around 10%. These experimental errors are similar to the much more expensive FTICR-MS which provides the same level of detail. For FTICR-MS the experimental error is estimated to be about 5% (Sleighter & Hatcher, 2011). However, the experimental error of both methods is larger than that of techniques focused on more global parameters such as elemental analysis for which the experimental error is around 2% for the amount of sulfur present in the gas oils studied in this article.

To validate the proposed quantification procedure test mixture 3 was used, which only contains four compounds. To simulate peak overlap between pure hydrocarbons and sulfur containing compounds, which is unavoidable in real crude oil fractions mixtures, an artificial GC method was created which forced the peak of phenanthrene and the peak of dibenzothiophenes to overlap. This is confirmed by the 2D peak resolution being only 0.48 for those peaks so the peaks are not baseline separated. Phenanthrene and dibenzothiophenes were quantified twice. Once using the procedure described in Section 3.4.4 and once using only the FID data (assuming only pure

hydrocarbons). Phenanthrene was quantified to be 2.08 ± 0.02 for the first method (with correction) and 2.34 ± 0.02 for the second method (without correction). It is clear that a significant overestimation (14%) occurs when it is not corrected for the amount of dibenzothiophenes. After correcting the overestimation is only 1.24 % which is well within the proposed 3.7% error margin.

3.5.2 Single injection technique versus double injection technique

Order of magnitude differences in sulfur levels in a sample will have an effect on the optimum GC × GC conditions and detector settings. Therefore the conditions are optimized separately for test mixture 1 and test mixture 2. In case of test mixture 1 the high amount of sulfur requires that the optimized conditions for the FID and the SCD coincide at a split flow of 50 ml.min^{-1} and a detector range for the FID of 10 (see Table 3.3). However, in case of test mixture 2 the lower amount of sulfur results in a lower split flow needed to ensure maximal sensitivity on the SCD. Since test mixture 2 contains a similar amount of sulfur in comparison to the gas oils (see Table 3.1), test mixture 2 is used for the remainder of this chapter. For each of the optimized conditions three repeat analysis of test mixture 2 have been carried out. Since the optimal FID conditions and the suboptimal FID/SCD conditions were found to be identical these repeat analyses were only carried out once. Depending on the amount of sulfur either the optimal FID or the optimal SCD conditions will overlap with the suboptimal FID/SCD conditions due to the way the suboptimal conditions are obtained. As mentioned in Section 2.3 the sensitivity of one detector is maximized without exceeding the linear range of the other detector (instead of just maximizing sensitivity regardless of the other detector). Not exceeding the linear range means operating the detector at the borders of its linear range or thus at maximal sensitivity for that injector. It is clear that depending on the amount of sulfur either the SCD or the FID will be operating at maximal

sensitivity. Table 3.5 shows the quantified mass fractions, the 95% confidence interval and the relative error compared to the real mass fractions (based on the sample preparation). When the conditions are optimized for either the SCD or the FID the boundaries of the 95% confidence interval are within ±3.4% of the average value. However, when the GC × GC conditions are not optimized for the used detector (e.g. using the SCD to quantify sulfur when GC × GC conditions have been optimized for the FID) these boundaries increase up to 9%. The error of the overall method is thus increased up to 9%. Although the double injection method requires two injections the additional time is compensated by the lower overall error of the double injection method as compared to the single injection method. The choice of the optimal method thus becomes a time versus accuracy question. In this article the authors prefer the higher accuracy of the double injection method for the analysis of the unknown crude oil derived fractions (gas oils). Since a double injection technique results in a decreased experimental error the benefit of putting the FID and the SCD in series could be questioned since a flameless burner SCD would have an even lower detection limit in the ppb range. This is because in a stand-alone flameless burner SCD the sulfur compounds are not diluted in combustion gases in comparison to the FID or the FID/SCD in series. The lower detection limit of the flameless burner SCD could be useful for samples with ultra-low amounts of sulfur (ppb range). However, the concentration of sulfur in the compounds of the studied samples is well within the ppm range (10 ppm S and higher). The increased sensitivity would drive the response of the detector for these compounds outside of its linear range (Beens & Tijssen, 1997) and thus a higher split flow would be needed making the overall effect on the experimental error negligible. Furthermore, the FID already combusts the hydrocarbons, which are several orders of magnitude larger in concentration, while in a stand-alone flameless burner SCD these hydrocarbons would also be oxidized inside the SCD. The

former results in less soot formation inside the SCD but could also increases the concentration of

SO inside the detector thus increasing the sensitivity as reported by Beens and Tijssen (1997).

Table 3.5: Average quantified mass fractions, 95% confidence interval and relative error with respect to the real mass fractions of three repeat injections for optimized conditions for FID and SCD for test mixture 2

	Optimal FID and suboptimal FID/SCD			Optimal SCD		
	Mass fraction (wt%)	95% confidence interval (%)	Error (%)	Mass fraction (wt%)	95% confidence interval (%)	Error (%)
On FID						
Styrene	3.1±0.4	12.90	-1.33	3.2±0.7	21.88	0.89
Bromobenzene*	6.13	-	-	6.13	-	-
Decane	2.7±0.2	7.41	0.68	2.7±0.5	18.52	2.89
Naphthalene	3.8±0.3	7.89	-2.14	3.9±0.7	17.95	0.80
Dodecane	2.8±0.2	7.14	-1.25	2.8±0.2	7.14	-2.46
Hexadecane	3.0±0.1	3.33	-3.16	2.9±0.3	10.34	-5.43
Phenanthrene	2.4±0.1	4.17	2.83	2.4±0.1	4.17	0.52
Fluoranthene	1.4±0.1	7.14	-1.22	1.3±0.2	15.38	-5.47
On SCD						
Thiophene	0.25±0.04	16.00	1.54	0.25±0.01	4.00	1.83
1-pentanethiol	0.20±0.03	15.00	3.13	0.20±0.01	2.00	0.81
3-chlorothiophene[+]	0.34	-	-	0.34	-	-
Benzothiophene	0.31±0.06	19.35	-0.45	0.31±0.01	3.23	0.40
2-methylbenzothiophene	0.26±0.05	19.23	-1.51	0.27±0.01	3.70	0.30
1-decanethiol	0.21±0.02	9.52	0.81	0.208±0.01	0.48	-0.38
Dibenzothiophene	0.26±0.01	1.54	-9.01	0.29±0.03	10.34	0.26

*Internal standard for the FID, [+] Internal standard for the SCD

3.5.3 Analysis of crude oil derived fractions

Both a FID and a SCD analysis of each of the gas oils has been carried out using the

methodology and conditions described in Section 3.3.3. Two injections were carried out: one

injection with optimal conditions for the FID detector and another injection with optimal

conditions for the SCD detector. Figure 3.3 shows the color plots of both chromatograms with the

tentatively identified groups. The roof/tile structure of the SCD chromatogram is retained and no

wrap around is observed on neither SCD nor FID chromatogram. As stated previously overlap between groups of sulfur compounds with hydrocarbon groups (same color on both chromatograms) is unavoidable as can be seen in Figure 3.3. For example thiols overlap with monoaromatics, benzothiophene homologues overlap with diaromatics and dibenzothiophenes overlap with triaromatics. Also visible on Figure 3.3 is extra tailing of the peaks on the SCD chromatogram. This tailing is attributed to the slow response of the detector electronics rather than to potential dead volumes in the chemiluminescence chamber and/or PFA transfer line between burner and reaction chamber. The vacuum in the reaction chamber assures that the residence time of the analyte is in the order of 5 ms in this zone (Blomberg et al., 2004; Ruiz-Guerrero et al., 2006). Note that no tailing is visible on the FID since detection of these peaks happens before the SCD. Figure 3.4 shows a comparison of the PAH obtained without information about the sulfur compounds and after correcting the FID data using the results obtained on the SCD. If no additional SCD analysis is carried out and all polycyclic aromatic compounds would be identified as PAH to the degree of uncertainty on the measured mass fractions could be up to 161% for PAH compounds with 3 rings. The latter shows the lack of the identification of the PASH on the FID as well as a clear overestimation of the PAH in this worst case scenario. In reality the major PASH would be correctly identified if an additional MS analysis of the sample would be carried out (Van Geem et al., 2010). However, it should be clear that due to significant peak overlap of sulfur containing compounds and hydrocarbons it is impossible to correctly identify and resolve all the sulfur compounds. The latter is the case for a compound such as dibenzothiophene. In principle it can easily be identified on the FID chromatogram, however, its homologues overlap too much with other polycyclic aromatic hydrocarbons containing three aromatic rings like substituted phenantrenes and anthracenes.
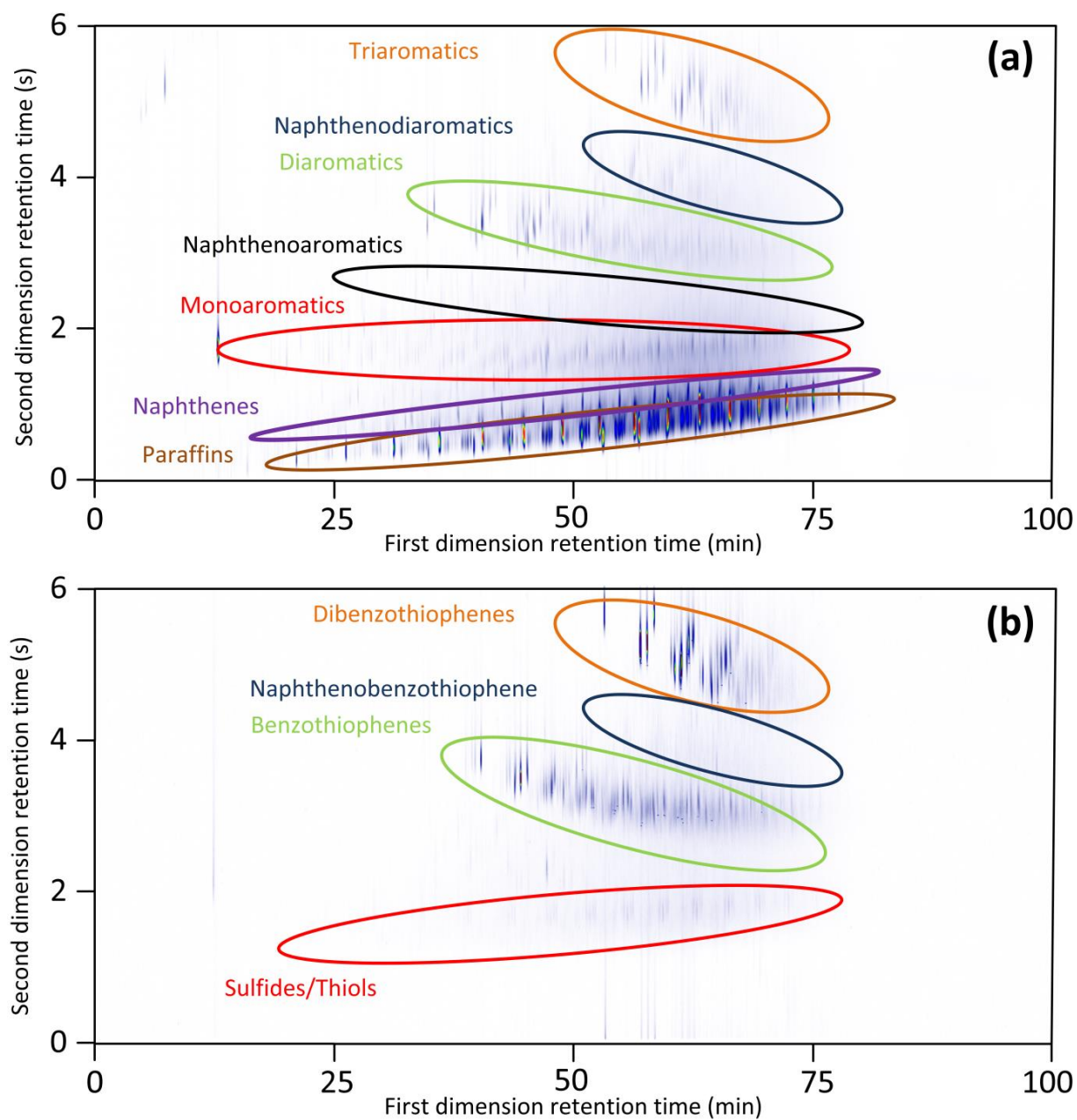
Figure 3.3. GC × GC chromatograms of gas oil A with different groups depicted: (a) FID chromatogram, (b) SCD chromatogram
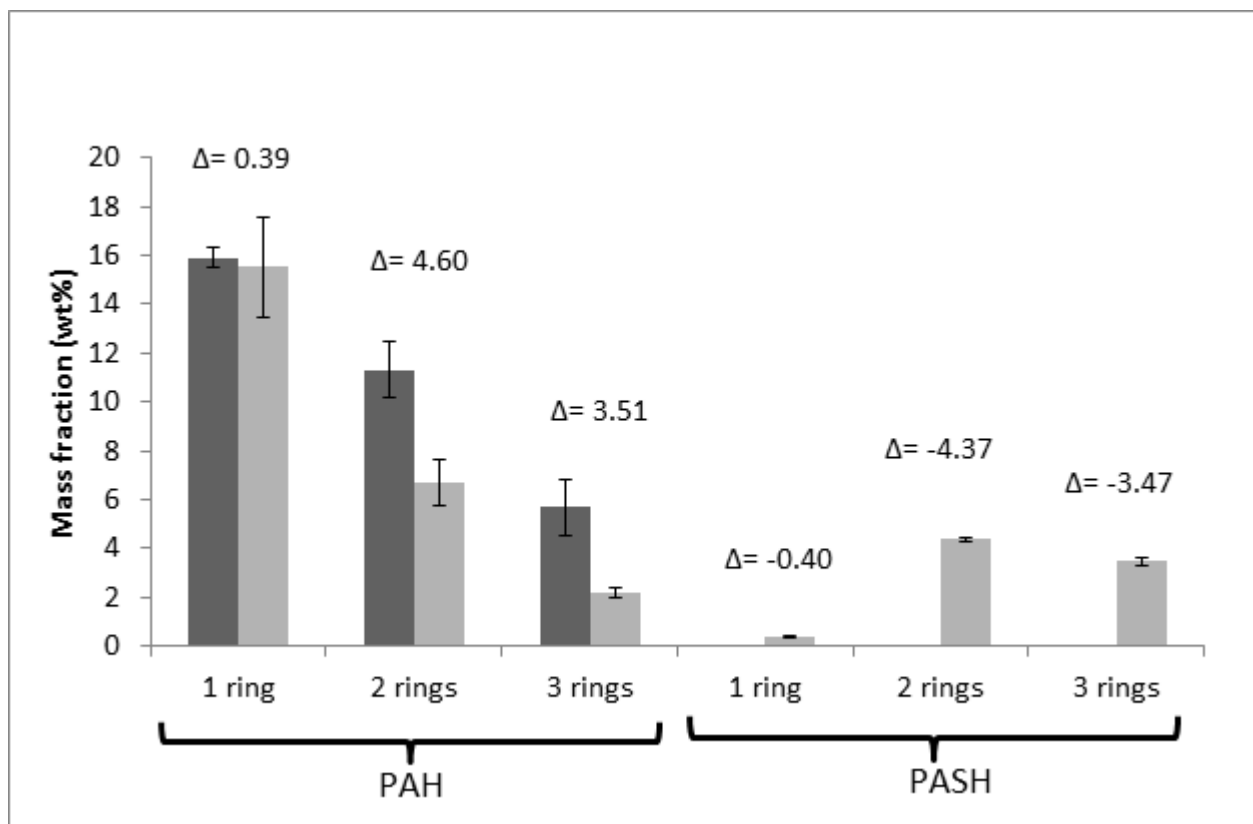
Figure 3.4. Comparison of the PAH composition before and after correcting the FID data. Δ indicates the difference between corrected and uncorrected results. Error bars indicate the 95% confidence interval. ■ Uncorrected results ▢ Corrected results

Figure 3.5 shows the corrected group type analysis of gas oils A, B and C. Similar conclusions could be drawn if these were compared to the uncorrected group type analysis. Using the analytical methodology discussed in Section 3.3.3 and the group type analysis results given in Figure 3.5 it is possible to calculate an elemental composition of the three gas oils. This calculated elemental composition is given in Table 3.1 and shows that a good agreement is obtained between the calculated elemental composition of the gas oils and the elemental composition obtained using the elemental analyzer. This result is a first double-check of the discussed procedure. Note that such a verification cannot be done when using the method of

Mahe et al. (2011) because the total amount of sulfur obtained from the elemental analyzer is needed to calculate the mass fractions of the compounds visible on the SCD. After quantifying all the compounds (both PA(S)H and non-PA(S)H's) the sum of the quantities of all the compounds should be close to 100%. For gas oils A, B and C this sum is respectively 102.5 wt%, 100.5 wt% and 99.9 wt%. This overall mass balance provides a second verification of the accuracy of the results and is well within the proposed error of 3.4%.

Figure 3.5 shows the carbon distribution of the different PA(S)H's. The aromatic compounds are mainly mono-aromatic hydrocarbons. Depending on the amount of sulfur present in the sample (gas oil A > gas oil B > gas oil C) the importance of the PASH can be significant as compared to the PAH. In case of gas oil A the amount of PAH (24.4 wt%) is only three times higher than the amount of PASH (8.25 wt%), while in the case of gas oil C it is around 24 times higher. The PASH mainly consists of benzothiophene and to lesser extent dibenzothiophene homologues. The amount of thiophenes is low as compared to benzothiophenes and dibenzothiophenes. The PASH seems to be mainly located in the 10% to 90% boiling point range and no very light or very heavy sulfur containing compounds were found. A detailed analysis of all three gas oils can be found in Appendix B.
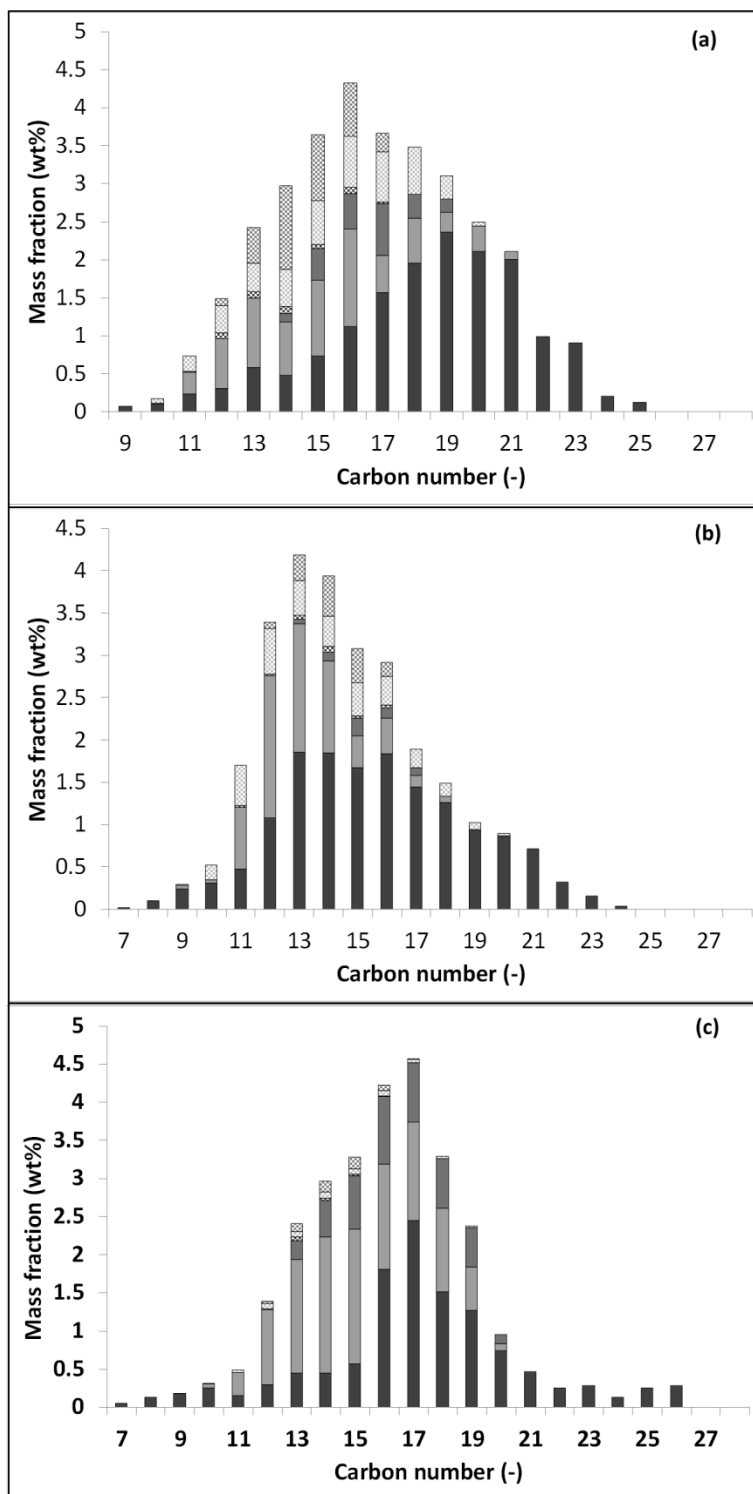
Figure 3.5. Distribution of PA(S)H by type and carbon number for the three gas oils:

(a) Gas oil A, (b) Gas oil b, (c) Gas oil c

■ 1 ring PAH ■ 2 ring PAH ■ 3 ring PAH ▨ 1 ring PASH ▨ 2 ring PASH ▨ 3 ring PASH

3.6 Conclusion

Comprehensive two-dimensional GC coupled to both the FID and the SCD was used to quantify both the PAH and the PASH in three commercial gas oils with improved accuracy and repeatability. The new analytical methodology allows accounting for potential peak overlap of sulfur compounds with the hydrocarbon matrix on the FID chromatogram. The latter requires the use of two internal standards, i.e. bromobenzene and 3-chlorothiophene. The method was validated using test mixtures and the overall error of the method was determined to be 9% when a single injection method was used, while it was calculated to be 3.4% when a double injection method was used. These experimental errors are in the same range as the much more expensive FTICR-MS technique. Application of the methodology to three commercial gas oils containing different amounts of sulfur reveals that depending on the fraction the total amount of polycyclic aromatic hydrocarbons that contain sulfur varies between 4 and 33%. Using only data from the FID detector these sulfur containing compounds would be incorrectly quantified as polycyclic aromatic hydrocarbons leading to significant errors in the quantification of some PAH of more than 150 %.

3.7 References

Adlard, E. R. (1995). Chromatography in the petroleum industry.
ASTM-D2425, 2009, Standard Test Method for Hydrocarbon Types in Middle Distillates by
        Mass Spectrometry.ASTM International, West Conshohocken, PA, 2003,
        DOI:10.1520/D2425-04R09
ASTM-D2622, 2010, Standard Test Method for Sulfur in Petroleum Products by Wavelength
        Dispersive X-ray Fluorescence Spectrometry.ASTM International, West Conshohocken,
        PA, 2003, DOI:10.1520/D2622-10
ASTM-D5186, 2009, Standard Test Method for Determination of Aromatic Content and
        Polynuclear Aromatic Content of Diesel Fuels and Aviation Turbine Fuels by
        Supercritical Fluid Chromatography.ASTM International, West Conshohocken, PA, 2003,
        DOI:10.1520/D5186-03R09

ASTM-D5453, 2012, Standard Test Method for Determination of Total Sulfur in Light Hydrocarbons, Spark Ignition Engine Fuel, Diesel Engine Fuel, and Engine Oil by Ultraviolet Fluorescence.ASTM International, West Conshohocken, PA, 2003, DOI:10.1520/D5453-12

ASTM-D5504, 2012, Standard Test Method for Determination of Sulfur Compounds in Natural Gas and Gaseous Fuels by Gas Chromatography and Chemiluminescence.ASTM International, West Conshohocken, PA, 2003, DOI:10.1520/D5504-12

ASTM-D6379, 2011, Standard Test Method for Determination of Aromatic Hydrocarbon Types in Aviation Fuels and Petroleum Distillates—High Performance Liquid Chromatography Method with Refractive Index Detection.ASTM International, West Conshohocken, PA, 2003, DOI:10.1520/D6379-11

ASTM-D6591, 2011, Standard Test Method for Determination of Aromatic Hydrocarbon Types in Middle Distillates—High Performance Liquid Chromatography Method with Refractive Index Detection.ASTM International, West Conshohocken, PA, 2003, DOI:10.1520/D6591-11

Ávila, B. M. F., Vaz, B. G., Pereira, R., Gomes, A. O., Pereira, R. C. L., Corilo, Y. E., Simas, R. C., Nascimento, H. D. L., Eberlin, M. N., & Azevedo, D. A. (2012). Comprehensive Chemical Composition of Gas Oil Cuts Using Two-Dimensional Gas Chromatography with Time-of-Flight Mass Spectrometry and Electrospray Ionization Coupled to Fourier Transform Ion Cyclotron Resonance Mass Spectrometry. Energy & Fuels, 26, 5069-5079.

Bacaud, R., Cebolla, V. L., Membrado, L., Matt, M., Pessayre, S., & Galvez, E. M. (2002). Evolution of sulfur compounds and hydrocarbons classes in diesel fuels during hydrodesulfurization. Combined use of thin-layer chromatography and GC-sulfur-selective chemiluminescence detection. Industrial & Engineering Chemistry Research, 41, 6005-6014.

Bailey, R. (2005). Injectors for capillary gas chromatography and their application to environmental analysis. Journal of Environmental Monitoring, 7, 1054-1058.

Beens, J., Boelens, H., Tijssen, R., & Blomberg, J. (1998). Quantitative Aspects of Comprehensive Two-Dimensional Gas Chromatography (GC×GC). Journal of High Resolution Chromatography, 21, 47-54.

Beens, J., Janssen, H.-G., Adahchour, M., & Brinkman, U. A. T. (2005). Flow regime at ambient outlet pressure and its influence in comprehensive two-dimensional gas chromatography. Journal of Chromatography A, 1086, 141-150.

Beens, J., & Tijssen, R. (1997). The characterization and quantitation of sulfur-containing compounds in (heavy) middle distillates by LC-GC-FID-SCD. Hrc-Journal of High Resolution Chromatography, 20, 131-137.

Blomberg, J., Riemersma, T., van Zuijlen, M., & Chaabani, H. (2004). Comprehensive two-dimensional gas chromatography coupled with fast sulphur-chemiluminescence detection: implications of detector electronics. Journal of Chromatography A, 1050, 77-84.

Chin, S.-T., Wu, Z.-Y., Morrison, P. D., & Marriott, P. J. (2010). Observations on comprehensive two dimensional gas chromatography coupled with flame photometric detection for sulfur- and phosphorus-containing compounds. Analytical Methods, 2, 243-253.

Del Río, D., Rey, M., Sedran, U., & de la Puente, G. (2011). Combined PFPD–FID assessment of sulfur in liquid fuels. Fuel Processing Technology, 92, 2278-2284.

Dutriez, T., Courtiade, M., Thiebaut, D., Dulot, H., Bertoncini, F., Vial, J., & Hennion, M. C. (2009). High-temperature two-dimensional gas chromatography of hydrocarbons up to nC(60) for analysis of vacuum gas oils. Journal of Chromatography A, 1216, 2905-2912.

Dutriez, T., Thiebaut, D., Courtiade, M., Dulot, H., Bertoncini, F., & Hennion, M. C. (2013). Application to SFC-GC x GC to heavy petroleum fractions analysis. Fuel, 104, 583-592.

Fernandez-Lima, F. A., Becker, C., McKenna, A. M., Rodgers, R. P., Marshall, A. G., & Russell, D. H. (2009). Petroleum Crude Oil Characterization by IMS-MS and FTICR MS. Analytical Chemistry, 81, 9941-9947.

Hua, R. X., Li, Y. Y., Liu, W., Zheng, J. C., Wei, H. B., Wang, J. H., Lu, X., Kong, H. W., & Xu, G. W. (2003). Determination of sulfur-containing compounds in diesel oils by comprehensive two-dimensional gas chromatography with a sulfur chemiluminescence detector. Journal of Chromatography A, 1019, 101-109.

Hua, R. X., Wang, J. H., Kong, H. W., Liu, J., Lu, X., & Xu, G. W. (2004). Analysis of sulfur-containing compounds in crude oils by comprehensive two-dimensional gas chromatography with sulfur chemiluminescence detection. Journal of Separation Science, 27, 691-698.

Kelly L.C., R., P. (2010). Detection and identification of sulfur compounds in an Australian jet fuel: Defence Science and Technology Organisation.

Lee, I. C., & Ubanyionwu, H. C. (2008). Determination of sulfur contaminants in military jet fuels. Fuel, 87, 312-318.

Lei, Z., Huhman, D. V., & Sumner, L. W. (2011). Mass Spectrometry Strategies in Metabolomics. Journal of Biological Chemistry, 286, 25435-25442.

Liu, P., Shi, Q., Chung, K. H., Zhang, Y., Pan, N., Zhao, S., & Xu, C. (2010). Molecular Characterization of Sulfur Compounds in Venezuela Crude Oil and Its SARA Fractions by Electrospray Ionization Fourier Transform Ion Cyclotron Resonance Mass Spectrometry. Energy & Fuels, 24, 5089-5096.

Liu, P., Shi, Q., Pan, N., Zhang, Y., Chung, K. H., Zhao, S., & Xu, C. (2011). Distribution of Sulfides and Thiophenic Compounds in VGO Subfractions: Characterized by Positive-Ion Electrospray Fourier Transform Ion Cyclotron Resonance Mass Spectrometry. Energy & Fuels, 25, 3014-3020.

Mahe, L., Dutriez, T., Courtiade, M., Thiebaut, D., Dulot, H., & Bertoncini, F. (2011). Global approach for the selection of high temperature comprehensive two-dimensional gas chromatography experimental conditions and quantitative analysis in regards to sulfur-containing compounds in heavy petroleum cuts. Journal of Chromatography A, 1218, 534-544.

Moustafa, N. E., & Andersson, J. T. (2011). Analysis of polycyclic aromatic sulfur heterocycles in Egyptian petroleum condensate and volatile oils by gas chromatography with atomic emission detection. Fuel Processing Technology, 92, 547-555.

Ong, R., Lundstedt, S., Haglund, P., & Marriott, P. (2003). Pressurised liquid extraction–comprehensive two-dimensional gas chromatography for fast-screening of polycyclic aromatic hydrocarbons in soil. Journal of Chromatography A, 1019, 221-232.

Pang, W., Lee, J.-K., Yoon, S.-H., Mochida, I., Ida, T., & Ushio, M. (2010). Compositional analysis of deasphalted oils from Arabian crude and their hydrocracked products. Fuel Processing Technology, 91, 1517-1524.

Pena-Abaurrea, M., Ye, F., Blasco, J., & Ramos, L. (2012). Evaluation of comprehensive two-dimensional gas chromatography–time-of-flight-mass spectrometry for the analysis of

polycyclic aromatic hydrocarbons in sediments. Journal of Chromatography A*, 1256, 222-231.

Rathsack, P., & Otto, M. (2014). Classification of chemical compound classes in slow pyrolysis liquids from brown coal using comprehensive gas-chromatography mass-spectrometry. Fuel*, 116, 841-849.

Reichenbach, S. E., Kottapalli, V., Ni, M. T., & Visvanathan, A. (2005). Computer language for identifying chemicals with comprehensive two-dimensional gas chromatography and mass spectrometry. Journal of Chromatography A*, 1071, 263-269.

Reyniers, M., & Froment, G. F. (1995). Influence of metal-surface and sulfur addition on coke deposition in the thermal cracking of hydrocarbons. Industrial & Engineering Chemistry Research*, 34, 773-785.

Robinson, C. J. (1971). Low-resolution mass spectrometric determination of aromatics and saturates in petroleum fractions. Analytical Chemistry*, 43, 1425-1434.

Ruiz-Guerrero, R., Vendeuvre, C., Thiebaut, D., Bertoncini, F., & Espinat, D. (2006). Comparison of comprehensive two-dimensional gas chromatography coupled with sulfur-chemiluminescence detector to standard methods for speciation of sulfur-containing compounds in middle distillates. Journal of Chromatographic Science*, 44, 566-573.

Schulz, H., Böhringer, W., Ousmanov, F., & Waller, P. (1999). Refractory sulfur compounds in gas oils. Fuel Processing Technology*, 61, 5-41.

Sleighter, R. L., & Hatcher, P. G. (2011). Fourier Transform Mass Spectrometry for the Molecular Level Characterization of Natural Organic Matter: Instrument Capabilities, Applications, and Limitations, Fourier Transforms. Approach to Scientific Principles InTech.

Stumpf, Á., Tolvaj, K., & Juhász, M. (1998). Detailed analysis of sulfur compounds in gasoline range petroleum products with high-resolution gas chromatography–atomic emission detection using group-selective chemical treatment. Journal of Chromatography A*, 819, 67-74.

Van Geem, K. M., Pyl, S. P., Reyniers, M. F., Vercammen, J., Beens, J., & Marin, G. B. (2010). On-line analysis of complex hydrocarbon mixtures using comprehensive two-dimensional gas chromatography. Journal of Chromatography A*, 1217, 6623-6633.

van Stee, L. L. P., Beens, J., Vreuls, R. J. J., & Brinkman, U. A. T. (2003). Comprehensive two-dimensional gas chromatography with atomic emission detection and correlation with mass spectrometric detection: principles and application in petrochemical analysis. Journal of Chromatography A*, 1019, 89-99.

Ventura, G. T., Simoneit, B. R. T., Nelson, R. K., & Reddy, C. M. (2012). The composition, origin and fate of complex mixtures in the maltene fractions of hydrothermal petroleum assessed by comprehensive two-dimensional gas chromatography. Organic Geochemistry*, 45, 48-65.

Wang, J. D., Reyniers, M. F., Van Geem, K. M., & Marin, G. B. (2008). Influence of silicon and silicon/sulfur-containing additives on coke formation during steam cracking of hydrocarbons. Industrial & Engineering Chemistry Research*, 47, 1468-1482.

Xu, X., McDonald, L. M., McGowan, C. W., & Glinski, R. J. (1995). Examination of sulfur forms in coal by direct pyrolysis and chemiluminescence detection. Fuel*, 74, 1499-1504.

Zeigler, C., Wilton, N., & Robbat, A. (2012). Toward the Accurate Analysis of C1–C4 Polycyclic Aromatic Sulfur Heterocycles. Analytical Chemistry*, 84, 2245-2252.

Chapter 4: Analysis of shale oil using

GC × GC – FID/SCD/NCD/TOF-MS

4.1 Abstract

The detailed composition of a shale oil was determined using a novel comprehensive 2D gas chromatographic (GC × GC) method. Four different detectors (flame ionization detector (FID), sulfur chemiluminescence detector (SCD), nitrogen chemiluminescence detector (NCD) and time of flight mass spectrometer (TOF-MS)) mounted on different GC × GC's were used. The use of two internal standards; 2-chloropyridine and 3-chlorothiophene; allowed quantification of the shale oil's composition by carbon number and by structural class. 19 different classes were detected in the shale oil: paraffins, isoparaffins, olefins/mononaphthenes, dinaphthenes, monoaromatics, naphthenoaromatics, diaromatics, naphthenodiaromatics, triaromatics, thiols/sulfides, benzothiophenes, naphtenobenzothiophenes, dibenzothiophenes, pyridines, anilines, quinolines, indoles, acridines and carbazoles. A significant amount of sulfur and nitrogen containing compounds, 2.23 wt% and 4.29 wt% respectively, were detected. In addition to sulfur and nitrogen containing compounds phenol homologues were also quantified.

4.2 Introduction

In 2012 total worldwide energy demand was 5.51×10^{20} J ("Total Energy Consumption," 2012) and is expected to grow to 7.06×10^{20} J by 2035 (Newell & Iler, 2013). About 80% of this energy was provided by fossil fuels (crude oil, coal and natural gas) (Na et al., 2012). With only a limited amount of crude oil available and a decline in the discovery of conventional reservoirs (Washburn & Birdwell, 2013) there is a need to investigate alternative energy resources. The most promising one on short notice is the vast resources of oil shale (Tiwari & Deo, 2012; Al-Makhadmeh et al., 2013). Oil shale is a fine-grained sedimentary rock containing kerogen, a mixture of organic chemical compounds with a molar mass as high as 1000 g.mol^{-1} (Na et al., 2012; Guo et al., 2014). Kerogen mainly consists of carbon and hydrogen, but low amounts of organic oxygen, nitrogen, and sulfur compounds are also present. Oxygen, nitrogen and sulfur are associated with carbon atoms in various structural forms, which are the building blocks of the whole molecular structure of kerogen (Tong et al., 2011). Extraction of oil and gas from oil shale is based on retorting or pyrolysis. Upon heating to approximately 773 K without oxygen, the kerogen decomposes to yield shale oil, gas, and char, which remains in the shale residues. The produced shale oil is a mixture that is similar to petroleum containing thousands of hydrocarbon, oxygen-, sulfur- and nitrogen-containing organic compounds (Guo & Ruan, 1995). Those nitrogen and sulfur containing compounds have an adverse influence on the shale oils' potential exploitation as substitute transport fuels (Williams & Chishti, 2001). In addition combustion of nitrogen and sulfur containing compounds leads to the emission of NO_x and SO_x which are an important source of air pollution and acid rain (Blomberg et al., 2004; Dutriez et al., 2011). As such the presence of these sulfur and nitrogen containing compounds lowers the quality of the

produced shale oil, making it less attractive than sweet crude oil because of the additional upgrading processes that will be required before the shale oil can be used in a refinery (Na et al., 2012). Currently there is only limited information available about the composition of the produced shale oils (Kumar et al., 2013; Tong et al., 2013; Sun et al., 2014), as research on oil shale pyrolysis is mainly focused on the investigation of the overall yields of shale oil, gas and cokes (Ballice et al., 1996; Gersten et al., 2000; Johannes et al., 2007; Amer et al., 2014).

Some efforts have been made to gain additional insight in the oxygen containing compounds present in shale oil (Geng et al., 2012). Geng et al. used a fractionation technique applicable for crude oil, coal liquids and shale oil samples, to divide the mixture into different acid, basic and neutral fractions, separating the oxygenates from the hydrocarbon matrix (Farcasiu, 1977; Černý et al., 1990; Granda et al., 1990; Willsch et al., 1997; Geng et al., 2012) and making their analysis possible with techniques such as GC─MS. Oxygenates reported to be present in shale oil are phenols, indanols, naphthols, phenylphenols, fluorenols, phenanthrenols, ketones and esters (Willsch et al., 1997; Geng et al., 2012).

However detailed compositional information of the produced shale oil and a proper methodology to determine a detailed composition of shale oil are essential for further improving the production process and to better assess required upgrading strategies.

Several techniques to obtain more information about the detailed composition of shale oils have been developed and applied. One of the most used techniques is GC-MS (Shue & Yen, 1981; Rovere et al., 1983; Rovere et al., 1990; Ekinci et al., 1994; Geng et al., 2012; Amer et al., 2013; Gentzis, 2013; Sun et al., 2014). A disadvantage of GC-MS is that in a fuel the complex hydrocarbon matrix fragmentation will interfere with other hetero-compounds of interest because the hydrocarbon content is several orders of magnitude larger (Kelly & Rawson, 2010). Heart-

cutting multidimensional gas chromatography is a first step forward (Tranchida et al., 2012) but comprehensive two-dimensional gas chromatography (GC × GC) is a lot more powerful. Another technique that has been used successfully to obtain information about the heteroatom content of shale oil is FT-ICR MS (Bae et al., 2010; Shi et al., 2010; Geng et al., 2012). The advantage of this technique is that it can identify the elemental composition, double bond equivalents, rings plus double bonds to carbon, and the carbon number, based on ultra-high-resolution and accurate mass measurements (Fernandez-Lima et al., 2009). The disadvantage of FT-ICR-MS is the formidable cost of the device which prohibits its widespread availability and routine use (Lei et al., 2011).

In the present work a new methodology to gain more insight into the detailed composition of shale oil is described and applied based on the combination of the results from different GC × GC chromatograms. GC × GC's are coupled with a flame ionization detector (FID), sulfur chemiluminescence detector (SCD), nitrogen chemiluminescence detector (NCD) and a time of flight mass spectrometer (TOF-MS). GC × GC – FID (Dallüge et al., 2003; Wang & Zhang, 2007; Adam et al., 2008; Dutriez et al., 2009; Dutriez et al., 2010; Van Geem et al., 2010; van der Westhuizen et al., 2011), GC × GC – SCD (Hua et al., 2003; Hua et al., 2004; Ruiz-Guerrero et al., 2006; Yang & Wang, 2010; Mahe et al., 2011), GC × GC – NCD (Adam et al., 2007; Adam et al., 2009; Lissitsyna et al., 2013) and GC × GC – TOF-MS (Adam et al., 2007; Adam et al., 2008; Van Geem et al., 2010; van der Westhuizen et al., 2011) have already been shown to be valuable techniques in the analysis of crude oil derived fractions. One of the main difficulties is combining the information obtained using these different detectors to allow detection and quantification of hydrocarbon compounds, sulfur containing compounds and nitrogen containing compounds inside the shale oil. A quantitative separation in 19 different classes is obtained:

paraffins, isoparaffins, olefins/mononaphthenes, dinaphthenes, monoaromatics, naphthenoaromatics, diaromatics, naphthenodiaromatics, triaromatics, thiols/sulfides, benzothiophenes, naphtenobenzothiophenes, dibenzothiophenes, pyridines, anilines, quinolines, indoles, acridines and carbazoles. A distribution based on carbon number is obtained for each individual group. In addition the phenols in the shale oil are also quantified. The information derived from the chromatograms gives an unprecedented insight into the composition of shale oils.

4.3 Experimental

4.3.1 Samples and chemicals

Analytical gases (helium, oxygen, nitrogen, hydrogen and air) were provided at a minimum purity of 99.99% (Air Liquide, Belgium). 3-chlorothiophene was purchased from Sigma-Aldrich with a minimum purity of 98%. 2-chloropyridine, hexane, o-cresol, 2,3-dimethylphenol, 2,3,5-trimethylphenol and 4-isopropyl-3-methylphenol were also purchased from Sigma-Aldrich with a minimum purity of 99%. Dichloromethane was purchased from Chem-Lab at a minimum purity of 98% while acetone was purchased from Chem-Lab at a minimum purity of 99.5%. The shale oil sample was derived from oil shale from the Piceance Basin in Colorado, USA. The elemental composition of the shale oil was determined using a Flash EA2000 (Interscience, Belgium) equipped with a TCD. The elemental composition is based on three repeat analyses of the shale oil and can be found in Table 4.1.

Table 4.1: Measured elemental composition of the shale oil by elemental analysis (EA) and based on the GC analysis and the elemental composition of a reference crude oil sample

	Shale oil (EA)	Shale oil (GC × GC)	Light crude oil
C (wt%)	85.3 ± 0.4	85.4	86.4
H (wt%)	13.12 ± 0.05	13.8	13.5
S (wt%)	0.46 ± 0.05	0.47	<0.1
N (wt%)	0.40 ± 0.01	0.38	<0.1
O (wt%)	0.17 ± 0.01	0.04	<0.1

4.3.2 **Sample preparation**

Four different samples of the shale oil sample were prepared for the separate analysis of the sample on GC × GC – FID, GC × GC –SCD, GC × GC – NCD and GC × GC – TOF-MS. An internal standard was added to the samples for the FID, NCD and SCD. The internal standards for each of the chromatograms were chosen in such a way that they were properly separated from all other peaks as will be illustrated further on. An additional pre-requisite is that for the NCD and SCD analysis nitrogen or sulfur also needs to be present in the internal standards. Therefore for the FID and the SCD analysis 3-chlorothiophene was used, while for the NCD analysis 2-chloropyridine was used. The amount of internal standard that is added is chosen in such a way that the internal standard would have a similar peak height as the compounds quantified by the internal standard. This resulted in 2 wt% of 3-chlorothiophene for the FID analysis, 400 ppm of 3-chlorothiophene for the SCD analysis and 1000 ppm of 2-chloropyridine for the NCD analysis. Different quantities of internal standard are needed because of the large difference in concentration between hydrocarbons (wt% level) and hetero-atom containing compounds (ppm level) in the shale oil.

To help with the identification of the nitrogen compounds (using TOF-MS) preparative chromatography was carried out. A solid phase extraction (SPE) according to Lissitsyna et al. (2013) extracted the N-compounds and separated the shale oil into three fractions. This was done using 0.5 g silica SPE cartridges with a volume of 3 ml (Restek). The SPE column was activated using 6 ml of hexane prior to applying 2 ml of sample. The hydrocarbon matrix was eluted from the column using 9 ml of hexane while the nitrogen containing compounds stayed on the column. Afterwards the column was washed with two solvents providing two different nitrogen containing fractions. The first fraction was obtained by flushing with 9 ml of dichloromethane while the second fraction was obtained by flushing the column with 6 ml of acetone.

4.3.3 GC × GC – FID/SCD/NCD/TOF-MS analysis

All experiments were carried out using three Thermo Scientific TRACE GC×GC's (Interscience, Belgium). For modulation all devices were equipped with a dual stage cryogenic liquid CO_2 modulator (Tranchida et al., 2011). All devices were equipped with an FID. In addition the first device was equipped with an SCD, the second device was equipped an NCD while the third device was equipped with a TOF-MS. For the FID H_2, air and N_2 (make-up gas) flow rates were respectively 35, 350 and 35 ml.min^{-1}. The FID temperature was set at 573 K and the data acquisition rate was 100 Hz. For the SCD the H_2 and air flow rates were set at 45 and 5 ml.min^{-1} respectively while the burner temperature was set at 1073 K. The data acquisition rate of the SCD was set at 100 Hz. For the NCD the H_2 and O_2 flow rates were set at 5 and 11 ml.min^{-1} respectively while the burner temperature was set at 1193 K. The data acquisition rate of the NCD was also set at 100 Hz. For the TOF-MS the data acquisition rate was set at 30 spectra.s^{-1} with the scanning range set from 40 to 400 amu. The TOF-MS uses electron impact ionization. The GC interface temperature was set at 553 K and the source temperature was set at 473 K. The

split/splitless injector temperature was set at 573 K. The split flow rate was varied to obtain maximal sensitivity for the used detector without exceeding its linear range. The optimal split flow rate for the FID detector was found to be 150 ml.min^{-1} at an FID detector range of 10 while the optimal split flow rate for the SCD, NCD and TOF-MS was found to be 10 ml.min^{-1}. The first and second dimension columns were connected to a piece of deactivated fused silica column by means of a SilTite™ metal ferrule from SGE. The column set consisted of a non-polar first dimension column (MXT-1, Restek, 60 m × 0.25 mm, 0.25 µm) and a mid-polar second dimension column (BPX-50, SGE, 2 m × 0.25 mm, 0.25 µm) placed in the same oven. Helium was used as a carrier gas at a constant flow rate of 2.1 ml.min^{-1}. A temperature program was applied. It starts at 313 K and goes up to 643 K at a rate of 3 K/min. The temperature is held constant at 643 K for 10 min. Modulation was carried out on the piece of deactivated column. The modulation period was optimized to be as low as possible (maximal resolution in first dimension) without causing wrap-around (Mondello, 2012). This was done by varying the modulation period from 5 to 8 seconds. This resulted for the column combination used in our work to an optimal modulation time of 7 seconds. Table 4.2 shows an overview of the used GC × GC conditions.

Table 4.2: Overview of the GC x GC conditions

Detector	FID	NCD	SCD	TOF-MS
Injection				
Temperature	573 K	573 K	573 K	573 K
Split flow	150 ml.min^{-1}	10 ml.min^{-1}	10 ml.min^{-1}	10 ml.min^{-1}
Carrier gas	2.1 ml.min^{-1}	2.1 ml.min^{-1}	2.1 ml.min^{-1}	2.1 ml.min^{-1}
Oven program	313 to 643 K at 3 K/min 10 min at 643 K	313 to 643 K at 3 K/min 10 min at 643 K	313 to 643 K at 3 K/min 10 min at 643 K	313 to 643 K at 3 K/min 10 min at 643 K
Modulation time	7 s	7 s	7 s	7 s
Detector				
Temperature	573 K	1073 K	1193 K	-
Range	10	1	1	-
Acquisition rate	100 Hz	100 Hz	100 Hz	30 Hz

4.4 Quantification procedure

4.4.1 Data acquisition and Identification

Data acquisition was performed using Thermo Scientific's Chrom-Card data system for the FID,

SCD and NCD while Thermo Scientific's XCalibur was used for the TOF-MS. The raw data was

exported to a cdf file and imported into GCImage (Zoex, USA). GCImage performed the contour

plotting, retention time measurement, peak fitting and blob integration. Each blob was tentatively

identified by both a group and a carbon number. Tentative identification was done based on

literature data and Kovats retention indices (Miloslav et al., 2014). In addition the structured chromatogram the orthogonal separation of GC × GC provides was also used to aid in the identification of the compounds. As mentioned previously, an important disadvantage of using a GC-MS is that the fragmentation pattern of the complex hydrocarbon matrix will interfere with the hetero-compounds of interest due to the fact that hydrocarbon compounds are several orders of magnitude larger in concentration than the heteroatomic compounds. Even for GC × GC – TOF-MS the hetero-compounds can still overlap with the hydrocarbon matrix. Due to this interference only a limited amount of (non-overlapping) hetero-compounds could be tentatively identified in this way. To solve this problem for nitrogen containing species a qualitative solid phase extraction (SPE) was carried out before injection on the GC × GC - TOF-MS. All fractions were injected on the TOF-MS to help identify the nitrogen species. Finally the peak name, 1D retention time, 2D retention time and peak volume were exported as a csv file.

4.4.2 Quantification procedure

The mass fraction of each compound on the FID can be calculated using the mass fraction (w_i) of the internal standard (3-chlorothiophene) w_{st}:

$$w_i = \frac{f_i \cdot V_i}{f_{st} \cdot V_{st}} \cdot w_{st} \qquad (4.1)$$

where f_i is the relative response factor for compound i, V_i is the peak volume of compound i, f_{st} is the relative response factor of the internal standard and V_{st} is the peak volume of the internal standard. It has been demonstrated that various isomeric hydrocarbons, produce only slightly different relative FID responses, and hence that a fair approximation of the relative response factor (in respect to methane) may be written as (Beens et al., 1998):

$$f_i = \frac{M_i}{M_{CH4} \cdot N_{C,i}}$$

(4.2)

where M_i is the molar mass of compound i, $N_{c,i}$ is the carbon number of compound i and M_{ch4} is the molar mass of methane. This approximation removes the need to calibrate for each compound present in the mixture. Calibration was however carried out for 3-chlorothiophene, since it is used as an internal standard and the presence of a halogen atom is expected to influence the response factor significantly. Calibration showed that the relative response factor, f_i, of 3-chlorothiophene is 1.94 for the FID while based on the effective carbon number 1.85 would be expected. Since 2-chloropyridine was not used for the FID analysis no calibration was carried out for this component.

For the SCD and NCD a similar method can be adopted. However since the response of both the SCD and the NCD detector is linear and equimolar to the amount of sulfur and nitrogen respectively (Mahe et al., 2011) (and not the amount of the compound) following equation can be written:

$$w_i = \frac{V_i}{V_{st}} \cdot w_{st} \cdot \frac{M_i}{N_i \cdot M_{st_i}}$$

(4.3)

where N_i is the number of sulfur or nitrogen atoms in compound i and M_{st} the molar mass of the sulfur or nitrogen standard (3-chlorothiophene and 2-chloropyridine respectively). Since these sulfur and nitrogen compounds are also visible on the FID a correction procedure, described in Chapter 3, was applied to correct for the overlapping sulfur containing hydrocarbons. No correction procedure was applied for the nitrogen containing hydrocarbons since only a limited amount of the nitrogen containing compounds overlap with the hydrocarbons. All of these calculations are handled by an in-house written excel macro.

In addition to the nitrogen and sulfur containing compounds the TOF-MS analysis showed that also phenol homologues are present. Phenol homologues were substituted phenols with a hydrocarbon chain as one substituent or multiple hydrocarbon chain substituents. These compounds were grouped by the total number of carbon atoms present in the substituents, e.g. C1 phenols, C2 phenols, C3 phenols, C4 phenols. In an attempt to quantify these compounds a quantitative TOF-MS analysis was carried out. Quantitative TOF-MS analysis was done using a 5-point linear calibration curve for the compounds of interest (C1 phenols, C2 phenols, C3 phenols, C4 phenols). The peaks were integrated using the selected ion chromatograms in GCImage. It was assumed that all isomers of phenols with the same carbon number give the same response towards the selected ion and thus only one reference compound was selected for each isomer. The selected ions as well as the used reference compound for each isomer is listed in Table 4.3. The calibration curve was positioned so that the peak volume of the component of interest inside the shale oil is within the lower and upper point of the calibration curve allowing for the component to be quantified using interpolation. A multiple correlation coefficient (R^2) of at least 0.99 was obtained for all four calibration curves.

After analysis the mass fractions of all the quantified compounds are added and only if the total sum of the mass fractions is between 97 wt% and 103 wt% is the analysis considered acceptable after which all the mass fractions are normalized to 100 wt%. An overview of the global method used to get the final composition of the shale oil is shown in Figure 4.1.
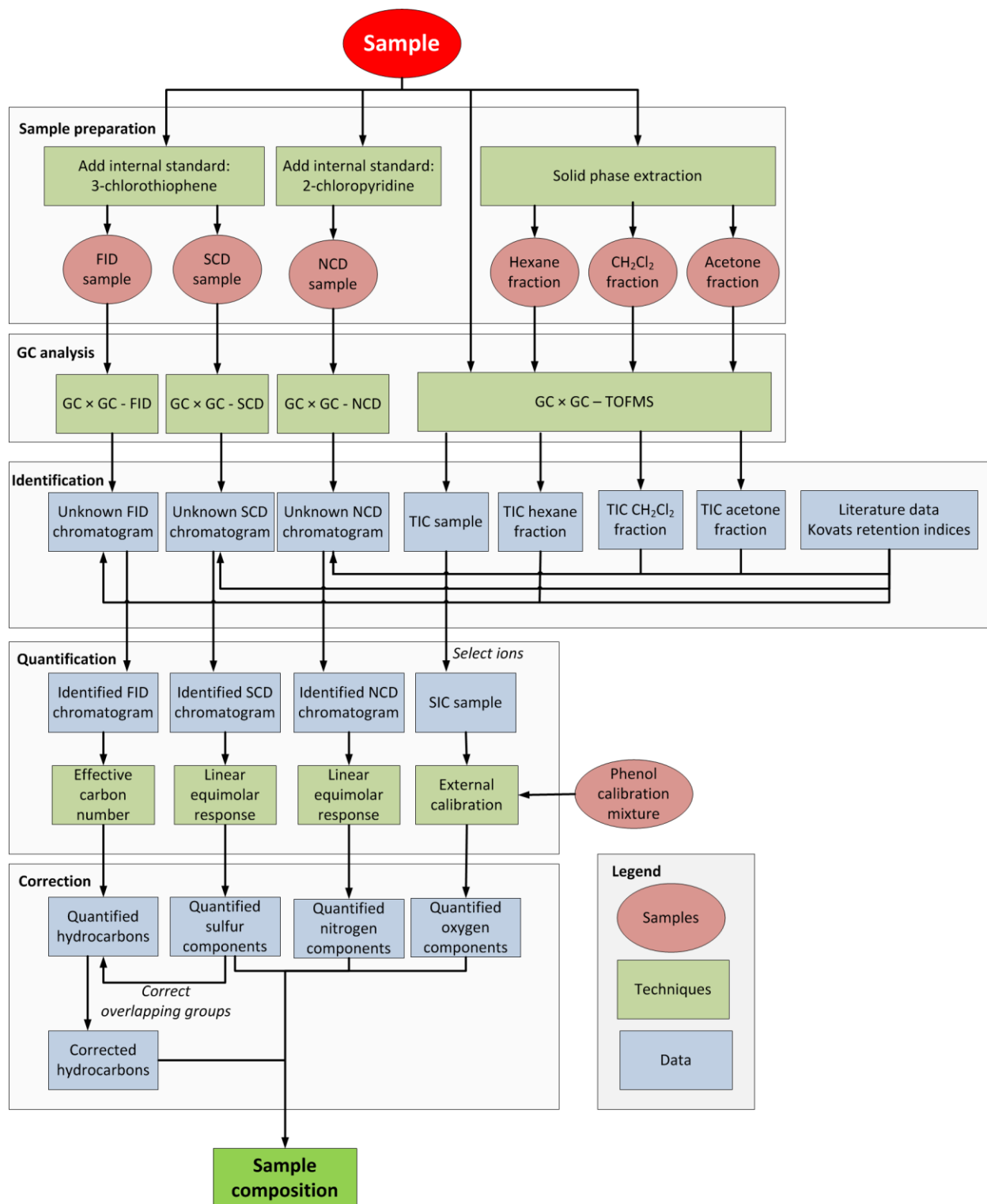
Figure 4.1: Overview of the analytical method (TIC = total ion chromatogram, SIC = single ion chromatogram)

Table 4.3: Reference compound and selected ion for the different detected phenol homologues

Group name	Reference compound	Selected ion (m/z)
C1 Phenols	O-cresol	108
C2 Phenols	2,3-dimethylphenol	122
C3 Phenols	2,3,5-trimethylphenol	136
C4 Phenols	4-isopropyl-3-methylphenol	150

4.5 Results and discussion

Figure 4.2 shows the GC × GC – FID chromatogram of the shale oil. As can be seen different groups (n-paraffins, isoparaffins, olefins/mononaphthenes, dinaphthenes, monoaromatics, naphthenoaromatics, diaromatics, naphthenodiaromatics and triaromatics) can be found using the orthogonal separation of the GC × GC. In addition to a group name a carbon number can be easily assigned using the "roof tile structure" (Marriott & Shellie, 2002; Schoenmakers et al., 2003; Mondello et al., 2008). This structure is obtained because increased branching leads to a reduced retention in the second dimension, resulting in so-called roof-tiles, i.e. ascending bands of isomeric compounds, which aids the interpretation of the chromatogram (Schoenmakers et al., 2000; von Mühlen et al., 2006; Adahchour et al., 2008). Figure 4.2 also shows that the internal standard (3-chlorothiophene) is adequately separated from the other compounds. This is confirmed by the 2D resolution, as defined by Dutriez et al. (2009), of this peak which is 15. This value is far higher than the recommended value of 1 which ensures good separation of the peak. Table 4.1 shows the elemental composition of the shale oil as well as the elemental composition of a light Arabian crude oil. It is clear that the shale oil has a higher content of sulfur and nitrogen but also oxygen contributing to the lower quality of the shale oil as compared to light crude oil. This is also confirmed by the GC × GC – NCD chromatogram of the shale oil shown in Figure 4.3 showing the presence of nitrogen containing hydrocarbons. Similar as with

the FID chromatogram the orthogonal separation of GC × GC allows for the assignments of different groups while the roof-tile structure allows for the assignment of a carbon number. These nitrogen containing compounds (pyridines, anilines, quinolines, indoles, acridines and carbazoles) were already detected in middle distillates, as reported by Lissitsyna et al. (2013). As mentioned 2-chloropyridine was chosen as an internal standards as it is sufficiently separated from the rest of the compounds and the 2D resolution of this peak is 23. The presence of nitrogen in the molecules increases the second dimension retention times causing wrap-around for the polycyclic aromatic nitrogen containing compounds with more than 2 rings namely the acridines and the carbazoles, see Figure 4.3. The wrap-around is however acceptable since both the acridines and the carbazoles are still completely separated from the other groups visible on the NCD chromatogram. An advantage of this increased second dimension retention time is that it can also be used to separate the nitrogen containing compounds from the hydrocarbons allowing in principle to use TOF-MS to identify and quantify those nitrogen compounds without resorting to a N-selective detector as has been done by Flego and Zannoni (2011). Flego and Zannoni however did not report the presence of pyridines. This could be caused by overlap of these compounds with the hydrocarbon matrix.
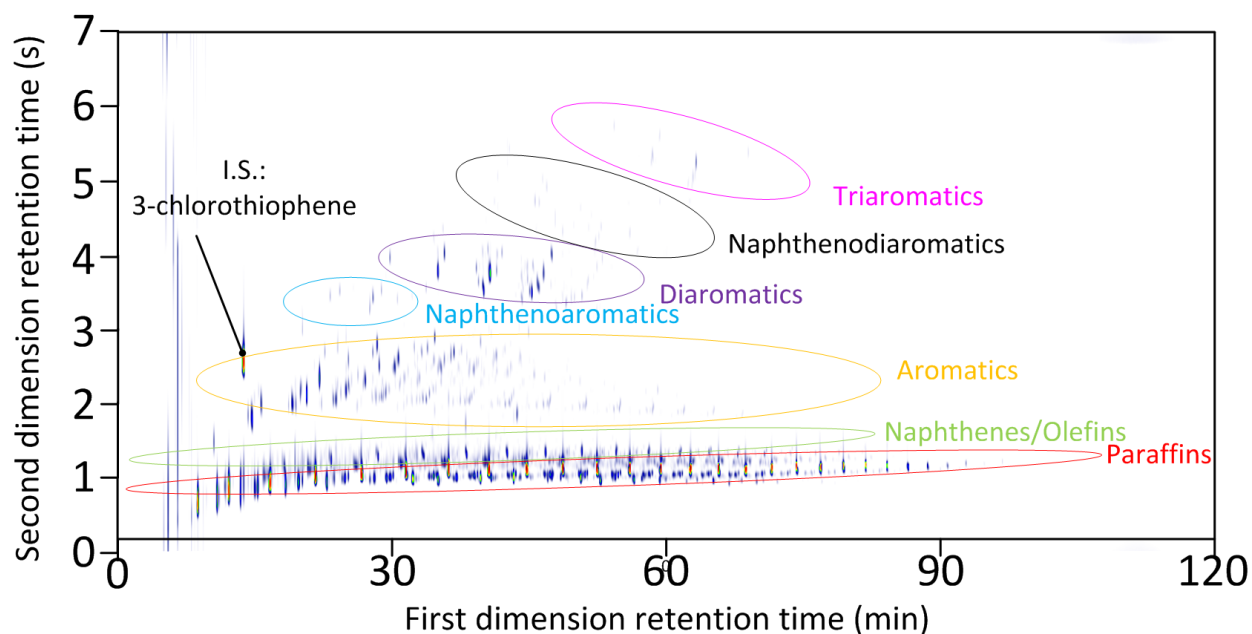
Figure 4.2: GC × GC – FID chromatogram of the shale oil samples with different hydrocarbon group types
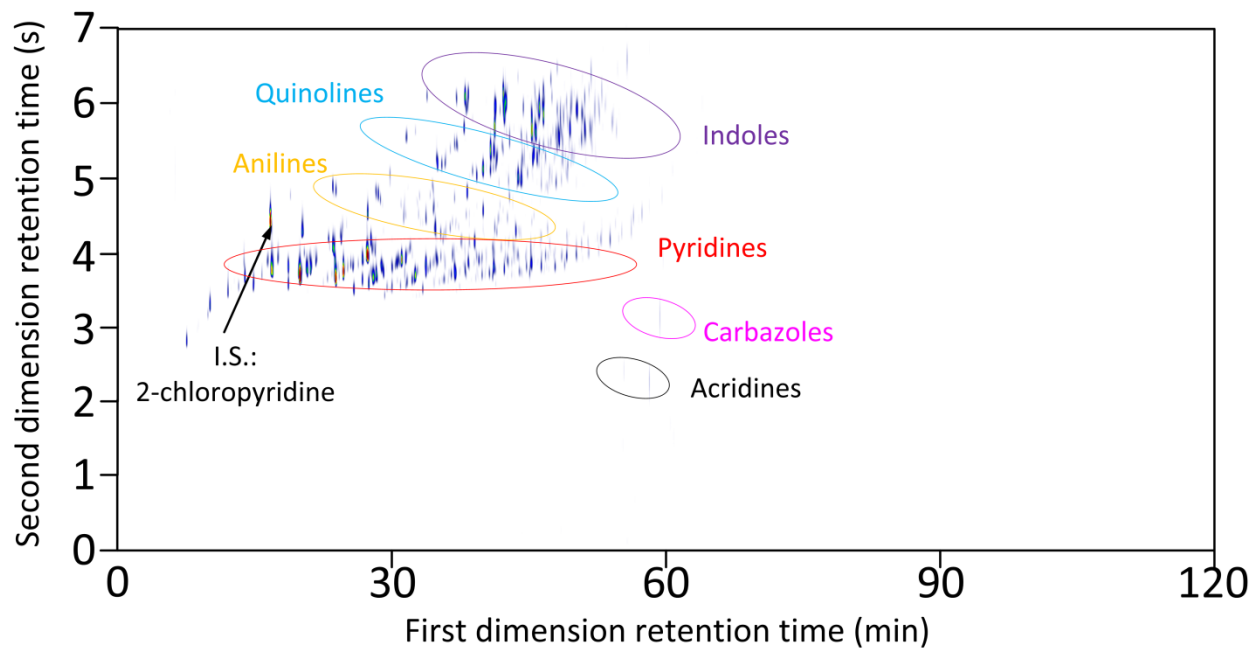
Figure 4.3: GC × GC – NCD chromatogram of the shale oil samples with different nitrogen containing

hydrocarbon group types

Figure 4.4 shows the GC × GC – SCD analysis and confirms the presence of sulfur containing hydrocarbons. Similar as with the FID chromatogram the orthogonal separation of GC × GC allows for the assignments of different groups in the chromatogram while the roof-tile structure allows for the assignment of a carbon number. These sulfur containing hydrocarbons (thiols/sulfides, benzothiophenes, naphthenobenzothiophenes and dibenzothiophenes) are also typically present in crude oils at low concentrations (Blomberg et al., 2004; Dijkmans et al., 2014). Again the peak of the internal standard (3-chlorothiophene) is separated from the rest of the compounds and the 2D resolution of this peak is 16. The second dimension retention time of all three chromatograms (Figure 4.2-4.4) has been matched using the internal standards (3-chlorothiophene and 2-chloropyridine). Figure 4.2 and Figure 4.4 show that no wrap-around occurs for the pure hydrocarbons and the sulfur containing hydrocarbons.

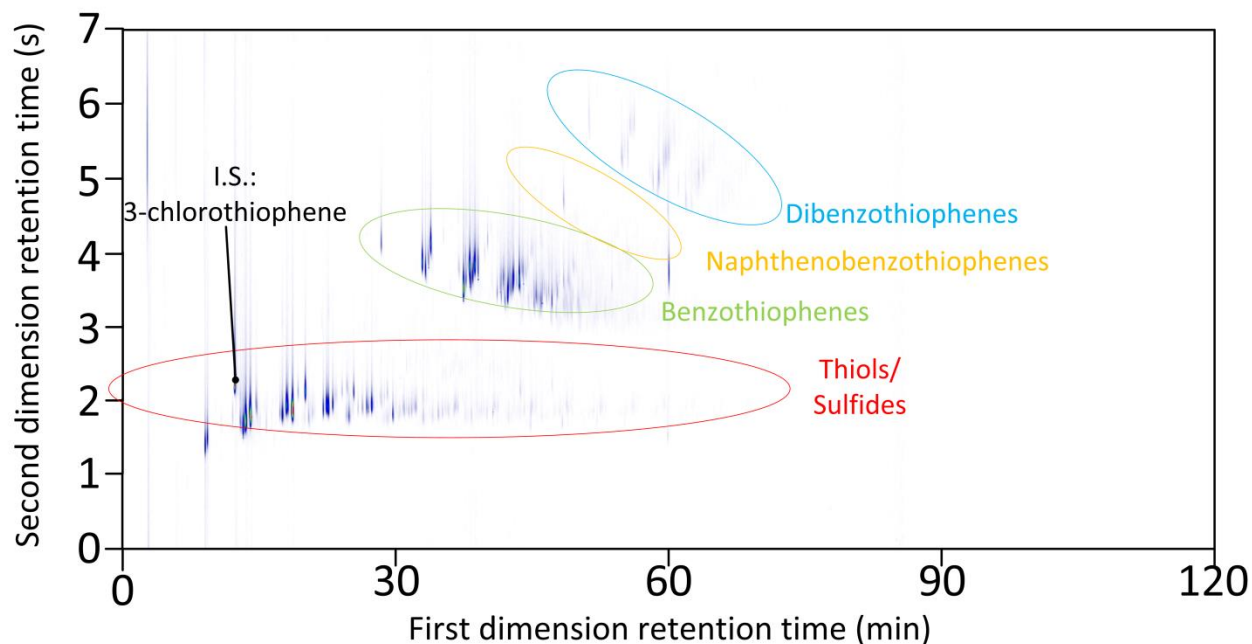**Figure 4.4: GC × GC – SCD chromatogram of the shale oil samples with different sulfur containing hydrocarbon group types**

It is clear from Figure 4.2, Figure 4.3 and Figure 4.4 that the sulfur and some of the nitrogen containing compounds which should also be visible on the FID chromatogram overlap mostly with the hydrocarbons. For the sulfur compounds a correction procedure was used to correct the quantities of hydrocarbons for these overlapping sulfur compounds as was done in Chapter 3. For nitrogen compounds however, this contribution has been neglected. The reason for this is twofold. First due to the relative low amounts of nitrogen in the shale oil (see Table 4.1) this contribution is expected to be negligible. Secondly, and more importantly, as mentioned by Flego and Zannoni (2011) most of the nitrogen compounds are adequately separated from the hydrocarbon matrix due to their high second dimension retention time. This can also be seen by comparing Figure 4.2 and Figure 4.3. Most nitrogen containing compounds are located in an area were no peaks are visible on the FID and thus most nitrogen containing compounds are not quantified based on the FID chromatogram.

During identification of the compounds using GC × GC –TOF-MS the presence of phenols in the shale oil was also revealed. This is further confirmed by Figure 4.5 which shows the selected ion chromatogram (m/e = 108,122,136,150) of the shale oil. The selected ions correspond to the molecular ion of different phenol homologues (C1-C4 phenols). Figure 4.5 also marks the different phenol homologues and both the roof-tile structure of the chromatogram as the TOF-MS confirm the carbon number of those homologues. Besides phenols other oxygenates that have been reported in shale oil are: indanols, naphthols, phenylphenols, fluorenols, phenanthrenols, ketones and esters (Willsch et al., 1997; Geng et al., 2012). Due to their overlap with the hydrocarbon matrix these compounds were not identified but in literature several methods have been reported that are able to quantify oxygenates in crude oil, coal liquids and shale oil by fractionation of the mixture in different acid, basic and neutral fractions, separating

the oxygenates from the hydrocarbon matrix (Farcasiu, 1977; Černý et al., 1990; Granda et al., 1990; Willsch et al., 1997; Geng et al., 2012).
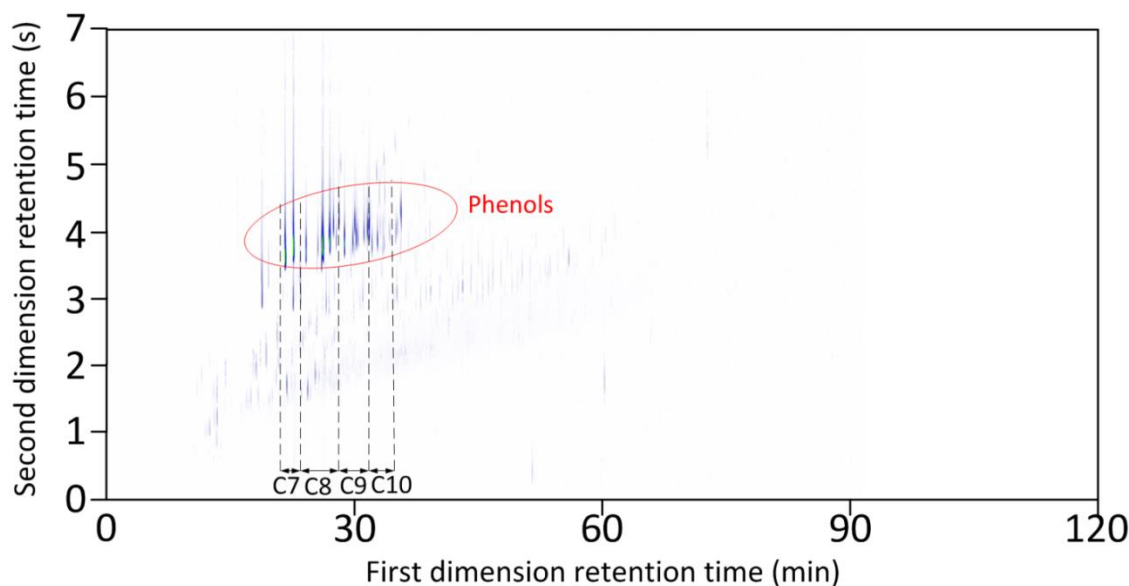
Figure 4.5: GC × GC – TOF-MS SIC chromatogram of the shale oil samples depicting the different phenol homologues (Selected ions: 108, 122, 136, and 150)

Using the previously acquired identification by group type and carbon number the composition of the shale oil was quantified using the procedure in Section 4.4.2. Table 4.4 shows the group type and carbon number distribution of the shale oil. Similar to crude oils the major part of the oil consists of normal and branched paraffins (up to 60 wt%). Other major groups include the olefins/mononaphthenes and the monoaromatics with 12.7 wt% and 11.0 wt% respectively. It also shows that a significant amount of the shale oil consists of sulfur and nitrogen containing compounds (2.2 wt% and 4.2 wt% respectively).

The major part of the nitrogen containing compounds is attributed to the presence of pyridines and indoles (1.98 wt%, and 1.10 wt% respectively). The rest of the nitrogen containing compounds is present in the form of quinolines and anilines (0.59 wt% and 0.46 wt%

respectively) while only a very small fraction of the nitrogen containing compounds are acridines and carbazoles (0.04 wt% and 0.04 wt% respectively).

The major part of the sulfur containing compounds is attributed to the presence of thiols/sulfides and benzothiophenes (0.93 wt% and 1.10 wt% respectively) while only a very small part of the sulfur containing compounds are naphthenobenzothiophenes and dibenzothiophenes (0.01 wt% and 0.16 wt% respectively). Total nitrogen and sulfur content as estimated by the GC × GC composition is 0.38 wt% and 0.47 wt% respectively which corresponds to the elemental composition given in Table 4.1 where the amount of nitrogen and sulfur is 0.40 wt% and 0.46 wt% respectively. Total amount of carbon and hydrogen is estimated at 85.4 wt% and 13.8 wt%. The estimated mass fraction of hydrogen is slightly higher as what is mentioned in Table 4.1. This is probably caused by the lack of identification and quantification of the oxygen containing compounds which should be present according to the elemental analysis.

Some of the oxygenate compounds (C1 – C4 phenols) could be identified and quantified using TOF-MS but only a small portion of the oxygen present in the sample could be attributed to these compounds. The identified and quantified phenols add up to around 0.34 wt% of the mixture which only accounts for 23% of the oxygen detected by the elemental analyzer. Oxygenates such as indanols, naphthols, phenylphenols, fluorenols, phenanthrenols, ketones and esters are overlapping with the hydrocarbon matrix and using the current technique these compounds were not identified or quantified and thus contribute towards the uncertainty of the method.

Table 4.4: Normalized composition of the shale oil by group type and by carbon number of all detected compounds (P = n-paraffins, I = iso-paraffins, MN = olefins/mononaphthenes, DN = dinaphthenes, MA = monoaromatics, NA = naphthenoaromatics, DA = diaromatics, NDA = naphthenodiaromatics, TA = triaromatics, Pd = pyridines, An = anilines, Q = quinolines, In = indoles, Ac = acridines, Ca = carbazoles, T = thiols/sulfides, BT = benzothiophenes, NBT = naphthenobenzothiophenes, DBT = dibenzothiophenes, Ph = phenols)

#C	P	I	MN	DN	MA	NA	DA	NDA	TA	Pd	An	Q	In	Ac	Ca	T	BT	NBT	DBT	Ph	Total
5	0.00	0.00	0.00	0.00	0.00	0.00	0.00	0.00	0.00	0.01	0.00	0.00	0.00	0.00	0.00	0.24	0.00	0.00	0.00	0.00	0.25
6	1.62	2.30	0.00	0.00	0.00	0.00	0.00	0.00	0.00	0.04	0.00	0.00	0.00	0.00	0.00	0.25	0.00	0.00	0.00	0.00	4.21
7	2.26	1.48	0.00	0.00	0.11	0.00	0.00	0.00	0.00	0.11	0.02	0.00	0.00	0.00	0.00	0.16	0.00	0.00	0.00	0.07	4.19
8	2.20	1.98	0.00	0.00	0.70	0.00	0.00	0.00	0.00	0.26	0.05	0.00	0.01	0.00	0.00	0.10	0.02	0.00	0.00	0.11	5.41
9	2.36	2.24	0.57	0.00	1.68	0.00	0.00	0.00	0.00	0.47	0.07	0.01	0.06	0.00	0.00	0.07	0.14	0.00	0.00	0.12	7.79
10	2.33	1.53	0.86	0.00	1.78	0.39	0.05	0.00	0.00	0.15	0.11	0.08	0.17	0.00	0.00	0.04	0.33	0.00	0.00	0.05	7.87
11	2.33	1.18	1.09	0.00	1.36	0.33	0.40	0.01	0.00	0.18	0.11	0.17	0.28	0.00	0.00	0.03	0.33	0.00	0.00	0.00	7.77
12	2.36	0.98	1.21	0.01	0.95	0.26	1.01	0.16	0.00	0.12	0.08	0.19	0.30	0.00	0.00	0.03	0.20	0.01	0.01	0.00	7.84
13	2.31	1.41	1.14	0.13	0.88	0.42	1.08	0.20	0.00	0.18	0.03	0.12	0.16	0.00	0.02	0.02	0.06	0.00	0.03	0.00	8.19
14	2.28	1.09	1.06	0.14	0.62	0.34	0.76	0.40	0.03	0.17	0.00	0.03	0.14	0.01	0.02	0.00	0.03	0.00	0.08	0.00	7.20
15	2.24	1.06	0.91	0.26	0.81	0.26	0.41	0.33	0.17	0.13	0.00	0.00	0.00	0.02	0.00	0.00	0.01	0.00	0.04	0.00	6.65
16	2.22	0.71	0.78	0.18	0.50	0.16	0.24	0.16	0.40	0.10	0.00	0.00	0.00	0.00	0.00	0.00	0.00	0.00	0.00	0.00	5.43
17	2.09	0.85	0.88	0.10	0.49	0.11	0.14	0.10	0.14	0.05	0.00	0.00	0.00	0.00	0.00	0.00	0.00	0.00	0.00	0.00	4.94
18	2.00	0.81	0.92	0.09	0.30	0.09	0.03	0.07	0.00	0.03	0.00	0.00	0.00	0.00	0.00	0.00	0.00	0.00	0.00	0.00	4.33
19	1.65	0.73	0.58	0.09	0.26	0.09	0.00	0.00	0.00	0.00	0.00	0.00	0.00	0.00	0.00	0.00	0.00	0.00	0.00	0.00	3.40
20	1.55	0.48	0.76	0.06	0.20	0.00	0.00	0.00	0.00	0.00	0.00	0.00	0.00	0.00	0.00	0.00	0.00	0.00	0.00	0.00	3.03
21	1.37	0.38	0.58	0.07	0.18	0.00	0.00	0.00	0.00	0.00	0.00	0.00	0.00	0.00	0.00	0.00	0.00	0.00	0.00	0.00	2.59
22	1.36	0.37	0.43	0.05	0.10	0.00	0.00	0.00	0.00	0.00	0.00	0.00	0.00	0.00	0.00	0.00	0.00	0.00	0.00	0.00	2.30
23	1.13	0.32	0.28	0.04	0.05	0.00	0.00	0.00	0.00	0.00	0.00	0.00	0.00	0.00	0.00	0.00	0.00	0.00	0.00	0.00	1.81
24	0.90	0.25	0.20	0.01	0.03	0.00	0.00	0.00	0.00	0.00	0.00	0.00	0.00	0.00	0.00	0.00	0.00	0.00	0.00	0.00	1.38
25	0.78	0.07	0.16	0.00	0.00	0.00	0.00	0.00	0.00	0.00	0.00	0.00	0.00	0.00	0.00	0.00	0.00	0.00	0.00	0.00	1.00
26	0.60	0.08	0.09	0.00	0.00	0.00	0.00	0.00	0.00	0.00	0.00	0.00	0.00	0.00	0.00	0.00	0.00	0.00	0.00	0.00	0.77
27	0.46	0.06	0.08	0.00	0.00	0.00	0.00	0.00	0.00	0.00	0.00	0.00	0.00	0.00	0.00	0.00	0.00	0.00	0.00	0.00	0.60
28	0.31	0.05	0.05	0.00	0.00	0.00	0.00	0.00	0.00	0.00	0.00	0.00	0.00	0.00	0.00	0.00	0.00	0.00	0.00	0.00	0.40
29	0.21	0.03	0.03	0.00	0.00	0.00	0.00	0.00	0.00	0.00	0.00	0.00	0.00	0.00	0.00	0.00	0.00	0.00	0.00	0.00	0.27
30	0.13	0.03	0.03	0.00	0.00	0.00	0.00	0.00	0.00	0.00	0.00	0.00	0.00	0.00	0.00	0.00	0.00	0.00	0.00	0.00	0.18
31	0.05	0.02	0.02	0.00	0.00	0.00	0.00	0.00	0.00	0.00	0.00	0.00	0.00	0.00	0.00	0.00	0.00	0.00	0.00	0.00	0.09
32	0.03	0.02	0.02	0.00	0.00	0.00	0.00	0.00	0.00	0.00	0.00	0.00	0.00	0.00	0.00	0.00	0.00	0.00	0.00	0.00	0.07
33	0.02	0.01	0.00	0.00	0.00	0.00	0.00	0.00	0.00	0.00	0.00	0.00	0.00	0.00	0.00	0.00	0.00	0.00	0.00	0.00	0.03
Total	39.08	20.50	12.71	1.21	11.00	2.43	4.14	1.42	0.74	1.98	0.46	0.59	1.10	0.04	0.04	0.93	1.10	0.01	0.16	0.34	100.00

4.6 Conclusion

A GC × GC technique has been successfully applied for the analysis of the detailed composition of a shale oil. The method combines the information of four different detectors on the GC × GC: a flame ionization detector (FID), a sulfur chemiluminescence detector (SCD), a nitrogen chemiluminescence detector (NCD) and a time of flight mass spectrometer (TOF-MS). Combination of the information supplied by the four detectors allows for the quantification of the composition of the shale oil by carbon number and division into 19 different classes namely paraffins, isoparaffins, olefins/mononaphthenes, dinaphthenes, monoaromatics, naphthenoaromatics, diaromatics, naphthenodiaromatics, triaromatics, thiols/sulfides, benzothiophenes, naphtenobenzothiophenes, dibenzothiophenes, pyridines, anilines, quinolines, indoles, acridines and carbazoles. In addition the TOF-MS revealed the presence of phenolic compounds. The analysis of the shale oil shows that the major part of the shale oil consists of pure hydrocarbons (93 wt%), with normal and branches paraffins (60 wt%) as main class of compounds, followed by olefins/mononaphthenes and monoaromatics with 12.7 wt% and 11.0 wt% respectively. Significant amounts of sulfur and nitrogen containing compounds are also detected and quantified (2.2 wt% and 4.2 wt% respectively). The sulfur containing compounds consist mainly of thiols/sulfides and benzothiophenes and to a lesser extend of naphthenobenzothiophenes and dibenzothiophenes. The nitrogen containing compounds consist mainly out of pyridines and indoles followed by the anilines and quinolines and to a lesser extend acridines and carbazoles.

Elemental analysis shows that also 0.33 wt% of oxygen is present in the shale oil. This is in-line with the GC × GC –TOF-MS analysis results that clearly show the presence of 0.34 wt% of

phenol homologues. However, only part of the oxygen containing compounds could be quantified (only 23% of the total oxygen content) because oxygen selective detection in complex hydrocarbon matrices remains a challenge.

4.7 References

Adahchour, M., Beens, J., & Brinkman, U. A. T. (2008). Recent developments in the application of comprehensive two-dimensional gas chromatography. Journal of Chromatography A, 1186, 67-108.

Adam, F., Bertoncini, F., Brodusch, N., Durand, E., Thiébaut, D., Espinat, D., & Hennion, M.-C. (2007). New benchmark for basic and neutral nitrogen compounds speciation in middle distillates using comprehensive two-dimensional gas chromatography. Journal of Chromatography A, 1148, 55-64.

Adam, F., Bertoncini, F., Coupard, V., Charon, N., Thiébaut, D., Espinat, D., & Hennion, M.-C. (2008). Using comprehensive two-dimensional gas chromatography for the analysis of oxygenates in middle distillates: I. Determination of the nature of biodiesels blend in diesel fuel. Journal of Chromatography A, 1186, 236-244.

Adam, F., Bertoncini, F., Dartiguelongue, C., Marchand, K., Thiébaut, D., & Hennion, M.-C. (2009). Comprehensive two-dimensional gas chromatography for basic and neutral nitrogen speciation in middle distillates. Fuel, 88, 938-946.

Al-Makhadmeh, L., Maier, J., Al-Harahsheh, M., & Scheffknecht, G. (2013). Oxy-fuel technology: An experimental investigations into oil shale combustion under oxy-fuel conditions. Fuel, 103, 421-429.

Amer, M. W., Marshall, M., Fei, Y., Jackson, W. R., Gorbaty, M. L., Cassidy, P. J., & Chaffee, A. L. (2013). Comparison of the yields and structure of fuels derived from freshwater algae (torbanite) and marine algae (El-Lajjun oil shale). Fuel, 105, 83-89.

Amer, M. W., Marshall, M., Fei, Y., Jackson, W. R., Gorbaty, M. L., Cassidy, P. J., & Chaffee, A. L. (2014). A comparison of the structure and reactivity of five Jordanian oil shales from different locations. Fuel, 119, 313-322.

Bae, E., Na, J.-G., Chung, S. H., Kim, H. S., & Kim, S. (2010). Identification of about 30 000 Chemical Components in Shale Oils by Electrospray Ionization (ESI) and Atmospheric Pressure Photoionization (APPI) Coupled with 15 T Fourier Transform Ion Cyclotron Resonance Mass Spectrometry (FT-ICR MS) and a Comparison to Conventional Oil. Energy & Fuels, 24, 2563-2569.

Ballice, L., Yüksel, M., Saglam, M., & Schulz, H. (1996). Evolution of volatile products from oil shales by temperature-programmed pyrolysis. Fuel, 75, 453-458.

Beens, J., Boelens, H., Tijssen, R., & Blomberg, J. (1998). Quantitative Aspects of Comprehensive Two-Dimensional Gas Chromatography (GC×GC). Journal of High Resolution Chromatography, 21, 47-54.

Blomberg, J., Riemersma, T., van Zuijlen, M., & Chaabani, H. (2004). Comprehensive two-dimensional gas chromatography coupled with fast sulphur-chemiluminescence detection: implications of detector electronics. Journal of Chromatography A, 1050, 77-84.

Černý, J., Pavlíková, H., & Machovič, V. (1990). Compound-class fractionation of coal-derived liquids by extrography. Fuel, 69, 966-971.

Dallüge, J., Beens, J., & Brinkman, U. A. T. (2003). Comprehensive two-dimensional gas chromatography: a powerful and versatile analytical tool. Journal of Chromatography A, 1000, 69-108.

Dijkmans, T., Van Geem, K. M., Djokic, M. R., & Marin, G. B. (2014). Combined Comprehensive Two-Dimensional Gas Chromatography Analysis of Polyaromatic Hydrocarbons/Polyaromatic Sulfur-Containing Hydrocarbons (PAH/PASH) in Complex Matrices. Industrial & Engineering Chemistry Research, (In Press).

Dutriez, T., Borras, J., Courtiade, M., Thiébaut, D., Dulot, H., Bertoncini, F., & Hennion, M.-C. (2011). Challenge in the speciation of nitrogen-containing compounds in heavy petroleum fractions by high temperature comprehensive two-dimensional gas chromatography. Journal of Chromatography A, 1218, 3190-3199.

Dutriez, T., Courtiade, M., Thiebaut, D., Dulot, H., Bertoncini, F., Vial, J., & Hennion, M. C. (2009). High-temperature two-dimensional gas chromatography of hydrocarbons up to nC(60) for analysis of vacuum gas oils. Journal of Chromatography A, 1216, 2905-2912.

Dutriez, T., Courtiade, M., Thiebaut, D., Dulot, H., & Hennion, M. C. (2010). Improved hydrocarbons analysis of heavy petroleum fractions by high temperature comprehensive two-dimensional gas chromatography. Fuel, 89, 2338-2345.

Ekinci, E., Türkay, S., Çitiroğlu, M., & Akar, A. (1994). Nitrogen compounds in pyrolysis produced liquids from two Turkish oil shales. Fuel Processing Technology, 37, 175-184.

Farcasiu, M. (1977). Fractionation and structural characterization of coal liquids. Fuel, 56, 9-14.

Fernandez-Lima, F. A., Becker, C., McKenna, A. M., Rodgers, R. P., Marshall, A. G., & Russell, D. H. (2009). Petroleum Crude Oil Characterization by IMS-MS and FTICR MS. Analytical Chemistry, 81, 9941-9947.

Flego, C., & Zannoni, C. (2011). N-containing species in crude oil fractions: An identification and quantification method by comprehensive two-dimensional gas chromatography coupled with quadrupole mass spectrometry. Fuel, 90, 2863-2869.

Geng, C. C., Li, S. Y., Ma, Y., Yue, C. T., He, J. L., & Shang, W. Z. (2012). Analysis and Identification of Oxygen Compounds in Longkou Shale Oil and Shenmu Coal Tar. Oil Shale, 29, 322-333.

Gentzis, T. (2013). Geochemical characterization of an oil seep from the Bagua Basin, north-central Peru. International Journal of Coal Geology, 108, 18-26.

Gersten, J., Fainberg, V., Hetsroni, G., & Shindler, Y. (2000). Kinetic study of the thermal decomposition of polypropylene, oil shale, and their mixture. Fuel, 79, 1679-1686.

Granda, M., Bermejo, J., Moinelo, S. R., & Menendez, R. (1990). Application of extrography for characterization of coal tar and petroleum pitches. Fuel, 69, 702-705.

Guo, H., Lin, J., Yang, Y., & Liu, Y. (2014). Effect of minerals on the self-heating retorting of oil shale: Self-heating effect and shale-oil production. Fuel, 118, 186-193.

Guo, S., & Ruan, Z. (1995). The composition of Fushun and Maoming shale oils. Fuel, 74, 1719-1721.

Hua, R. X., Li, Y. Y., Liu, W., Zheng, J. C., Wei, H. B., Wang, J. H., Lu, X., Kong, H. W., & Xu, G. W. (2003). Determination of sulfur-containing compounds in diesel oils by comprehensive two-dimensional gas chromatography with a sulfur chemiluminescence detector. Journal of Chromatography A, 1019, 101-109.

Hua, R. X., Wang, J. H., Kong, H. W., Liu, J., Lu, X., & Xu, G. W. (2004). Analysis of sulfur-containing compounds in crude oils by comprehensive two-dimensional gas chromatography with sulfur chemiluminescence detection. Journal of Separation Science, 27, 691-698.

Johannes, I., Kruusement, K., & Veski, R. (2007). Evaluation of oil potential and pyrolysis kinetics of renewable fuel and shale samples by Rock-Eval analyzer. Journal of Analytical and Applied Pyrolysis, 79, 183-190.

Kelly, L. C., & Rawson, P. (2010). Detection and identification of sulfur compounds in an Australian jet fuel: Defence Science and Technology Organisation.

Kumar, R., Bansal, V., Badhe, R. M., Madhira, I. S. S., Sugumaran, V., Ahmed, S., Christopher, J., Patel, M. B., & Basu, B. (2013). Characterization of Indian origin oil shale using advanced analytical techniques. Fuel, 113, 610-616.

Lei, Z., Huhman, D. V., & Sumner, L. W. (2011). Mass Spectrometry Strategies in Metabolomics. Journal of Biological Chemistry, 286, 25435-25442.

Lissitsyna, K., Huertas, S., Quintero, L. C., & Polo, L. M. (2013). Novel simple method for quantitation of nitrogen compounds in middle distillates using solid phase extraction and comprehensive two-dimensional gas chromatography. Fuel, 104, 752-757.

Mahe, L., Dutriez, T., Courtiade, M., Thiebaut, D., Dulot, H., & Bertoncini, F. (2011). Global approach for the selection of high temperature comprehensive two-dimensional gas chromatography experimental conditions and quantitative analysis in regards to sulfur-containing compounds in heavy petroleum cuts. Journal of Chromatography A, 1218, 534-544.

Marriott, P., & Shellie, R. (2002). Principles and applications of comprehensive two-dimensional gas chromatography. Trac-Trends in Analytical Chemistry, 21, 573-583.

Miloslav, N., Jiri, J., & Bedrich, K. (2014). Compendium of Chemical Terminology: Gold book. In: International Union of Pure and Applied Chemistry.

Mondello, L. (2012). Fundemental Principles of Comprehensive 2D GC. In: Shimadzu.

Mondello, L., Tranchida, P. Q., Dugo, P., & Dugo, G. (2008). Comprehensive two-dimensional gas chromatography-mass spectrometry: A review. Mass Spectrometry Reviews, 27, 101-124.

Na, J. G., Im, C. H., Chung, S. H., & Lee, K. B. (2012). Effect of oil shale retorting temperature on shale oil yield and properties. Fuel, 95, 131-135.

Newell, R. G., & Iler, S. (2013). The Global Energy Outlook: National Bureau of Economic Research.

Rovere, C. E., Crisp, P. T., Ellis, J., & Bolton, P. D. (1983). Chemical characterization of shale oil from Condor, Australia. Fuel, 62, 1274-1282.

Rovere, C. E., Crisp, P. T., Ellis, J., & Korth, J. (1990). Chemical class separation of shale oils by low pressure liquid chromatography on thermally-modified adsorbants. Fuel, 69, 1099-1104.

Ruiz-Guerrero, R., Vendeuvre, C., Thiebaut, D., Bertoncini, F., & Espinat, D. (2006). Comparison of comprehensive two-dimensional gas chromatography coupled with sulfur-chemiluminescence detector to standard methods for speciation of sulfur-containing compounds in middle distillates. Journal of Chromatographic Science, 44, 566-573.

Schoenmakers, P., Marriott, P., & Beens, J. (2003). Nomenclature and conventions in comprehensive multidimensional chromatography. Lc Gc Europe, 16, 335-339.

Schoenmakers, P. J., Oomen, J. L. M. M., Blomberg, J., Genuit, W., & van Velzen, G. (2000). Comparison of comprehensive two-dimensional gas chromatography and gas chromatography − mass spectrometry for the characterization of complex hydrocarbon mixtures. Journal of Chromatography A, 892, 29-46.

Shi, Q., Yan, Y., Wu, X., Li, S., Chung, K. H., Zhao, S., & Xu, C. (2010). Identification of Dihydroxy Aromatic Compounds in a Low-Temperature Pyrolysis Coal Tar by Gas Chromatography−Mass Spectrometry (GC−MS) and Fourier Transform Ion Cyclotron Resonance Mass Spectrometry (FT-ICR MS). Energy & Fuels, 24, 5533-5538.

Shue, F.-F., & Yen, T. F. (1981). Concentration and selective identification of nitrogen- and oxygen-containing compounds in shale oil. Analytical Chemistry, 53, 2081-2084.

Sun, Y., Bai, F., Liu, B., Liu, Y., Guo, M., Guo, W., Wang, Q., Lü, X., Yang, F., & Yang, Y. (2014). Characterization of the oil shale products derived via topochemical reaction method. Fuel, 115, 338-346.

Tiwari, P., & Deo, M. (2012). Compositional and kinetic analysis of oil shale pyrolysis using TGA-MS. Fuel, 94, 333-341.

Tong, J., Han, X., Wang, S., & Jiang, X. (2011). Evaluation of Structural Characteristics of Huadian Oil Shale Kerogen Using Direct Techniques (Solid-State 13C NMR, XPS, FT-IR, and XRD). Energy & Fuels, 25, 4006-4013.

Tong, J., Liu, J. G., Han, X. X., Wang, S., & Jiang, X. M. (2013). Characterization of nitrogen-containing species in Huadian shale oil by electrospray ionization Fourier transform ion cyclotron resonance mass spectrometry. Fuel, 104, 365-371.

Total Energy Consumption. (2012) http:\\yearbook.enerdata.net

Tranchida, P. Q., Purcaro, G., Dugo, P., & Mondello, L. (2011). Modulators for comprehensive two-dimensional gas chromatography. Trac-Trends in Analytical Chemistry, 30, 1437-1461.

Tranchida, P. Q., Sciarrone, D., Dugo, P., & Mondello, L. (2012). Heart-cutting multidimensional gas chromatography: A review of recent evolution, applications, and future prospects. Analytica Chimica Acta, 716, 66-75.

van der Westhuizen, R., Ajam, M., De Coning, P., Beens, J., de Villiers, A., & Sandra, P. (2011). Comprehensive two-dimensional gas chromatography for the analysis of synthetic and crude-derived jet fuels. Journal of Chromatography A, 1218, 4478-4486.

Van Geem, K. M., Pyl, S. P., Reyniers, M. F., Vercammen, J., Beens, J., & Marin, G. B. (2010). On-line analysis of complex hydrocarbon mixtures using comprehensive two-dimensional gas chromatography. Journal of Chromatography A, 1217, 6623-6633.

von Mühlen, C., Zini, C. A., Caramão, E. B., & Marriott, P. J. (2006). Applications of comprehensive two-dimensional gas chromatography to the characterization of petrochemical and related samples. Journal of Chromatography A, 1105, 39-50.

Wang, F. C. Y., & Zhang, L. (2007). Chemical composition of group II lubricant oil studied by high-resolution gas chromatography and comprehensive two-dimensional gas chromatography. Energy & Fuels, 21, 3477-3483.

Washburn, K. E., & Birdwell, J. E. (2013). Updated methodology for nuclear magnetic resonance characterization of shales. Journal of Magnetic Resonance, 233, 17-28.

Williams, P. T., & Chishti, H. M. (2001). Reaction of nitrogen and sulphur compounds during catalytic hydrotreatment of shale oil. Fuel, 80, 957-963.

Willsch, H., Clegg, H., Horsfield, B., Radke, M., & Wilkes, H. (1997). Liquid Chromatographic Separation of Sediment, Rock, and Coal Extracts and Crude Oil into Compound Classes. *Analytical Chemistry,* 69, 4203-4209.

Yang, Y. T., & Wang, Z. (2010). Determination of Sulfur-containing Compounds in Straight Run Diesel Oil by Comprehensive Two Dimensional Gas Chromatography. *Chinese Journal of Analytical Chemistry,* 38, 1805-1808.

Chapter 5: Molecular reconstruction of crude oil derived feedstocks

5.1 Introduction

Chemical plants and oil refineries typically process streams which contain mixtures of a large number of molecular species, e.g. several thousand of hydrocarbon species (Quann, 1998). These streams are used as feedstocks in reactors and unit operations. In an attempt to model these reactors and unit operations using simulation models a detailed composition of the feedstock becomes important. As mentioned before several analytical techniques are available which can provide this type of detailed composition. For example in Chapters 2, 3 and 4 $GC \times GC$ augmented with several different detectors types (FID, SCD, NCD, TOF-MS) has been discussed. The proposed methodology was able to quantify the pure hydrocarbons as well as the sulfur- and nitrogen- containing hydrocarbons by dividing the compounds based on a group name and carbon number. The main disadvantage of these analytical techniques is that they are time consuming and prone to errors (Van Geem et al., 2007). This makes that these techniques are rarely used in plant operation and scheduling. However, the dynamic nature of a modern refinery or chemical plant results into streams that can change on a daily or hourly basis and nowadays these analytical techniques are being replaced with numerical procedures which can reconstruct the detailed composition of a feedstock based on readily available commercial indices (Allen & Liguras, 1991; Campbell & Klein, 1997; Hudebine & Verstraete, 2004; Hudebine et al., 2011). These indices, e.g. the average molar mass of the mixture, some boiling points of a distillation

curve, the specific density, the global PINA mass fractions, etc., can be determined by means of relatively simple, cheap and standardized analytical procedures (Riazi, 2005). Although these indices are not representative for all the chemical and structural variety that such mixtures can contain typically a feedstock is identified and distinguished on the market based on these commercial indices. The great advantage of these reconstruction methods is that they are very fast and cheap once developed in comparison to the more detailed analytical methods. In addition most of the commercial indices are often supplied by the vendor of the feedstock.

Determining the molecular composition based on only these macroscopic properties is not easy since there is no unique relationship between a combination of commercial indices and the detailed composition of a complex mixture. Molecular reconstruction therefore needs to select a single detailed molecular composition out of all theoretically possible compositions matching the given indices. Two types of methods can be distinguished in literature. Both methods select a single detailed composition out of all the theoretically possible compositions. The first method selects the detailed molecular composition by optimizing a specific objective function in addition to the constraints given by the commercial indices. Different types of objective functions are used such as theoretical derived objective functions, which include the Gibbs free energy (Ha et al., 2005) or Shannon Entropy (Hudebine & Verstraete, 2004; Van Geem et al., 2007; Van Geem et al., 2008; Pyl et al., 2010), but also other types of cost functions are possible (Albahri, 2005; Androulakis et al., 2005). Due to the theoretical approach of these methods they can be applied for a wide range of feedstocks depending on the molecular library that is used. This molecular library can also be obtained using stochastic Monte-Carlo generation of the components constituting the mixture (Neurock et al., 1994; Trauth et al., 1994; Hudebine & Verstraete, 2004).

In this way, not only the composition but also the identities of the mixture components are derived from the available macroscopic data.

The second method is based upon a large set of analytical data to train either artificial neural networks (Joo et al., 2001; Pyl et al., 2010) or other types of empirical correlations (Dente et al., 1979). It is clear that these methods are limited to feedstocks that are similar to the feedstocks used in the analytical database and the method is thus not easily extended towards other feedstocks severely limiting the use of the method.

Chapter 3 and Chapter 4 showed that next to pure hydrocarbons significant amounts of sulfur- and nitrogen-containing hydrocarbons can be present in these types of feedstocks. Literature describing feedstock reconstruction including sulfur containing hydrocarbons remains limited, among others because of the limited analytical data available for these sulfur containing hydrocarbons. López García et al. (2010) used a statistical reconstruction method in which they represent the feedstock by carbon number and chemical family. Twenty-eight different chemical families were used including sulfur and nitrogen containing families. Sulfur species were represented by 6 different chemical families namely sulfides/thiols, thiophenes, benzothiophenes, alkyldibenzothiophenes, 4-alkyldibenzothiophenes and 4,6-alkyldibenzothiophenes. López García et al. (2010) did not validate the data for the sulfur compounds. Only a comparison between the commercial indices specified as input and those reconstructed was shown which, as expected, agrees very well. No comparison was made with more detailed sulfur data such as the distribution of sulfur compounds as function of carbon number.

Hudebine and Verstraete (2011) reported the reconstruction of FCC gasoline's using Shannon entropy maximization. Their compound library contained around 1800 compounds and was divided into 21 chemical families including thiols, sulfides and thiophenes. Again no validation

data of these sulfur containing hydrocarbons is reported as only parity plots are shown of the 230 compounds measured using a GC analysis. No further specification of the compounds is made.

In this chapter an existing method based on Shannon entropy maximization is investigated (Van Geem et al., 2007; Pyl, 2013). In this chapter the molecular library of this method will be extended so that it is able to model the increasingly heavier oil fractions that were studied in Chapter 2 but also sulfur containing hydrocarbons that were found to be present in significant amounts in Chapter 3 and Chapter 4.

For this reason the library of the method is extended towards a carbon number of 45 using group contribution methods (Hudebine et al., 2011; Hudebine & Verstraete, 2011), but also the classes of sulfur containing compounds that were identified in Chapter 3 and Chapter 4 were added to the library. At present no nitrogen containing compounds were added to the library.

In addition to the extension of the library several commercial indices related to these sulfur compounds have been added to the list of potential commercial indices that the method can account for in an attempt to improve the reconstruction of these sulfur compounds. These commercial indices include the total sulfur content, the aromatic sulfur content but also group type analysis based on 15 different groups.

The developed method has been tested using the vacuum gas oils studied in Chapter 2 as well as the atmospheric gas oils studied in Chapter 3. The results of the reconstruction are compared with the results of the detailed analytical compositions. The relevance of these additional commercial indices related to sulfur is also investigated.

5.2 Feedstock reconstruction

5.2.1 Methodology

The reconstruction method used in this chapter is discussed by Van Geem et al. (2007) and Pyl et al. (2010). It is based on the maximization of the Shannon Entropy which was originally formulated in the information theory developed by Shannon (1948). A short overview of the method will be given in this chapter. The Shannon entropy is defined as:

$$S(y_i) = -\sum_{i=1}^{n} y_i . ln(y_i) \tag{5.1}$$

where

$$\sum_{i=1}^{n} y_i = 1 \tag{5.2}$$

In our case y_i is the mole fraction of one of the n compounds in the library. The maximization of the entropy is constrained by the commercial indices that are specified for the feedstock. The numerical translation of these constraints should take into account the correlation between the supplied commercial indices and the unknown mole fractions. Correlations for density, elemental composition and boiling point curve can be expressed by mixing rules or similar correlations. For each commercial indices (k) the following constraint can then be written:
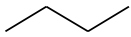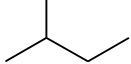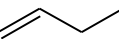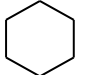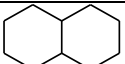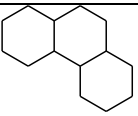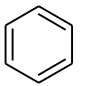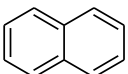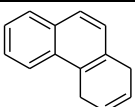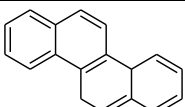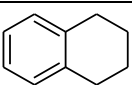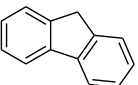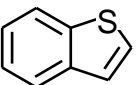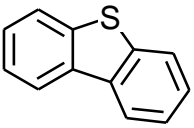
$$p_k - f_k(y_i) = 0 \tag{5.3}$$

Where p_k is the actual value of the commercial indices and f_k is the correlation that can be written between the mole fractions of the mixture and the commercial indices of that mixture. Due to the analytical errors most of the constraints are not exact constraints and the standard deviation of the measured analytical methods has to be taken into account (Hudebine & Verstraete, 2004). Maximization of the Shannon entropy under these constraints means that out

of all theoretical possible mixtures that meet these constraints the composition with the maximum Shannon entropy is chosen. Since the Shannon entropy is directly proportional to the mixing entropy (Pyl et al., 2010) it means that from all possible mixtures the mixture with the highest mixing entropy is chosen.

It is clear that the choice of the molecular library is the basis of the method as the constraints are directly related to physical properties of the molecules present in this library. This molecular library specifies which molecules are considered in the reconstruction and which not. For each of these molecules the physical properties, e.g., normal boiling point, molar mass, density, etc., that are necessary to calculate the commercial indices of a (theoretical) mixture need to be known and need to be available in the library. The feedstocks studied in this chapter contain a very broad range of compounds and the molecular library must thus contain a very broad range of compounds for the reconstruction of these feedstocks. However as mentioned in Chapter 2 currently no analytical method is capable of distinguishing between all the isomers and no kinetic model takes all of these compounds into account. As such creating a molecular library which includes all of these isomers, which moreover have very similar physical properties, is not useful. Instead, in line with the GC × GC analysis specific groups and carbon number were used to represent to compounds present in the mixture. Both hydrocarbons and sulfur containing compounds detected in Chapter 2, 3 and 4 were included in this library. At present no nitrogen containing compounds have been added to the library because of the limited data available regarding nitrogen components and crude oil mixtures. The final library consists of 816 (pseudo)-compounds ranging from carbon number 1 up to a carbon number of 45 and consisting of 15 different groups. Table 5.1 gives an overview of the 15 different groups and their minimum and maximum carbon number.

Table 5.1: Overview of the pseudo-compounds considered

Group type	Characteristic structure	Carbon range
n-paraffins		1-45
Isoparaffins		4-45
Olefins		3-45
Mononaphthenes		5-45
Dinaphthenes		9-43
Trinaphthenes		13-44
Monoaromatics		6-45
Diaromatics		10-43
Triaromatics		14-39
Tetra-aromatics		16-37
Naphthenoaromatics		9-44
Naphthenodiaromatics		13-41
Thiols/Sulfides	—SH	1-45
Benzothiophenes		8-44
Dibenzothiophenes		12-44

The physical properties of all of these (pseudo-)compounds need to be present in the library. As stated previously, these physical properties include density, normal boiling point and elemental composition. The determination of the elemental composition is straightforward but the determination of the density and the boiling point is more difficult. For the lowest molar mass compounds in each homologous series the density and boiling point are retrieved from NIST Chemistry Webbook ("NIST Chemistry WebBook, NIST Standard Reference Database Number 69," 2009) or API Technical Databook ("API Technical Data Book," 2005). For heavier compounds the density and boiling point are derived from the properties of these light compounds and group contribution methods (Hudebine et al., 2011; Hudebine & Verstraete, 2011). In order to do so, heavy pseudo-compounds are assigned a single representative structure, based on the characteristic structures shown in Table 5.1, and methyl groups are added to this characteristic structure as a single chain to increase the carbon number of the compound.

The assignment of the group types within the library (e.g. PINA analysis) for sulfur containing hydrocarbons is less straightforward as no information is available as to where these compounds end up during these types of analysis. The used assignment is based upon the GC × GC analysis provided in Chapter 3 where the thiols and sulfides overlap with the monoaromatics, the benzothiophenes overlap with the diaromatics and the dibenzothiophenes overlap with the triaromatics. As such all three groups contribute to the aromatic fraction of a PINA analysis.

Usually it is not necessary to include the complete carbon range of all the compounds belonging to a certain class in the library of the feedstock reconstruction. Therefore several filters are applied on a large global library before the calculation of the mole fractions starts. These filters permit to automatically select a subset of compounds from the entire library based on the available macroscopic properties. For example, compounds with a boiling point significantly

higher than the final boiling point or lower than the initial boiling point of the feedstock can be safely excluded. Similarly, compounds can be excluded based on the available group-type composition or elemental analysis. For example for all gas oils used no olefins were included in the reduced library as they were not detected.

Finding the global maximum of the non-linear problem defined by Equations 5.1, 5.2 and 5.3 is not an easy task. An advantage of the Shannon entropy maximization method compared to other optimization methods is the simple solution strategy for the problem. The Lagrange multiplier method can be used to reduce the non-linear optimization problem with constraints to a non-linear optimization problem without constraints. If in addition all the constraints are linear the problem can be transformed from a non-linear function of the mole fractions to a non-linear function with k (number of constraints) variables (Hudebine & Verstraete, 2004; Van Geem et al., 2007). This simplified objective function can than easily be optimized using Rosenbrock's method (Rosenbrock, 1960). Due to the analytical errors most of the constraints are not exact constraints and the standard deviation of the measured analytical methods is thus incorporated into the final objective function (Van Geem et al., 2007).

Pyl (2013) already showed that this linearity is the case for the commercial indices of the original method. However to better reconstruct the sulfur containing hydrocarbons additional indices specific for sulfur compounds were added.

A first choice is replacing the C/H ratio from the original method with the elemental composition of the feedstock (wt% C, H and S). The mass fraction of carbon can for example be calculated as follows:

$$w_C = \frac{\sum_{i=1}^{n} x_i \, M_C \, N_{C,i}}{\sum_{i=1}^{n} x_i \, M_i} \tag{5.4}$$

This can be transformed into a linear constraint for the Shannon entropy maximization algorithm:

$$\sum_{i=1}^{n}\left(w_c\, M_i - N_{C,i}\, M_C\right)x_i = 0 \tag{5.5}$$

Similar equations can be derived for hydrogen and sulfur:

$$\sum_{i=1}^{n}\left(w_H\, M_i - N_{H,i}\, M_H\right)x_i = 0 \tag{5.6}$$

$$\sum_{i=1}^{n}\left(w_S\, M_i - N_{S,i}\, M_S\right)x_i = 0 \tag{5.7}$$

More detailed sulfur speciation methods can help improving the reconstruction of sulfur compounds even further. Several more detailed sulfur type speciation methods are available using a variety of analytical techniques. Mass spectroscopic techniques (coupled to gas chromatography) allow for the differentiation between different sulfur groups (Robinson, 1971; Fafet et al., 1999; López García et al., 2002; Zeigler et al., 2012). Note that these mass selective techniques have their limitations (Hegazi & Andersson, 2007) as was also mentioned in Chapter 3 and Chapter 4.

Other techniques that can supply additional information about the distribution of sulfur compounds in the feedstock are gas chromatographic techniques coupled to an element selective detector (Stumpf et al., 1998; Schulz et al., 1999; Hua et al., 2004; Nylén et al., 2004; Mahe et al., 2011; Moustafa & Andersson, 2011). All these techniques supply additional information about the sulfur present in the feedstock and most of these techniques report the presence of aromatic sulfur containing hydrocarbons under the form of benzothiophenes and dibenzothiophenes. This information can be used for example to derive the total aromatic sulfur present in the mixture. This aromatic sulfur determination allows a clear differentiation between the thiols/sulfides and

the benzothiophenes and dibenzothiophenes as only the latter two will contribute towards aromatic sulfur. The derived constraint is very similar to Equation .5.7.

$$\sum_{i=1}^{n} \left(w_{S,aro} \, M_i - N_{S,aro,i} \, M_S \right) x_i = 0$$

(5.8)

Mercaptan sulfur is another property which is easy to measure as shown by a variety of standard methods (UOP163, 2010; ASTM-D4952, 2012; ASTM-D3227, 2013). Mercaptan sulfur is the sulfur that is present in thiols or mercaptans. Mercaptan sulfur does not account for the sulfur originating from sulfides. Thiols and sulfides were however grouped in Chapter 3 and Chapter 4 due to the lack of separation on $GC \times GC - SCD$. In this respect no differentiation was made in the library of the reconstruction method. It is thus impossible to calculate mercaptan sulfur with the current chemical families in the library without putting more effort in the analysis. This could be resolved by a preparative LC separation which separates the sulfides from the non-sulfides (Green et al., 1993) prior to injection on $GC \times GC - SCD$.

Some of the above mentioned sulfur speciation techniques can also be used to obtain a group type distribution of the sulfur compounds (specifying the amount of thiols/sulfides, benzothiophenes and dibenzothiophenes directly). This group type distribution could also be used as additional commercial indices as has been done by López García et al. (2010). This would provide additional information for the reconstruction method.

5.2.2 Procedures

In the first part of this chapter the results of the reconstruction of the pure hydrocarbons for vacuum gas oils will be verified and compared to the results in Chapter 2. Reconstruction is done based on use a PINA analysis, ASTM-D2887 boiling point curve, density and H/C ratio of the feedstock.

In the second part of this chapter the value of different combinations of commercial indices will be studied to see which combination is most effective in accurately predicting the concentrations of the sulfur compounds inside the gas oils analyzed in Chapter 3. The first three combinations all use PINA analysis data, ASTM-D2887 boiling point curve and density of the feedstock. In the first combination no additional information about sulfur will be supplied and only the H/C ratio will be given in addition to the other commercial indices. In the second combination the elemental composition in terms of C, H and S will be given so the total amount of sulfur in the sample will be known. In the third combination the amount of aromatic sulfur will be specified in addition to the elemental composition. In the last combination instead of the PINA analysis a detailed group type analysis will be supplied. This group type analysis consists of 12 groups namely n-paraffins, isoparaffins, mononaphthenes, dinaphthenes, monoaromatics, naphthenoaromatics, diaromatics, naphthenodiaromatics, triaromatics, thiols/sulfides, benzothiophenes and dibenzothiophenes and is based on the analysis of the gas oils in Chapter 3. An overview of the combinations of commercial indices is given in Table 5.2.

Table 5.2: Different combinations of commercial indices

	Comb. 1	Comb.2	Comb.3	Comb.4
Density	Yes	Yes	Yes	Yes
Total Sulfur	No	Yes	Yes	No
Aromatic Sulfur	No	No	Yes	No
Group Type analysis	PINA			Detailed
Boiling point curve	ASTM-D2887			

5.3 Results and discussion

5.3.1 Reconstruction of the vacuum gas oil

The method in Section 5.2 was used to reconstruct the three VGO's analyzed using GC × GC in Chapter 2. Table 5.3 shows for example both the analytical and reconstructed commercial indices of VGO A. It is clear that the algorithm is able to accurately predict all the specified commercial indices. For the commercial indices related to the initial and final boiling points of the distillation curves the difference is larger because of the larger standard deviation as the analytical error is larger (Riazi, 2005).

Table 5.3: Analytical and reconstructed commercial indices specified for VGO A

	Analytical	Reconstructed
H/C (mol.mol^{-1})	1.77	1.76
Density (kg.m^{-3})	862	861
PINA analysis (wt%)		
P	17.3	17.4
I	21.3	21.3
N	17.3	17.3
A	44.1	44.0
ASTM-D2887 (K)		
0%	399	423
10%	550	533
30%	595	591
50%	625	623
70%	650	648
90%	684	691
100%	775	803

Figure 5.1 shows the analytical and reconstructed carbon distributions of different groups (n-paraffins, isoparaffins, naphthenes and monoaromatics). The reconstructed carbon number distribution of these feedstocks agrees well with the analytical data. Only for the aromatics the reconstructed curve is lower and broader than the analytical curve.
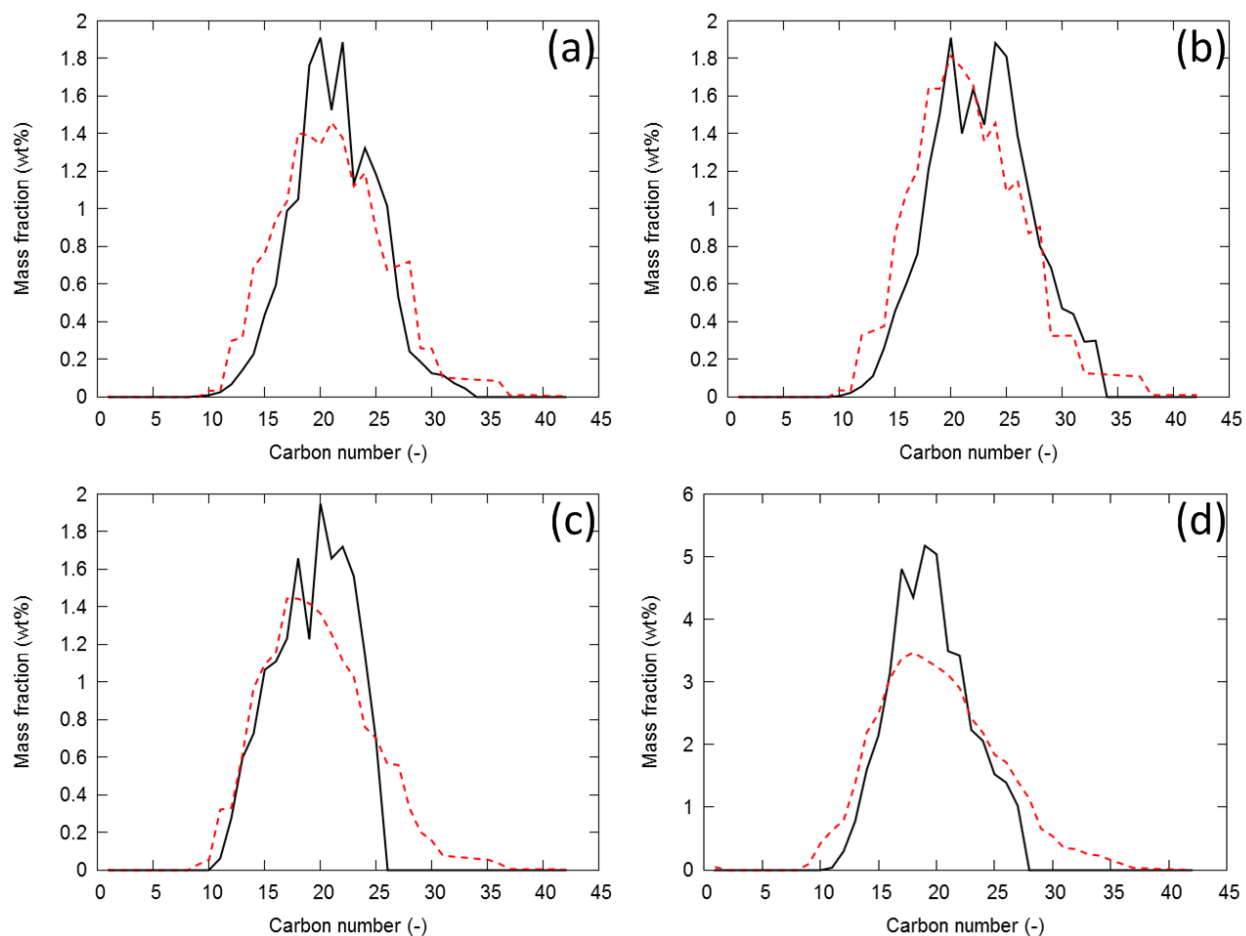
Figure 5.1: Analytical (▬) and reconstructed (⋯) carbon number distributions for VGO A: (a) n-paraffins, (b) iso-paraffins, (c) naphthenes,(d) aromatics using the PINA analysis, H/C ratio, density and ASTM-D2887 boiling point curve

Although the reconstruction of the carbon number distribution of these four global groups is good the distribution between the different sub-group types shows some deviations. Table 5.4 shows the detailed group type analysis of VGO A for both the analytical and the reconstructed approach. The reconstructed amount of n-paraffins and isoparaffins agrees well with the analytically calculated values. This is expected as it was one of the constraints imposed during the Shannon entropy maximization. For the aromatics a reasonable agreement is obtained between the

reconstructed and the analytical values: the mono-aromatics are being underestimated by about 5 wt% while the other groups (with mainly the naphtheno-aromatics) are overestimated. For the naphthenes the mononaphthenes are being underestimated by about 10 wt% while the dinaphthenes and trinaphthenes are being overestimated. Due to the similar properties of these compounds and the inability of any of the specified commercial indices to differentiate between those compounds it is in line with expectations that the Shannon entropy algorithm tends to distribute these compounds more or less evenly. The latter does clearly not seem to be the case in real mixtures. Additional commercial indices which are able to distinguish between these groups a commercial index could solve this issue.

Similar conclusions can be seen when reconstructing VGO B and VGO C and the parity plots of both VGO's is given in Figure 5.2.

Table 5.4: Detailed group type analysis of VGO A for both the analytical as the reconstructed approach using the PINA analysis, H/C ratio, density and ASTM-D2887 boiling point curve: P=n-paraffins, I=isoparaffins, MN=mononaphthenes, DN=dinaphthenes, TN=trinaphthenes MA=monoaromatics, NA=naphthenoaromatics, DA=diaromatics, NDA=naphthenodiaromatics, TrA=Triaromatics, NTrA=naphthenotriaromatics

	P	I	MN	DN	TN	MA	DA	TrA	TeA	NA	NDA
Reconstructed	17.4	21.3	6.4	5.8	5.2	11.9	8.8	4.3	2.4	10.6	6.1
Analytical	17.3	21.3	15.4	1.9	0	16.9	8.5	4.0	0.1	7.4	6.6
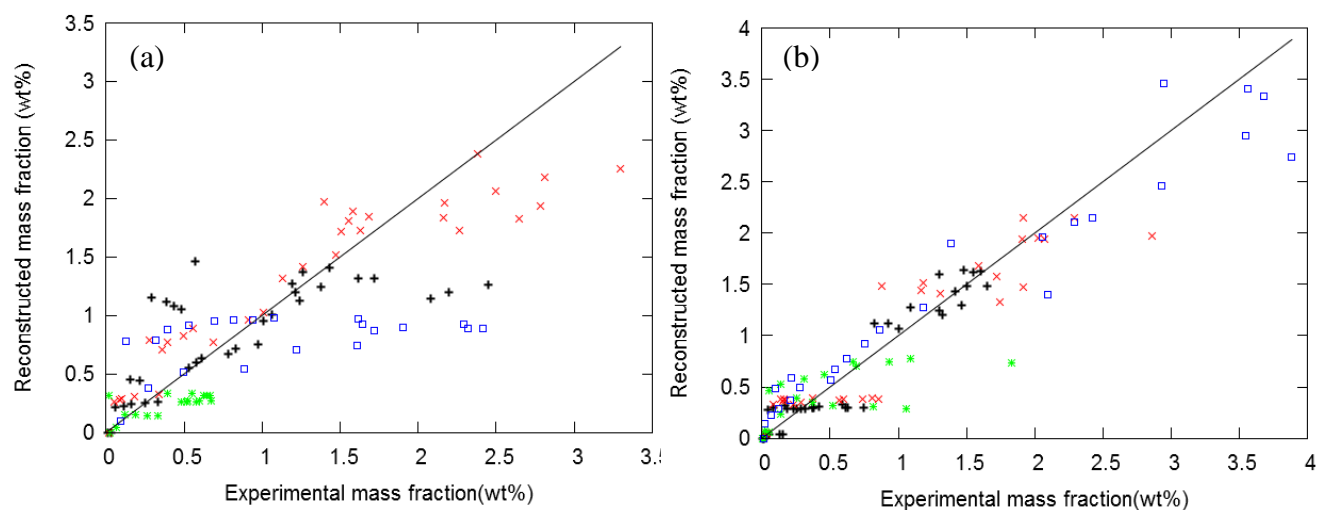
Figure 5.2: Parity plots of the feedstock reconstruction for VGO B (a) and VGO C (b) using the PINA analysis, H/C ratio, density and ASTM-D2887 boiling point curve: ✛ **n-paraffins;** ✕ **isoparaffins;** ✱ **naphthenes;** ☐ **aromatics;** ─**diagonal**

Table 5.5: Analytical and reconstructed commercial indices specified for Gas oil A using combination 3 of the commercial indices (e.g. Table 5.2)

	Analytical	Reconstructed
Elemental analysis (wt%)		
C	85.7	85.7
H	13.1	13.1
S	1.3	1.3
Aromatic S (wt%)	0.15	0.15
Density (kg.m^{-3})	0.830	0.840
PINA analysis (wt%)		
P	24.3	24.3
I	29.7	29.7
N	13.5	13.5
A	32.5	32.5
ASTM-D2887 (K)		
0%	409	404
10%	535	531
30%	576	576
50%	602	601
70%	622	625
90%	655	670
100%	705	734

5.3.2 Reconstruction of the gas oils

Reconstruction was carried out using the different combinations of commercial indices specified in Table 5.2. Table 5.5 shows the analytical and reconstructed commercial indices of gas oil A. Similar as was the case with VGO A the reconstructed commercial indices correspond to the analytical commercial indices with the exception of the initial in the final boiling which have a higher standard deviation.

In Figure 5.3 the reconstructed carbon number distributions for the different combinations of commercial indices and the analytical carbon number distribution of the thiols/sulfides, the benzothiophenes and the dibenzothiophenes are shown for Gasoil A. Depending on the combination of commercial indices used there can be a large difference between the analytical carbon number distribution and the reconstructed carbon number distribution. From Figure 5.3 it is clear that the amount of sulfur compounds is being underestimated for all groups if no sulfur indices are being specified (combination 1: red dashed line). This is confirmed by the total amount of sulfur calculated from the reconstructed composition (0.93 wt%) which is significantly lower than the analytically determined total amount of sulfur (1.34 wt%). For gas oil C, e.g. Figure 5.4, the amount of sulfur containing hydrocarbons is however being overestimated when no commercial indices related to sulfur are being specified (combination 1: red dashed line). This is again confirmed by comparing the total amount of sulfur for the analytical (0.16 wt%) and the reconstructed feedstock (1.00 wt%). These sulfur compounds overlapped in the $GC \times GC$ analysis, e.g. Chapter 3, with hydrocarbon compounds which had similar properties as the sulfur compounds, e.g. benzothiophenes overlapped with diaromatics. Because these compounds have similar properties for most of the specified commercial indices the Shannon entropy maximization method has difficulties differentiating between them. In line with what was seen

for the VGO reconstruction the Shannon entropy method thus distributes more or less equally between the different groups. However the difference between gas oil A and gas oil C was that in case of the former there were more sulfur containing hydrocarbons than pure hydrocarbons. In case of the latter there were more pure hydrocarbons than sulfur containing hydrocarbons. This explains why in case of gas oil A the sulfur containing hydrocarbons are being underestimated while in case of gas oil C the sulfur containing hydrocarbons are being overestimated. The algorithm distributes evenly between the pure and sulfur containing hydrocarbons due to the lack of commercial indices.

To eliminate the over prediction and under prediction of the sulfur compounds an additional commercial index was specified namely the total amount of sulfur (combination 2: Green dotted line). When adding the total amount of sulfur more information is obtained regarding the distribution between the amount of pure hydrocarbons and the amount of sulfur containing hydrocarbons. The total amount of sulfur for both the analytical (1.3 wt% for gas oil A) and reconstructed feedstock (1.3 wt% for gas oil A) now matches. From Figure 5.3 and Figure 5.4 it is clear that in both cases an improvement is obtained although the amount of thiols/sulfides is being overestimated while the amount of benzothiophenes and dibenzothiophenes is being underestimated.
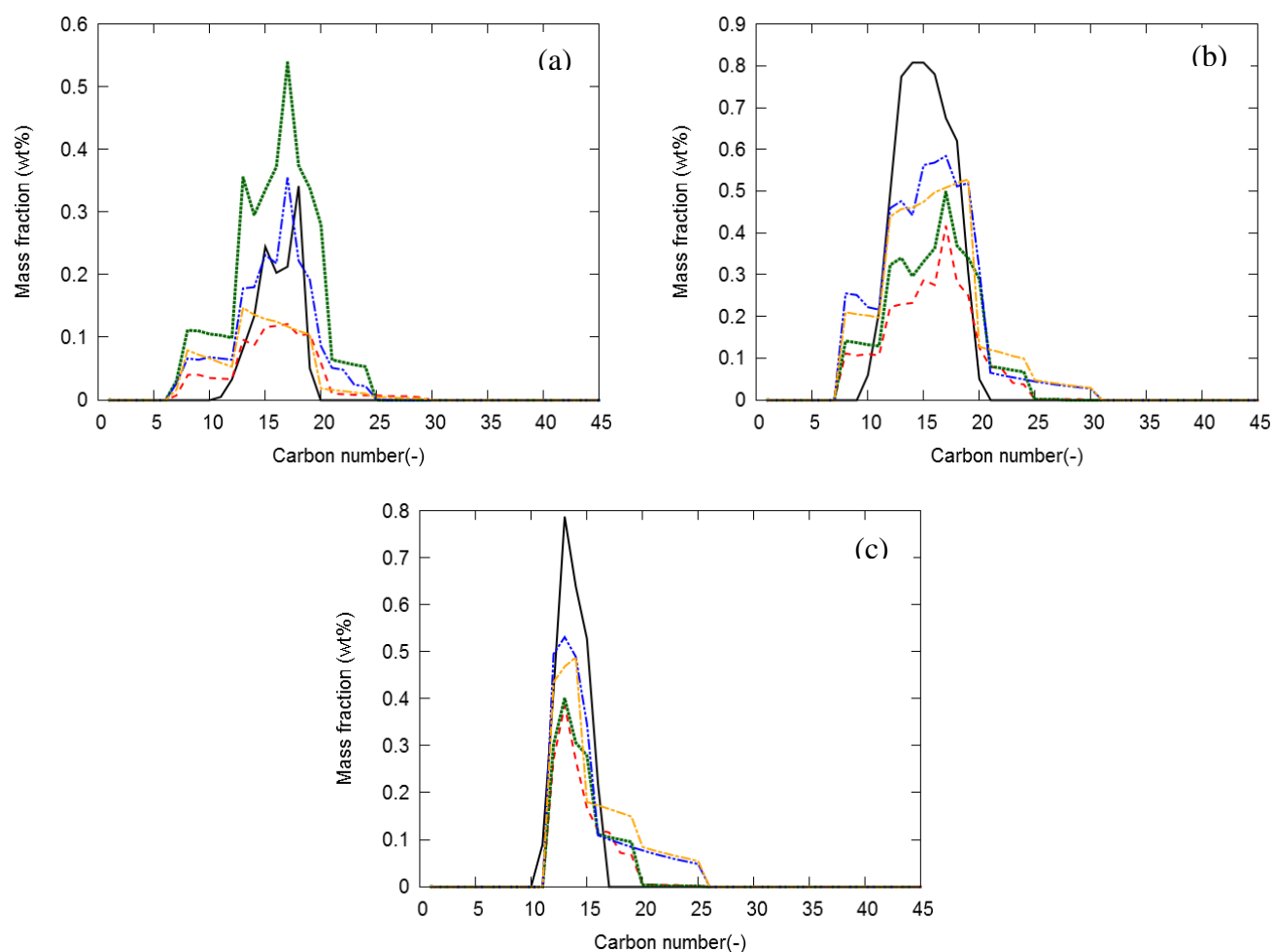
Figure 5.3: Reconstructed and analytical carbon number distributions of the thiols/sulfides (a), the benzothiophenes (b) and the dibenzothiophenes (c) in Gasoil A using different combinations of commercial indices (see Table 5.2): ──Analytical distribution; ▪▪▪Combination 1: No sulfur indices specified; ▪▪▪▪Combination 2: total sulfur specified; ──·Combination 3: total sulfur and aromatic sulfur specified; ──·Combination 4: detailed group type analysis
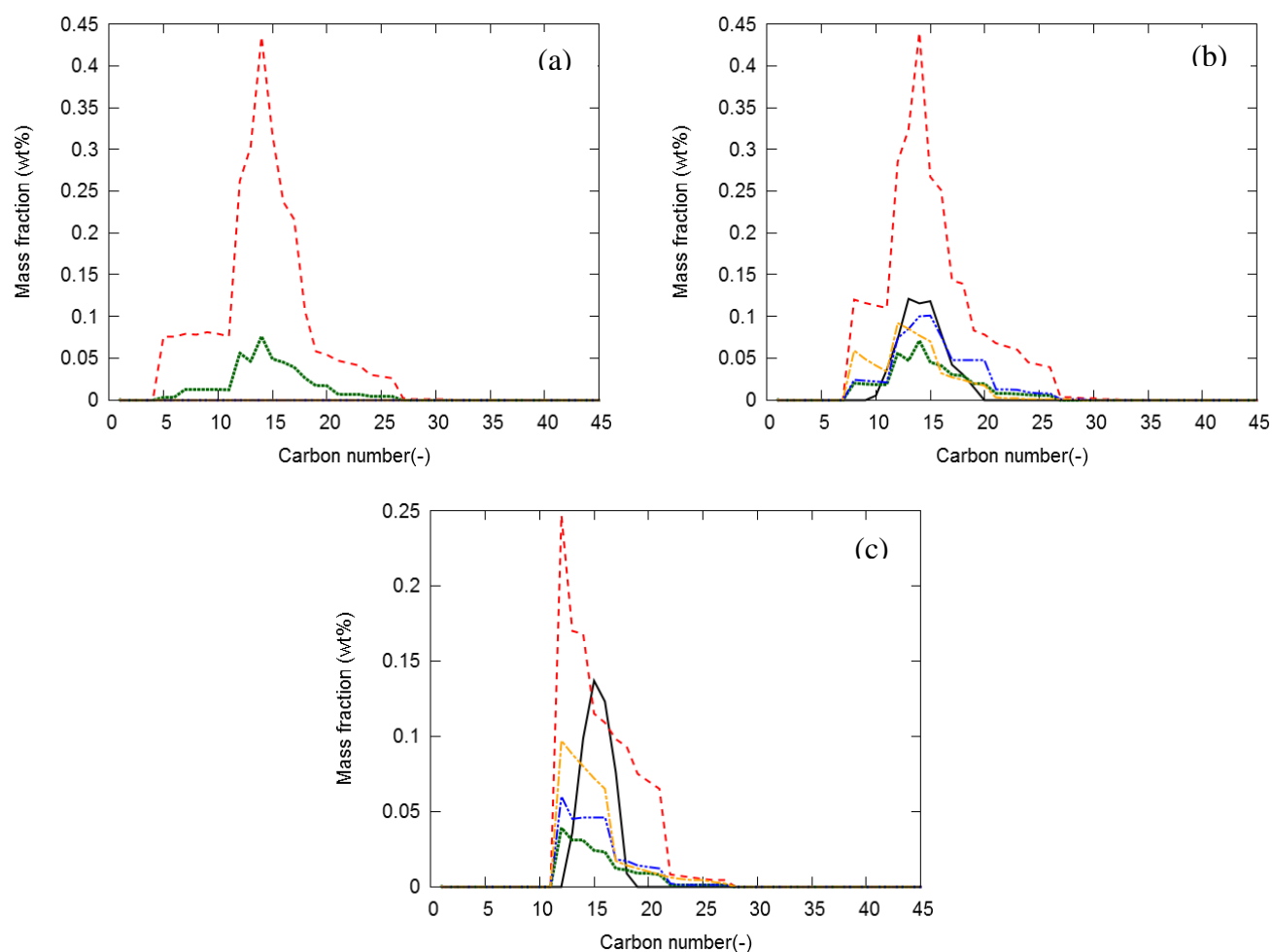
Figure 5.4: Reconstructed and analytical carbon number distributions of the thiols/sulfides [some curves coincide with the x-axis] (a), the benzothiophenes (b) and the dibenzothiophenes (c) in Gasoil C using different combinations of commercial indices (see Table 5.2): ━━ **Analytical distribution;** ▪ ▪ **Combination 1: No sulfur indices specified;** ▪▪▪▪ **Combination 2: total sulfur specified;** ▬▪ **Combination 3: total sulfur and aromatic sulfur;** ▬ ▪ **Combination 4: detailed group type analysis (on x-axis)**

To improve the distribution between the different sulfur groups a second commercial index related to sulfur was added namely the aromatic sulfur content (combination 3: Blue dash-dot-dot line), which results in a further improvement of the reconstructed composition. Figure 5.3 shows that the distribution of thiols/sulfides, benzothiophenes and dibenzothiophenes is being accurately predicted but that the reconstructed distribution of benzothiophenes and dibenzothiophenes is slightly lower and broader than the analytical determined distribution.

When a detailed group type distribution is given (combination 4: Orange dash-dot line) no significant improvement is observed as compared to combination 3. In case of Gas oil A (see Figure 5.3) the reconstructed distribution of the thiols/sulfides is even a lot broader and lower than the analytical determined distribution. For benzothiophenes and dibenzothiophenes the reconstructed distributions of combination 3 and combination 4 seem to be more or less identical (see Figure 5.3 and Figure 5.4). Combination 3 thus seems a good combination of commercial indices as the amount of additional information needed remains limited to the amount of total sulfur and the amount of aromatic sulfur and no detailed information regarding the group type analysis is needed.

Figure 5.5 shows the carbon number distribution of the n-paraffins, isoparaffins, naphthenes and aromatics for gas oil A using combination 3 (see Table 5.2). It shows the additional indices supplied specifically to improve the reconstruction of the sulfur containing compounds do not affect the reconstruction of the pure hydrocarbons and that the reconstructed distributions correspond well with the analytical determined distributions.

Note that although no nitrogen compounds were included in this chapter a similar approach could be applied for these nitrogen compounds. Physical properties of the nitrogen compounds in the library could be calculated using group additivity and additional commercial indices that could be

used to improve the reconstruction of nitrogen in a similar way as sulfur. Such indices could be the total nitrogen content (ASTM-D4629, 2012), the neutral nitrogen content and/or the basic nitrogen content (UOP269, 2010) as they would allow to differentiate between the pure and sulfur containing components but also allow to for example differentiate the indoles from the quinolines. However additional analytical data regarding nitrogen content in crude oil fractions is needed (using the method described in Chapter 4) to properly validate the method.
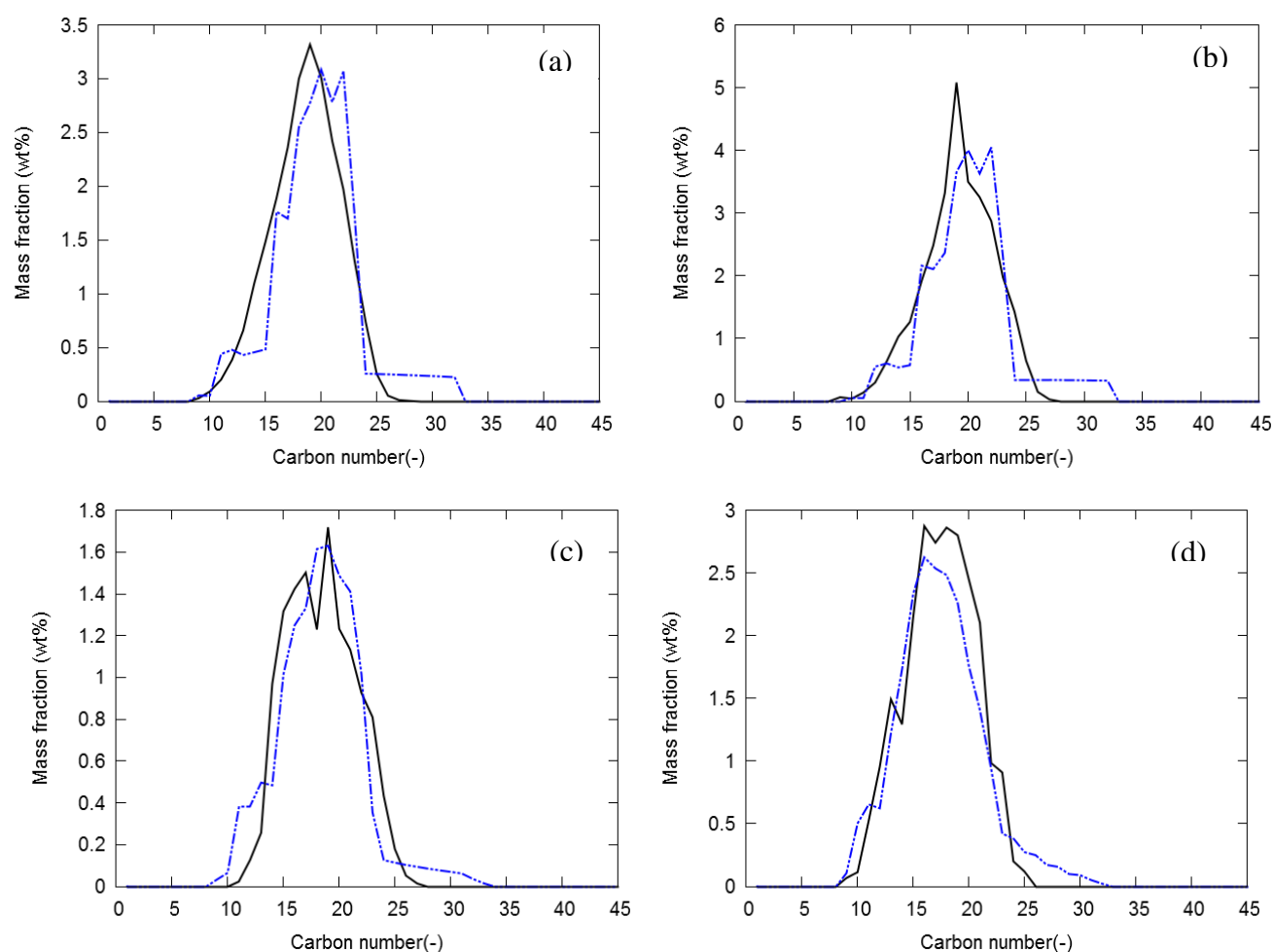

Figure 5.5: Reconstructed and analytical carbon number distributions of the n-paraffins (a), the isoparaffins (b), the naphthenes (c) and the aromatics (d) in Gasoil A: ▬Analytical distribution; ─∙─ Combination 3: total sulfur and aromatic sulfur specified (see Table 5.2)

5.4 Conclusions

A reconstruction method based on Shannon entropy maximization was presented which is able to reconstruct the detailed composition of feedstocks up to vacuum gas oils and including sulfur containing hydrocarbons. The library of the method included hydrocarbons up to a carbon number of 45. The library was further divided into 12 chemical families related to pure hydrocarbons; n-paraffins, isoparaffins, olefins, mononaphthenes, dinaphthenes, trinaphthenes, mono-aromatics, naphthenoaromatics, diaromatics, naphthenodiaromatics, triaromatics and tetra-aromatics; and 3 sulfur related chemical families; Thiols/sulfides, benzothiophenes and dibenzothiophenes.

The method was applied on three vacuum gas oils and three atmospheric gas oils analyzed in Chapter 2 en Chapter 3 respectively. For all feedstocks the reconstructed carbon number distribution of all feedstocks agrees well with the analytical data. Furthermore the reconstruction of the vacuum gas oils showed that reconstructed mass fractions of the global groups (n-paraffins, i-paraffins, naphthenes and aromatics) corresponded to the analytical measured mass fractions of these groups. However the distribution between the different sub-group types show some deviations. For the aromatics the mono-aromatics are being underestimated while mainly naphthenoaromatics are being overestimated. This is also the case for the naphthenes were the mononaphthenes are being underestimated in favor of the dinaphthenes and trinaphthenes. Because of the similar physical and chemical properties of these compounds the Shannon entropy algorithm tends to distribute these compounds more or less evenly which is not the case in the analytically determined composition. Additional commercial indices which are able to distinguish between these groups could solve this issue.

For the reconstruction of sulfur containing hydrocarbons four different combinations of commercial indices were compared to assess which combination of commercial indices gives the most reliable results.

The first three combinations all used the PINA analysis data, the ASTM-D2887 boiling point curve and the density of the feedstock. In addition to these commercial indices the first combination supplied the H/C ratio, the second combination supplied the elemental composition in terms of C, H and S while the third combination supplied in addition to the elemental composition in terms of C, H and S the aromatic sulfur content. The final combination supplied instead of the PINA analysis a detailed group type analysis based on the groups specified in Chapter 3.

The first two combinations fail to accurately predict the composition of the gas oils. In case of the first combination (no commercial indices related to sulfur specified) the total amount of sulfur and thus the total amount of sulfur containing hydrocarbons deviates from the analytical determined quantities as no information regarding total sulfur is available. The second combination (only total sulfur specified as a commercial indices related to sulfur) overestimated thiols/sulfides while the amount of benzothiophenes and dibenzothiophenes was underestimated.

Both the third (total sulfur and aromatic sulfur specified) and the fourth combination (detailed group type analysis specified) were able to match the analytical determined quantities of the sulfur containing hydrocarbons. Although additional commercial indices were specified, no effect was seen on the reconstruction of pure hydrocarbons. The third combination however required significant less information as compared to the fourth combination while no difference in accuracy was observed between both methods.

5.5 References

Albahri, T. A. (2005). Molecularly explicit characterization model (MECM) for light petroleum fractions. Industrial & Engineering Chemistry Research, 44, 9286-9298.

Allen, D. T., & Liguras, D. (1991). Structural Models Of Catalytic Cracking Chemistry - A Case-Study Of A Group Contribution Approach To Lumped Kinetic Modeling: Van Nostrand, R.

Androulakis, I. P., Weisel, M. D., Hsu, C. S., Qian, K. N., Green, L. A., Farrell, J. T., & Nakakita, K. (2005). An integrated approach for creating model diesel fuels. Energy & Fuels, 19, 111-119.

API Technical Data Book (7th edition). (2005). The American Petroleum Institute and EPCON international,.

ASTM-D3227, 2013, Standard Test Method for (Thiol Mercaptan) Sulfur in Gasoline, Kerosine, Aviation Turbine, and Distillate Fuels (Potentiometric Method).ASTM International, West Conshohocken, PA, 2003, DOI:10.1520/D3227

ASTM-D4629, 2012, Standard Test Method for Trace Nitrogen in Liquid Petroleum Hydrocarbons by Syringe/Inlet Oxidative Combustion and Chemiluminescence Detection.ASTM International, West Conshohocken, PA, 2003, DOI:10.1520/D4629-12

ASTM-D4952, 2012, Standard Test Method for Qualitative Analysis for Active Sulfur Species in Fuels and Solvents (Doctor Test).ASTM International, West Conshohocken, PA, 2003, DOI:10.1520/D4952-12

Campbell, D. M., & Klein, M. T. (1997). Construction of a molecular representation of a complex feedstock by Monte Carlo and quadrature methods. Applied Catalysis a-General, 160, 41-54.

Dente, M., Ranzi, E., & Goossens, A. G. (1979). Detailed prediction of olefin yields from hydrocarbon pyrolysis through a fundamental simulation model (SPYRO). Computers & Chemical Engineering, 3, 61-75.

Fafet, A., Bonnard, J., & Prigent, F. (1999). New Developments in Mass Spectrometry for Group-Type Analysis of Petroleum Cuts (First Part). Oil & Gas Science and Technology - Rev. IFP, 54, 439-452.

Green, J. B., Yu, S. K. T., Pearson, C. D., & Reynolds, J. W. (1993). Analysis of sulfur compound types in asphalt. Energy & Fuels, 7, 119-126.

Ha, Z. Y., Ring, Z., & Liu, S. J. (2005). Derivation of molecular representations of middle distillates. Energy & Fuels, 19, 2378-2393.

Hegazi, A. H., & Andersson, J. T. (2007). Limitations to GC-MS Determination of Sulfur-Containing Polycyclic Aromatic Compounds in Geochemical, Petroleum, and Environmental Investigations. Energy & Fuels, 21, 3375-3384.

Hua, R. X., Wang, J. H., Kong, H. W., Liu, J., Lu, X., & Xu, G. W. (2004). Analysis of sulfur-containing compounds in crude oils by comprehensive two-dimensional gas chromatography with sulfur chemiluminescence detection. Journal of Separation Science, 27, 691-698.

Hudebine, D., Verstraete, J., & Chapus, T. (2011). Statistical Reconstruction of Gas Oil Cuts. Oil & Gas Science and Technology-Revue D Ifp Energies Nouvelles, 66, 461-477.

Hudebine, D., & Verstraete, J. J. (2004). Molecular reconstruction of LCO gasoils from overall petroleum analyses. Chemical Engineering Science, 59, 4755-4763.

Hudebine, D., & Verstraete, J. J. (2011). Reconstruction of Petroleum Feedstocks by Entropy Maximization. Application to FCC Gasolines. Oil & Gas Science and Technology-Revue D Ifp Energies Nouvelles, 66, 437-460.

Joo, E., Park, S., & Lee, M. (2001). Pyrolysis reaction mechanism for industrial naphtha cracking furnaces. Industrial & Engineering Chemistry Research, 40, 2409-2415.

López García, C., Becchi, M., Grenier-Loustalot, M. F., Païsse, O., & Szymanski, R. (2002). Analysis of Aromatic Sulfur Compounds in Gas Oils Using GC with Sulfur Chemiluminescence Detection and High-Resolution MS. Analytical Chemistry, 74, 3849-3857.

López García, C., Hudebine, D., Schweitzer, J. M., Verstraete, J. J., & Ferré, D. (2010). In-depth modeling of gas oil hydrotreating: From feedstock reconstruction to reactor stability analysis. Catalysis Today, 150, 279-299.

Mahe, L., Dutriez, T., Courtiade, M., Thiebaut, D., Dulot, H., & Bertoncini, F. (2011). Global approach for the selection of high temperature comprehensive two-dimensional gas chromatography experimental conditions and quantitative analysis in regards to sulfur-containing compounds in heavy petroleum cuts. Journal of Chromatography A, 1218, 534-544.

Moustafa, N. E., & Andersson, J. T. (2011). Analysis of polycyclic aromatic sulfur heterocycles in Egyptian petroleum condensate and volatile oils by gas chromatography with atomic emission detection. Fuel Processing Technology, 92, 547-555.

Neurock, M., Nigam, A., Trauth, D., & Klein, M. T. (1994). Molecular representation of complex hydrocarbon feedstocks through efficient characterization and stochastic algorithms. Chemical Engineering Science, 49, 4153-4177.

NIST Chemistry WebBook, NIST Standard Reference Database Number 69. (2009). Gaithersburg MD: National Institute of Standards and Technology.

Nylén, U., Delgado, J. F., Järås, S., & Boutonnet, M. (2004). Characterization of alkylated aromatic sulphur compounds in light cycle oil from hydrotreated vacuum gas oil using GC-SCD. Fuel Processing Technology, 86, 223-234.

Pyl, S. P. (2013). Sustainable Production of Light Olefins: from Fossil to Renewable Resources. Ugent.

Pyl, S. P., Van Geem, K. M., Reyniers, M. F., & Marin, G. B. (2010). Molecular Reconstruction of Complex Hydrocarbon Mixtures: An Application of Principal Component Analysis. AIChE Journal, 56, 3174-3188.

Quann, R. J. (1998). Modeling the chemistry of complex petroleum mixtures. Environmental Health Perspectives, 106, 1441-1448.

Riazi, M. R. (2005). Characterization of petroleum fractions: ASTM International.

Robinson, C. J. (1971). Low-resolution mass spectrometric determination of aromatics and saturates in petroleum fractions. Analytical Chemistry, 43, 1425-1434.

Rosenbrock, H. H. (1960). An Automatic Method For Finding The Greatest Or Least Value Of A Function. Computer Journal, 3, 175-184.

Schulz, H., Böhringer, W., Ousmanov, F., & Waller, P. (1999). Refractory sulfur compounds in gas oils. Fuel Processing Technology, 61, 5-41.

Shannon, C. E. (1948). The mathematical theory of communication. MD Computing, 14, 306-317.

Stumpf, Á., Tolvaj, K., & Juhász, M. (1998). Detailed analysis of sulfur compounds in gasoline range petroleum products with high-resolution gas chromatography–atomic emission

detection using group-selective chemical treatment. Journal of Chromatography A*, 819*, 67-74.

Trauth, D. M., Stark, S. M., Petti, T. F., Neurock, M., & Klein, M. T. (1994). Representation of the Molecular Structure of Petroleum Resid through Characterization and Monte Carlo Modeling. Energy & Fuels*, 8*, 576-580.

UOP163, 2010, Hydrogen Sulfide and Mercaptan Sulfur in Liquid Hydrocarbons by Potentiometric Titration.ASTM International, West Conshohocken, PA, 2003,

UOP269, 2010, Nitrogen Bases in Hydrocarbons by Potentiometric Titration.ASTM International, West Conshohocken, PA, 2003,

Van Geem, K. M., Hudebine, D., Reyniers, M. F., Wahl, F., Verstraete, J. J., & Marin, G. B. (2007). Molecular reconstruction of naphtha steam cracking feedstocks based on commercial indices. Computers & Chemical Engineering*, 31*, 1020-1034.

Van Geem, K. M., Reyniers, M. F., & Marin, G. B. (2008). Challenges of modeling steam cracking of heavy feedstocks. Oil & Gas Science and Technology-Revue De L Institut Francais Du Petrole*, 63*, 79-94.

Zeigler, C., Wilton, N., & Robbat, A. (2012). Toward the Accurate Analysis of C1–C4 Polycyclic Aromatic Sulfur Heterocycles. Analytical Chemistry*, 84*, 2245-2252.

Chapter 6: Single event microkinetic model for steam cracking

6.1 Introduction

The importance of the steam cracking process to the petrochemical industry has justified the continuous interest for developing new and better mathematical simulation models during the last four decades. Mathematical modeling has the important advantage that once the model is developed, results can be easily gathered and computer simulations take only a limited time (Dente et al., 1979). In general these simulation models consist of 2 parts: a kinetic model, i.e. reaction network and the physical properties of the considered species in the network, and a solver that solves the relevant reactor model equations. The general buildup of such simulation models is given in Figure 6.1. This model accounts for both the chemical reactions and the physical transport phenomena.

In this chapter the fundamental simulation model for steam cracking (COILSIM1D) will be discussed that is used throughout this work. As shown in Figure 6.1 COILSIM1D consist of 2 parts: a single event microkinetic model based on the free-radical mechanism and a solver that solves the reactor model equations. In case of COILSIM1D a 1D plug flow reactor is assumed. In the next paragraphs the microkinetic model, the reactor model as well as the solver will be discussed. The methods for calculating the physical properties of the species and materials will also be discussed. Attention is paid to improvements in the computational efficiency of the model.
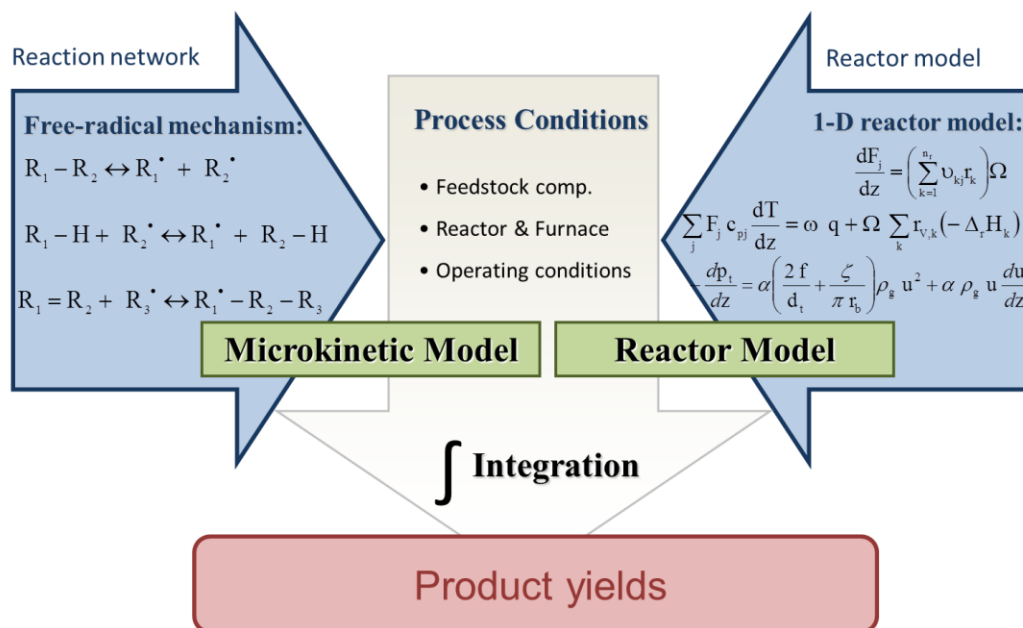
Figure 6.1: Illustration of the general construction of a single event microkinetic model for the steam cracking of hydrocarbons (after Van Geem (2006))

6.2 The kinetic model (CRACKSIM)

6.2.1 Global reaction network

Since the pioneer work of Rice and coworkers (Rice, 1931; Rice & Herzfeld, 1934; Kossiakoff & Rice, 1943) there is a general consensus that steam cracking of hydrocarbons proceeds through a free radical mechanism and that three important elementary reaction families can be distinguished:

1. Carbon-Carbon and Carbon-Hydrogen bond scissions or its reverse reaction the radical-radical recombinations

$$R_1\text{-}R_2 \rightleftharpoons R_1^\bullet + R_2^\bullet \tag{6.1}$$
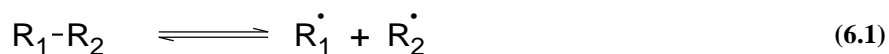
2. Hydrogen abstraction reactions which can occur both intra- and intermolecular

$$R_1\text{-}H + R_2^\bullet \rightleftharpoons R_1^\bullet + R_2\text{-}H \tag{6.2}$$
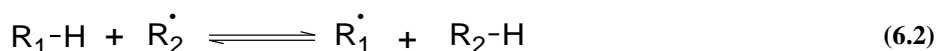
3. Radical addition to olefins and the reverse β scission of radicals which can occur both

    intra- and intermolecular

$$\overset{\bullet}{R_1} \; + \; R_2{=}R_3 \; \Longleftrightarrow \; R_1{-}R_2{-}\overset{\bullet}{R_3} \tag{6.3}$$
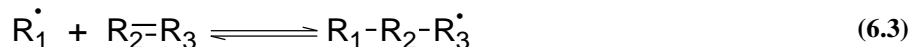
Although these three elementary reaction families are the dominant reaction families for steam

cracking other reaction families can also be important. One of these elementary reaction families

are the electrocyclizations. An electrocyclic reaction is the concerted interconversion of a

conjugated polyene and a cycloalkene. Consider for example the following electrocyclic reaction

of 1,3,5-hexatriene with the formation of 1,3 cyclohexadiene:

$$\tag{6.4}$$
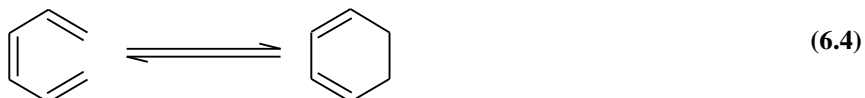
Electrocyclizations are very fast reactions (Schiess & Dinkel, 1981) and are important routes

towards the formation of aromatic compounds (Jutz, 1978; Kopinke et al., 1987).

Although there is a general consensus about the free radical mechanism for cracking paraffins

this is not the case when olefins are cracked. Olefins disappear via a combination of radical

reactions and elementary molecular reaction pathways (Benson, 1970). The latter are mostly

retro-ene reactions (Warth et al., 2000; Ranzi et al., 2001). The reverse reaction is the ene

reaction and is the joining of a double or triple bond to an alkene reactant having a transferable

allylic hydrogen. For example the retro-ene reaction of 1-hexene gives two propene molecules:

$$\tag{6.5}$$
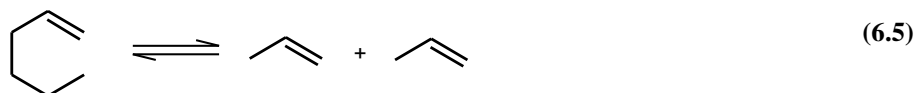
Many years ago Dente et al. (1979) already constructed a very detailed kinetic model (Spyro)

based on these elementary reactions. The final kinetic model consisted of 86 molecules and 18

radicals which could undergo about 2000 reactions. However nowadays computers are used not

only to solve the simulation numerically, but also to generate the network, construct the model

and calculate the kinetic parameters based on the reaction families mentioned above. A key difficulty of these network generation programs is that they produce large numbers of kinetically unimportant elementary reactions and species. Several assumptions help to retain the mechanism within manageable sizes. In the current reaction network the μ radical hypothesis is surely the most important assumption. This hypothesis assumes that bimolecular reactions can be neglected for radicals with more than 5 carbon atoms (Ranzi et al., 1983). This allows distinguishing between two types of networks: the monomolecular μ network and the β network, which contains both mono- and bimolecular reactions. The kinetics for the former network can be described by analytical expressions based on the quasi steady state assumption (QSSA) for the radical reaction intermediates (Hillewaert et al., 1988; Vercauteren, 1991).

For species with 5 or less carbon atoms the μ radical hypothesis does not hold, making it no longer possible to use the analytical expressions based on the QSSA. Therefore it is necessary to store their reactions in a separate sub network; the β network. It is immediately clear that the separation of radicals into μ and β radicals based on the number of carbon atoms is very rough. Several exceptions on this rule of thumb exist, e.g. the benzyl radical and the indenyl radical, which according to the previously defined rule are not considered in the β network, are involved in bimolecular reactions . Also several other radicals can have both a β and μ character, such as radicals with no possibility of C-C scissions and no possibility of isomerization followed by a C-C scission. Consider the 3-methyl-3-pentene-2-yl radical that can only decompose via a slow C-H scission. It is clear that this reaction path is not the dominant disappearance route for 3-methyl-3-pentene-2-yl but addition reactions will be in most cases much more important under steam cracking conditions. A similar reasoning also holds for the 1-phenyl-2-pentene-4-yl radical.

Hence, some radicals with more than 5 carbon atoms cannot be considered as pure μ radicals without introducing errors.

The previous results show that the separation of radicals into μ and β radicals based on the number of carbon atoms is too rough. Therefore it is necessary to introduce another category of radicals; the so called C_6^+ β and $\beta\mu$ radicals. For these radicals the bimolecular reactions such as addition reactions and hydrogen abstraction reactions are not negligible, and consequently these reactions should be included in the β network. The β network further includes the reactions of the smaller radicals. In Figure 6.2 an overview is given of the construction of the complete microkinetic model. The β network and the μ network are discussed further in Section 6.2.2 and Section 6.2.3 respectively.
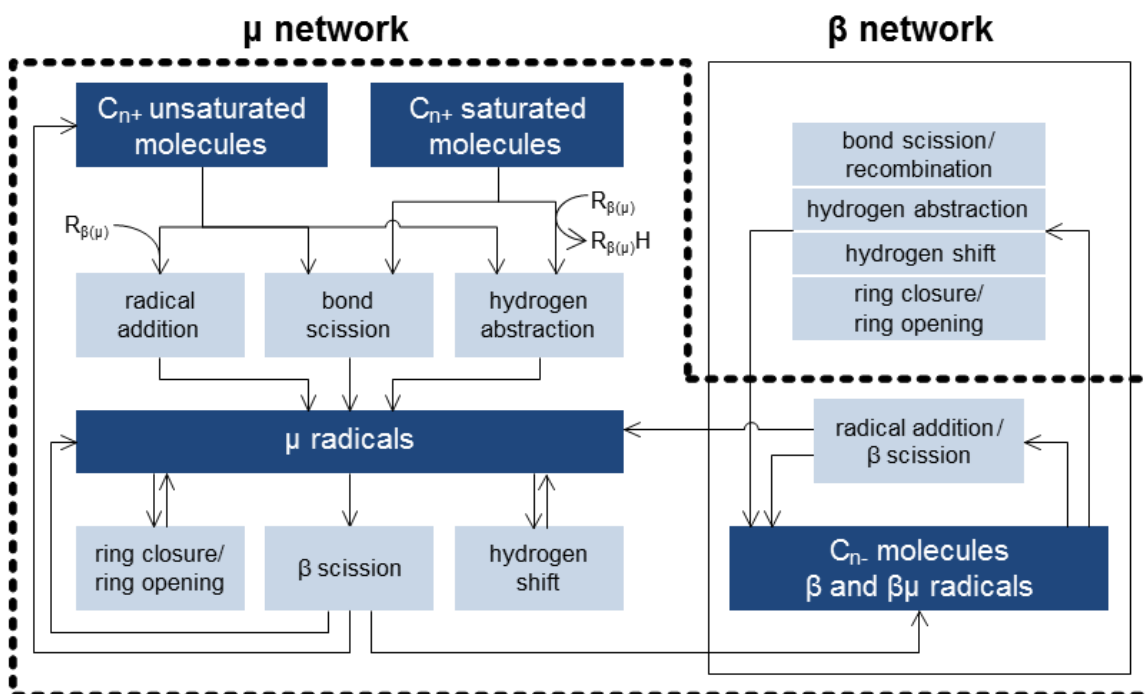
Figure 6.2: Structure of and reaction families in the single-event microkinetic

(SEMK) model – μ network and β network (Pyl, 2013)

6.2.2 β network

The β network considers all reactions from the three reaction families for species with 5 or less carbon atoms. The presented β network is taken from Pyl (2013) and contains 1324 reversible elementary reactions: 114 recombination/bond scission reactions, 73 intermolecular addition/β-scission reactions, 1128 intermolecular hydrogen abstraction reactions, 6 intramolecular hydrogen abstraction reactions (or hydrogen shift reactions), 2 intramolecular addition/β-scission reactions (or ring closure/ring opening reactions), and 1 (retro-)ene reaction between 51 molecules and 43 β(μ) radicals.

6.2.3 μ network

The existence of radicals with a pure μ character is essential for separating the reaction network into two parts: a β and a μ network (Ranzi et al., 2001). As stated earlier for radicals with a μ character the monomolecular β scission and isomerization reactions are much faster than the bimolecular hydrogen abstraction and addition reactions. Clymans and Froment (1984) and Hillewaert et al. (1988) concluded, based on experimental results, that this assumption surely holds for heavy paraffinic and iso-paraffinic radicals. Under typical steam cracking conditions these authors observed no saturated products with a chain length of more than 5 carbon atoms, except for non-converted feedstock molecules. An example is shown in Figure 6.3 where a paraffinic feedstock, Figure 6.3a, containing mostly C14-C18 n-paraffins is cracked. The effluent at low outlet temperatures, Figure 6.3b, shows that only unconverted C14-C18 n-paraffins are present and that no n-dodecane or n-tridecane is being formed. Moreover no C18 olefins are being formed, e.g. n-octadecene. The latter product could be formed after addition of the primary octadecyl radical to ethene followed by a β scission resulting in a n-icosyl radical.
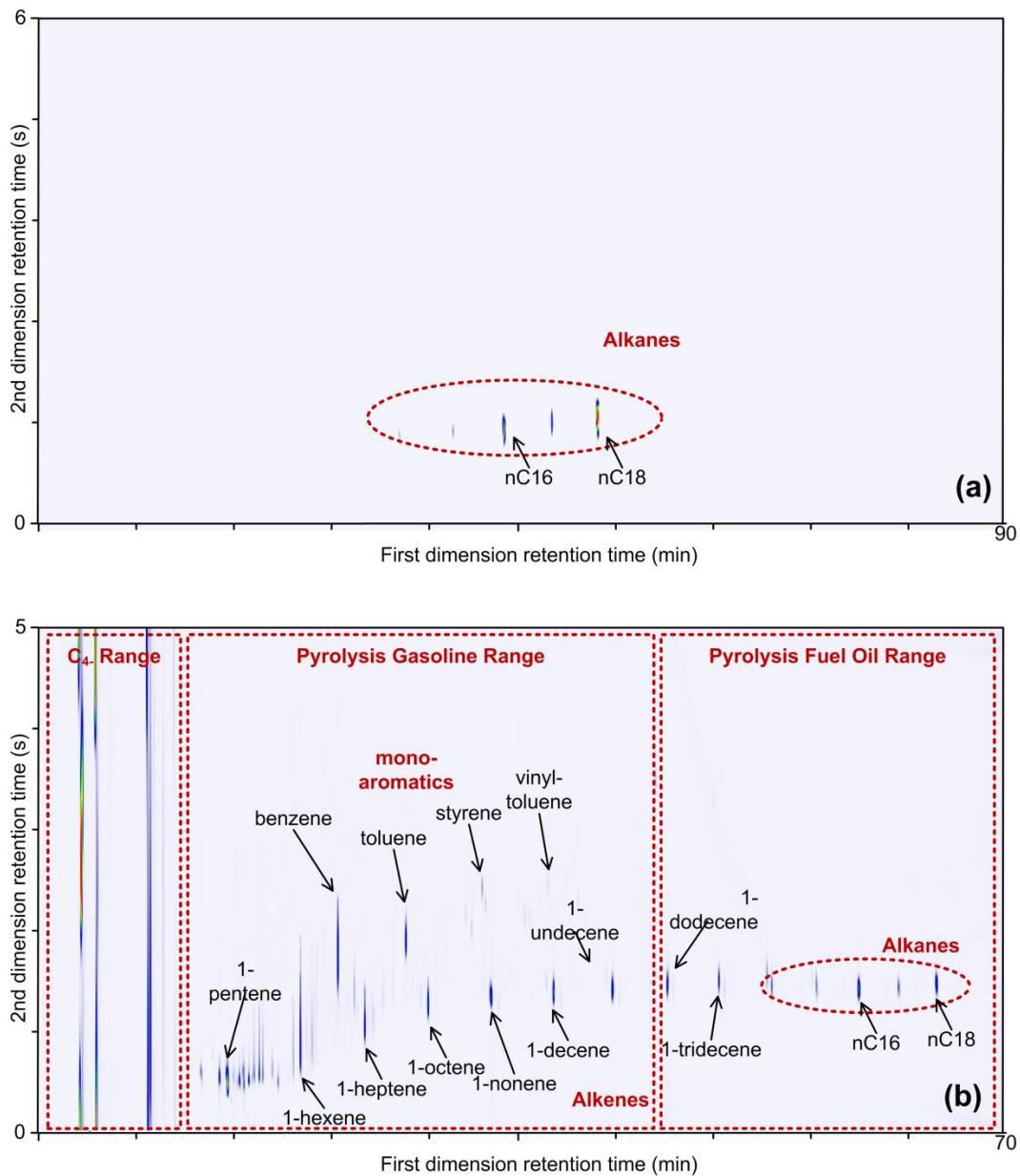
Figure 6.3: (a) GC × GC chromatogram of paraffinic C16-C18 feedstock (HDO-F) and (b) GC × GC chromatogram of on-line sampled reactor effluents during HDO-F steam cracking [COT = 775 °C, FHDO-F = 4 kg h−1, CIP = 2.1 bar, COP = 1.7 bar, CIT = 550 °C, δ = 0.45 kg kg−1] (Dijkmans et al., 2013)

The existence of radicals with a pure μ character enables the generation of reaction schemes for these radicals describing their disappearance via a set of monomolecular reaction steps (Ranzi et al., 2001). Because they are only involved in monomolecular reactions, the resulting set of differential equations for the μ radicals is linear in their concentrations. These concentrations can then be easily eliminated of the set of model equations if the quasi steady state is assumed for the concentrations of the μ radicals. This hypothesis assumes that the net rate of formation of highly reactive reaction intermediates in a reaction sequence equals zero (Bodenstein & Lütkemeyer, 1924). The unknown concentrations of the reactive reaction intermediates can then be found as the solution of the set of linear algebraic equations (Ranzi et al., 2001).

Three primary reactions are considered in the μ network. These primary reactions produce the initial μ radicals either through C-C scission reactions of molecules, hydrogen abstraction reactions by β and βμ radicals and addition reactions to olefins by β and βμ radicals. Based on these three primary reactions a reaction network is generated for each molecule with 6 or more carbon atoms. These three primary reactions all lead to the formation of a number of μ radicals which decompose further via β scissions and isomerization reactions to olefins and β and βμ radicals

In Figure 6.4 an example of a reaction scheme generated for n-nonane is shown starting from the C-C scission reactions of this molecule. The initiation occurs through the cleavage of a C-C bond, resulting in two radicals. These radicals react further in the propagation reactions until either a β molecule or radical (red species) is formed or a μ olefin (blue species) is formed. The latter have similar decomposition schemes with some additional reaction possibilities, e.g. ring formation, due to the presence of the double bond. In contrast to the β network, the μ network is thus a collection of these independent sub-networks that are appended to the β network. Each sub-

network is defined by its reactants (in this case n-nonane) and by the starting reaction family (in this case C-C scission) that transforms these reactants into the initial pool of μ radicals. There are two types of sub-networks. The first type contains primary decomposition pathways of larger molecules (typically C_{6+}) starting from hydrogen abstraction or bond scission. The second type is only possible when starting molecule is unsaturated. These unsaturated molecules can also undergo a radical addition or a retro-ene decomposition, i.e. a concerted pericyclic reaction resulting in smaller unsaturated molecules.

The automatic generation of these sub-networks is made possible by representing molecules and radicals with binary connectivity matrices and manipulation of these matrices to execute reactions and identify products, as first discussed by Clymans and Froment (1984). These authors applied the proposed concepts to automatic generation of primary decomposition reactions of normal and branched paraffins. Later, the computer codes were extended to generate the decomposition pathways of naphthenes and aromatics by Hillewaert et al. (1988). In this work the decomposition mechanisms of long-chain unsaturated molecules, i.e. the primary decomposition products of all saturated feedstock molecules, have been thoroughly revised. In particular the competition between β scission, hydrogen shift (intramolecular hydrogen abstraction) as well as ring closure/ring opening reactions (intramolecular β scissions and their reverse intramolecular addition) for unsaturated μ radicals is now systematically taken into account. In addition, sub-networks for the secondary hydrocarbon growth, starting from radical additions, have been generated.
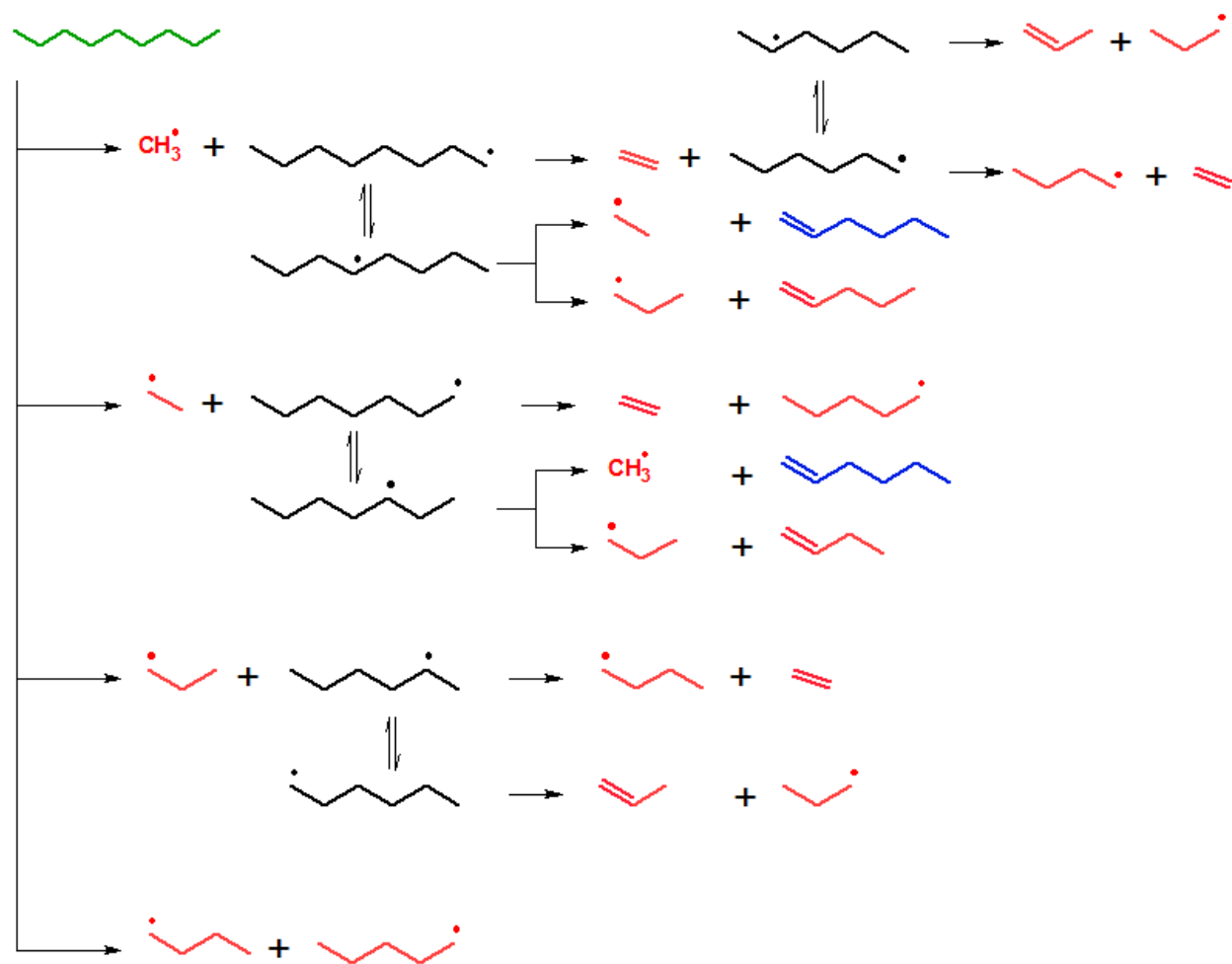
Figure 6.4: Reaction scheme for n-nonane starting from a C-C scission reaction: Green = Feed molecule,

Black = Formed µ-radical, Red = β molecule or radical, Blue = µ olefin

In order to keep the number of species in the final model within limits, three strategies are applied (Pyl, 2013): (i) application of a pseudo-component representation of the feedstock by *a posteriori* lumping, (ii) *in situ* lumping of primary product molecules, and (iii) application of the quasi steady state approximation (QSSA) for µ radicals.

Application of a pseudo-component representation is especially useful when numerous isomers are present in the feed. For example, explicitly accounting for every possible C_{6+} iso-paraffin is basically impossible. However, the reactivity of different isomers can be significantly different and the specific location and number of branches needs to be accounted for during the generation

of their µ network decomposition sub-networks. Nevertheless, *a posteriori* lumping (i.e. after network generation) of these sub-networks permits to reduce the number of compounds and consequently the number of continuity equations that has to be accounted for in the final model. For example, the µ network decomposition sub-networks of individual C_8 iso-paraffins, e.g. 2-methyl-heptadecane, 3-methyl-heptadecane, 2.3-dimethyl-hexadecane, etc., can be conveniently lumped into a single decomposition scheme for the pseudo-component (IPARC18) by imposing a fixed relative abundance of each isomer. Thus, each pseudo-component is defined by its type, e.g. iso-paraffin, and its carbon number, e.g. C_{18}. In principle, the relative abundance of each isomer is different for each feedstock. However, Ranzi et al. (2001) showed that the relative abundance of iso-paraffinic isomers in straight-run naphtha's is quasi-independent of its source. It is therefore viable to adopt a fixed set of weights per type of feedstock, e.g. straight-run naphtha, FCC naphtha, hydrotreated gas oil, etc. The importance of this fixed set of weights also decreases as the carbon number of the isoparaffins increases and the reactivity of the different isomers becomes similar. Table 6.1 shows the selectivity towards ethene, propene, the methyl radical and the hydrogen radical for decomposition schemes initialized by hydrogen abstraction of different isoparaffins. It is clear that as the carbon number increases the difference between the selectivity of different isomers decreases and that thus the importance the fixed set of weights decreases.

Table 6.1: Selectivities for important products for the decomposition of different isoparaffins initialized by hydrogen abstraction at 1073K. Me = methyl, Et = ethyl, DM = dimethyl, H = hydrogen

	C10			C15			C20		
	3-Me	3-Et	2,3-DM	3-Me	3-Et	2,3-DM	3-Me	3-Et	2,3-DM
ethene	0.20	0.21	0.08	0.36	0.39	0.28	0.49	0.52	0.42
propene	0.02	0.02	0.02	0.03	0.03	0.03	0.03	0.03	0.03
Me radical	0.10	0.15	0.31	0.11	0.14	0.27	0.11	0.14	0.24
H radical	0.15	0.19	0.24	0.13	0.15	0.13	0.11	0.12	0.16

Secondly, heavy unsaturated product molecules, i.e. C_{7+} acyclic olefins and C_{9+} cyclic olefins, are lumped on the fly (i.e. during network generation) into a limited number of pseudo- compounds, which are again completely defined by a carbon number and a type. For C_{7+} acyclic olefins, a distinction is made between six types of compounds: α-olefins, other straight chain olefins, branched olefins, straight chain di-olefins and branched di-olefins. For C_{9+} cyclic olefins a distinction is made between endo-mono-cyclic olefins, exo-mono-cyclic olefins, mono-cyclic di-olefins mono-aromatic olefins, di-cyclic olefins, di-cyclic di-olefins, naphtheno-aromatics, naphtheno-aromatic olefins, di-aromatics and tri-aromatics.

This lumping strategy results in manageable but sufficiently detailed pseudo-component representation of the heavy unsaturated primary products. In contrast, a much higher level of detail is taken into account for acyclic olefins with 6 or less carbon atoms and cyclic olefins with 8 or less carbon atoms because of their higher abundance and importance for the formation of aromatics.

The final strategy consists of application of the quasi-steady state approximation (QSSA) for μ

radicals. In combination with the μ radical hypothesis, application of QSSA to all μ radicals in a

certain sub-network results in a set of linear algebraic equations that can be solved during

network generation (Ranzi et al., 2001). Doing so, the concentrations of all μ radicals are

expressed as a function of the concentrations of the starting reactants of the sub-network.

Consequently, the rate-of-production of each molecule and β(μ) radical that is formed in the sub-

network is determined by these reactant concentrations only, i.e. not by the concentrations of

intermediate μ radicals (Dente et al., 1979; Ranzi et al., 2001; Dente et al., 2007; Van Geem et al.,

2008). This results in a drastic reduction of the number of species and the number of continuity

equations that has to be accounted for in the final model without sacrificing its fundamental

nature. In addition, the stiffness of the final set of differential equations is reduced. Each sub-

network thus results into a global reaction. For example for the decomposition scheme shown in

Figure 6.4 the following global reaction can be obtained

$$
n\,C_9H_{20} \rightarrow \sum_{j=1}^{n_{ol}} \frac{k^{pseudo}(O_j)}{\left(\sum_{i=1}^{4} k_i\right)}\, O_j + \sum_{l=1}^{n_{rad}} \frac{k^{pseudo}(\beta)}{\left(\sum_{i=1}^{4} k_i\right)}\, \beta
\tag{6.6}
$$
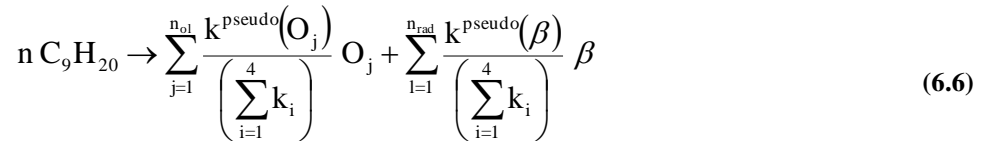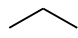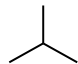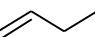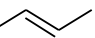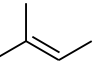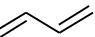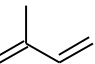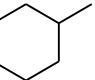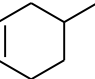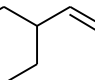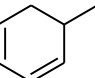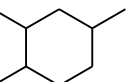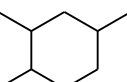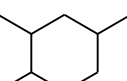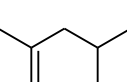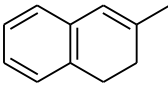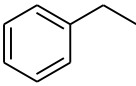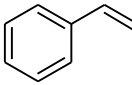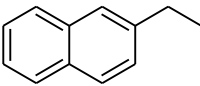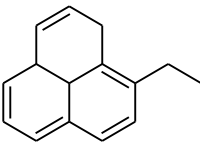
Table 6.2 shows that even with the applied lumping and reduction strategies the number of

species, and especially the number of olefins in the final model remains quite high. Nevertheless,

without these strategies the number of species would be impractically large.

Table 6.2: Overview of the total number of (pseudo-) compounds in the complete network

Classes of compounds	Number of (pseudo-) compounds	Example structure	Carbon range
Molecules	**727**		$C_0 - C_{26}$
hydrogen	1	H_2	C_0
n-paraffins	33		$C_1 - C_{33}$
iso-paraffins[1]	84		$C_4 - C_{33}$
α-Olefins	31		$C_2 - C_{32}$
Other straight chain olefins	29		$C_4 - C_{32}$
Branched olefins	32		$C_4 - C_{32}$
Straight chain di-olefins	32		$C_2 - C_{31}$
Branched di-olefins	28		$C_5 - C_{31}$
Monocyclic saturates	90		$C_5 - C_{33}$
Endo-mono-cyclic olefins	52		$C_5 - C_{32}$
Exo-mono-cyclic olefins	25		$C_8 - C_{32}$
Mono-cyclic di-olefins	53		$C_5 - C_{31}$
Di-cyclic saturates	24		$C_{10} - C_{33}$
Di-cyclic olefins	23		$C_{10} - C_{32}$
Di-cyclic di-olefins	22		$C_{10} - C_{31}$
Naphtheno-aromatics	24		$C_{10} - C_{33}$

Classes of compounds	Number of (pseudo-)compounds	Example structure	Carbon range
Naphtheno-aromatic olefins	23		$C_{10} - C_{32}$
Mono-aromatics	51		$C_6 - C_{33}$
Aromatic olefins	25		$C_8 - C_{32}$
Di-aromatics	25		$C_{10} - C_{33}$
Tri-aromatics	20		$C_{14} - C_{33}$
$\beta(\mu)$ radicals[2]	43	-	$C_0 - C_7$
Total	**770**		$C_0 - C_{33}$

[1] After lumping of isomers. Some isomers exist both in a lump or as a pure component

[2] μ radicals are not explicitly included in the final model by application of the quasi steady state approximation

6.2.4 Thermodynamic, transport and kinetic data

Accurate thermodynamic data is crucial to calculate the rate coefficient of the reverse reactions based on the equilibrium coefficient and the rate coefficient of the forward reaction. Benson's group additive method (Benson, 1976) is widely employed by several stand-alone programs, e.g. THERM (Ritter & Bozzelli, 1991), THERGAS (Muller et al., 1995), ThermoDataEstimator (RMG) (Green et al., 2011), Genesys (Vandewiele et al., 2012), to automatically calculate standard enthalpies of formation, entropies, and heat capacities.

In this thesis, thermodynamic data of all C_{5+} molecules are determined in the form of NASA polynomials (Gordon & McBride, 1971) which are determined by group additivity using Genesys (Vandewiele et al., 2012). The thermodynamic data of all C_{4-} molecules, β radicals and βμ radicals have been determined directly from first principles using the high-accuracy CBS-QB3 compound method with corrections for all internal rotations (Sabbe et al., 2005; Sabbe et al., 2008a). The adopted thermodynamic data of cyclopentadienyl radical was determined by Sharma and Green (Sharma & Green, 2009).

All required transport data is calculated using correlations based on the critical temperature, pressure and volume. The critical temperature pressure and volume of all molecules is calculated using Joback's group additive method (Joback & Reid, 1987) which is implemented in RMG's TransportDataEstimator. The contribution of radicals towards the transport properties such as viscosity of the mixture has been neglected and thus no transport properties were estimated for these species.

Group additive calculation of reaction rate coefficients is accomplished by the implementation of a comprehensive framework, which is a consistent extension of Benson's group additivity concept to transition state theory (Saeys et al., 2004; Saeys et al., 2006; Sabbe et al., 2008b; Sabbe et al., 2010a; Sabbe et al., 2010b; Sabbe et al., 2011). This framework allows automatic calculation of Arrhenius parameters, and subsequently rate coefficients, using Equations 6.7 to 6.9.

$$k(T) = n_e \tilde{A} \, exp\left(\frac{-E_a}{RT}\right) \tag{6.7}$$

$$E_a = E_{a,ref} + \sum_{i=1}^{n} \Delta GAV_{E_a,i}^0 \tag{6.8}$$

$$\log \tilde{A} = \log \tilde{A}_{ref} + \sum_{i=1}^{n} \Delta GAV_{\tilde{A},i}^{0} \tag{6.9}$$

All reactions are classified into a limited number of reaction families based on structural similarities of their transition states. The activation energy E_a and the single-event pre-exponential factor $\tilde{A}$ of a certain reaction are obtained by adding contributions to $E_{a,ref}$ and $\tilde{A}_{ref}$ which are the single-event Arrhenius parameters of the elementary reaction family reference reaction, cfr. Equation 6.8 and 6.9. The standard group additive values ΔGAV_i^0 for each of the n contributions depend on the elementary reaction family. It accounts for the structural differences between the reactants of the considered reaction and the reference reaction but also accounts for the structural differences between the transition states of the considered reaction and the reference reaction. The number of contributions equals the number of carbon atoms directly involved in the transition state moiety, i.e. typically 2 or 3. Finally, the reaction rate coefficient is obtained, using Equation 6.7 in which n_e is the number of single events, i.e. a symmetry contribution that takes into account the internal and external symmetry number and the number of optical isomers of reactants and transition state. This symmetry contribution is not straightforward to calculate automatically, and instead, n_e is approximated by the so-called reaction path degeneracy, i.e. the number of structurally equivalent reaction paths from reactant(s) to products. However, without certain correction factors, this can lead to important discrepancies with the actual number of single-events, i.e. the number of energetically equivalent reaction paths from reactant(s) to transition state. Therefore, based on the extensive set of reactions published by Sabbe et al. (Sabbe et al., 2008b; Sabbe et al., 2010a; Sabbe et al., 2010b; Sabbe et al., 2011), a limited set of correction factors was obtained to improve the automatic calculation of n_e. For example for hydrogen abstractions, the number of single events is the

product of the reaction path degeneracy, i.e. the number of structurally equivalent hydrogen atoms, and a correction factor that depends on the nature of the abstracting radical (e.g. 2 for methyl, 1 for vinylic radicals, 2 for primary radicals, etc.).

Nowadays a new code called SIGMA, which can calculate the number of single events based on the symmetry contributions of the transition state (Vandewiele, 2014), could be used. However translating the connectivity matrix used by Hillewaert et al. (1988) and the rules corresponding to a reaction family into a transition state representation usable by SIGMA remains a challenge.

The majority of the reference parameters and group additive values have been determined from first principles after which they have been fitted to a broad experimental database of pilot plant experiments (see Section 6.6).

6.2.5 Coking model

One of the main problems in the steam cracking of hydrocarbons for olefin production is coke formation. Coke is a carbonaceous solid residue that deposits on the internal surface of the reactor and downstream equipment during steam cracking of hydrocarbons. Reducing coke formation is considered one of the main research areas where significant improvements of this mature process still seems to be possible. As coke accumulates, the pressure drop over the reactor increases gradually, lowering the ethene selectivity, and thus the profit (Wysiekierski et al., 1999). Additionally, the heat input to the reactor must increase because the coke layer functions as an extra resistance for heat transfer to the process gas. This leads to higher external tube wall temperatures over the course of time. Fuel consumption of the burners in the furnace increases by approximately 5% in comparison to start-of-run conditions if the same severity is desired (Zimmermann & Walzl, 2000). When the maximum operation temperature of the reactor is reached, the unit is shut down to remove the cokes. These temperatures are close to 1375 K for

traditional high performance alloys and can reach 1425 K for certain specialized alloys (Jakobi, 2009). Decoking is carried out by feeding air and/or steam to the reactor (Schools & Froment, 1997; Heynderickx et al., 2006). This cyclic coking and decoking operation causes aging of the material, which has a negative impact on the process by increasing the rates of coke formation (Zimmermann et al., 1998; Zychlinski et al., 2002; Nishiyama & Otsuka, 2005).

To be able to obtain an estimate of the run length of a reactor a reliable coking model is needed. In literature a wide range of models coking models is available. In this work two different coking models were used to obtain accurate predictions of the coking rate regardless of the used feedstock. The first model was proposed by Plehiers et al. (1990) and is based on two coking precursors (ethene and propene):

$$r_c = k_1 \frac{C(C_2H_4)^2}{C(C_3H_6)} + k_2C(C_2H_4) + k_3C(C_3H_6) \tag{6.10}$$

with the rate coefficients evaluated at the interface temperature:

$$k = A.\exp\left(\frac{-E_a}{RT_{int}}\right) \tag{6.11}$$

The model of Plehiers et al. can be efficiently used with light feed stocks, such as ethane and propane feedstocks. The second model is developed by Reyniers et al. (1994). Reyniers et al. developed an equation for the coking rate which can effectively be used when cracking naphtha feedstocks:

$$\begin{aligned} r_c = \; & k_1[C(C_2H_2) + B_1.C(PD)] \; + \; k_2[C(C_2H_4) + B_2.C(C_3H_6)] \\ & + k_3[C(1C_4H_8) + B_3.C(iC_4H_8)] \; + \; k_4[C(C_4H_6) + B_4C(CPD)] \\ & + k_5C(benzene) + k_6[C(toluene) + B_5C(xylene)] + k_7C(styrene) \end{aligned} \tag{6.12}$$

The rate coefficients are also evaluated at the interface temperature as was the case with the model of Plehiers.

The model of Plehiers will be used for all simulations using gaseous feedstocks (e.g. ethane, propane and LPG) while the model of Reyniers will be used for all liquid feedstocks (naphtha, gas condensate and gas oils).

6.3 The reactor model

6.3.1 Reactor model equations

Steam cracking is a non-isothermal, non-adiabatic and non-isobaric process. Due to the high velocities and thus high Reynolds numbers of the cracked gas inside the inner tube it can be assumed that no radial gradients are present inside the inner tube (Gal & Lakatos, 2008), except for the temperature in a film close to the wall in which all resistance to heat transfer is located (Froment et al., 2011). This approximation however does not hold for ethane cracking where important radial gradients exist for both the temperature and the concentration of the species as is demonstrated by Van Geem et al. (2004). The influence on the yields at the outlet of the reactor are however minor. In this work a one-dimensional plug flow reactor model, in which no thermal gradients are assumed, is used. For a plug flow reactor the steady-state continuity equation for a component j in the process-gas mixture over an infinitesimal volume element with cross-sectional surface area Ω, circumference ω and length dz is given by:

$$\frac{dF_j}{dz} = \left(\sum_{k=1}^{n_r} v_{kj} r_k \right) \Omega \tag{6.13}$$

With F_j the molar flow rate of component j, v_{kj} the stoichiometric coefficient of component j in reaction k and r_k the reaction rate of reaction k.

In the same reactor the energy equation is given by:

$$\sum_{j=1}^{n_s} F_j c_{p,j} \frac{dT_g}{dz} = \omega q + \Omega \sum_{k=1}^{n_r} r_k \cdot (-\Delta H_k) \tag{6.14}$$

With q the heat flux to the process gas, c_{pj} the molar heat capacity of component j at temperature T_g and ΔH_k the reaction enthalpy of reaction k.

The momentum balance accounting for friction and changes in momentum can be written as Equation 6.15:.

$$\frac{dp_{t,g}}{dz} = -\left(\frac{2f}{d_i - 2d_c} + \frac{\zeta}{\pi r_b}\right) \rho_g v_g^2 - \rho_g v_g \frac{dv_g}{dz} \tag{6.15}$$

with $p_{t,g}$ the total pressure, f the Fanning friction factor, ρ_g the density of the gas mixture, v the velocity and ζ the additional resistance coefficient for bends (Nekrasov, 1968). The first term on the right hand side of Equation 6.15 is the pressure drop due to friction while the second term is the pressure drop due to acceleration. The Fanning friction factor can be calculated using Prandtl's Equation (Prandtl, 1949).

$$\sqrt{f} = \frac{1}{4.\log_{10}(Re.\sqrt{f}) - 0.4} \tag{6.16}$$

The initial conditions for Equation 6.13-6.15 can be written as:

$$F_j(z = 0) = F_{j,0}, \qquad T_g(z = 0) = CIT, \qquad p_{t,g}(z = 0) = CIP \tag{6.17}$$

The continuity equations for the formation of coke can be written as (Plehiers et al., 1990):

$$\frac{\partial C_{cokes}}{\partial t} = r_c \tag{6.18}$$

$$C_{cokes} = 0 \tag{6.19}$$

Since the time scale for the formation of cokes is order of magnitudes lower than the time scale of all other reactions occurring in the kinetic model the quasi steady state assumption can be

applied with respect to time or in other words the solution of Equation 6.13-6.15 is assumed constant over a time step and the effect of coke formation through Equation 6.18 is updated explicitly at the end of each time step (Huntrods et al., 1989).

6.3.2 Solving the reactor model equations

The reactor model equations to be solved are given by Equations 6.13,6.14 and 6.15 and the initial conditions given by Equation 6.17. Equation 6.14 and 6.15 only have to be considered when, respectively, the temperature and/or pressure profile are not imposed. The production rate of each component j by the reaction k can be expressed as a function of the concentration of the involved species. The resulting set of continuity equations forms a system of stiff non-linear first order differential equations. The stiffness is caused by the large difference (several orders of magnitude) between the eigenvalues caused by the large differences in reactivity of the molecular and radical species. To overcome the stiffness problem a numerical procedure described by Dente et al. (1979) is applied. In this procedure the net production rate of each component is split in a cumulative rate of formation term and a similar rate of disappearance term. Next, the rate of disappearance is assumed to be quasi-proportional to the mass fraction of the component, leading to the introduction of a pseudo rate coefficient. The resulting non-homogeneous first order differential equation is then integrated over a reactor length increment Δz small enough to consider the cumulative rate of formation and the pseudo rate coefficient to depend on z only. Based on the different magnitude and behavior of these variables for molecular and radical species the resulting integral equations are then further evaluated. The increment Δz is chosen in such a way that (based on a number of criteria) the mean values for the cumulative rate of formation and the pseudo rate coefficient can be used for the molecular species, while a number of terms in the equation approach unity for the radical species, allowing an analytical integration.

Because values of the cumulative rate of formation and the pseudo rate coefficient at the end of each interval Δz appear in the resulting algebraic equations, iteration for each interval is finally required. The calculations proceed until convergence is reached (Clymans, 1982). Finally, it should be remarked that the method presented for the radical species is a numerical equivalent of the well-known quasi steady state assumption (Dente et al., 1979), i.e. assuming steady state for certain species in each increment of the integration, leading to a set of algebraic equations to be solved simultaneously with the differential equations for the remaining species.

Dente et al. (1979) also proposed to solve the energy and momentum equations in an iterative manner, decoupled from the continuity equations, by means of a straightforward finite difference method.

To perform a simulation of an industrial furnace the heat flux from the furnace to the radiant tubes is required. The heat flux profile acts as a set of boundary conditions for the simulation. However, in industrial cracking units, there is often no detailed information about the heat flux profile to the reactor available. In an industrial reactor the pressure at the reactor outlet is traditionally set as low as possible, depending on the separation train following the reactor and the coil inlet pressure (CIP) is not known either. Using the initial pressure and the heat flux profile as initial and boundary conditions thus implies several problems for industrial applications. That is, these parameters are not easily accessible in industrial steam cracking furnaces

For an industrial furnace a pressure related severity index (either COP or the ethene to ethane yield ratio) and one of the temperature related severity indices (P/E-ratio, COT, etc.) could replace the specified inlet conditions (Van Geem et al., 2005). For instance the outlet pressure can replace the inlet pressure as a boundary condition. The inlet pressure becomes then a changeable process condition to obtain the desired outlet specification. Similarly, the heat flux

profile is adapted to meet the set COT or another temperature related severity index. The replacement of the heat flux profile by one process variable at the reactor outlet is not that straightforward. The heat flux profile consists of a number of fluxes that strongly vary along the reactor. This results in an ill posed problem because if for example the reactor is divided in n segments $n-1$ degrees of freedom remain, and hence, an endless number of solutions can be found that meet the specified process variable at the outlet. Fortunately, the heat flux profile along the reactor has been studied extensively (Heynderickx & Nozawa, 2005; Habibi et al., 2007; Stefanidis et al., 2008). This allows predefining the shape of the heat flux profile depending on the used industrial furnace. Indeed, the value of the heat flux at the reactor inlet combined with the predefined profile shape, allows determining the complete heat flux profile.

The original initial boundary value problem is now translated in a two point boundary condition problem that can be solved using the shooting technique (Meade et al., 1996). Therefore two process variables need to be determined at the reactor outlet, one accounting for temperature effects, and another one that is related to the pressure. A number of severity indices can be used to define the boundary condition problem. The resulting problem is solved using Broyden's method (Broyden, 1965). Figure 6.5 gives a total overview of how the simulations are performed. The red box depicts a typical shooting simulation while the blue box depicts the decoupling of Equation 6.18 and the performing of a run length simulation by step wise progression through time.
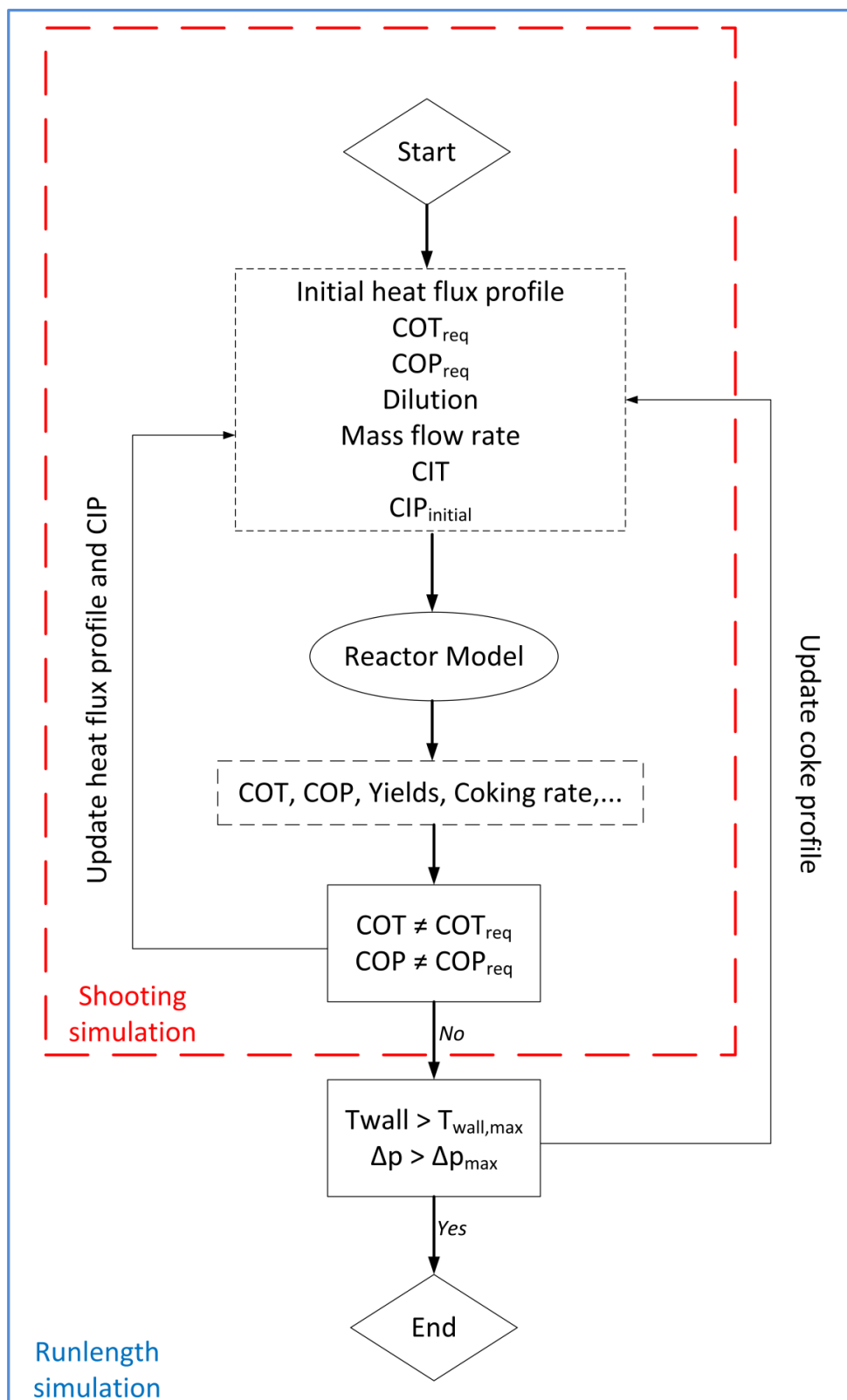
Figure 6.5: Overview of the different steps in a simulation

6.3.3 Radial energy transport

The first term of the right hand side of the energy equation (Equation 6.14) corresponds to the heat flux over the reactor wall. The second term of the right hand side corresponds to the thermal power accompanying the endothermic steam cracking process. If the heat flux profile is given Equation 6.14 can be solved however sometimes the external wall temperature $T_{w,ext}$ profile is given and the internal heat flux q should first be calculated. It could also be that the heat flux is given and the internal wall temperature is needed for the calculation of the coking rate. For these calculations additional equations are necessary.
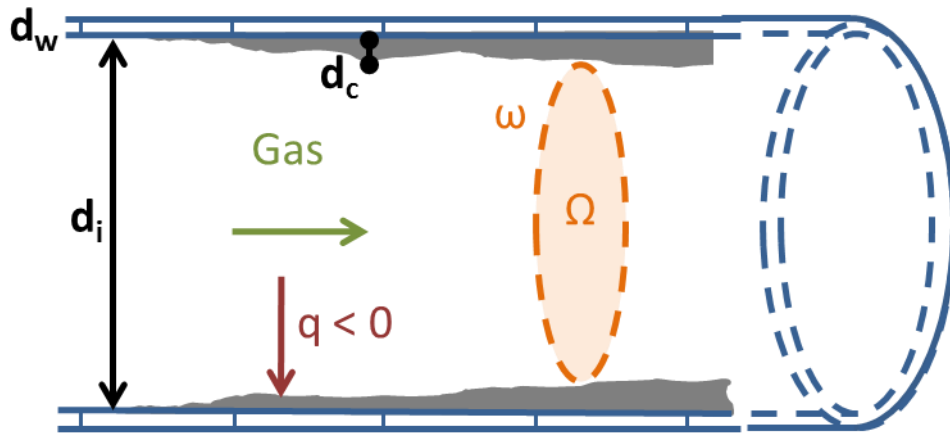
Figure 6.6: Geometry of a reactor tube

Figure 6.6 shows the typical geometry of a reactor tube. For the heat flux profile the following equation can be written:

$$q = U.\left(T_{ext} - T_g\right) \tag{6.20}$$

With T_{ext} being the external wall temperature and U being the overall heat transfer coefficient which can be calculated using Equation 6.21.

$$\frac{1}{U} = \frac{1}{\alpha_i} + \frac{d_w}{\lambda_w} \cdot \frac{d_i - 2d_c}{M_{lm}(d_i, d_i + 2d_w)} + \frac{d_c}{\lambda_c} \cdot \frac{d_i - 2d_c}{M_{lm}(d_i - 2d_c, d_i)} \tag{6.21}$$

with $M_{lm}(x, y)$ the logarithmic mean of x and y. Equation 6.20 and 6.21 can be used to calculate the heat flux profile based on the external wall temperature or the external wall temperature based on the heat flux profile. The gas/cokes interface temperature $(T_{c,int})$ can be calculated using the following equation:

$$q = \alpha_i \cdot \left(T_{c,int} - T_g\right) \tag{6.22}$$

while the internal wall temperature $(T_{w,int})$ of the tube can be calculated using:

$$q = \left(\frac{1}{\alpha_i} + \frac{d_c}{\lambda_c} \cdot \frac{d_i - 2d_c}{M_{lm}(d_i - 2d_c, d_i)}\right)^{-1} \cdot \left(T_{w,int} - T_g\right) \tag{6.23}$$

The thermal conductivity of the cokes is dependent on the type of cokes that is formed inside the reactor and could thus be viewed as an adjustable parameter. In the present work a value of 6.45 W.m^{-1}.K^{1} was used.

6.4 Calculation of physical and transport properties

6.4.1 Specific heat c$_p$, Standard enthalpy of formation h^0 and standard entropy of formation s^0

In this work the thermodynamic data are calculated using the NASA polynomials of Gordon and McBride (1971). The following equations can be used to calculate the specific heat, standard enthalpy of formation and standard entropy of formation respectively:

$$\frac{c_p}{R} = a_1 + a_2 T + a_3 T^2 + a_4 T^3 + a_5 T^4 \tag{6.24}$$

$$\frac{h^0}{RT} = a_1 + a_2 \frac{T}{2} + a_3 \frac{T^2}{3} + a_4 \frac{T^3}{4} + a_5 \frac{T^4}{5} + \frac{a_6}{T} \tag{6.25}$$

$$\frac{s^0}{R} = a_1 ln(T) + a_2 T + a_3 \frac{T^2}{2} + a_4 \frac{T^3}{3} + a_5 \frac{T^4}{4} + a_7 \tag{6.26}$$

6.4.2 Thermal conductivity of the wall λ_w

The conduction coefficient of the wall depends on the wall material and the temperature. For all calculations in this thesis the correlation for stainless steel is used unless stated differently. This results in the following equation (Reid et al., 1979):

$$\lambda_w = 2.014\ 10^{-3} + 7.216\ 10^{-6}T \tag{6.27}$$

6.4.3 Convection coefficient α

The convection coefficient for smooth tubes can be obtained from the Dittus-Boelter correlation:

$$Nu = 0.023Re^{0.8}Pr^{0.4} \tag{6.28}$$

The Reynolds, Nusselt and the Prandtl number are defined as follows:

$$Re = \frac{vd_i\rho}{\mu} \tag{6.29}$$

$$Pr = \frac{\mu c_p}{\lambda_g} \tag{6.30}$$

$$Nu = \frac{\alpha\ d_i}{\lambda_g} \tag{6.31}$$

6.4.4 Friction factor f

Several correlations are available for the calculation of the Fanning friction factor. For rough straight tubes the friction factor f is obtained from the Colebrook equation (Lira, 2013):

$$\frac{1}{\sqrt{f}} = -2.\log_{10}\left(\frac{\epsilon}{3.7.d_h} + \frac{2.51}{Re.\sqrt{f}}\right) \tag{6.32}$$

with d_h is the hydraulic diameter and ϵ the roughness height of the tube. In case of a circular tube the hydraulic diameter is equal to the diameter of the tube. This equation simplifies to Equation 6.33 for smooth straight tubes ($\varepsilon = 0$).

$$\frac{1}{\sqrt{f}} = -2.\log_{10}\left(\frac{2.51}{Re.\sqrt{f}}\right)$$

(6.33)

To account for the influence of non-uniformity of the process gas over the cross section of the tube the friction factor is corrected by multiplying with:

$$\left(\frac{\mu_w}{\mu}\right)$$

(6.34)

with μ_w being the process gas viscosity at the internal wall temperature.

6.4.5 The viscosity

The calculation of the mixture of the gas required both the evaluation of the pure viscosity coefficients as well as the calculation of the viscosity of the mixture using mixing rules. In COILSIM1D the viscosity of pure compounds is calculated using the theory of corresponding states and more in particular the approach of Stiel and Thodos (Stiel & Thodos, 1961) is used. For non-polar gasses this results in:

$$\mu_i.\zeta_i = 17.78 \times 10^{-7}\left(4.58\,T_{r,i} - 1.67\right)^{5/8}$$

(6.35)

When the reduced temperature is greater than 1.5. In Equation 6.35 ζ is the reduced, inverse viscosity which can be written as

$$\zeta_i = 0.176\left(\frac{T_{c,i}^{1/6}}{M_i^{1/3}.p_{c,i}^{2/3}}\right)$$

(6.36)

The values for the critical temperature and critical temperature were already discussed in Section 6.2.4. For polar gasses such as hydrogen and water Stiel and Thodos obtained a similar expression (Stiel & Thodos, 1961).

With the viscosities of the pure compounds known, the viscosity of the mixture can be calculated using Wilke's Formula (Poling et al., 2001):

$$\mu = \sum_{i=1}^{n_c} \frac{\mu_i}{1 + \sum_{j=1}^{n_c} \phi_{ij} \frac{F_j}{F_i}} \tag{6.37}$$

Equation 6.38 requires the evaluation of the following coefficients:

$$\phi_{ij} = \frac{[1 + \left(\eta_i/\eta_j\right)^{1/2} (M_i/M_j)^{1/4}]^2}{[8\,(1 + M_i/M_j)]^{1/2}} \tag{6.38}$$

It is clear that these coefficients are temperature dependent via the temperature dependence of the viscosity of the pure compounds, and hence, they need to be re-evaluated each time the temperature changes.

6.4.6 Thermal conductivity of the gas

The thermal conductivity is calculated in the same way as the viscosity:

$$\lambda_g = \sum_{i=1}^{n_c} \frac{\lambda_i}{1 + \sum_{j=1}^{n_c} 1.065\phi_{ij} \frac{F_j}{F_i}} \tag{6.39}$$

For the calculation of the thermal conductivity of a pure compound the modified Eucken correlation is used (Brodkey & Hershey, 1998):

$$\frac{\lambda_i}{\mu_i} = 1.32c_{v,i} + \frac{1.4728\ 10^4}{M_i} \tag{6.40}$$

6.5 Improvements to the solution procedure

Even with today's computer architecture simulation codes need to be designed efficiently to keep the simulation time as low as possible and they should require only a minimum amount of memory storage while maintaining an adequate accuracy. This becomes especially important when more complex optimization routines are being used or when results are needed within a certain time window. An example where low simulation times thus becomes important is when a

simulator is used for the online optimization of a running plant (Pierucci et al., 1996). The optimization should be finished in a reasonable amount of time so that the set points of the control systems can be changed before the input, e.g. feedstock composition, has changed. COISLIM1D already applies several chemical methods to keep the size of the mechanism and thus the total simulation time limited. As mentioned in Section 6.2.3 the μ hypothesis allows for the algebraic elimination of the concentration of all the μ radicals and thus drastically decreases the amount of differential equations that needs to be solved without influencing the fundamental nature of the model. Another advantage of the μ hypothesis is that it allows for the elimination of species that will never be formed based on the feedstock composition. For example if decane is used as a feedstock no undecane or heavier paraffins will be allowed to form due to the μ hypothesis and thus for these species no differential equations will need to be solved.

In addition to the μ hypothesis a specialized numerical procedure to overcome the stiffness of the resulting differential equations is used (Dente et al., 1979). The advantage of the solver proposed by Dente et al. is that the time to integrate the differential equations is a factor 3 to 5 smaller than when a typical stiff solver such as DASSL is used (Van Geem, 2006).

To further improve the computational efficiency of the simulation model extensive profiling of the computer code is carried out to identify and improve the most time consuming routines.

6.5.1 Profiling of COILSIM1D

The first step in speeding up the code is to evaluate the calculations which are the most time consuming. This can be done by so-called profiling. Using a profiling tool a developer can see which functions are called, how much execution time they consume, and how control and data flows between them (Sloane & Roberts, 2014). Profiling of COILSIM1D was done using PGProf ("PGPROF profiler guide," 2014) looking at three cases. PGProf® is a graphical profiler which

comes with the compilers from PGI® ("PGI Compiler Reference Manual," 2014). An overview

of the settings of these simulations is given in Table 6.3.

Table 6.3: Overview of the three simulation cases

Simulation		Case 1 T & P profile	Case 2 Heat flux profile	Case 3 COT and COP
Conditions				
Temperature severity	(K or -)	Isothermal: 1073	Heat flux Case 1	COT = 1123
Pressure severity	(Pa)	Isobaric: 172.10^3	CIP = 240.10^3	COP = 172.10^3
HC Flow rate	(kg.s^{-1})	0.194	0.194	0.194
Dilution	(-)	0.35	0.35	0.35
Reactor				
Type	(-)	Millisecond		
Length (m)	(m)	10		
Diameter (m)	(m)	0.03		
Feedstock				
Type	(-)	Kerosene		
Boiling range	(K)	421-551		
Density	(kg.m^{-3})	0.7987		
n-paraffins	(wt%)	14.3		
isoparaffins	(wt%)	21.1		
Naphthenes	(wt%)	45.8		
Aromatics	(wt%)	18.9		

The feedstock for all three cases was the same kerosene. The detailed composition of the latter

was based on the commercial indices using SIMCO (see Chapter 2). The composition of the

reconstructed feedstock resulted into 357 compounds (excluding the radicals for which QSSA is

applied) being taken into account in the kinetic network. The major difference between the

simulations is however the type of simulation that is carried out. For Simulation Case 1 both the

temperature and pressure profile are specified as an isothermal and isobaric profile respectively.

As mentioned in Section 6.3.1 there is no need to solve the energy and momentum balances to

obtain the product distribution at the end of the reactor.

To include both the energy and momentum balance into the equation Simulation Case 2 is based upon an imposed heat flux profile. The latter was first calculated based upon Simulation Case 1. Since the temperature and the pressure are now only known at the inlet of the reactor both the energy and momentum balances need to be integrated to be able to obtain the product distribution at the outlet of the reactor. This requires the evaluation of thermodynamic and transport properties of the mixture that were not needed in case of Simulation Case 1. The last simulation case only supplies the temperature and pressure at the outlet of the reactor. As is described in Section 6.3.2 COILSIM1D imposes a heat flux profile shape and adjusts the heat flux profile as well as the inlet pressure of the reactor to match these outlet conditions. Simulation Case 3 is in that respect very similar to simulation Case 2 since each step in the shooting algorithm is basically a simulation specifying the heat flux profile and inlet conditions of the reactor (see Figure 6.5).

Figure 6.7 shows the results of the profiling study. The evaluation of the reaction rates is among the most costly subroutines when the temperature and pressure profile is specified. When both temperature and pressure profile are given and only the material balances need to be solved the calculation of the rates takes about 85% of the total time (Case 1). However when in addition the energy and momentum balances need to be solved it only uses between 10 and 30% of the total time (Case 2 and 3). In these cases the evaluation of the viscosity of the gas phase becomes significantly more time consuming and the viscosity calculation take between 75 and 85% of the total time. This viscosity is needed to calculate the friction coefficient which is needed to solve the momentum balance. In addition the viscosity is used to calculate the Reynolds number which is used to calculate the convection coefficient inside the tube (see Section 6.4.3). The increasing

complexity of the simulation when going from Case 1 to Case 3 is also clearly visible in the total simulation time which goes from only 0.48 s to 23.03 s.
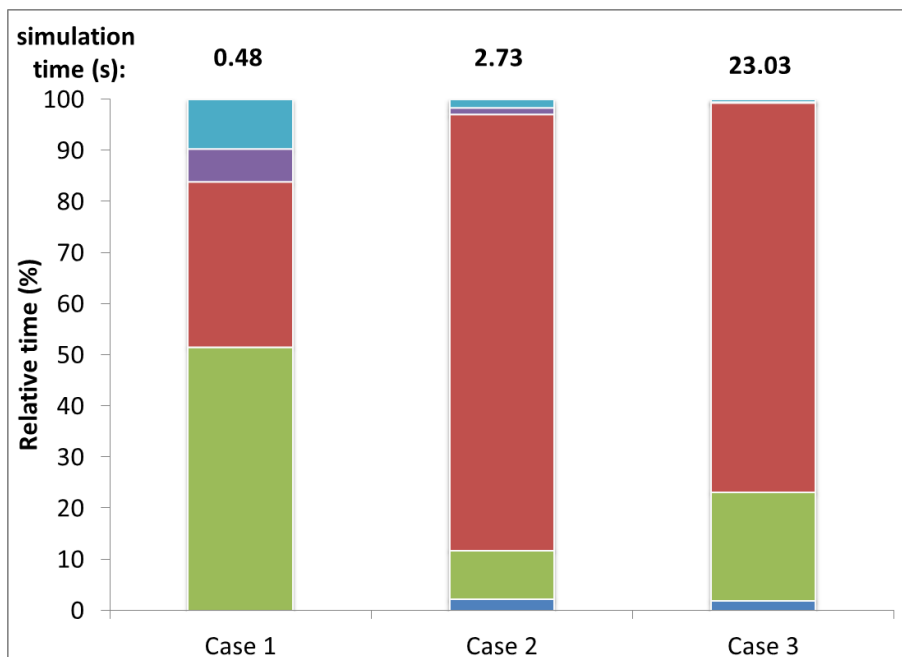
Figure 6.7: Relative time consumption of different subroutines for CPU calculations using a kerosene feedstock: ▪ Solver; ▪ Rate of production; ▪ Viscosity; ▪ Reading input data; ▪ Other calculations

6.5.2 Analyzing the viscosity calculations

The calculation of the viscosity is required to integrate the momentum balance (Equation 6.15) and to calculate the wall temperatures (see Section 6.3.3). It is however not directly involved in the integration of the continuity equations and the energy equation. It however indirectly influences the pressure in the reactor and thus the concentration of the species but this contribution is low and does not have a significant influence on the final yields of a simulation. It does however directly influence the wall temperatures of the reactor and as such the coking rate. Thus for accurate predictions of the coking rate and the run length accurate calculations of the viscosity are required.

For the evaluation of the viscosity coefficients (see Section 6.4.5) the Wilke coefficient matrix needs to be evaluated. The coefficient matrix consists of $n_{species} \times n_{species}$ elements. Each element requires a single evaluation of Equation 6.38. It is clear that the calculation time of this coefficient matrix scales quadratically with the number of species while for the other calculations this scaling is linear. Figure 6.8 shows the total time spent doing viscosity calculations for different feedstocks and thus different network sizes. For all feedstocks simulation Case 3 was used (see Table 6.3). The curve shows a clear quadratic trend which corresponds to the fact that the algorithm is of second-order. The latter is confirmed when a second order polynomial is fitted through the data points. This results in the following equation:

$$t = 0.0002n_c{}^2 - 0.0144n_c \qquad (6.41)$$

Equation 6.41 fits the data with a coefficient of determination, R^2, of 0.999 and the curve is also depicted in Figure 6.8.
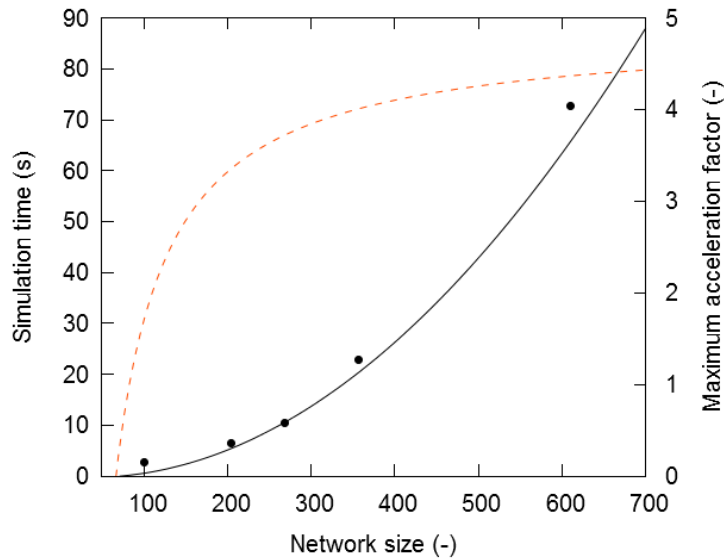
Figure 6.8: Left axis: Total duration of viscosity calculations (●) and fitted second order polynomial (——),

Right axis: Theoretical calculated maximum acceleration factor (----)

Based on the relative time consumption of the viscosity calculations a theoretical maximum acceleration factor can be calculated using the following equation:

$$A = \frac{1}{(1 - t_{visc,rel})} \tag{6.42}$$

With $t_{visc,rel}$ the relative time consumption of the viscosity calculations and A the maximum theoretical acceleration factor. This equation assumes that a maximal acceleration factor is obtained when the viscosity calculations happen instantaneous. In reality this is however not possible but preferably the actual acceleration factor should be as close to the theoretical maximum as possible. Figure 6.8 shows this theoretical maximal acceleration factor possible in COILSIM1D by optimizing the viscosity calculations. This maximum acceleration factor goes from only 1.75 for smaller networks (101 molecules) to 4.29 for the larger networks (610 molecules) in COILSIM1D.

6.5.3 Using the GPU for viscosity calculations

Equation 6.38 shows that the calculation of the Wilke coefficients is non-recursive or that each Wilke coefficient can be evaluated without needing the value of another Wilke coefficient. The latter makes the calculations of the Wilke coefficients an ideal candidate to be executed in parallel, either on the CPU or on the GPU. Here the evaluation of the Wilke coefficients is parallelized on a GPU. In Figure 6.9 a comparison is made between the original CPU algorithm of the viscosity subroutine and the modified CPU/GPU version. The main idea behind the calculations remains essentially the same. Several do loops in the original code have been replaced with single GPU subroutines, so called kernels. Since the GPU device does not have direct access to the memory of the machine the used variables need to be copied from the

machine memory to the GPU or device memory. These transfer operations have been added to the new subroutine.

The calculations on the GPU include three different kernels. One for the evaluation of the viscosity of the pure compounds, one for the evaluation of the Wilke coefficients and one for the evaluation of the viscosity of the mixture. It is clear that the first two kernels are non-recursive but that the third kernel is recursive, and hence, each parallel calculation has an influence on the same variable, i.e. the total viscosity of the process gas. To avoid so called race conditions (Robert & Barton, 1992) a reduction technique needs to be applied (Farber, 2011). For this reason a balanced tree reduction technique was used (Akimasa & Kiminori, 2011).

Table 6.4 shows the acceleration factor at different network sizes when COILSIM1D is calculated on a hybrid CPU/GPU system. The acceleration factor ranges from only 0.9 for smaller networks (101 molecules) to 3.5 for the larger networks (610 molecules). For example the simulation time for a network with 610 molecules is reduced from 72.4s to 20.8s when the hybrid CPU/GPU version is used. For smaller network sizes the acceleration factor is negligible or even lower than one. This is caused by an increased relative importance of the copy operation (see the red parallelogram on Figure 6.9) from the CPU memory to the GPU memory and vice versa. Table 6.4 also shows the theoretical maximum acceleration factor of the program. The acceleration factor of the new algorithm approximates the theoretical maximum acceleration factor. Thus further optimizing the viscosity calculations will only yield a limited acceleration. Further acceleration could be obtained by looking at the Rate of production routine and this is discussed in Chapter 9.
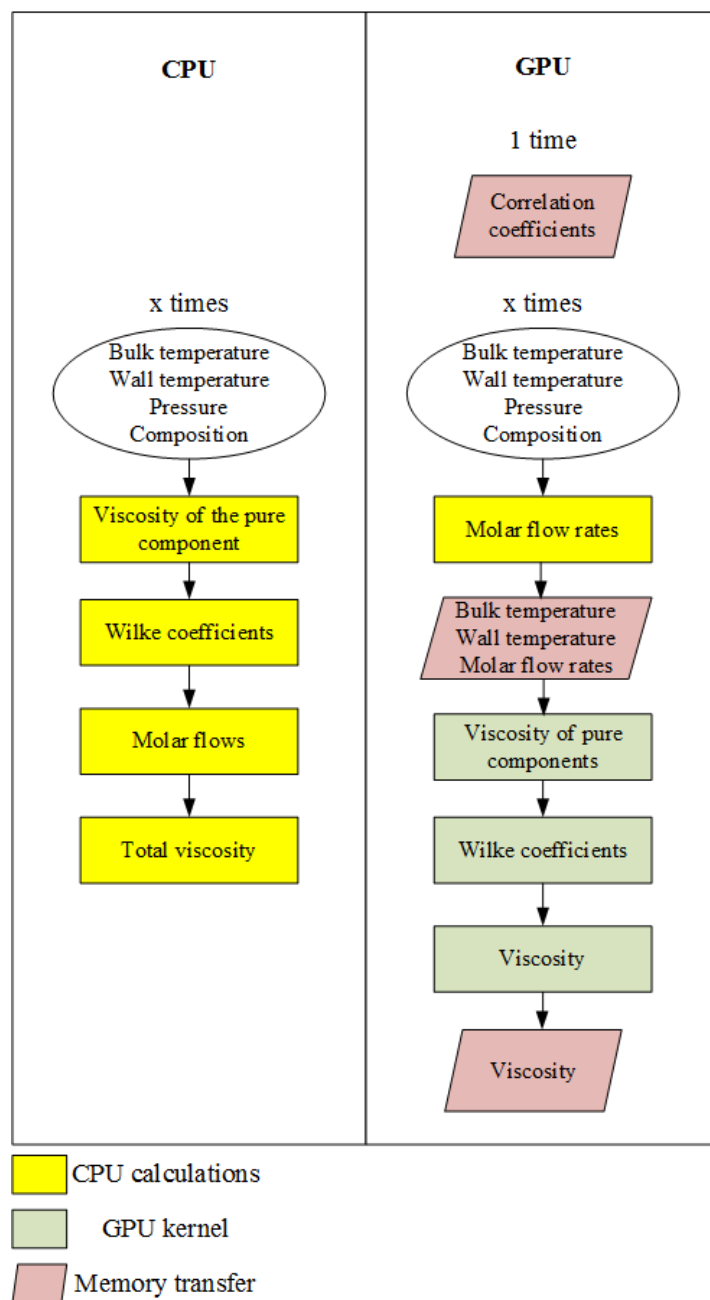
Figure 6.9: Flow sheet of the calculations in the physical property subroutine. Left: CPU version. Right: CPU/GPU version

Table 6.4: Acceleration factor of COILSIM1D when comparing a CPU simulation with a CPU/GPU hybrid simulation:

Number of compounds	Acceleration factor viscosity calculations	Acceleration factor COILSIM1D	Acceleration factor theoretical
101	1.04	0.91	1.75
205	2.82	1.92	3.09
269	3.83	2.22	3.54
357	7.14	2.96	4.43
610	15.75	3.49	4.29

The CPU/GPU hybrid version of COILSIM1D is thus able to quickly calculate the yields at the outlet of the reactor in a matter of seconds. Due to these very short simulation times COILSIM1D can easily be used in more complex simulations such as optimization (see Chapter 8) or as an on-line tool in industrial plants.

6.5.4 Tabulation of the Wilke coefficients

As the viscosity coefficient does not directly influences the yields (except through differences in pressure) an approximated value could be used rather than evaluating the viscosity at every integration step. A simple approximation could be to tabulate the Wilke coefficients at fixed temperature intervals. In each integration step the tabulated values would be used instead of calculating the exact values. Another approximation could be to use an average value for the viscosity throughout the reactor and thus in the latter case only a single evaluation of the viscosity would be needed. The results of both approximations are shown in Table 6.5. It shows that increasing the temperature interval at which the Wilke coefficients are tabulated, does indeed decrease the total simulation time. Increasing the temperature interval beyond 20 K does not have a significant effect on the total simulation time as at this point most of the time is spent

evaluating Equation 6.37. The error introduced at the different temperature intervals is also negligible and the error on the coking rate does not exceed more than 2% compared to the base case even at a temperature interval of 100 K. In addition no significant influence is seen on the pressure drop and as a result the yields are the same in all cases. Using an average value of the viscosity can decrease the simulation time even further as in this case Equation 6.37 is only evaluated once. This does however have a significant effect on the predicted values. The error on the viscosity and coking rate exceeds 20%. This difference in the coking rate results into wrong predictions of the runlength and thus using an average value of the viscosity is not recommended. The error on the pressure drop is however still minor (1.3%) and has no influence on the predicted yields.

Table 6.5: Calculated values of viscosity, internal wall temperature and coking rate at the position where the difference between the base case and the average value approximation is maximal. Relative difference of the method using tabulation of the Wilke coefficients or an average value for the viscosity with the base case.

	Base case	Tabulation interval					Average value
		1 K	5 K	20 K	50 K	100 K	
		Relative difference with base case (%)					
Viscosity (10^6 Pa.s)	23.5	0.00	0.02	0.06	0.86	2.34	24.00
Pressure drop (10^3 Pa)	69.5	0.00	0.03	0.07	0.09	0.14	1.29
Internal wall temperature (K)	1116	0.00	0.00	0.00	0.04	0.10	1.15
Coking rate (10^6 kg.m^{-2}.s^{-1})	0.70	0.01	0.01	0.03	0.69	1.96	23.01
	Total Time						
Time viscosity calculations (s)	19.9	14.2	7.6	6.4	5.9	5.7	0.0
Time total calculations (s)	24.0	18.4	11.6	10.2	10.0	9.6	4.0

The acceleration of tabulating the Wilke coefficients, e.g. a factor of 2.35 using intervals of 20 K, is about the same as using the GPU, e.g. 2.96. Both techniques could however be combined to obtain additional acceleration as will be discussed in Chapter 9.

6.6 Validation of single event microkinetic model

The developed kinetic model has been extensively validated using both pilot plant data from the unit described by Van Geem et al. (2008) and plant data were available for a broad range of feedstocks. Figure 6.10 shows the parity plots of the two major products ethene and propene for a wide range of feedstocks (from ethane up to gas oil). A good agreement is obtained within the experimental data and almost all the data points are within the 5% error margins depicted by the lines for all feedstocks.
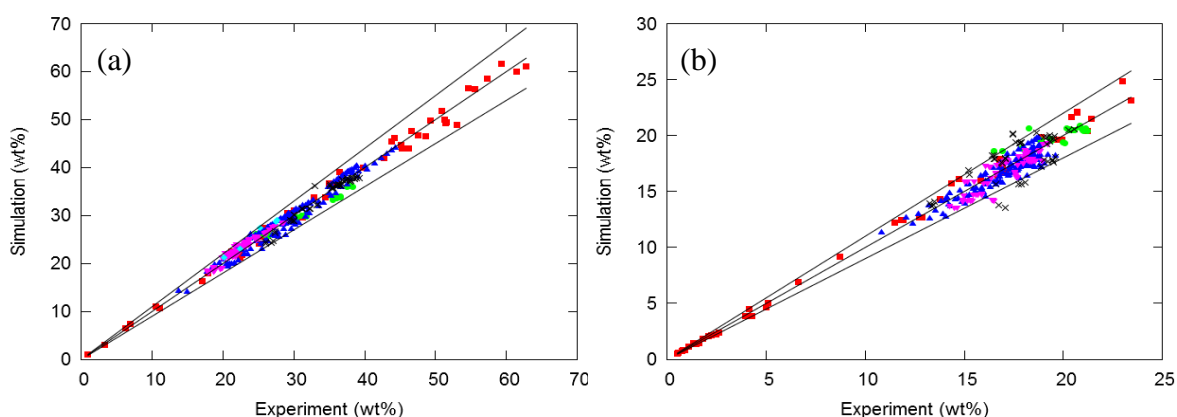
Figure 6.10: Validation of the major products ethene (a) and propene (b): ■ **Ethane and propane experiments;** ● **butane experiments;** ▲ **naphtha experiments;** ▼ **gas condensate experiments;** ◆ **gas oil experiments** ✕ **Other experiments. Lines represent the first bissectrice and the 5% error lines.**

Figure 6.11 on the other hand shows some of the minor products (hydrogen, methane and 1,3-butadiene) for the same feedstocks. A good agreement is obtained between the experimental and simulated data as most points are within the 10% error margin depicted by the lines. The ability of the kinetic model to accurately predict the major products allows the study of the multi-objective optimization for a wide variety of available feedstocks and also allows for the study of co-cracking different feedstocks since it is not limited by the feedstock composition between ethane and gasoil.
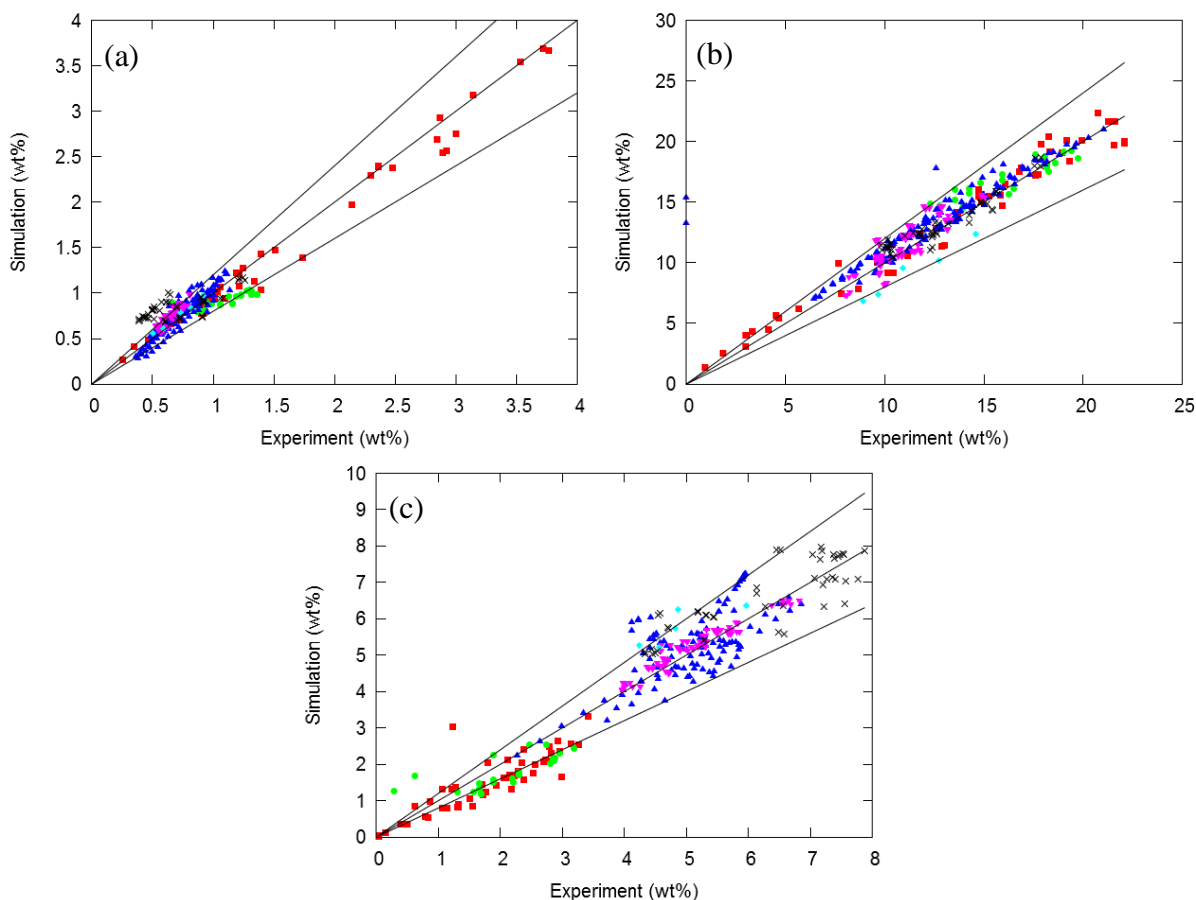
Figure 6.11: Validation of the minor products hydrogen (a), methane(b) and 1,3-butadiene (c): ■ **Ethane and propane experiments;** ● **butane experiments;** ▲**naphtha experiments;** ▼ **gas condensate experiments;** ◆ **gas oil experiments** ✕ **Other experiments. Lines represent the first bissectrice and the 10% error lines.**

6.7 Conclusions

A single event microkinetic model (CRACKSIM) for steam cracking of hydrocarbons based on the free radical mechanism is presented and is incorporated into a one dimensional plug flow reactor model (COILSIM1D). The microkinetic model is divided in two sub models: the β network and the monomolecular μ network. In the latter monomolecular reactions dominate for radical species with more than 5 carbon atoms (μ radicals). Furthermore applying the QSSA on these μ radicals allows to derive analytical expressions for these radical reaction intermediates

allowing to drastically reduce the number of species for which the mass balances need to be solved and thus drastically decrease the final simulation time.

Additionally a specialized numerical procedure proposed by Dente et al. (1979) is used to solve the resulting differential equations for a 1D plug flow reactor which is more efficient than using a generalized stiff solver. The computational efficiency of COILSIM1D has been further improved by performing the calculation of the viscosity of the mixture on the GPU. This improvement accelerated COILSIM1D with a factor of 3.5 for a reduced kinetic network which takes into account 610 molecular species.

The final model is able to accurately predict the yields of the major products (ethene and propene) as well as the by-products for a wide range of feedstocks (from ethane up to gas oils) in a matter of seconds. Due to the accurate and fast prediction of the yields at the outlet of COILSIM1D can easily be implemented in more complex simulation types such as optimization or used as an on-line tool in industrial plants.

6.8 References

Akimasa, M., & Kiminori, M. (2011). Balanced trees inhabiting functional parallel programming. *SIGPLAN Notices, 46*, 117-128.

Benson, S. W. (1970). Some Recent Developments in the Gas-Phase Pyrolysis of Hydrocarbons. Refining Petroleum for Chemicals (pp. 1-19): American Chemical Society.

Benson, S. W. (1976). Thermochemical Kinetics: Methods for the Estimation of Thermochemical Data and Rate Parameters: John Wiley & Sons.

Bodenstein, M., & Lütkemeyer, H. (1924). Die photochemische Bildung von Bromwasserstoff und die Bildungsgeschwindigkeit der Brommolekel aus den Atomen: Akad Verlagges.

Brodkey, R. S., & Hershey, H. C. (1998). Transport Phenomena: A unified approach: McGraw-Hill.

Broyden, C. G. (1965). A Class Of Methods For Solving Nonlinear Simultaneous Equations. *Mathematics of Computation, 19*, 557-593.

Clymans, P. (1982). De Productie van Olefinen uit Gasolies en de Rigoureuze Simulatie van de Thermische Kraking. Ugent.

Clymans, P. J., & Froment, G. F. (1984). Computer-generation of reaction paths and rate-equations in the thermal-cracking of normal and branched paraffins. Computers & Chemical Engineering, 8, 137-142.

Dente, M., Bozzano, G., Faravelli, T., Marongiu, A., Pierucci, S., & Ranzi, E. (2007). Kinetic Modelling of Pyrolysis Processes in Gas and Condensed Phase. Advances in Chemical Engineering (Vol. 32, pp. 51-166): Academic Press.

Dente, M., Ranzi, E., & Goossens, A. G. (1979). Detailed prediction of olefin yields from hydrocarbon pyrolysis through a fundamental simulation model (SPYRO). Computers & Chemical Engineering, 3, 61-75.

Dijkmans, T., Pyl, S. P., Reyniers, M.-F., Abhari, R., Van Geem, K. M., & Marin, G. B. (2013). Production of bio-ethene and propene: alternatives for bulk chemicals and polymers. Green Chemistry, 15, 3064-3076.

Farber, R. (2011). CUDA: Application design and development: Elsevier.

Froment, G. F., Bischoff, K. B., & De Wilde, J. (2011). Chemical reactor analysis and design (3th edition): Wiley.

Gal, T., & Lakatos, B. G. (2008). Thermal cracking of recycled hydrocarbon gas-mixtures for re-pyrolysis: Operational analysis of some industrial furnaces. Applied Thermal Engineering, 28, 218-225.

Gordon, S., & McBride, B. J. (1971). Computer program for calculation of complex chemical equilibrium compositions rocket performance incident and reflected shocks, and Chapman-Jouguet detonations.

Green, W. H., Allen, J. W., Ashcraft, R. W., Beran, G. J., Goldsmith, C. F., Harper, M. R., Jalan, A., Magoon, G. R., Matheu, D. M., Petway, S., Raman, S., Sharma, S., Van Geem, K. M., Song, J., Wen, J., West, R. H., Wong, A., Wong, H.-W., Yelvington, P. E., & Yu, J. (2011). RMG - Reaction Mechanism Generator v3.3.   http://rmg.sourceforge.net/

Habibi, A., Merci, B., & Heynderickx, G. J. (2007). Impact of radiation models in CFD simulations of steam cracking furnaces. Computers & Chemical Engineering, 31, 1389-1406.

Heynderickx, G. J., & Nozawa, M. (2005). Banded gas and nongray surface radiation models for high-emissivity coatings. AIChE Journal, 51, 2721-2736.

Heynderickx, G. J., Schools, E. M., & Marin, G. B. (2006). Optimization of the decoking procedure of an ethane cracker with a steam/air mixture. Industrial & Engineering Chemistry Research, 45, 7520-7529.

Hillewaert, L. P., Dierickx, J. L., & Froment, G. F. (1988). Computer-Generation of Reaction Schemes and Rate-Equations for Thermal Cracking. AIChE Journal, 34, 17-24.

Huntrods, R. S., Nighswander, J. A., Mehrotra, A. K., & Behie, L. A. (1989). Modeling of coke formation in gas quenchers of industrial ethane cracking furnaces. Chemical Engineering Research and Design, 67, 632-638.

Jakobi, D., van de Moesdijk C., Karduck, P., von Richthofen A. (2009). Tailor-made materials for high temperature applications: New strategies for radiant coil material development. In NACE. Atlanta, GA: NACE International.

Joback, K. G., & Reid, R. C. (1987). Estimation of Pure Component Properties from Group-Contributions. Chemical Engineering Communications, 57, 233-243.

Jutz, J. C. (1978). Aromatic and heteroaromatic compounds by electrocyclic ring-closure with elimination. Organic Chemistry (Vol. 73, pp. 125-230): Springer.

Kopinke, F. D., Zimmermann, G., & Ondruschka, B. (1987). Tendencies of aromatization in steam cracking of hydrocarbons. Industrial & Engineering Chemistry Research, 26, 2393-2397.

Kossiakoff, A., & Rice, F. O. (1943). Thermal Decomposition of Hydrocarbons, Resonance Stabilization and Isomerization of Free Radicals. Journal of the American Chemical Society, 65, 590-595.

Lira, I. (2013). On the Uncertainties Stemming from Use of the Colebrook-White Equation. Industrial & Engineering Chemistry Research, 52, 7550-7555.

Meade, D. B., Haran, B. S., & White, R. E. (1996). The shooting technique for the solution of two-point boundary value problems. Mapletech, 3, 85-93.

Muller, C., Michel, V., Scacchi, G., & Come, G. M. (1995). THERGAS - A computer program for the evaluation of thermochemical data of molecules and free-radicals in the gas-phase. Journal de Chimie Physique et de Physico-Chimie Biologique, 92, 1154-1178.

Nekrasov, B. (1968). Hidraulica: Editorial Pueblo y Educacion.

Nishiyama, Y., & Otsuka, N. (2005). Degradation of surface oxide scale on Fe-Ni-Cr-Si alloys upon cyclic coking and decoking procedures in a simulated ethylene pyrolysis gas environment. Corrosion, 61, 84-93.

PGI Compiler Reference Manual. (2014). The Portland Group.

PGPROF profiler guide. (2014). The Portland Group.

Pierucci, S., Brandani, P., Ranzi, E., & Sogaro, A. (1996). An industrial application of an on-line data reconciliation and optimization problem. Computers & Chemical Engineering, 20, 1539-1544.

Plehiers, P. M., Reyniers, G. C., & Froment, G. F. (1990). Simulation of the run length of an ethane cracking furnace. Industrial & Engineering Chemistry Research, 29, 636-641.

Poling, B. R., Prausnitz, J. M., & O'Connel, J. P. (2001). Properties of gases and liquids: McGraw-Hill.

Prandtl, L. (1949). Führer durch die Strömungslehre: Vieweg und Sohn.

Pyl, S. P. (2013). Sustainable Production of Light Olefins: from Fossil to Renewable Resources. Ugent.

Ranzi, E., Dente, M., Goldaniga, A., Bozzano, G., & Faravelli, T. (2001). Lumping procedures in detailed kinetic modeling of gasification, pyrolysis, partial oxidation and combustion of hydrocarbon mixtures. Progress in Energy and Combustion Science, 27, 99-139.

Ranzi, E., Dente, M., Pierucci, S., & Biardi, G. (1983). Initial product distributions from pyrolysis of normal and branched paraffins. Industrial & Engineering Chemistry Fundamentals, 22, 132-139.

Reyniers, G. C., Froment, G. F., Kopinke, F. D., & Zimmermann, G. (1994). Coke formation in the thermal cracking of hydrocarbons 4. Modeling of coke formation in naphtha cracking. Industrial & Engineering Chemistry Research, 33, 2584-2590.

Rice, F. O. (1931). The Thermal Decomposition of Organic Compounds from the Standpoint of Free Radicals. I. Saturated Hydrocarbons. Journal of the American Chemical Society, 53, 1959-1972.

Rice, F. O., & Herzfeld, K. F. (1934). The Thermal Decomposition of Organic Compounds from the Standpoint of Free Radicals. VI. The Mechanism of Some Chain Reactions. Journal of the American Chemical Society, 56, 284-289.

Ritter, E. R., & Bozzelli, J. W. (1991). THERM - Thermodynamic Property Estimation for Gas-phase Radicals and Molecules. International Journal of Chemical Kinetics, 23, 767-778.

Robert, H. B. N., & Barton, P. M. (1992). What are race conditions?: Some issues and formalizations. Letters on Programming Languages and Systems, 1, 74-88.

Sabbe, M. K., De Vleeschouwer, F., Reyniers, M. F., Waroquier, M., & Marin, G. B. (2008a). First Principles Based Group Additive Values for the Gas Phase Standard Entropy and Heat Capacity of Hydrocarbons and Hydrocarbon Radicals. Journal of Physical Chemistry A, 112, 12235-12251.

Sabbe, M. K., Reyniers, M. F., Van Speybroeck, V., Waroquier, M., & Marin, G. B. (2008b). Carbon-centered radical addition and beta-scission reactions: Modeling of activation energies and pre-exponential factors. ChemPhysChem, 9, 124-140.

Sabbe, M. K., Reyniers, M. F., Waroquier, M., & Marin, G. B. (2010a). Hydrogen Radical Additions to Unsaturated Hydrocarbons and the Reverse beta-Scission Reactions: Modeling of Activation Energies and Pre-Exponential Factors. ChemPhysChem, 11, 195-210.

Sabbe, M. K., Saeys, M., Reyniers, M. F., Marin, G. B., Van Speybroeck, V., & Waroquier, M. (2005). Group additive values for the gas phase standard enthalpy of formation of hydrocarbons and hydrocarbon radicals. Journal of Physical Chemistry A, 109, 7466-7480.

Sabbe, M. K., Van Geem, K. M., Reyniers, M.-F., & Marin, G. B. (2011). First principle-based simulation of ethane steam cracking. AIChE Journal, 57, 482-496.

Sabbe, M. K., Vandeputte, A. G., Reyniers, M. F., Waroquier, M., & Marin, G. B. (2010b). Modeling the influence of resonance stabilization on the kinetics of hydrogen abstractions. Physical Chemistry Chemical Physics, 12, 1278-1298.

Saeys, M., Reyniers, M. F., Marin, G. B., Van Speybroeck, V., & Waroquier, M. (2004). Ab initio group contribution method for activation energies for radical additions. AIChE Journal, 50, 426-444.

Saeys, M., Reyniers, M. F., Van Speybroeck, V., Waroquier, M., & Marin, G. B. (2006). Ab initio group contribution method for activation energies of hydrogen abstraction reactions. ChemPhysChem, 7, 188-199.

Schiess, P., & Dinkel, R. (1981). Über den Anteil sigmatroper 1, 5-Wanderung von Kohlenwasserstoffgruppen bei der thermolytischen Skelettisomerisierung 5,5-disubstituierter 1, 3-Cyclohexadiene. Helvetica Chimica Acta, 64, 801-812.

Schools, E. M., & Froment, G. F. (1997). Simulation of decoking of thermal cracking coils by steam/air-mixtures. AIChE Journal, 43, 118-126.

Sharma, S., & Green, W. H. (2009). Computed Rate Coefficients and Product Yields for c-C(5)H(5) + CH(3) -> Products. Journal of Physical Chemistry A, 113, 8871-8882.

Sloane, A. M., & Roberts, M. (2014). Domain-specific program profiling and its application to attribute grammars and term rewriting. Science of Computer Programming, http://dx.doi.org/10.1016/j.scico.2014.1002.1011.

Stefanidis, G. D., Van Geem, K. M., Heynderickx, G. J., & Marin, G. B. (2008). Evaluation of high-emissivity coatings in steam cracking furnaces using a non-grey gas radiation model. Chemical Engineering Journal, 137, 411-421.

Stiel, L. I., & Thodos, G. (1961). The viscosity of nonpolar gases at normal pressures. AIChE Journal, 7, 611-615.

Van Geem, K. M. (2006). Single Event Microkinetic Model for Steam Cracking of Hydrocarbons. Ugent.

Van Geem, K. M., Heynderickx, G. J., & Marin, G. B. (2004). Effect of radial temperature profiles on yields in steam cracking. AIChE Journal, 50, 173-183.

Van Geem, K. M., Reyniers, M. F., & Marin, G. B. (2005). Two severity indices for scale-up of steam cracking coils. Industrial & Engineering Chemistry Research, 44, 3402-3411.

Van Geem, K. M., Reyniers, M. F., & Marin, G. B. (2008). Challenges of modeling steam cracking of heavy feedstocks. Oil & Gas Science and Technology-Revue De L Institut Francais Du Petrole, 63, 79-94.

Vandewiele, N. (2014). Kinetic Model Construction using Chemoinformatics. Ugent.

Vandewiele, N. M., Van Geem, K. M., Reyniers, M. F., & Marin, G. B. (2012). Genesys: Kinetic model construction using chemo-informatics. Chemical Engineering Journal, 207, 526-538.

Vercauteren, C. (1991). Rigoureuze Kinetische Schema's voor de Thermische Kraking van Koolwaterstoffen.

Warth, V., Battin-Leclerc, F., Fournet, R., Glaude, P. A., Come, G. M., & Scacchi, G. (2000). Computer based generation of reaction mechanisms for gas-phase oxidation. Computers & Chemistry, 24, 541-560.

Wysiekierski, A. G., Fisher, G., & Schillmoller, C. M. (1999). Control coking for olefins plants. Hydrocarbon Processing, 78, 97-100.

Zimmermann, G., Zychlinski, W., Woerde, H. M., & van den Oosterkamp, P. (1998). Absolute rates of coke formation: A relative measure for the assessment of the chemical behavior of high-temperature steels of different sources. Industrial & Engineering Chemistry Research, 37, 4302-4305.

Zimmermann, H., & Walzl, R. (2000). Ethylene. Ullmann's Encyclopedia of Industrial Chemistry (pp. 465-529): Wiley.

Zychlinski, W., Wynns, K. A., & Ganser, B. (2002). Characterization of material samples for coking behavior of HP40 material both coated and uncoated using naphtha and ethane feedstock. Materials and Corrosion-Werkstoffe Und Korrosion, 53, 30-36.

Chapter 7: Modeling of industrial transfer line exchangers for steam cracking

7.1 Introduction

Steam cracking of ethane, propane, naphtha or gas oils is and will most probably be the main production process for olefins (e.g. ethene and propene), aromatics (e.g. benzene), methane and hydrogen (Edwin & Balchen, 2001) in the coming decades. The cracking process occurs in the radiant coils of a furnace where gas flows at low pressure and temperatures between 1023 K and 1173 K depending on the feedstock used. The highly reactive cracked gas must be quickly quenched below a critical temperature within a very short time lapse of milliseconds to provide the highest yield. The critical temperature range, below which the effluent must be cooled to avoid reactions, lies between 923 K and 973 K. The rapid cooling or quenching takes place in the transfer line exchangers (TLE) where the high heat content is used to produce high pressure steam. Early on, the standard practice for cooling the pyrolysis furnace effluent gas was by direct oil or water injection and no heat was recovered. Today such methods are unacceptable. In 1960 the first double pipe TLE's were developed to recover the enormous heat available from the cracking process by producing high-pressure steam. For naphtha cracking, up to 45 % of the fired input duty can be recovered in the form of high pressure steam while 30 % is consumed by the reaction and 19 % of the energy is still present in the mixture after cooling inside the TLE. The

remaining 7 % are stack losses (G. Schmidt, 2010). The gas outlet temperatures of a TLE typically range from 600 to 700 K depending on the type of feed.

One of the main issues in the steam cracking of hydrocarbons for olefin production is coke formation. Coke deposits on the inside of the reactor affect the operation of the reactor but also the TLE. These coke deposits reduce the efficiency of heat transfer inside the TLE and thus raise the gas outlet temperature of TLE and slows down the cooling process. For naphtha cracking, the TLE outlet temperature typically increases 20-50 K during the first 2 days and the increase then levels off to a few kelvins per day (Dhuyvetter et al., 2001).

Three principal mechanisms for coke mechanism have been proposed based on experimental data: catalytic coke formation, heterogeneous non-catalytic coke formation and homogeneous non catalytic coke formation. Catalytic coke formation mainly occurs in the initial stages of a cracking run when the hydrocarbons are brought in contact with a bare metal surface. This type of coke formation is closely associated with the metal surface and the wall material plays an important role. During this stage typically filamentous coke or "whiskers" are produced. Once the metal surface is covered with an initial coke layer the heterogeneous non-catalytic mechanism becomes more important. In this mechanism coke is formed via free radical reactions between the already existing coke layer on surface and coke precursors from the gas phase. This type of coke is characterized by the formation of a dense coke matrix. The heterogeneous non-catalytic coke formation is regarded as the main contributor of the three coking routes in the reactor since it practically operates over most of the cracking run.

At very high temperatures and with heavier feedstocks containing more aromatics another type of coke formation can be important as the effluent is cooled down. This homogeneous non-catalytic

type of coke is the result from gas phase reactions with polyaromatics which produces tar and liquid droplets. These droplets can impinge, collide, and adhere to the wall, where they are incorporated into the coke matrix (Cai et al., 2002; Towfighi et al., 2002).

Coke deposited in TLEs reduces both heat transfer and the amount of steam generated to such an extent that the equipment must be cleaned. In addition to the previous three mechanisms other mechanisms have been proposed for TLE coking (Zimmermann & Walzl, 2000):

- Spalled coke produced in the radiant coil is carried into the TLE inlet cone where it blocks some of the tubes on the TLE entry tube sheet. Such fouling is most relevant for ethane cracking.

- Poor flow distribution in the entry cone and at the tube sheet causes eddies and back mixing. Long residence time in these dead zones accompanied by relatively high temperatures can increase tar and coke production.

- Heavy polynuclear aromatics and other high-boiling compounds in the cracked gas physically condense on the cool TLE tube walls. This is particularly true for gas oil and heavy naphtha feedstocks. The condensed high-boiling substances are gradually converted to coke like materials. This mechanism is supported by the fact that fouling is fastest at the start of the run (SOR). Typically the TLE outlet temperatures increase by 50–100 K during the first day or two in gas oil cracking. Deposits during this period reduce the heat-transfer rate, and inner surface temperature at a given location in a tube becomes higher than the original clean wall temperature. The fouling rate drops as the surface temperature increases and with time process gas temperature slowly increases. The main difference with homogeneous non-catalytic coke formation is that in case of

homogeneous non-catalytic coke formation the liquid droplets are produced in the gas phase instead of condensing directly on the cold wall.

Most of the modeling efforts in the field of steam cracking have been focused on the radiant coil because typically the reactor section determines the run length of the furnace and not the TLE (Dente et al., 1979; van Goethem et al., 2001; Van Geem et al., 2004; Van Geem et al., 2008; Shokrollahi Yancheshmeh et al., 2013). Modeling of transfer line exchangers is rarely discussed in literature (Herrmann & Burghardt, 1994; Knight & Corry, 2003; Manafzadeh et al., 2003; Jin et al., 2013) and, if done, important simplification assumptions are made like in the work of Jin et al. (2013) and Manafzadeh et al. (2003) but the effect of these simplifications is not addressed. Assumptions include: neglecting of any reactions apart from coke formation and neglecting the outer tube convective thermal resistance. In addition these models only model the gas phase side of the TLE and no information of the water/steam side of the TLE is obtained. In particular no information about the amount of heat that is recovered in the form of high pressure steam is obtained. One of the reasons is that most industrial TLE's are operated based on a thermosiphon principle, which is obviously more difficult to model than when a fixed flow of water is sent through the heat exchanger . Hence, no information regarding the amount of water circulation inside the thermosiphon is obtained because the water side is not modeled. The latter also implies that these models cannot assess for example the effect of heat losses towards the environment inside the TLE. To minimize these heat losses to the environment the TLE is considered insulated (Schoepe & Stueckrath, 2008) and the effect of this insulation can thus not be captured by these models.

It is clear from the preceding discussion that modeling of a TLE can be significantly improved. and therefore an extensive model for the TLE has been developed. The model describes both the phenomena occurring on the process gas side of the TLE and on the water/steam side. In addition the model takes into account the geometry of the thermosiphon, which allows calculating the water circulation rate in the thermosiphon as well as estimating the steam production. Additionally, the model includes a coke formation model that includes contribution of heterogeneous non-catalytic coke formation and condensation coke formation, and accounts for the effect of the total thermal resistance of TLE . The model is used to simulate two industrial TLE's; one TLE part of a millisecond furnace fed with propane, and a second case in which the TLE of a naphtha furnace is modeled. Both simulation cases will be used to test the assumptions made in literature as well as to study the effect of coke formation inside the TLE. Also the effect of heat losses towards the environment both in the TLE and in the adiabatic section connecting the TLE to the radiant coil will be investigated.

7.2 Mathematical model

7.2.1 Model of the process gas side

At present mostly double piped TLE's are produced. In this TLE the cracked gas flows through the inner tube while the water/steam mixture flows throughout the outer tube, e.g. Figure 7.1. The conditions inside the TLE are non-isothermal, non-adiabatic and non-isobaric. As a consequence the TLE model needs to include continuity, energy and momentum equations. Due to the high velocities and thus high Reynolds numbers (10^5-10^6) of the cracked gas inside the inner tube it can be assumed that no radial gradients are present inside the inner tube (Gal & Lakatos, 2008),

except for the temperature localized in the film close to the wall in which all resistance to heat

transfer is located (Froment et al., 2011). Thus for the tubular TLE a one-dimensional plug flow

reactor model in which no thermal gradients are assumed can be used. The resulting equations

are:

$$\frac{dF_j}{dz} = \left(\sum_{k=1}^{n_r} v_{kj} r_k \right) \Omega \tag{7.1}$$

$$\sum_{j=1}^{n_s} F_j c_{p,j} \frac{dT_g}{dz} = \omega q + \Omega \sum_{k=1}^{n_r} r_k.(-\Delta H_k) \tag{7.2}$$

$$\frac{dp_{t,g}}{dz} = -\left(\frac{2f}{d_i - 2d_c} + \frac{\zeta}{\pi r_b} \right) \rho_g v_g^2 - \rho_g v_g \frac{dv_g}{dz} \tag{7.3}$$

$$F_j(z=0) = F_{j,0}, T_g(z=0) = T_{g,0}, p_{t,g}(z=0) = p_{g,0} \tag{7.4}$$

These equations have already been described in Section 6.3. The most important characteristics

of the process gas side of the TLE are depicted in Figure 7.1. The heat flux q shown in Figure 7.1

corresponds in this case to the heat that is removed due to the water/steam mixture flowing

through the outside tube. For what follows q is defined based on the surface area at the interface

between cokes and gas in the inner tube. This flux can be calculated using Equation 7.5:

$$q = U.\left(T_{wa} - T_g \right) \tag{7.5}$$

The overall heat transfer coefficient U is given by:

$$\frac{1}{U} = \frac{1}{\alpha_i} + \frac{d_w}{\lambda_w}.\frac{d_i - 2d_c}{M_{lm}(d_i, d_i + 2d_w)} + \frac{d_c}{\lambda_c}.\frac{d_i - 2d_c}{M_{lm}(d_i - 2d_c, d_i)} + \frac{1}{\alpha_o}.\frac{d_i - 2d_c}{d_i + 2.d_w} \tag{7.6}$$

With $M_{lm}(x, y)$ the logarithmic mean of x and y. Both Equation 7.5 and Equation 7.6 contain

variables of the outer tube (T_{wa} and α_o). The calculation of these variables will be discussed in

Section 7.2.2. Equation 7.6 also takes into account any coke that can be formed on the inside of the tube. However, it does not take into account any fouling that might occur in the outside tube. In this work the thermal conductivity of the metal (λ_w) is calculated using Huntrods et al. (1989) for standard stainless steel:

$$\lambda_w = 24.4 + 0.0041.(T_w - 977.6) \tag{7.7}$$
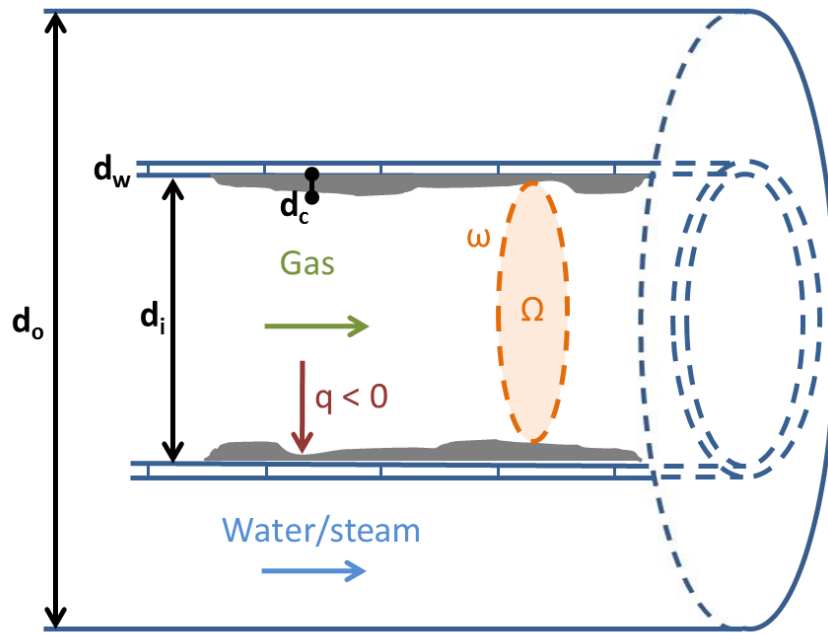
Figure 7.1: Geometry of a double pipe transfer line exchanger

7.2.2 **Modeling of the water/steam side**

The laws of the conservation of mass, energy and momentum for the water/steam side in the outer tube can be simplified because of the lack of reaction. Instead water will vaporize and form steam. Taking this consideration into account the total continuity equation can be written as:

$$\frac{d(F_{wa,l})}{dz} = -\frac{d(F_{wa,g})}{dz} \tag{7.8}$$

with $F_{wa,l}$ the molar flow rate of liquid water and $F_{wa,g}$ the molar flow rate of steam. While for

the same reactor the energy balance can be written as

$$\left(F_{wa,l}c_{p,wa,l} + F_{wa,g}c_{p,wa,g}\right)\frac{dT_{wa}}{dz} = \omega q + (-\Delta H_{vap}).\frac{d(F_{wa,l})}{dz} \tag{7.9}$$

with ΔH_{vap} the vaporization enthalpy of water at the temperature T_{wa}, $c_{p,wa,l}$ and $c_{p,wa,g}$ the heat

capacity of liquid water and steam respectively. Equation 7.9 can even be further simplified.

When the mixture is boiling $\frac{dT_{wa}}{dz}$ becomes negligible and when no boiling occurs $\frac{d(F_{wa,l})}{dz}$ is equal

to 0.

In the momentum equation the pressure drop due to gravitational changes is also no longer

negligible since the TLE tubes are in vertical alignment and the gravitational force on liquid

water is much higher than on the process gas. An additional gravitational term thus needs to be

added:

$$\frac{dp_{t,wa}}{dz} = -\frac{2f}{d_h}\rho_{wa}v_{wa}^2 - \rho_{wa}v_{wa}\frac{dv_{wa}}{dz} - \rho_{wa}g\frac{dh}{dz} \tag{7.10}$$

Compared to Equation 7.3 an additional term related to the gravitational pressure drop is present

in Equation 7.10. For a vertically oriented tube the term $\frac{dh}{dz}$ is equal to 1. In the Colebrook

equation (Equation 6.32), used to calculate the friction coefficient, the hydraulic diameter d_h is

used:

$$d_h = d_o - (d_i + 2.d_w) \tag{7.12}$$

The initial conditions corresponding with Equations 7.8-7.10 are given by:

$$F_{wa,l}(z = 0) = F_{wa,l,0} \qquad\qquad F_{wa,g}(z = 0) = F_{wa,g,0}$$

$$\tag{7.13}$$

$$T_{wa}(z = 0) = T_{wa,0} \qquad\qquad p_{t,wa}(z = 0) = p_{wa,0}$$

All thermodynamic and transport properties related to the water and steam are calculated using the correlations proposed by Schmidt and Grigull (1979). Equation 7.5 connects the differential equations of the inner tube with those of the outer tube. If the heat flux q is known a priori the inner tube equations can be integrated completely separate from the outer tube equations.

7.2.3 **Kinetic and coking model**

As mentioned in Section 7.1 most TLE studies exclude reactions in the inner tube of the TLE due to the low temperatures inside the TLE. However in some cases unwanted reactions are unavoidable near the entrance. In these extreme cases the composition entering the TLE can thus change significantly. Keeping this in mind the kinetic model CRACKSIM (Van Geem et al., 2008) was used inside the TLE to be able to simulate these compositional changes. As mentioned in Section 6.6 the kinetic model CRACKSIM is able to accurately predict the yields of feedstocks ranging from ethane to gas oils over a broad range of experimental conditions and should thus also be usable inside the TLE.

Coke formation under TLE conditions is not completely understood yet. What is known is that coking consists of 2 important contributions:

1. Heterogeneous non-catalytic coke formation at the beginning of the TLE
2. Physical condensation cokes near the end of the TLE

Therefore a new coking model was constructed that accounts for both contributions. For the heterogeneous non-catalytic contribution the coking model by Plehiers et al. (1990) was used while for the condensation mechanisms the parameters were adjusted to match experimental data obtained on the pilot plant. Industrial data were used for the validation of the developed model.

The pilot plant unit was thoroughly described by Dhuyvetter et al. (2001) and by Van Geem et al. (2010). The coking model can thus be described by the following equation:

$$r_c = r_c^{thermal} + r_c^{condensation} \tag{7.14}$$

For contribution of the condensation cokes a model was proposed similar to the one developed by Zhang and Watkinson (2005). The formation of condensation cokes is assumed to be equal to the radial mass transfer of a coking precursor from the bulk to the wall:

$$r_c^{condensation} = k_m \cdot \left(\frac{p_{B,g}}{R.T_g} - \frac{p_{B,w}^*}{R.T_w} \right) \tag{7.15}$$

In Equation 7.15 k_m is the mass transfer coefficient, $p_{B,g}$ is the partial pressure of a heavy component B which can condense on the wall and $p_{B,w}^*$ is the vapor pressure of component B at the internal wall temperature. For a fully developed turbulent flow the mass transfer coefficient can be calculated by (Zhang & Watkinson, 2005):

$$k_m = \frac{0.023 Re^{0.8} Sc^{0.33} D_{Bm}}{d_i} \tag{7.16}$$

with Sc the Schmidt number and D_{Bm} the diffusion coefficient of component B in the mixture M. The binary diffusion coefficient and the Schmidt number are geometry independent and this thus leads to the following equation for the mass transfer coefficient:

$$k_m = \frac{A.Re^{0.8}}{d_i} \tag{7.17}$$

The Reynolds number dependence needs to be accounted for in this equation since both pilot scale and industrial scale data are used. The vapor pressure of component B can be calculated from the Clausius-Clayperon equation:

$$ln\left(\frac{p_{B,w}^*}{p_{atm}}\right) = -\frac{\Delta H_{vap,B}}{R} \cdot \left(\frac{1}{T_w} - \frac{1}{T_{boil,B}}\right) \qquad \textbf{(7.18)}$$

where p_{atm} is the absolute atmospheric pressure, $\Delta H_{vap,B}$ is the vaporization enthalpy of condensable component B and $T_{boil,B}$ is the boiling point of the condensable component B. In this equation both $\Delta H_{vap,B}$ and $T_{boil,B}$ are assumed to be adjustable parameters. Based on the work of Kopinke et al. (1993), who concluded that the relative rate constants for TLE fouling for triaromatics were 10 times higher than non-aromatic, mono-aromatic and diaromatics compounds, triaromatics and heavier compounds were chosen to represent component B. The adjustable parameters were fitted to experimental pilot plant data for different gas condensates and different reactor (COT = 1073-1113K, Dilution = 0.3 − 1.0) and TLE (TLE$_{out}$ =625-725K) operating conditions. This resulted into values of 83 kJ/mol for $\Delta H_{vap,B}$, 1.66 10^{-5} m^2.s^{-1} for A and 932 K for the boiling point of B. For comparison pyrene has a boiling point of 676 K and a vaporization enthalpy of 63 kJ/mol while coronene has a boiling point of 800 K and a vaporization enthalpy of 77 kJ/mol.

Figure 7.2 shows the parity plot after fitting. It is clear that the coking model does not capture all the trends present in the experimental data but the calculated values are in the right order of magnitude of the experimental data.
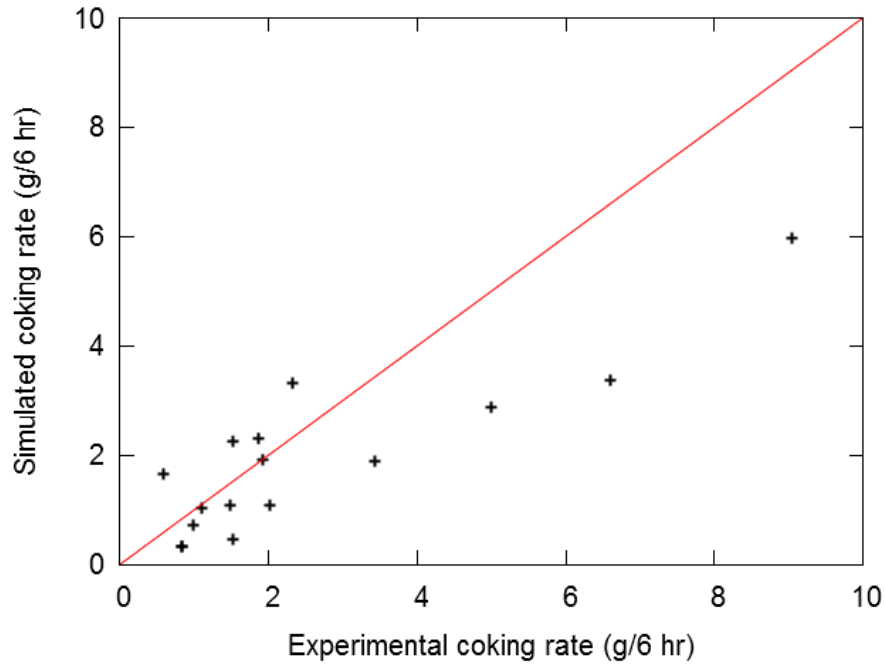
Figure 7.2: Simulated versus experimental measured coking rates on a pilot plant scale for gas condensates

7.2.4 Initialization procedure and convergence algorithm

As mentioned in Section 7.2.2 Equation 7.5 connects the differential equations of the inner tube with the differential equations of the outer tube. If the heat flux profile, $q(z)$, is known throughout the tube the differential equations of the inner and the outer tube could be integrated separately if the appropriate initial conditions are known.

In this procedure the temperature and pressure profiles of the cracking gas and the convection coefficients (α_i, and α_o) are calculated based on an initial guess of the heat flux profile by solving the two sets of differential equations separately. Equation 7.5 and 7.6 is then used to update the heat flux profile, if needed. To improve convergence a dampened method is used rather than using Equation 7.5 and 7.6 directly.

$$q_{update} = x \cdot q_{new} + (1-x) \cdot q_{old} \tag{7.19}$$

with x being the dampening factor, q_{new} being the heat flux profile calculated by Equation 7.5 and 7.6 and q_{old} being the initial guess used in the current iteration step. A dampening factor of 0.5 was found to be a good value to assure convergence. Obviously a good initial guess of the heat flux profile is also needed to assure convergence. This initial guess can be obtained by neglecting the outer tube convective thermal resistance, $\frac{1}{\alpha o}$, or assuming that the convective heat transfer in the outside tube,α_o, is infinite. In this case the external wall temperature of the inner tube is equal to the boiling point of water at the inlet conditions of water. With this assumption the equations of the inner tube can be easily integrated to obtain an initial guess of the heat flux profile to start the iterative procedure. The iteration is stopped when the squared difference between the old and the new heat flux profile is below a certain threshold value, e.g. when the sum of squares is lower than $20 \text{ kJ}^2 \cdot \text{m}^{-4}$.

Note that in industry the mass flow rate of water is often not known since the TLE is a thermosiphon, see Figure 7.3. In a thermosiphon the water flows through the TLE using the difference in density upstream and downstream of the TLE due to the vaporization of water. The mass flow rate is thus a result of balancing out Equation 7.20.

$$p_B - p_A = (p_B - p_C) + (p_C - p_A) \tag{7.20}$$

With $p_b - p_c$ derived from Equation 7.10, $p_B - p_A$ from Equation 7.21 and $p_C - p_A$ from Equation 7.22.
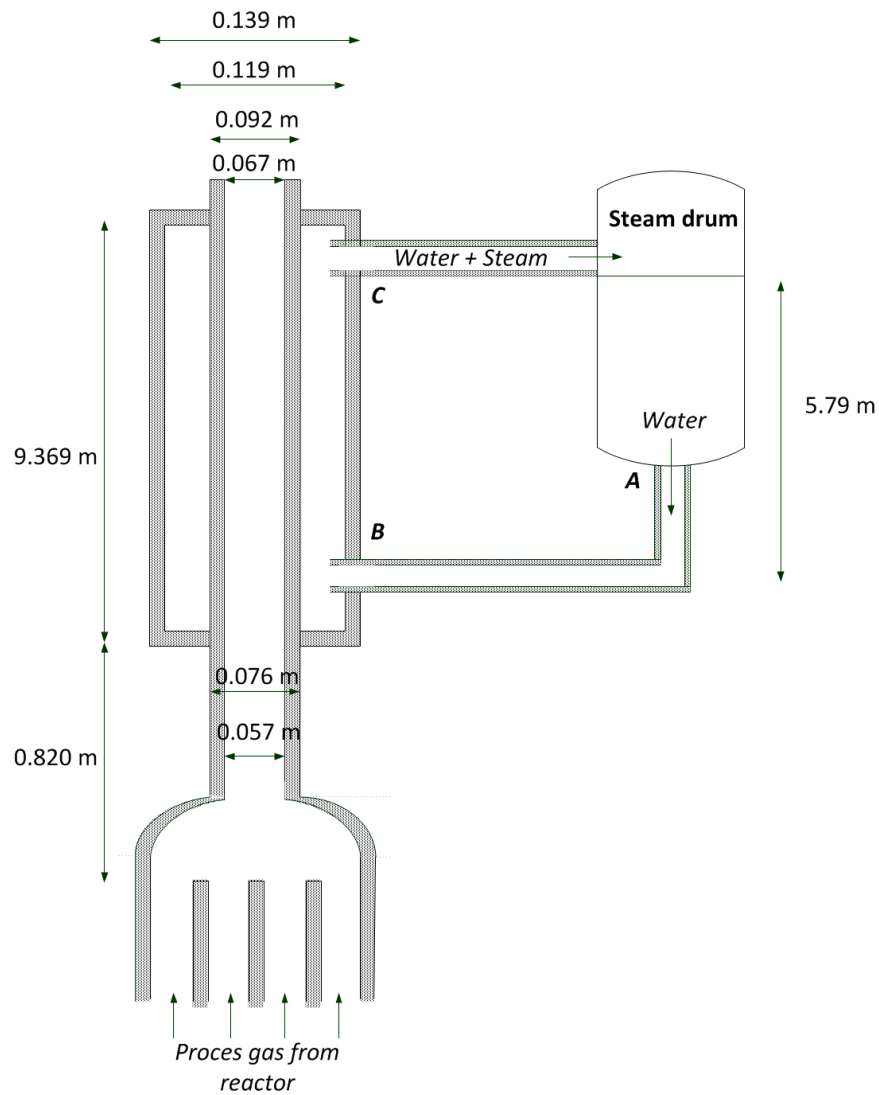
Figure 7.3: Basic schematic of a thermosiphon type TLE

$$p_B - p_A = g \cdot \left(\rho_{w,A} \cdot z_A - \rho_{w,B} \cdot z_B \right) - \Delta p_{AB} \tag{7.21}$$

$$p_C - p_A = g \cdot \left(\rho_{w,C} \cdot z_C - \rho_{w,D} \cdot z_A \right) - \Delta p_{CA} \tag{7.22}$$

With Δp_{AB} and Δp_{CA} the pressure drop due to friction between A and B and C and A respectively.

In case of Equation 7.21 and 7.22 it is assumed that the velocity from A to B and from C to A

remains constant and thus that the mass flow rate and steam quality (mass fraction of steam in the mixture) remain constant.

However if the mass flow rate is known the previously described iterative procedure can be used to obtain the heat flux profile at a given mass flow rate of water. The heat flux profile can be used together with Equation 7.20 to 7.22 to calculate a new estimate for the mass flow rate of water. To calculate this updated estimate for the mass flow rate of water the heat flux profile is kept fixed. At a given steam quality the mass flow rate of water can be calculated using the heat flux profile and Equations 7.10, 7.21 and 7.22 can be used to check if Equation 7.20 holds. If not the steam quality can be updated:

$$Dp = (p_B - p_A) - (p_B - p_C) - (p_C - p_A) \tag{7.23}$$

$$x_{steam,new} = x_{steam,old} \cdot \left(1 - \frac{Dp}{10^6}\right) \tag{7.24}$$

The iterative procedure is stopped when D_p becomes lower than a certain threshold value. In this work a threshold value of 10 Pa is used. Figure 7.4 shows an overview of the final iterative procedure used to integrate the set of differential equations inside the transfer line exchanger.
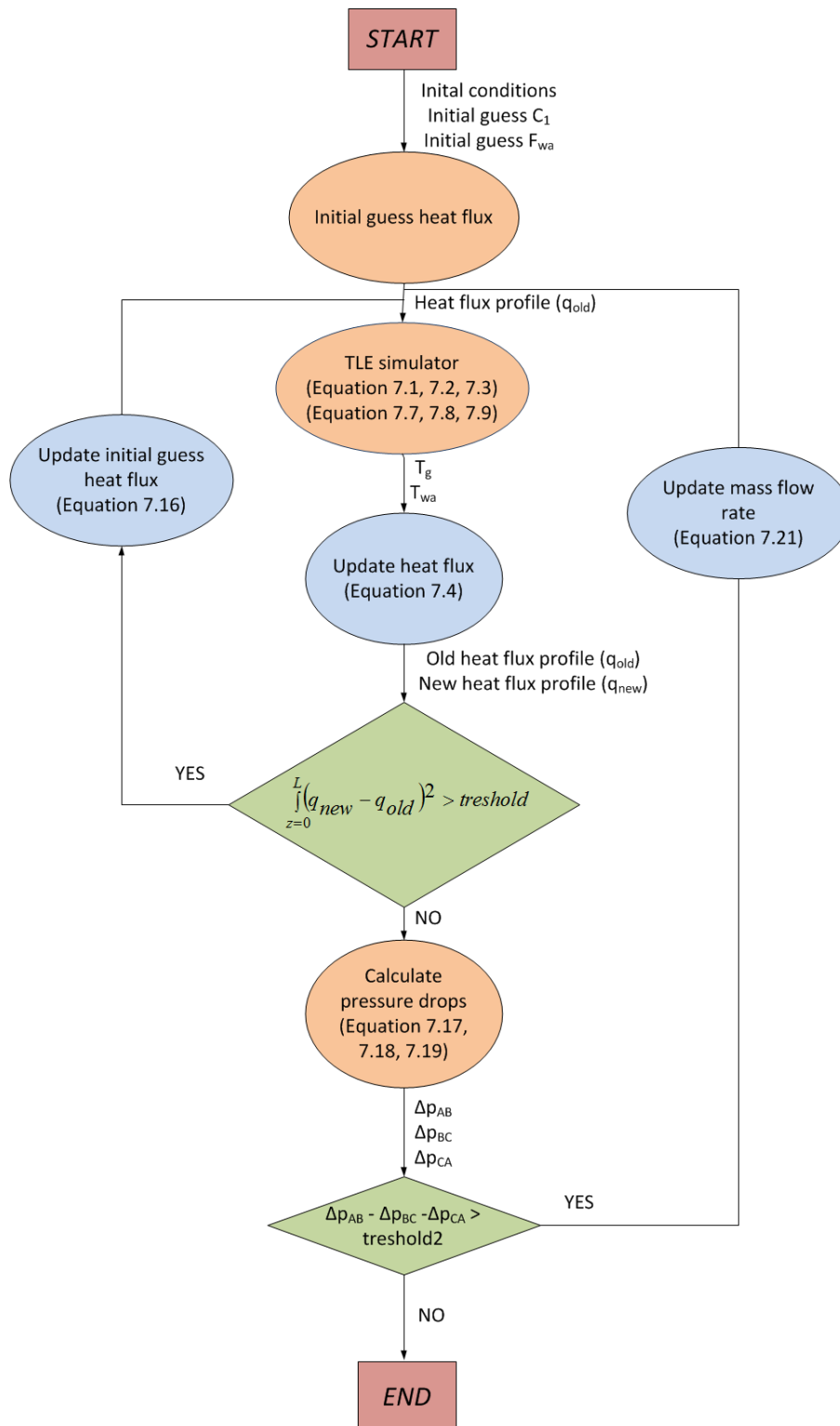
Figure 7.4: Iteration procedure for a thermosiphon based TLE

7.2.5 Simulation cases

Two industrial TLE's were simulated: a cracking furnace fed by naphtha and a cracking furnace fed with propane. The first case is the simulation of a millisecond furnace for propane cracking for which industrial data is available. The furnace consists of 160 millisecond reactors mounted in a single furnace. The length, internal diameter and wall thickness of these reactors is 10.5 m, 35 10^{-3} m and 6.75 10^{-3} m respectively. The operating conditions of the reactor and feedstock composition are given in Table 7.1.

Table 7.1: Operating conditions of the reactor of the millisecond furnace

Process variables	Value
Hydrocarbon mass flow rate (kg/s)	0.033
Dilution (-)	0.326
Coil inlet temperature (K)	903
Coil inlet pressure (Pa)	235.10^3
Coil outlet temperature (K)	1168
Coil outlet pressure (Pa)	206.10^3
Component	**Mass fraction (wt%)**
Propane	95.27
Ethane	1.05
i-butene	0.33
1-butene	0.27
2-butene	0.80
i-butane	1.93
n-butane	0.45
C5+	Rest

At the end of the furnace 4 millisecond reactors join and are connected to the primary TLE. Since the connecting volume is completely insulated it is assumed that it operates in an adiabatic way. The geometry of the TLE is shown in Figure 7.3 and consists of a double pipe heat exchanger cooled with water. The TLE is used to produce high pressure steam at a pressure of 11.10^6 Pa. The TLE is supplied with pressurized water by means of a thermosiphon located near the TLE's

and also depicted on Figure 7.3. The primary TLE cools the reactor effluent to a temperature around 873 K. After the primary TLE a secondary TLE, namely a tube and shell heat exchanger is used to further cool down the mixture. In the simulation only the primary TLE is simulated. It is assumed that the flow rate through the furnace is equally divided among all 160 reactors thus only 1 reactor and 1 TLE need to be simulated and the results can be extrapolated to the entire furnace by means of a multiplication. To eliminate the need of a full furnace simulation for the heat flux profile in the reactor the shooting method was used.

The second case is the simulation of a TLE of an industrial naphtha cracker. Since no data is known about the furnace and reactor geometry nor the exact composition of the feedstock is known a typical naphtha effluent is used to simulate the TLE. In addition no information about the thermosiphon system is available buts the design steam quality (10 wt%) at the outlet of the TLE was used to obtain the water flow rate of the TLE rather than calculating the full thermosiphon system. The geometry and operating conditions of this TLE are given in Table 7.2.

Table 7.2: TLE geometry and operating conditions for the TLE of the naphtha furnace

Geometry:	
Inner diameter gas tube (m)	0.08
Thickness gas tube (m)	0.008
Inner diameter outer tube (m)	0.133
Thickness outer tube (m)	0.0125
TLE length (m)	24
Operating conditions (single tube):	
Hydrocarbon mass flow rate (kg.s^{-1})	0.19
Dilution (-)	0.25
TLE inlet temperature (K)	1073
TLE inlet pressure (Pa)	191.10^3
Outlet steam quality (%)	10
TLE water pressure (Pa)	11.10^6

Both cases will be used to validate some of the commonly made assumptions to model a TLE as well as to investigate the effect of the main process variables on yields and steam production. Assumptions that will be looked at in particular are neglecting the reactions inside the TLE or neglecting the convective thermal resistance in the outer tube (Manafzadeh et al., 2003; Zhang & Watkinson, 2005; Jin et al., 2013). The effect of coke formation on heat transfer will also be studied. Finally the formation of cokes during the complete furnace run length will be studied.

7.3 Results and discussion

7.3.1 Case 1: TLE connected to a millisecond furnace

The simulation of the millisecond furnace requires that a full thermosiphon simulation is carried out. Table 7.3 shows the results of the simulations and the industrially measured values. A reasonable agreement is obtained between the simulated yields and the industrially measured yields at the outlet of the quench section. It is clear from Table 7.3 that significant reactions still occur after the gas leaves the coil because in the beginning of the TLE the temperature is well above 923 K. Most of the reactions seem to occur inside the adiabatic volume but even in the first part of the TLE some reactions still take place. When the temperature drops below 873 K all reaction rates seem sufficiently small not to alter the composition of the process gas anymore . It is clear that the ethene and propene yield are not accurately simulated if no reactions would be taken into account inside the TLE. Table 7.3 further shows that the TLE gas outlet temperature, the water temperature and the TLE outlet pressure agree well with the industrially measured values. The steam production seems to be overestimated but is difficult to compare this value directly to the reported industrial value because the latter only considers total production of

superheated high pressure steam. Note that it is not necessarily the case that all the steam produced in the TLE is used to create superheated steam. Globally the simulated model agrees well with the industrial data that is available.

Table 7.3: Simulated and industrial results for the millisecond furnace

	Reactor	Adiabatic volume	Quench	Industry[1]	Quench (without reactions)	Quench (coked)
Yields (wt%)						
H2	1.48	1.52	1.54	1.58	1.52	1.54
CH4	18.61	19.46	20.10	19.31	19.46	20.07
C2H2	0.32	0.33	0.28	0.76	0.33	0.28
C2H4	32.26	33.65	34.27	35.15	33.65	34.23
C2H6	3.42	3.51	3.63	2.85	3.51	3.63
C3H4(MA)	0.81	0.87	0.83	0.71[2]	0.87	0.83
C3H4(PD)	0.19	0.21	0.16		0.21	0.16
C3H6	19.59	19.13	18.76	16.98	19.13	18.77
C3H8	17.52	15.06	13.69	15.67	15.06	13.75
1;3-C4H6	1.27	1.39	1.40	1.88	1.39	1.40
1C4H8	0.64	0.61	0.55	1.24[3]	0.61	0.56
2C4H8	0.22	0.23	0.23		0.23	0.23
iC4H8	0.46	0.44	0.43	0.22	0.44	0.43
iC4H10	0.21	0.16	0.14	0.10	0.16	0.14
nC4H10	0.06	0.05	0.05	0.13	0.05	0.05
Other Properties						
Outlet temperature(K)	1168	1158	707	708	707	780
Outlet pressure (Pa)	205.10^3	205.10^3	191.10^3	177.10^3	191.10^3	177.10^3
Steam production (kg/s)	-	-	11.71	7.83[4]	11.74	9.92
Water temperature (K)	-	-	592	591	592	592

1)Measured downstream of the Quench
2)Lump of MA and PD
3)Lump of 1C4H8 and 2C4H8
4)Based on total high pressure steam production in plant

In a next step the model is used to validate some of the typical assumptions made in literature. A first assumption is that the outer tube convective thermal resistance is negligible as compared to the other contributions towards the overall heat transfer resistance or that the external wall temperature of the inner tube is equal to the boiling point of water at the given pressure. Figure

7.5 shows the contributions towards the thermal resistance inside the TLE. The three contributions (inner tube convective thermal resistance, inner tube conductive thermal resistance and outer tube convective thermal resistance) are shown as well as the total thermal resistance as defined by Equation 7.6. The calculations were based on a clean tube so d_c was set equal to 0. It shows that the major contribution is indeed the inner tube convective thermal resistance which contributes between 80 and 90% towards the total thermal resistance, while the outer tube convective thermal resistance is of the same order of magnitude as the inner tube conductive thermal resistance and contributes about 5 to 10% towards the total thermal resistance. The outer tube convective thermal resistance is not completely negligible compared to the total thermal resistance however its contribution becomes smaller towards the end of the TLE. Neglecting the outer tube convective thermal resistance will change the temperatures simulated inside the TLE. The outer wall temperature will drop by about 20 to 30 K increasing the cooling performance of the TLE. Also the TLE outlet temperature drops from 707 K to 701 K. In addition there is an influence on the internal wall temperature of the inner tube which affects the formation of cokes inside the TLE. This difference is around 20 K at the inlet of the TLE but drops to 5 K at the outlet of the TLE.
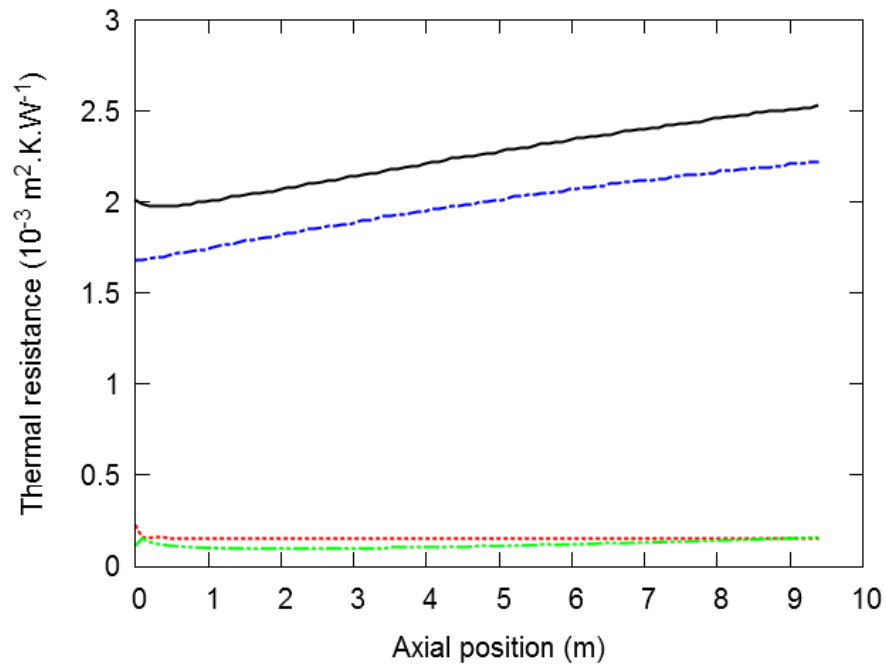
Figure 7.5: Thermal resistance inside a TLE for simulation case 1: ▬ Total thermal resistance; ▬▪▬ Inner tube convective thermal resistance; ▪▪▪▪ Inner tube conductive thermal resistance; ▬▪▪ Outer tube convective thermal resistance

A second assumption often made is neglecting reactions inside the TLE. It was already clear from the industrial simulation (see Table 7.3) that neglecting reactions inside the adiabatic volume has a significant effect on the predicted yields but that in this industrial case reaction even still occurs inside the quench zone. To further study effect the reactions inside the TLE were disabled. The results are shown in the last column of Table 7.3. It is clear that besides the yields there is no significant influence on the temperatures, pressures and steam production inside the TLE. The temperature decrease caused by the endothermicity of reactions is negligible compared to the rapid cooling caused by the water/steam mixture. In case of the millisecond furnace it seems to be important to take into account reactions happening inside the quench otherwise errors on the yield prediction will be made. For example the conversion of propane still increases by 1% in this

section. Reactions inside the adiabatic volume cannot be neglected either and have to be taken into account.

Note that it is not entirely correct to consider the adiabatic volume as completely adiabatic. Although it is heavily insulated heat losses can occur. To check the influence of these non-adiabatic losses a fixed heat flux was imposed for the adiabatic volume. If no insulation would be present around the outer tube the convective heat transfer due to the ambient air would be around $5.10^3 \text{ J.m}^{-2}.\text{s}^{-1}$ based on a convective heat transfer coefficient of ambient air of $20 \text{ W.m}^{-2}.\text{K}^{-1}$ (Thirumaleshwar, 2006). The fixed heat flux was thus varied between $-5.10^3 \text{ J.m}^{-2}.\text{s}^{-1}$ and $0 \text{ J.m}^{-2}.\text{s}^{-1}$ and the effect on yields and TLE inlet and outlet temperature was studied.

Figure 7.6 shows that even in the wide range of heat fluxes no significant effect is visible on the yields or the temperatures. Going from $-5.10^3 \text{ J.m}^{-2}.\text{s}^{-1}$ and $0 \text{ J.m}^{-2}.\text{s}^{-1}$ changes the yields of ethene and propene by less than 1% of their total value. The same is true for both temperatures. The adiabatic volume can thus safely be considered to be adiabatic.
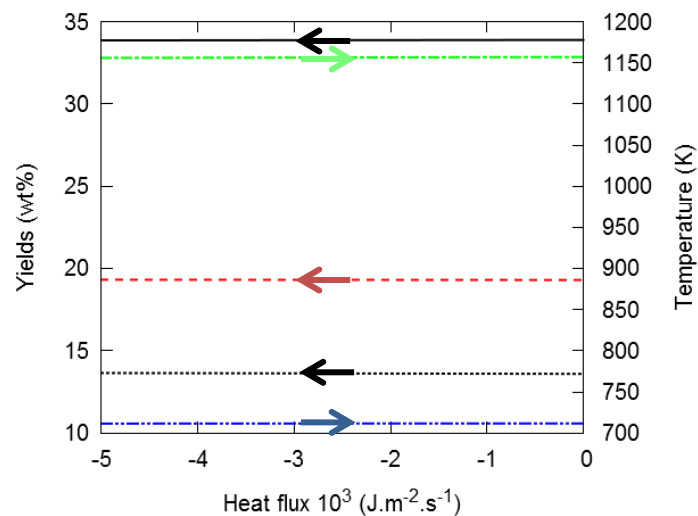
Figure 7.6: Influence of non-adiabatic heat changes in the adiabatic volume. Left axis: ▬Ethene yield; ▬ ▬ Propene yield; ▪▪▪Propane yield. Right axis: ▬ ▪ Quench inlet temperature; ▬▪▪Quench outlet temperature

In a similar way heat losses can occur in the outer tube of the TLE where the heat losses towards the environment are now being neglected. To study their effect a similar approach has been followed as for the adiabatic volume. Again a fixed heat flux varying from -5.10^3 J.m^{-2}.s^{-1} and 0 J.m^{-2}.s^{-1} is imposed. In this case no influence is observed on either the yields or the temperatures inside the TLE. However, as can be seen in Figure 7.7, the steam quality changes inside the TLE. The mass flow rate of water is more or less constant and the total steam production increases when more heat is available resulting in a higher steam quality. These changes in steam quality will have their effect on the outer tube convection coefficient but since the outer tube convective thermal resistance is almost negligible these minor changes to the convection coefficient will have no influence on the temperature profile inside the TLE and thus no influence on the yields at the outlet of the TLE. If an accurate estimate of the steam quality is not required these heat losses can be safely neglected.
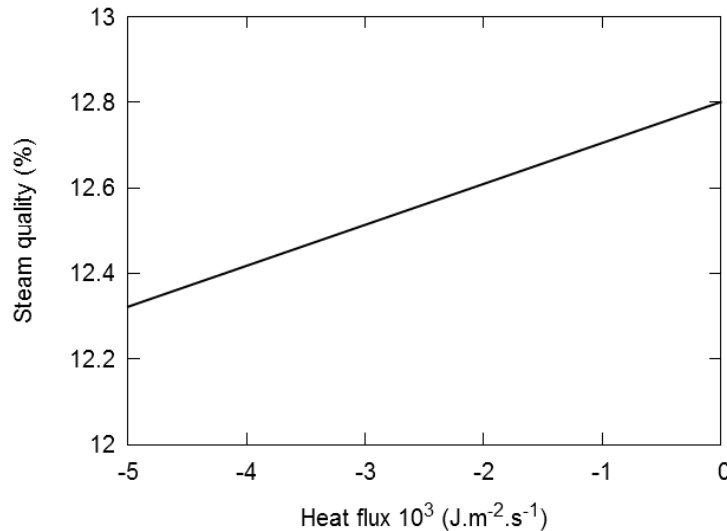
Figure 7.7: Steam quality as a function of the heat flux to the environment in the TLE

Since a TLE is operated based on a thermosiphon principle balancing Equation 7.20 is important to obtain the mass flow rate of water through the TLE. Three contributions are present in this equation: a static pressure drop, a momentum pressure drop and a frictional pressure drop. The first two contributions are easily calculated, however, the third contribution is calculated based on the Colebrook equation (Equation 6.32). Since this equation can contain variables which are not always precisely known (e.g. roughness) the effect of changing the friction is also studied. For example during the lifetime of a TLE it is also possible that the roughness changes, and these changes can be affected by fouling. To study the effect of changing friction the friction factor is multiplied with a factor which is varied from 0.8 up to 1.2. No changes were observed in the yields after the quench as well as for the temperature inside the TLE. Increasing the friction however increases the pressure drop and thus decreases the mass flow rate of water circulating inside the TLE. Since the heat flux profile remains unchanged the steam quality increases when the friction increases but the total steam production remains the same. The mass flow rate of water drops from 2.31 kg/s to 2.23 kg/s when the friction goes from 80% of its value to 120 % of its value. In the same range the steam quality rises from 12.6% to 13.0%.
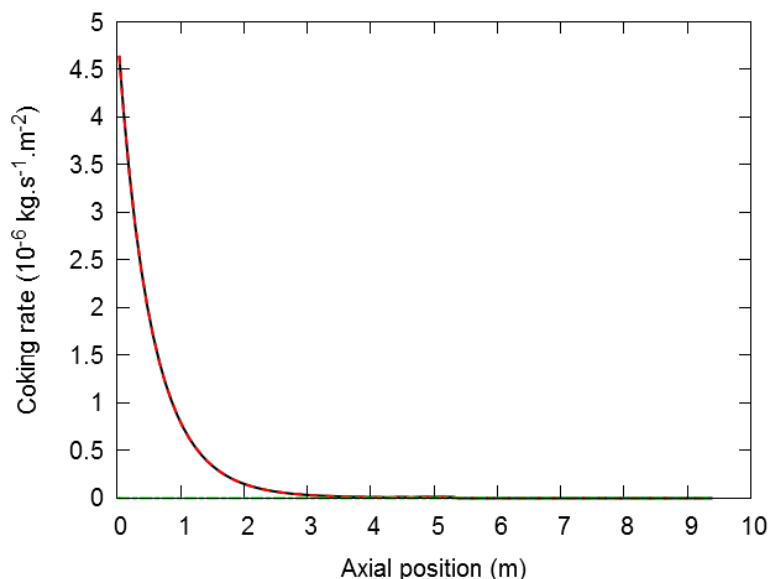
Figure 7.8: Contributions of the different coking mechanisms to the total cokes formation for the propane furnace : ▬Total coke formation; ▬ ▬ Heterogeneous non-catalytic coke formation; ▬▬Condensation coke formation.

In addition coke formation also occurs on the inner tube where the cracked gas is present. Figure 7.8 shows that the coking model predicts that the heterogeneous non-catalytic coke formation dominates at the beginning of the TLE and almost no condensation cokes is being formed due to the small fraction (<0.001wt%) of triaromatics being formed with this feedstock. The amount of cokes formed during the typical run length of a millisecond reactor (20 days) has no influence on the yields or the process variables of the TLE. However to study the effect of cokes inside the TLE a uniform coke layer of 5.10^{-3}m was imposed inside the TLE. To eliminate the effect of changes inside the radiant coil due to coke formation the outlet conditions of the radiant coil were fixed at start of run conditions which means that the radiant coil is kept in a bare state. Table 7.1 shows the results when the coke thickness profile is imposed inside the TLE. The TLE gas outlet temperature rises from 707 K to 780 K and the total steam production has dropped from 11.71

kg.s^{-1} to 9.92 kg.s^{-1}. No significant effect on the yields at the outlet of the TLE is visible even at slightly higher gas temperatures inside the TLE. A coke layer thus significantly increases the gas outlet temperature of the TLE and decreases the steam production. When coke is formed an additional thermal resistance comes in to play in Equation 7.6 which makes that the heat flux drops thus resulting in an increase in the gas outlet temperature and a decrease in the steam production. Depending on the amount of cokes that is formed (and thus on the feedstock that is used) these changes become significant. For heavier feedstocks (e.g. gas oils and heavier) the design of a TLE can play a critical role in determining the total run length of a furnace. If the TLE is badly designed for the cracked feedstock and a lot of cokes is formed inside the TLE the cooling power of the TLE can drop drastically and it is possible that the effluent mixture would still be reactive after the initial cooling inside the TLE.

7.3.2 Case 2: TLE connected to a naphtha furnace

In the second case and industrial naphtha furnace is simulated with limited amount of information about the geometry and operating conditions. Table 7.4 shows an overview of the simulated results as well as the industrial data that are available. It clearly shows that the gas outlet temperature after the TLE is being well predicted but the steam production is being overestimated as was the case for the millisecond furnace. All industrial values mentioned in Table 7.4 are design values and not operating values which could be a possible explanation for the difference. Table 7.4 again shows the effect of reaction. It is clear that some reaction still occurs inside the quench as the yield ethene increases by about 1 wt% inside the quench. No significant reactions seem to occur after the temperature drops below 673 K which is significantly lower than in case of the millisecond furnace. Reactions in the naphtha effluent seems to be occurring at lower

temperatures than was the case for the propane effluent. Disabling the reactions entirely seems to have no significant effect on the gas outlet temperature or the total steam production. Similar as for the millisecond furnace the endothermicity of the reactions seems to be negligible compared to the cooling done by the TLE. Again it seems important to include reactions happening inside the TLE to account for the small yield changes that happen inside the TLE (e.g. 5% for ethene). Even though these changes are small due to the large scale production of a steam cracking furnace these small yield changes can have a significant effect on the total profit of the plant.

Table 7.4: Simulated and industrial results for the naphtha furnace

	Before Quench	Quench	Industry[1]	Quench (without reactions)	Quench (coked)
Yields (wt%)					
H2	0.77	0.86		0.77	0.83
CH4	12.80	13.11		12.80	13.10
C2H2	0.08	0.06		0.08	0.05
C2H4	23.90	25.21		23.90	24.71
C2H6	3.84	2.68		3.84	3.21
C3H4(MA)	0.16	0.11		0.16	0.10
C3H4(PD)	0.18	0.17		0.18	0.17
C3H6	17.77	17.65	N/A	17.77	17.65
C3H8	0.40	0.39		0.40	0.39
1;3-C4H6	5.74	5.70		5.74	5.69
1C4H8	1.63	1.55		1.63	1.55
2C4H8	0.61	0.58		0.61	0.58
iC4H8	2.16	2.11		2.16	2.11
iC4H10	0.03	0.03		0.03	0.03
nC4H10	0.85	0.81		0.85	0.81
Other Properties					
Outlet temperature(K)	1073	625	623	624	663
Outlet pressure (Pa)	191.10^3	179.10^3	N/A	179.10^3	153.10^3
Steam production (kg/s)	-	0.300	0.247 – 0.262	0.302	0.279
Water temperature (K)	-	592	592	592	592

1) Based on design values

Neglecting the outer tube convective thermal resistance has the same effects as in case of the millisecond furnace. The difference in the external wall temperature of the inner tube drops by about 25 K at the beginning of the tube but quickly drops below 5 K as the contribution of the outer tube convective thermal resistance towards the total thermal resistance becomes smaller. This translates in a 20 K temperature difference at the metal/gas interface of the inner tube but this temperature difference quickly drops below 5K. The latter implies a 10 % overestimation of the coking rate at the beginning of the reactor, which quickly drops below 1 % when the temperature difference decreases. Thus, in case of the naphtha cracking furnace, the outer tube convective thermal resistance can safely be neglected without significantly influencing the results. The effect of non-adiabatic heat changes in the TLE has also been studied for the naphtha furnace, similarly as for the millisecond furnace. Again no significant influence can be seen on the yields or the TLE gas outlet temperature. The steam production however increases from 0.27 kg.s^{-1} to 0.30 kg.s^{-1}. Unaccounted heat losses towards the environment can thus be a (part of) the reason why the steam production is being overestimated.

Since no thermosiphon is being simulated in this case the effect of friction could not be investigated.

The effect of cokes is studied by simulating a coke thickness profile after 60 days using the coking model. Figure 7.9 shows the contributions of the different coke formation mechanisms for a bare tube. In contrast to the propane furnace the condensation cokes mechanisms now dominates throughout the reactor and only at the start of the reactor there is an amount of heterogeneous non-catalytic cokes being formed.

The reactor was kept in a bare state to exclude the effect of cokes being formed inside the radiant coil. The results are also shown in Table 7.4. In this case the gas outlet temperature of the TLE has risen up to 663 K and the steam production has dropped accordingly. The increased temperature inside the TLE also has an effect on the reactions occurring inside the TLE as the yields deviate from the bare tube case. In normal industrial operation the TLE does not seem to be a limiting factor for the run length for this furnace and feedstock. However allowing coke to stack inside the TLE is undesirable as an excessive amount of cokes inside the TLE can have a big impact on the operating efficiency of the TLE.
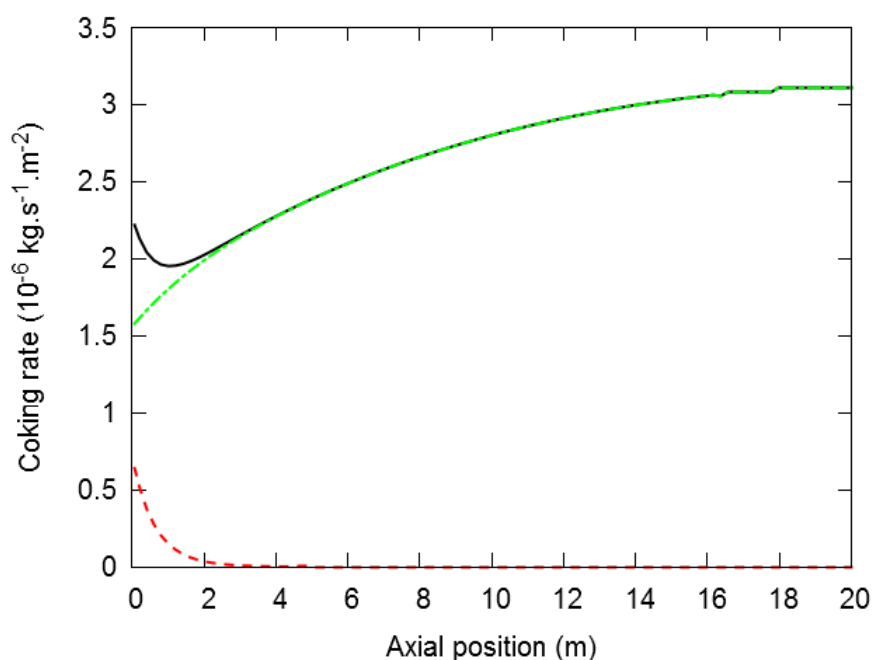
Figure 7.9: Contributions of the different coking mechanisms to the total cokes formation for the naphtha furnace : ——Total coke formation; – – Heterogeneous non-catalytic coke formation; —∙—Condensation coke formation.

7.4 Conclusions

A detailed model of a transfer line exchanger (TLE) in a steam cracker was developed. For the first time a detailed kinetic model to account for the free radical reactions is included, which proves to be essential because in the inlet part of the TLE significant secondary reactions still occur. In addition the model also accounts for the outer tube thermal convection coefficient in contrast to previous work which decreases the overall heat transfer efficiency . No changes in the product yields were simulated when the process gas temperature dropped below 873 K and 673 K for the propane and naphtha furnace respectively.

Validation against data from two industrial TLE's (from a millisecond furnace and a naphtha furnace) showed that neglecting the outer tube convective thermal resistance results in an increase of approximately 20 K of the external wall temperature of the inner tube and of the gas/metal interface temperature at the first part of the TLE . Near the end of the TLE the assumption becomes more accurate, resulting in a difference lower than 5 K. However in both cases the increased temperature had little effect on the coking rate predicted by the coking model proposed as well as on any of the other simulated values.

Heat losses towards the environment in the adiabatic volume or in the TLE did not have a significant effect on the product yields or the outlet temperature of the gas in the TLE. Heat losses in the TLE itself however could significantly influence the total amount of produced steam proving that insulation of the TLE is important. Similarly, changing the friction factor from 80% of its value to 120% of its value only seems to have a minor effect on the water flow rate and steam production.

Finally coke formation significantly affects the TLE's performance, increasing the gas outlet temperature of the and reducing the total steam production, illustrating the importance of coke mitigation in the TLE either by a good TLE design or regular decoking operations. Coke formation in the TLE of the millisecond furnace is mainly occurring in the inlet due to the light feedstock being used and thus the lack of condensable compounds (tri-aromatics and heavier) and thus the heterogeneous non-catalytic coke formation mechanism dominates. In case of the naphtha furnace coke build-up in the TLE significantly increased the TLE outlet temperature (40 K) and reduced the steam production.

7.5 References

Cai, H., Krzywicki, A., & Oballa, M. C. (2002). Coke formation in steam crackers for ethylene production. Chemical Engineering and Processing: Process Intensification, 41, 199-214.

Dente, M., Ranzi, E., & Goossens, A. G. (1979). Detailed prediction of olefin yields from hydrocarbon pyrolysis through a fundamental simulation model (SPYRO). Computers & Chemical Engineering, 3, 61-75.

Dhuyvetter, I., Reyniers, M. F., Froment, G. F., Marin, G. B., & Viennet, D. (2001). The influence of dimethyl disulfide on naphtha steam cracking. Industrial & Engineering Chemistry Research, 40, 4353-4362.

Edwin, E. H., & Balchen, J. G. (2001). Dynamic optimization and production planning of thermal cracking operation. Chemical Engineering Science, 56, 989-997.

Froment, G. F., Bischoff, K. B., & De Wilde, J. (2011). Chemical reactor analysis and design (3th edition): Wiley.

G. Schmidt, D. S. U., Dr. C. Geipel. (2010). Olefin Academy 2010 Cracking Furnace Technology http://olefin-academy.com/documents/Conferenceday1.pdf

Gal, T., & Lakatos, B. G. (2008). Thermal cracking of recycled hydrocarbon gas-mixtures for re-pyrolysis: Operational analysis of some industrial furnaces. Applied Thermal Engineering, 28, 218-225.

Herrmann, H., & Burghardt, W. (1994). Latest Developments in Transfer Line Exchanger Design for Ethylene Plants. In 6th Annual Ethylene Producers' Conference. Atlanta, Georgia.

Huntrods, R. S., Nighswander, J. A., Mehrotra, A. K., & Behie, L. A. (1989). Modeling of coke formation in gas quenchers of industrial ethane cracking furnaces. Chemical Engineering Research and Design, 67, 632-638.

Jin, Y. K., Li, J. L., Du, W. L., Wang, Z. L., & Qian, F. (2013). Outlet Temperature Correlation and Prediction of Transfer Line Exchanger in an Industrial Steam Ethylene Cracking Process. Chinese Journal of Chemical Engineering, 21, 388-394.

Knight, C., & Corry, J. B. (2003). Using Computational Fluid Dynamics (CFD) for Analysis of Transfer Line Exchangers. In 15th Ethylene Producers' Conference. New Orleans, Louisiana.

Kopinke, F. D., Bach, G., & Zimmermann, G. (1993). New Results About The Mechanism Of TLE Fouling In Steam Crackers. Journal of Analytical and Applied Pyrolysis, 27, 45-55.

Manafzadeh, H., Sadrameli, S. M., & Towfighi, J. (2003). Coke deposition by physical condensation of poly-cyclic hydrocarbons in the transfer line exchanger (TLX) of olefin plant. Applied Thermal Engineering, 23, 1347-1358.

Plehiers, P. M., Reyniers, G. C., & Froment, G. F. (1990). Simulation of the run length of an ethane cracking furnace. Industrial & Engineering Chemistry Research, 29, 636-641.

Schmidt, E., & Grigull, U. (1979). Properties of water and steam in SI-units: thermodynamische Eigenschaften von Wasser und Wasserdampf : 0-8000C, 0-1000 bar: Springer.

Schoepe, B. T., & Stueckrath, K. (2008). Transfer Line Exchangers in Ethylene Furnaces: Operating and Reliability Experience. In The 20th Ethylene Producers' Conference.

Shokrollahi Yancheshmeh, M. S., Seifzadeh Haghighi, S., Gholipour, M. R., Dehghani, O., Rahimpour, M. R., & Raeissi, S. (2013). Modeling of ethane pyrolysis process: A study on effects of steam and carbon dioxide on ethylene and hydrogen productions. Chemical Engineering Journal (Lausanne), 215-216, 550-560.

Thirumaleshwar, M. (2006). Fundamentals of Heat and Mass Transfer: Wiley.

Towfighi, J., Sandrameli, M., & Niaei, A. (2002). Coke Formation Mechanisms and Coke Inhibiting Methods in Pyrolysis Furnaces. Journal of Chemical Engineering of Japan, 35, 923-937.

Van Geem, K. M., Heynderickx, G. J., & Marin, G. B. (2004). Effect of radial temperature profiles on yields in steam cracking. AIChE Journal, 50, 173-183.

Van Geem, K. M., Pyl, S. P., Reyniers, M. F., Vercammen, J., Beens, J., & Marin, G. B. (2010). On-line analysis of complex hydrocarbon mixtures using comprehensive two-dimensional gas chromatography. Journal of Chromatography A, 1217, 6623-6633.

Van Geem, K. M., Reyniers, M. F., & Marin, G. B. (2008). Challenges of modeling steam cracking of heavy feedstocks. Oil & Gas Science and Technology-Revue De L Institut Francais Du Petrole, 63, 79-94.

van Goethem, M. W. M., Kleinendorst, F. I., van Leeuwen, C., & van Velzen, N. (2001). Equation-based SPYRO® model and solver for the simulation of the steam cracking process. Computers & Chemical Engineering, 25, 905-911.

Zhang, W. X., & Watkinson, A. P. (2005). Carbonaceous material deposition from heavy hydrocarbon vapors. 2. Mathematical modeling. Industrial & Engineering Chemistry Research, 44, 4092-4098.

Zimmermann, H., & Walzl, R. (2000). Ethylene. Ullmann's Encyclopedia of Industrial Chemistry (pp. 465-529): Wiley.

Chapter 8: Multi-objective optimization of an industrial steam cracking reactor

8.1 Introduction

Ethene is the base material for the production of most organic chemicals (Zimmermann & Walzl, 2000). More than 95% of its production comes from steam cracking of hydrocarbons. Typically ethane, propane, naphtha and gas oils are cracked within a tubular reactor to produce light olefins (e.g. ethene and propene), aromatics (e.g. benzene), methane and hydrogen (Edwin & Balchen, 2001). Ethane is the major feedstock for ethene production in North-America and Middle East, while in Europe and Asia mainly naphtha is used as feedstock (Nakamura, 2007). Due to the increasing demand of light oil fractions, e.g. naphtha, and depleting reserves of sweet crude oils heavier fractions (gas condensates, gas oils, and vacuum gas oils) and even crude oil (Tan & Peng, 2014) are becoming interesting steam cracker feedstocks (Singh et al., 2005). To ensure profitability steam crackers are operated closer to actual constraints (Ghashghaee & Karimzadeh, 2011). Modeling and optimization of a steam cracking reactor can be very beneficial in that respect (Keyvanloo et al., 2012). Hence optimization of the pyrolysis process has drawn continued attention from researchers (Edwin & Balchen, 2001; Ghashghaee & Karimzadeh, 2011; Nabavi et al., 2011). Over the years a wide range of different types of optimization have been carried out, which can be roughly divided into two main groups. Either optimization is done for a single objective; e.g. profit, or optimization is done towards multiple (conflicting) objectives. In the latter case there could not be a single solution that is best for all objectives but rather a set

of optimal solutions, known as Pareto-optimal solutions, that are equally good (Nabavi et al., 2011). In both cases the optimization can be based upon either free-radical based (Edwin & Balchen, 2001; Nabavi et al., 2009; Berreni & Wang, 2011), global (Gao et al., 2008) or correlation-based (Ghashghaee & Karimzadeh, 2011; Wang & Tang, 2013) kinetic models. For single-objective optimization a simple or complex profit function is the most important and only objective for an operating plant. However optimization can either be carried out for a single furnace (van Goethem et al., 2010; Ghashghaee & Karimzadeh, 2011) or for an entire plant (Lim et al., 2006, 2009; Liu et al., 2010). Full plant optimization requires scheduling of the downtime of the different furnaces and this strongly affects the profit. Including downtime of furnaces in the optimization transforms the problem to a mixed integer non-linear optimization problem. In these optimization problems the more simple process models are typically used to calculate the different process variables (yield, run length, heat input, etc.) so that the optimization can be completed in a reasonable amount of time (Lim et al., 2006).

At the other end of the spectrum several multi-objective optimization studies have been carried out but they are solely used for single furnace optimization studies. A variety of objective functions have already been used been used in literature. Nabavi et al. (2009) performed both bi- and tri-objective optimization with objectives like ethene yield (wt%), propene yield (wt%), ethene production (kg.s^{-1}), heat duty and run length of a furnaces while varying process variables like hydrocarbon flow rate, outlet pressure, outlet temperature, steam dilution and inlet temperature. Nabavi et al. (2009) used a kinetic model of LPG thermal cracking containing 146 elementary reactions including coke formation reactions that was developed by Towfighi et al. (2006). Gao et al. (2008) studied the maximization of both the yield of ethene and propene simultaneously while varying the outlet temperature. Gao et al. (2008) used a pyrolysis model

from Kumar and Kunzru (1985) that is valid for a specific naphtha and contains many global reactions. To compensate for the lack of agreement with industrial data several kinetic parameters of the model were re-fitted.

Common to all of the above mentioned optimization studies is the limited validity range of the used kinetic model, which makes generalization of the obtained results not trivial. Either a global or a correlation-based kinetic model is used, restricting its application to a specific feedstock and/or a single furnace. Free-radical based kinetic models are considered, but only when light gaseous feedstocks are cracked, where the product spectrum is not that complex and optimization is not that challenging. For heavier naphtha feedstocks optimization is a lot more important and challenging because of the lower profit margins and complex product spectrum. Therefore in this chapter a multi-objective optimization of an industrial steam cracking furnace is carried out using an extensive free-radical based kinetic model called CRACKSIM (described in Chapter 6). The latter is able to accurately predict the yields of feedstocks ranging from ethane up to gas oils and a wide range of different reactor geometries and operating conditions, as demonstrated in Chapter 6.

In the first part the role of the objective function is studied and evaluated. Two tri-objective optimizations and two single-objective optimizations are compared. The first multi-objective case is the maximization of the yield of ethene and propene (wt%) combined together with the minimization of the heat input (per kg feedstock) and the minimization of the maximum initial coking rate inside the reactor. The latter objective can be an estimate for the run length of the furnace at the given operating conditions as will be discussed further. The second case is the maximization of the sum of the ethene and propene production $(kg.s^{-1})$, the minimization of the operating expenses or OPEX (feedstock costs, energy costs,…) and the minimization of the

maximum initial coking rate. The single-objective optimizations either optimize gross profit on a yearly basis or per unit feedstock. Results of all four optimizations will be compared and discussed.

Next the multi-objective optimization of different types of feedstocks ranging from ethane up to atmospheric gas oils is discussed. On the one hand the optimization of two naphtha's of different qualities is compared to assess differences in composition within a class of feedstocks. On the other hand the optimization of 6 classes of feedstocks, i.e. ethane, propane, LPG, naphtha, gas condensate and gas oil, are compared. The differences between the Pareto front of the feedstocks in all these cases will be highlighted.

Finally, the multi-objective optimization for a furnace with a bare reactor tube will be compared with the multi-objective optimization for a furnace with a reactor tube containing a cokes layer representative for a furnace nearing decoking. Also the optimization for the co-cracking of an ethane/propane mixture will be discussed.

8.2 Multi-objective optimization

Multi-objective optimization is becoming more and more important in the chemical industry. The main goal in industry is of course to maximize profit while respecting the environmental constraints . However the revenue and cost of chemical installations is influenced by a variety of factors such as feedstock and product prices. These prices often depend on time and location and their relative importance can change significantly. This causes a limited scope of single-objective optimizations of a profit function and conclusions made from these studies are usually limited to the case at hand and the current ruling prices in that region. In addition, single-objective optimization studies only provide a single set of optimized process variables. This implies that no

alternative solutions can ever be obtained although they could be very useful in a rapidly varying (economic) environment, e.g. when planning becomes an issue or when day to day plant operation changes . In the specific case of steam cracking it is very useful to plan the decoking operation of the different furnaces so that there is minimal overlap of the furnaces' down-time. The start of run optimization based on maximal profit could in this case have resulted into process variables that are less beneficial in this short time frame where an alternative set of process variables could be more beneficial. In practice this would be resolved by performing a new single-objective optimization. If alternative solutions are available these process variables could just be selected out of this set of optimal solutions, and hence, making human interpretation easier and saving time.

For a nontrivial multi-objective optimization problem, there does not exist a single solution that simultaneously optimizes each objective. In that case, the objective functions are said to be conflicting, and there exists a possibly infinite number of Pareto optimal solutions. A solution is called non-dominated, Pareto optimal, Pareto efficient or non-inferior, if none of the objective functions can be improved without degrading some of the other objectives. Without additional subjective preference information, all Pareto optimal solutions are considered equally good.

A multi-objective optimization approach that looks for this Pareto set should achieve the following goals (Eckart et al., 2000):

- The algorithm should converge towards the true Pareto front of the problem
- The (best approximation of) Pareto front obtained by the algorithm should be uniformly distributed over the true Pareto front

Many methods (Fadaee & Radzi, 2012; Rada-Vilela et al., 2013; Yao & Ionel, 2013) are available for solving multi-objective optimization problems. A popular algorithm often used for

the multi-objective optimization of steam cracking is the elitist non-dominated sorting genetic algorithm (NSGA) or adaptations of this algorithm (Guria et al., 2005; Gao et al., 2008; Nabavi et al., 2009, 2011). In this chapter the elitist non-dominated sorting genetic algorithm with adapted jumping gene operator (NSGA-II-aJG) is used since it is about five times faster than the NSGA-II algorithm (Kasat & Gupta, 2003). The parameters for the selected optimization were chosen based on values of Nabavi et al. (2009) and are given in Table 8.1. The kinetic model (CRACKSIM), the reactor model (COILSIM1D,) and coking model, described in Chapter 6, are used for optimization.

Table 8.1: Parameters used in this study for the elitist non-dominated sorting genetic algorithm with adapting jumping gene operator (NSGA-II-aJG)

Parameter	Value
Number of individuals in the population	50
Number of generations	100
Cross over probability	0.8
Mutation probability	0.01
Length of replacing jumping gene	40
Seed for random number generator	0.8

A wide variety of objectives can be considered important for multi-objective optimization of steam cracking furnaces but not all the (combinations of) objectives will give useful results. In this chapter different objectives are proposed and the effect of two different objective combinations will be studied and compared with two classical single-objective optimizations. A first objective that is chosen is the sum of the ethene and propene yield. Ethene and propene are

the main source of income for a steam cracker and nowadays both these products have similar market prices in Europe. In January 2013 the global market price of ethene was 1382 $/t while the global market price of propene was 1340 $/t (Platts, 2013). The sum of the yields of ethene and propene can be a good objective instead of a separate objective for ethene and propene due to their similar prices, like was the case for the multi-objective optimization studied by Nabavi et al. (2009). Optimizing of four or more objective functions makes visualization and interpretation of the results difficult since a 4D dimensional or higher dimensional Pareto front are obtained, although it could be useful in the final decision making process. Using the sum instead of a separate objective function for ethene and propene limits the number of objective functions, and thus allows considering two other objective functions without overcomplicating the interpretation. Instead of using the sum of the ethene and propene yield, also the total production of ethene and propene can be considered as an objective. Although this objective differs hardly from the first objective, the total hydrocarbon flow rate obviously influences the production of ethene and propene, but also the yield of ethene and propene, and hence influences the results of the optimization. Equation 8.1 and 8.2 give the mathematical form of the primary first and the secondary first objective.

$$O_1 = w_{C2H4} + w_{C3H6} \tag{8.1}$$

$$O_1^* = (w_{C2H4} + w_{C3H6}).\dot{m} \tag{8.2}$$

A second important objective to consider in steam cracking is the run length of the furnace. Longer run lengths imply less shut downs of plant operations and thus a larger availability. The latter leads to increased production. It also decreases operational decoking costs. As explained in Chapter 6, a run length simulation can be considered as a series of consecutive time independent simulations. The amount of coke formed is then calculated by adding the amount of coke formed

in a certain time step to the existing coking layer in the reactor. As mentioned in Chapter 6 the model of Plehiers is used for gaseous feedstocks while the model of Reyniers is used for liquid feedstocks.
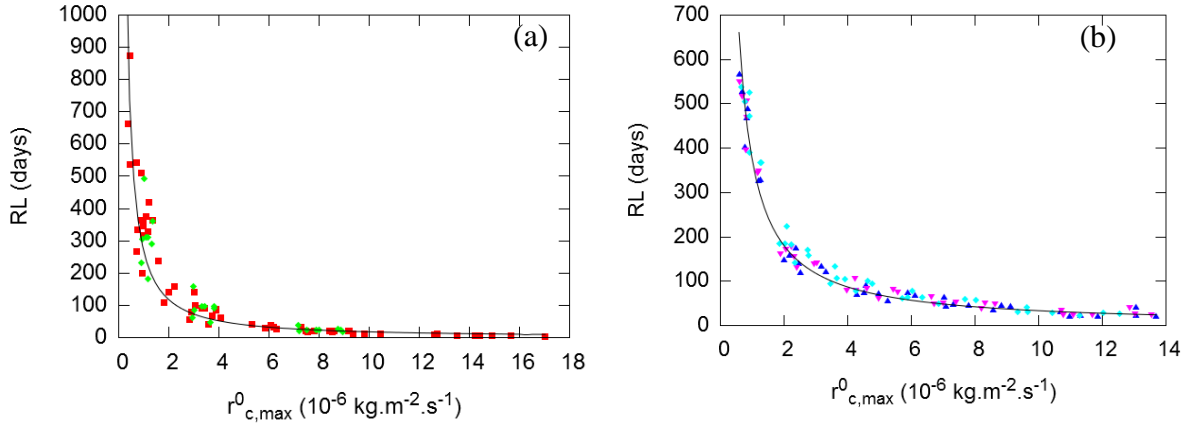
Figure 8.1: Fitting of runlength data to maximum initial coking rate for: (a) furnace 1 and (b) furnace 2 5 (see Table 8.4) : ■ **Ethane and propane;** ● **butane;** ▲ **Naphtha;** ▼ **Gas condensate;** ◆ **Gas oil**

Full line: (a) $RL = 2,25.10^{-5}.r_{c,max}^{0}{}^{-1.178}$ **(b)** $RL = 2,25.10^{-5}.r_{c,max}^{0}{}^{-1.178}$

Doing full run length simulations with an elaborate kinetic scheme is computationally very intensive as a reasonable number of time steps need to be taken to obtain an accurate prediction of the run length. Long simulation times are undesirable in multi-objective optimization since a large amount of simulations are required. For example using the values specified in Table 8.1, the NSGA-II-aJG algorithm would require 5000 simulations. Considering that at least for each run length simulation 10 time steps are needed, the optimization would require in total over 50.000 simulations. So instead of choosing the run length as second objective, the maximum initial coking rate at a certain axial position in the reactor was selected because a strong correlation is expected between both variables. This is illustrated in Figure 8.1 showing the run length plotted against the maximum initial coking rate ($r_{c,max}^{0}$) for the different feedstocks and reactors used in

this chapter. Different maximum initial coking rates and run lengths were obtained by varying all the process variables (COT, COP, dilution and hydrocarbon flow rate) that are considered variables in the optimization algorithm. For these hundred conditions a full run length simulation was carried out. Figure 8.1 also shows that a power function adequately describes the relation between the run length and the maximum initial coking rate. Surprisingly, a single power function can be used for a specific furnace regardless of the feedstock that is being used. This can be explained by the fact that the changes in run length by changing the feedstocks at fixed conditions are implicitly accounted for by the maximum initial coking rate. After optimization the fitted power function can be used to convert the maximum initial coking rate into an estimate of the total run length of the reactor or, if preferred, a total run length simulation can also be carried out for a limited amount of points part of the Pareto front. Equation 8.3 gives the mathematical form of the second objective.

$$O_2 = r^0_{c,max} \tag{8.3}$$

The steam cracking process is very energy-intensive as most reactions are highly endothermic, consuming about 8% of the total chemical industries' energy use (Ren et al., 2006). Improving the energy efficiency in the large gas-fired furnaces is thus one of the concerns for large plants. Hence, as third objective the heat input per kilogram feedstock has been selected. Since the third objective is related to the operating expenses of a plant (excluding feedstock costs) an alternative objective could be the operating expenses itself. The main operating expenses are the feedstock costs and the fuel gas costs. Typically high pressure steam, produced in the process by cooling down the effluent, is used to drive the process gas compressors and the compressors in the cold section. Since there is a big difference between the cost of the feedstock and the cost of fuel gas the prices have to be weighted:

$$O_3 = Q \tag{8.4}$$

$$O_3^* = \dot{m}.P_{feed} + Q.\dot{m}.\frac{100}{42}.\frac{1}{LHV_{CH4}}.P_{CH4} \tag{8.5}$$

Equation 8.5 also takes into account that the heat input into the reactor is about 42% of the total heat input required in the furnace (Zimmermann & Walzl, 2000). COILSIM1D calculates the former heat input and thus the required amount of fuel can be estimated. Equation 8.5 does not take into account capital expenditures. However since they are not influenced by the process variables these capital expenditures will only shift the Pareto front to higher values of the third objective but will have no influence on the overall conclusions.

For the single-objective optimization an estimated gross profit was used. This profit function combines all the objectives described before into a single function that gives an estimate of the profit on a yearly basis. As can be seen from Equation 8.6 it also includes the profit that could be made from some of the by-products that are being produced, e.g. benzene, 1,3-butadiene. Decoking operations are assumed to take two days and both operating expenses and revenue on decoking days are assumed to be 0. This results into the following objective function expressing gross profit on a yearly basis:

$$O_{s1} = \left[\left(\sum_{i=1}^{n_{productis}} \dot{m}.w_i.P_i \right) - \left(\dot{m}.P_{feed} + Q.\dot{m}.\frac{100}{42}.\frac{1}{LHV_{CH4}}.P_{CH4} \right) \right] \left[\left(\frac{365}{RL+2}.RL \right).24.3600 \right] \tag{8.6}$$

In this equation RL stands for the run length in days which can be estimated using the fitted curves from Figure 8.1. As an alternative the gross profit per unit could also be optimized. This results into the following objective function:

$$O_{s2} = \left[\left(\sum_{i=1}^{n_{productis}} w_i.P_i \right) - \left(P_{feed} + Q.\frac{100}{42}.\frac{1}{LHV_{CH4}}.P_{CH4} \right) \right] \tag{8.7}$$

The prices for the different feedstocks and products used in this chapter can be found in Table 8.2.

Table 8.2: Global or US prices of feedstocks and products at January 2013 ($/t)

Feedstocks		Products	
Ethane[1]	190	Ethene[2]	1382
Propane[1]	500	Propene[2]	1340
Naphtha[2]	900	Fuel gas[1]	194
Gas Condensate[3]	800	Hydrogen[4]	3510
Gas oil[2]	840	Butadiene[2]	1960
1) US prices from EIA (2013)		Benzene[2]	1400
2) Global prices from Platts (2013)		Toluene[2]	1280
3) US price from Schaefer (2013)		Xylene[2]	1560
4) US price from Clean Cities (2013)			

The parameters that could be varied to optimize the objective functions are process variables that can be set during the operations of a steam cracking furnace. Four process variables were chosen: COT, COP, dilution and hydrocarbon mass flow rate. It should be noted that the hydrocarbon mass flow rate can only be varied if the plant is furnace limited and the cold section of the plant is able to handle any hydrocarbon mass flow rate the furnace section can supply which is assumed in the present work. Optimization was carried out for a wide variety of feedstocks ranging from ethane up to gasoil, i.e. ethane, propane, LPG, naphtha, gas condensate and gas oil. This is only possible because a first principle model is used which has a very broad application range. The commercial indices of the liquid feedstocks are given in Table 8.3 and their detailed composition was obtained using SIMCO described in Chapter 5. Ethane and propane are cracked as a pure feedstock and LPG consisted of 5.18 wt% of ethane, 16.9 wt% of propane, 59.6 wt% of n-butane and 18.32 wt% of i-butane. Since the reactor design of a steam cracking plant is dependent on the feedstock (gas vs. liquid) that is being cracked, different reactor geometries were used depending on the aggregation state of the feed. For the gaseous feedstocks a swagged reactor geometry was used, while for the liquid feedstocks a split reactor geometry was used

(Zimmermann & Walzl, 2000). Table 8.4 gives an overview of the dimensions of both reactor geometries as well as the boundaries of the used parameters in the multi-objective optimization studies.

Table 8.3: Commercial indices of the liquid feedstocks

	Naphtha 1	Naphtha 2	Gas condensate	Gas oil
Density (kg.m^{-3})	0.678	0.706	0.734	0.824
Elemental Analysis (wt%)				
Carbon	84.1	84.8	85.5	86.3
Hydrogen	16.0	15.2	14.4	13.6
PINA analysis (wt%)				
Paraffins	38.8	36.5	32.3	24.2
Isoparaffins	47.6	32.8	33.2	30.0
Naphthenes	12.1	21.4	17.4	13.5
Aromatics	1.5	9.2	17.1	32.3
ASTM-D1160 (K)				
0 %	258	257	199	426
5 %	285	281	253	480
10 %	298	308	313	503
20 %	316	328	336	531
30 %	330	348	360	551
40 %	342	362	377	567
50 %	354	375	394	582
60 %	366	387	414	597
70 %	378	399	434	612
80 %	393	416	482	629
90 %	413	432	530	652
95 %	430	485	608	669
100 %	472	532	678	711

Table 8.4: Overview of the used reactor geometries in this study and the corresponding boundaries of the parameters

	Reactor 1	Reactor 2
Reactor geometry		
Type	Swagged reactor	Split reactor
Number of passes	8	6
Reactor length	79.5 m	53.72 m
Internal reactor diameter	0.120 m	Pass 1-4: 0.080 m
		Pass 5-6: 0.114 m
External reactor diameter	0.136 m	Pass 1-4: 0.096 m
		Pass 5-6: 0.130 m
Geometry		
COT	1123– 1173 K	973 - 1173 K
COP	$1.5 \cdot 10^6 – 2.3 \cdot 10^6$ Pa	$1.5 \cdot 10^6 – 2.3 \cdot 10^6$ Pa
Dilution	0.1 – 0.5	0.3 – 1.0
Hydrocarbon Mass flow rate (single reactor)	0.56 – 0.83 kg/s	0.34 – 0.51 kg/s
Ethane fraction	0 – 1	-

8.3 Results and discussion

8.3.1 Single-objective vs Multi-objective optimization

In this section single-objective optimization is compared to multi-objective optimization for naphtha cracking. Optimization was carried out based on the objectives [O_1]; ethene and propene yield (Equation 8.1), maximum initial coking rate (Equation 8.3) and heat duty (Equation 8.4), the objectives [O_2]; total production of ethene and propene (Equation 8.2), maximum initial coking rate (Equation 8.3) and operating expenses (Equation 8.5), or one of the two single-objective optimizations; gross profit or gross profit per unit feedstock. Figure 8.2 shows the Pareto front of the multi-objective optimization.
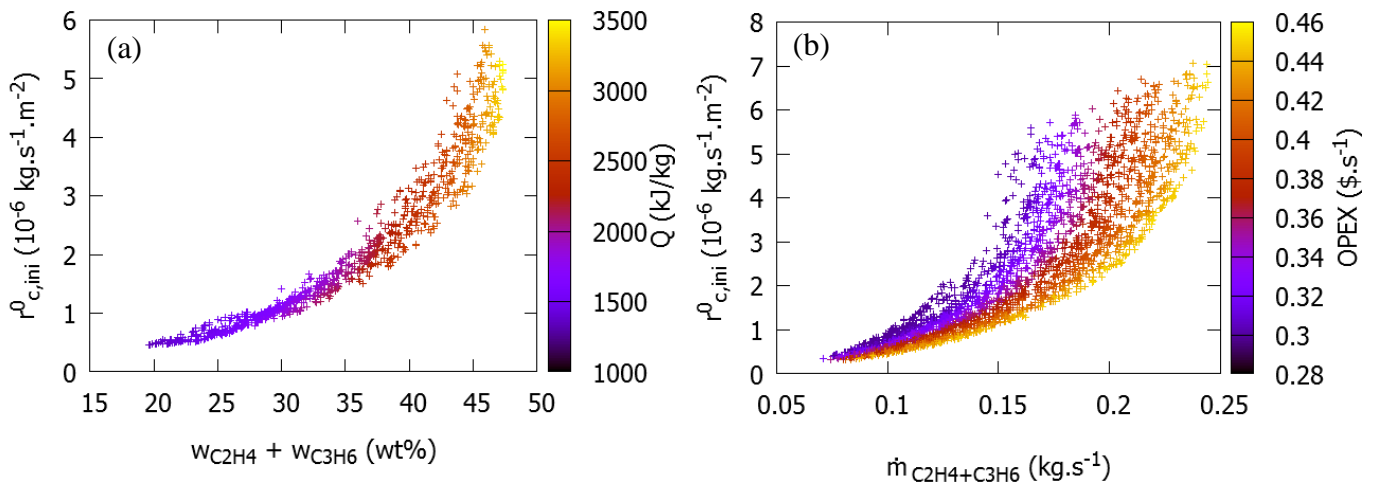
Figure 8.2: Pareto front for the optimization of naphtha 1 (properties in Table 8.3) with (a) the objectives defined by Equation 8.1, 8.3 and 8.4 [O_1]; (b) the objectives defined by Equation 8.2, 8.3 and 8.5 [O_2]

Since Figure 8.2 shows the results from 2 multi-objective optimizations with different objectives, a comparison is not straightforward. The most important process variable to optimize the product yields is not surprisingly the temperature, as shown in Figure 8.3. Increasing the COT will increase the yield but will require additional heat input . Increasing the heat input will also increase the wall temperatures and the interface temperature between the tube and the gas and

thus increase the coking rate. Hence, the three primary objectives seem to be strongly correlated, which can explain the limited surface area of the Pareto front. In case of the second multi-objective optimization [O_2] the total production of ethene and propene can in addition to the COT also be drastically influenced by the hydrocarbon mass flow rate (see Equation 8.2). At a fixed COT the production of ethene and propene can be increased by increasing the hydrocarbon mass flow rate which explains the higher surface area in Figure 8.3. Increasing the hydrocarbon mass flow rate off course also increases the operating expenses as can be seen in Figure 8.3.

In case of the primary objective functions [O_1], Figure 8.3a, no Pareto-optimal points are found beyond a COT of 1107 K. Above this temperature the yield of propene will drop faster than the increase in the yield in ethene and the total yield of ethene and propene thus decreases. Since increasing the COT also increases the heat input and the coking rate it also has a negative effect on both the second and third objective and no Pareto optimal solutions are obtained at higher temperatures. In case of the secondary objective [O_2] functions a higher maximum temperature of 1134 K is simulated. This higher temperature can be explained by the fact that, even although the yield of ethene and propene decreases past 1107 K, the decrease in the yield of ethene and propene can be compensated by increasing the hydrocarbon mass flow rate and thus increasing the total production of ethene and propene.

Going past 1134 K will influence all three objectives in a negative way (decrease the total production of ethene and propene, increase the operating expenses and increase the maximum initial coking rate as no Pareto optimal solutions were found past this point.
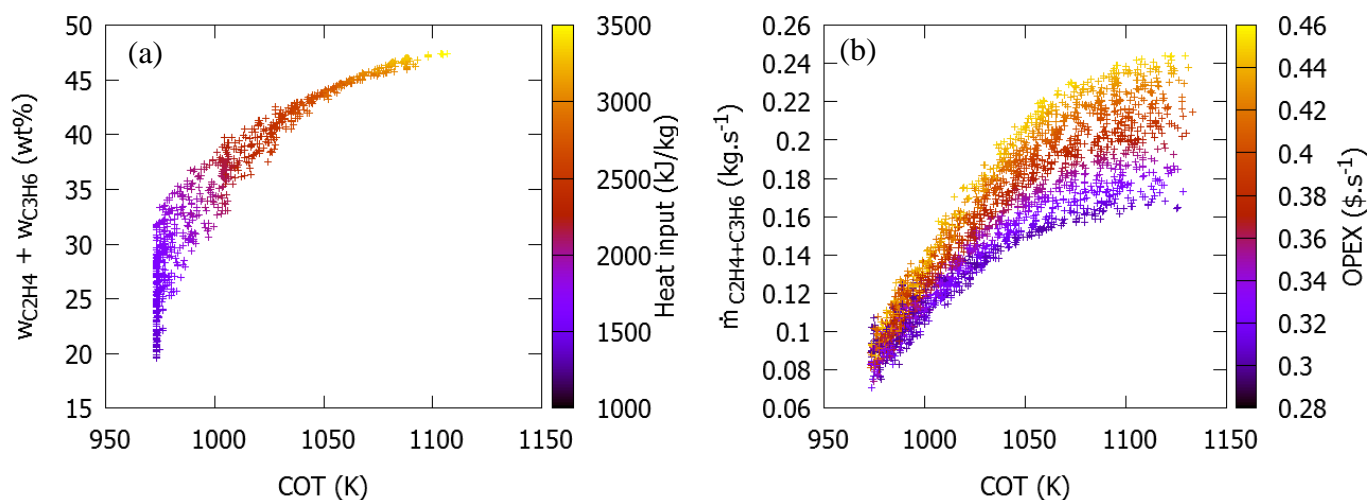
Figure 8.3: The first and third objective as a function of the COT for the cracking of naphtha 1 (properties in Table 8.3): (a) the objectives defined by Equation 8.1, 8.3 and 8.4 [O_1]; (b) the objectives defined by Equation 8.2, 8.3 and 8.5 [O_2]
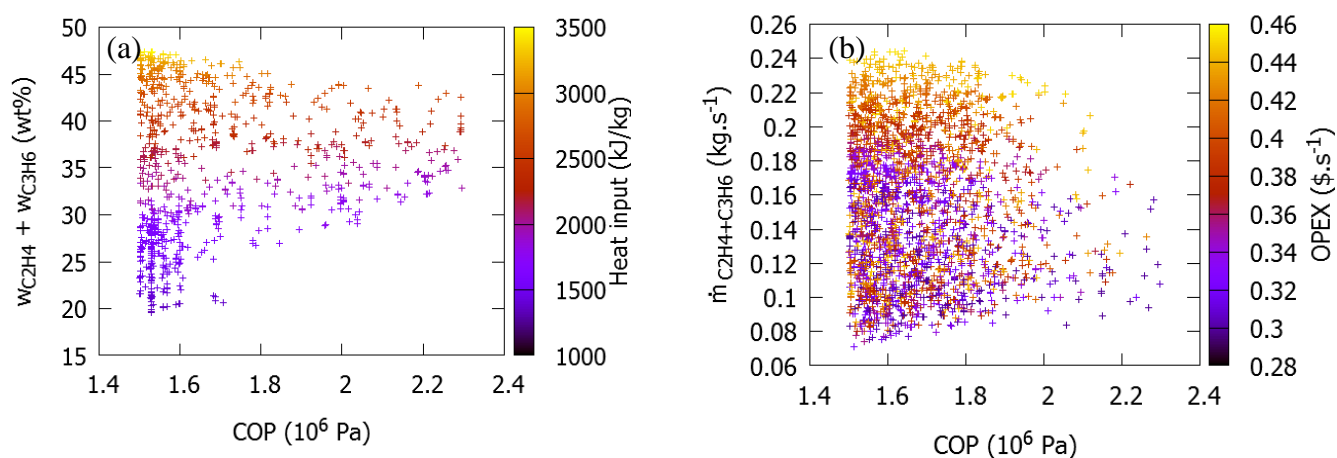
Figure 8.4: The first and third objective as a function of the COP for the cracking of naphtha 1 (properties in Table 8.3): (a) the objectives defined by Equation 8.1, 8.3 and 8.4 [O_1]; (b) the objectives defined by Equation 8.2, 8.3 and 8.5 [O_2]

Figure 8.4 shows the effect of the COP. A similar conclusion can be drawn for both sets of objective functions. As the COP decreases the density of points of the Pareto front increases and thus a lower COP is preferable. Due to Le Chatelier's principle a lower COP, and thus lower partial pressures of the compounds, limits the rates of secondary bimolecular reactions which

produce unwanted byproducts as well as coke without influencing the heat input significantly. A lower COP is thus desirable to increase the selectivity towards ethene and propene and reduce coke formation. However in industrial practice the lower limit would always be imposed by the separation train following the steam cracking unit.
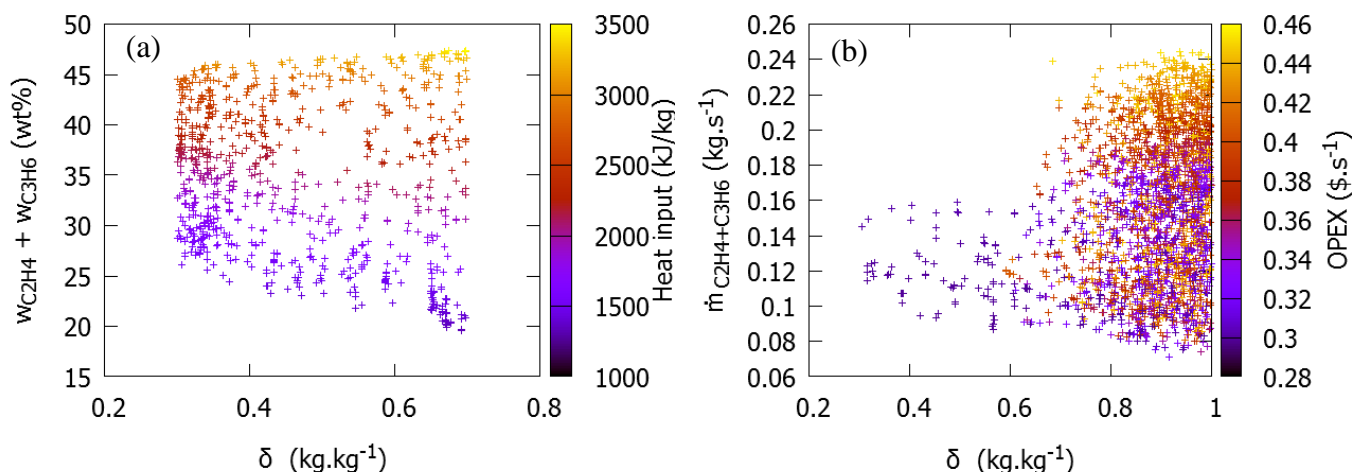
Figure 8.5: The first and third objective as a function of the dilution for the cracking of naphtha 1 (properties in Table 8.3): (a) the objectives defined by Equation 8.1, 8.3 and 8.4 [O$_1$]; (b) the objectives defined by Equation 8.2, 8.3 and 8.5 [O$_2$]

Figure 8.5 shows the effect of dilution on the first and third objective functions. It is clear that in case of the primary objective functions [O$_1$] that lower dilutions are preferred (Figure 8.5a), while in case of the secondary objective functions [O$_2$] higher dilutions are preferred (Figure 8.5b). Increasing the dilution has a similar effect on the selectivities as decreasing the COP as again the partial pressures of the compounds are reduced. However increasing the dilution also has a significant effect on the heat duty as more steam needs to be heated up from the inlet to the outlet temperature. The increase in dilution has a smaller effect on the yield of ethene and propene and the coking rate compared to the COT. However since increasing the dilution has significant effect on the heat input lower dilutions will be preferred in case of the primary objective functions [O$_1$]. In case of the secondary objective functions [O$_2$] the extra heat input will only have a very small

impact on the operating expenses since most of the operating expenses come from the feedstock

cost and thus in this case higher dilutions with higher selectivities will be preferred.
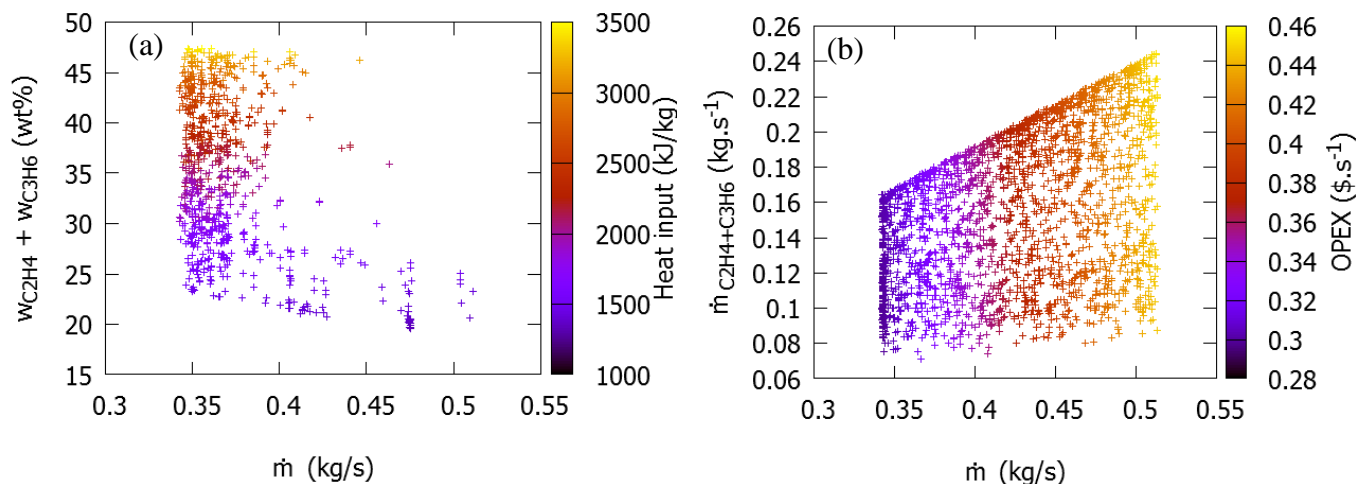
Figure 8.6: The first and third objective as a function of the hydrocarbon mass flow rate for the cracking of naphtha 1 (properties in Table 8.3): (a) the objectives defined by Equation 8.1, 8.3 and 8.4 [O_1]; (b) the objectives defined by Equation 8.2, 8.3 and 8.5 [O_2]

Figure 8.6 shows the effect of the hydrocarbon mass flow rate on the first and the third objective function. In case of the primary objective functions [O_1] (Figure 8.6a) the lowest hydrocarbon mass flow rates are favored. Lower hydrocarbon mass flow rates imply a larger space time and thus more time for reactions to occur increasing the yield of ethene and propene. The hydrocarbon mass flow rate has little influence on the heat input since it is expressed per kg feedstock. The hydrocarbon mass flow rate only has a limited influence on the coking rate thus lower hydrocarbon mass flow rates are favored. In case of the secondary objective functions [O_2] a high degree of scatter is seen (Figure 8.6b). Although decreasing the hydrocarbon mass flow rate (within its boundaries) will increase the yield of ethene and propene it will also decrease the total production of ethene and propene drastically (Equation 8.2). To increase the production capacity beyond 0.17 kg/s it becomes important to increase the hydrocarbon mass flow rate past the minimal value of 0.34 kg/s. This is because total yield of ethene and propene is maximally

50%. Due to this the maximum obtainable production ethene and propene is limited to half of the mass flow rate of the feedstock and thus to reach the high production capacities higher hydrocarbon mass flow rates of the feedstock are required. The front of the production capacity in Figure 8.6b follows this trend until the maximum hydrocarbon mass flow rate is reached.

From the set of Pareto-optimal solutions a single solution can be chosen based on a single-objective which combines the chosen objectives. For both multi-objective sets the single-objective functions proposed in Section 8.2 were used to select a solution out of all possible solutions. The chosen solutions are compared with the real optimal value for the single-objective optimization which was performed separately from the multi-objective optimization. Table 8.5 shows the results of these optimizations.

Table 8.5: Overview of the different optimal parameters and values of the single-objective functions for the cracking of naphtha 1 (properties in Table 8.3): [O_1] the objectives defined by Equation 8.1, 8.3 and 8.4; [O_2] the objectives defined by Equation 8.2, 8.3 and 8.5

Pareto front	Objective	COT (K)	COP (10^3 Pa)	δ (-)	$\dot{m}$ (kg.s-1)	O_{s1} (Eq. 8.6) (M\$.yr^{-1})	O_{s2} (Eq. 8.7) (\$.kg$_{feed}$$^{-1}$)
Single-objective optimization based upon the acquired Pareto front							
[O_1]	Gross profit	1098	156	0.67	0.41	2.64	0.206
[O_1]	Gross profit per unit	1106	153	0.70	0.38	2.56	0.237
[O_2]	Gross profit	1123	157	0.96	0.50	3.51	0.234
[O_2]	Gross profit per unit	1114	155	0.99	0.37	2.71	0.237
Single-objective optimization based upon the entire process variable space							
Gross profit (Eq. 8.6)		1124	164	0.90	0.49	3.51	0.235
Gross profit per unit (Eq. 8.7)		1113	152	0.99	0.40	2.88	0.237

From Table 8.5 it is clear that both the Pareto fronts obtained from the different objectives sets ([O_1] and [O_2]) can be used to represent the added value or profit per unit feedstock as the Pareto

front of both objective sets ([O_1] and [O_2]) includes the process variables obtained using single-objective optimization towards added value. However only the secondary objectives set [O_2] is able to capture the single-objective optimization towards gross profit as only this Pareto front includes the process variables of the single-objective optimization towards profit, although the objectives do not contain any information regarding the secondary products (1,3-butadiene, benzene,…). The profit gained from these secondary products is limited as compared to the profit gained from the primary products ethene and propene. In addition increasing the production of ethene and propene will in general also increase the production of fuel gas, benzene, toluene and xylene within the temperature range of the Pareto front. After the maximum temperature the decrease in production of ethene and propene is not compensated by the increased production of the aromatics and thus the point of maximum gross profit is included in the Pareto front.

The primary objective set [O_1] does not include any information regarding the feedstock price which can significantly influence the gross profit and thus does not include this maximum. The advantage of the first set of objectives is however that only a very limited amount of assumptions or prices are included. The only assumption made regarding prices was that the price of ethene and propene were similar. For the remaining sections in this chapter the secondary set of objectives [O_2] will be used since they can represent both single-objective optimizations important in industry.

8.3.2 Effect of the feedstock

Optimum conditions for steam cracking are strongly dependent on the composition of the feedstock. Therefore multi-objective optimization is applied to two naphtha's of a different

quality. In the second part the optimization results of six different feedstocks are discussed: ethane, propane, LPG, naphtha, gas condensate and gas oil.

Naphtha quality

In this section the optimization of two naphtha's of different quality are compared. The commercial indices of both naphtha's can be found in Table 8.3. Naphtha 2 has a significant higher amount of naphthenes and aromatics as compared to naphtha 1 (9.2 and 1.5 wt% respectively) and also has a higher final boiling point as naphtha 1 (532 and 472 K respectively).

Figure 8.7: Pareto front for the optimization of naphtha 2 (properties in Table 8.3) with the objectives defined by Equation 8.2, 8.3 and 8.5 [O$_2$]

Figure 8.7 shows the Pareto front for the multi-objective optimization of naphtha 2 using the secondary objectives [O$_2$]. When compared to Figure 8.2b it is clear that the production of ethene and propene is significantly lower for naphtha 2 as the Pareto front has shifted to the left compared to naphtha 1. The operating expenses are also slightly lower in case of naphtha 2. Aromatics hardly crack and thus these type of compounds need to be heated but do not contribute to the heat required for the endothermic cracking reactions. In case of naphtha 1 the larger

amount of paraffins makes that additional heat input is required, thus increasing the total fuel consumption. For both naphtha's the coking rate is of the same order of magnitude but difficult to compare as the process variables can be different. Conclusions regarding the COT, COP, dilution and hydrocarbon mass flow rate are identical for both naphtha's.

The advantage of naphtha 1 is an increased production of ethene and propene at the expense of higher operating expenses while in case of naphtha 2 the advantage lies in the lower operating expenses and the increased production of aromatics that are already present in the feedstock. To ultimately be able to choose between both naphtha's prices of fuel gas, ethene, propene and aromatics are important.

Using the prices mentioned in Table 8.2 a single optimal operation point can be determined, maximizing gross profit can be chosen from the Pareto front. For naphtha 1 and naphtha 2 these points are shown in Table 8.6. The final operating conditions for both naphtha's are the same, however, there is a significant reduction in profit in case of naphtha 2 due to the reduced production of ethene and propene. This is a very important observation, because it basically implies that once the optimum for a type of feedstock has been determined this will be more or less the optimal operating point for a different feedstock. The latter implies that comparing feedstocks can be done in very simple and efficient way, they just can be compared under identical conditions, only looking at their cost and the amount of ethene and propene that is produced. Note that due to the lower in quality of naphtha 2 it is clear that the market price will be lower as ethene producers will pay less to keep their profit margins the same. This lower price has not been taken into account for this comparison.

Table 8.6: Optimal point based on gross profit (Equation 8.6) chosen from the Pareto front for the multi-objective optimization of naphtha 1 and naphtha 2 (properties in Table 8.3) with the objectives defined by Equation 8.2, 8.3 and 8.5 [O_2]

Feedstock	COT (K)	COP (10^3 Pa)	δ (-)	$\dot{m}$ (kg.s^{-1})	O_{s1} (Eq. 8.6) (M\$.yr^{-1})
Naphtha 1	1123	157	0.96	0.50	3.51
Naphtha 2	1122	157	0.96	0.50	2.86

Gas vs. liquid feeds

In addition to the naphtha's the multi-objective optimization of different gaseous and heavy liquid feedstocks (ethane, propane, LPG, gas condensate and gas oil) was carried out. In case of propane, LPG, gas condensate and gas oil similar conclusions as in Section 8.3.1 for the secondary objective functions [O_2] can be drawn. As was the case with naphtha the COT is limited at certain threshold values beyond which the total production of ethene and propene will decrease. For propane, LPG, naphtha, gas condensate and gas oil these values are 1171 K, 1167 K, 1133 K, 1128 K and 1118 K respectively. Heavier feedstocks have a lower maximum temperature as the long chain paraffins are easier to crack than the short chain paraffins, and thus the maximum yield of ethene and propene is reached at lower temperatures. Higher temperatures could be reached if lower space times or higher hydrocarbon mass flow rates are allowed. Similar conclusions with respect to the COP, dilution and hydrocarbon mass flow rate are observed as was the case with naphtha. Lower pressures and higher dilutions are preferred due to the reasons explained in Section 8.3.1. The hydrocarbon mass flow rate is scattered within the process

boundaries except for the very high production capacities where a minimal flow rate was needed to reach these high production capacities.

For ethane cracking very similar conclusions can be drawn. However as can be seen from Figure 8.8 the maximum COT value of 1173 K is equal to the maximum COT allowed (see Table 8.4). The temperature after which the yield of ethene and propene begins to drop and thus also the total production of ethene and propene is located at an even higher temperature, around 1200 K. This maximal temperature is in the same range as was proposed by van Goethem et al. (2010) who concluded that the optimal temperature profile goes up to 1231 K for ethane.

Figure 8.8: The first and third objective as a function of the COT for the cracking of ethane using the objectives defined by Equation 8.2, 8.3 and 8.5 [O$_2$]

8.3.3 Comparison of a start of run Pareto front with an end of run Pareto front

One of the main problems during steam cracking is the formation of coke inside the reactor. Coke builds up inside the reactor influencing the heat transfer and the pressure drop in the reactor. Both changes will influence the proposed objective functions. For example an increased pressure drop

will result in an overall higher pressure inside the reactor if the COP is kept constant. To assess the effect of coke formation on the objective functions a multi-objective optimization of naphtha was carried out but instead of a bare tube an end of run coke profile is imposed inside the reactor. This coke profile was obtained by a full run length simulation and then imposing the coke profile obtained 5 days before decoking was needed.

Figure 8.9 shows the Pareto front of naphtha at end of run operations. When compared to the bare tube (Figure 8.2a) it can be seen that the formation of coke has a negative effect on all three objectives. The maximum production of ethene and propene that can be obtained in a bare tube is 0.24 $kg.s^{-1}$. In case of a coked tube this maximum production drops to a value of 0.23 $kg.s^{-1}$. In addition the maximum operating expenses increases from 0.45 $\$.s^{-1}$ to 0.50 $\$.s^{-1}$ which is an increase of 10%. Part of this can be explained by the higher COT that is reached. For a bare tube the COT threshold was located at 1133 K while for a coked tube this increases up to 1169 K. Due to the coke the reactor volume is reduced and thus the space time of a coked reactor is lower than that of a bare reactor. To obtain a similar yield of ethene and propene a higher COT is needed. Due to this increase in COT, the heat input the coking rate also increases in a coked tube. This reduced space time leads to lower values for the production of ethene and propene. Similar plots are obtained for both start of run optimization and end of run optimization for the COP, dilution and hydrocarbon mass flow rates.

Figure 8.9: Pareto front for the optimization of naphtha 1 (properties in Table 8.3) with the objectives defined by Equation 8.2, 8.3 and 8.5 [O$_2$] for a furnace nearing decoking operations

Table 8.7 shows the results when the optimal point for profit is selected out of the Pareto front. Since it is not useful to include the runlength in this calculation as it is already significantly lowered for the end of run operations Equation 8.6 was reduced to:

$$O_{s1} = \left[\left(\sum_{i=1}^{n_{productis}} \dot{m}.w_i.P_i \right) - \left(\dot{m}.P_{feed} + Q.\dot{m}.\frac{100}{42}.\frac{1}{LHV_{CH4}}.P_{CH4} \right) \right] [24.3600] \qquad \textbf{(8.8)}$$
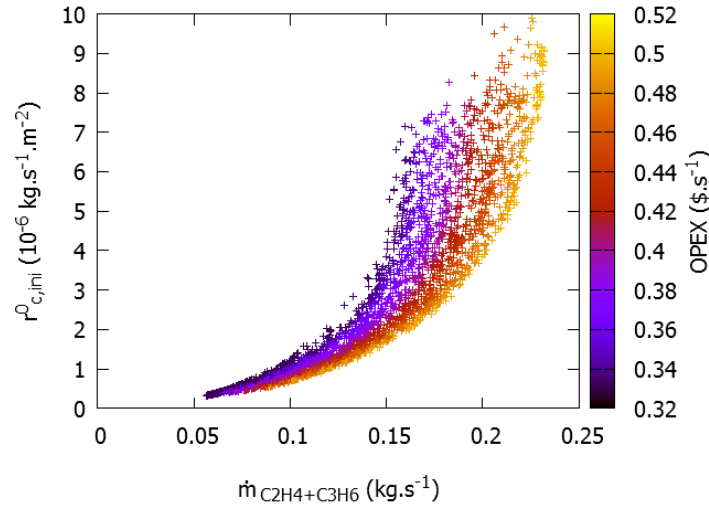
Table 8.7: Optimal point based on gross profit (Equation 8.6) chosen from the Pareto front for the multi-objective optimization of naphtha (properties in Table 8.3) for a start of run furnace and an end of run furnace with the objectives defined by Equation 8.2, 8.3 and 8.5 [O$_2$]

Time	COT (K)	COP (10^3 Pa)	Dilution (-)	Flow rate (kg.s^{-1})	O$_{s1}$ (Eq. 8.6) (M\$.yr^{-1})
Start of run	1123	157	0.96	0.50	3.51
End of run	1123	152	0.73	0.51	3.22

Table 8.7 shows that the reduced production capacity and the higher operating expenses have some impact on the profit made by the furnace as the total profit is decreased by around 10% when the furnace is nearing the decoking operations. Most of the operational parameters remain the same except for dilution which has decreased. The latter parameter was decreased to compensate the reduced space time due to the lowered diameter in the reactor due to cokes formation.

8.3.4 Co-cracking of ethane and propane

When studying co-cracking prices of the two feedstocks have an important effect on the optimization and the final profit. If those prices are not included in the optimization algorithm, as is the case with the primary objective functions, the multi-objective optimization will usually end up preferring one pure feedstock. In the case of co-cracking of ethane and propane this feedstock will be propane. Only at very high selectivities for ethene and propene, ethane will be preferred as only an ethane feedstock is able to reach these selectivities. However the cost of propane is about 3 times higher than the cost of ethane, e.g. Table 8.2, so only cracking propane is a priori not the preferred optimum. To take into account the prices of ethane and propane the secondary objective functions need to be used.

Figure 8.10 shows the results of the multi-objective optimization using the secondary objective functions [O$_2$]. When looking at Figure 8.10f it is clear that increasing the ethane fraction drastically reduces the operating expenses (due to the higher cost of propane). The points with the highest operating expenses thus correspond to the highest propane fractions. From Figure 8.10b it is clear that at the same COT a higher ethene and propene production can be achieved by increasing the operating expenses (or thus the propane fraction). Increasing the propane fraction at the same COT thus results in higher operating expenses but also in more profit. The final

impact on the profit will thus be dependent on both the prices of ethene and propene but also of ethane and propane. The surface area of the COT is also significantly higher than all of the other cases studied. Next to the major impact of the COT on the total production capacity the additional parameter (ethane fraction) also has a major impact on the production capacity. Figure 8.10c and Figure 8.10d show the COP and the dilution respectively as function of the secondary first and third objective function. No real conclusions can be drawn based on these process variables as they are highly scattered between the lower and the upper bounds and have only little influence in comparison to the other parameters. Figure 8.10e shows the hydrocarbon mass flow rate as a function of the secondary first and third objective function [O_2]. In this case higher hydrocarbon mass flow rates seem to be preferred as they increase the total production of ethene and propene. Although they also increase the operating expenses. However the impact of the feedstock on the operating expenses is lower than in case of naphtha (see Section 8.3.1) which is more expensive than ethane and propane.
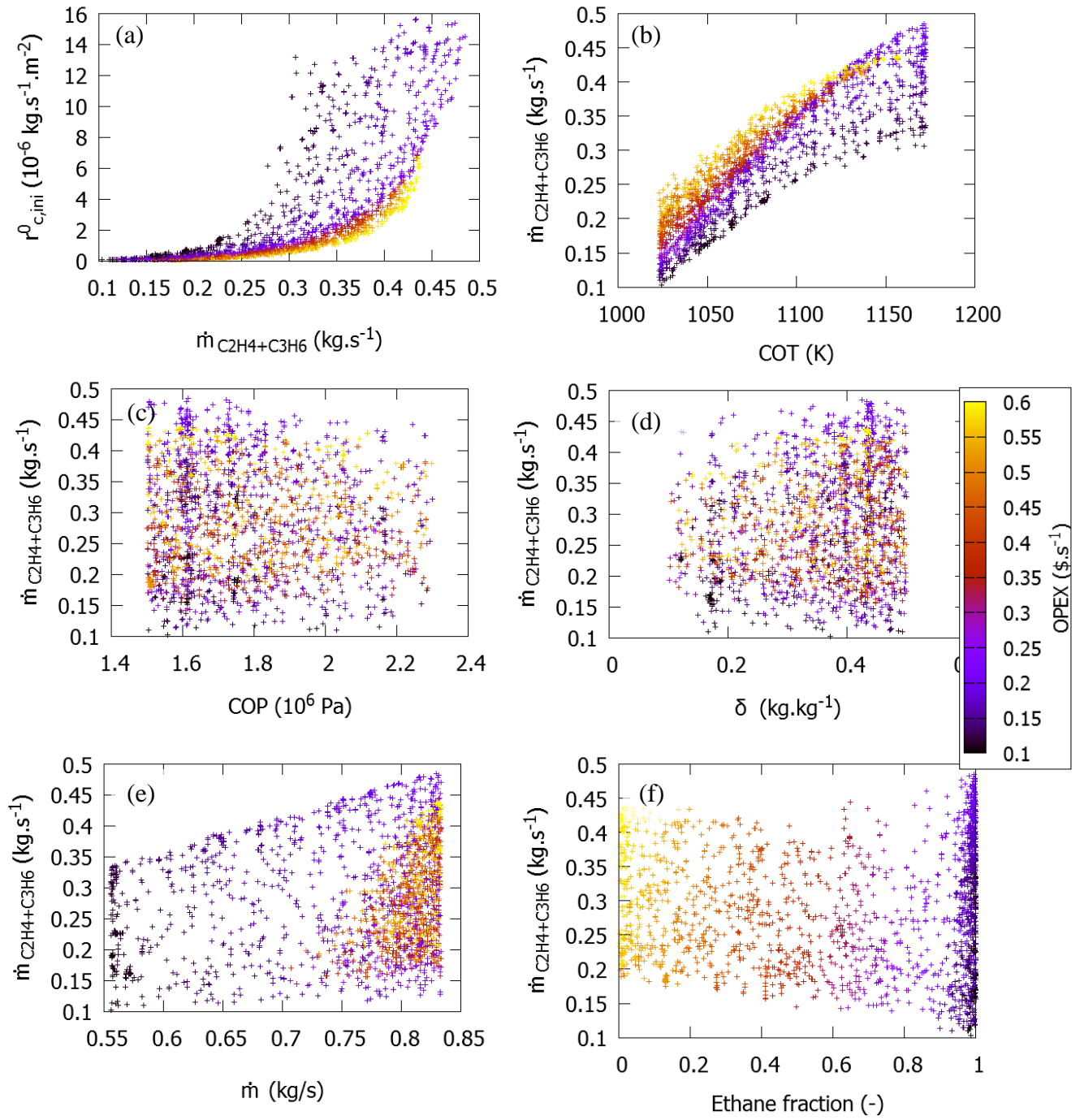
Figure 8.10: Pareto front and decision variables corresponding to the Pareto front using the secondary objective functions: Pareto front (a); COT (b); COP (c); Dilution (d); Mass flow rate (e); Ethane fraction (f)

Table 8.8: Optimal point based on gross profit (Equation 8.6) chosen from the Pareto front for the multi-objective optimization of the co-cracking of ethane and propane with the objectives defined by Equation 8.2, 8.3 and 8.5 [O_2]

Feedstock	COT (K)	COP (10^3 Pa)	δ (-)	$\dot{m}$ (kg.s^{-1})	C2H4 frac. (-)	O_{s1} (Eq. 8.6) (M\$.yr^{-1})
Ethane/Propane	1125	167	0.43	0.81	1.0	6.39

Table 8.8 shows the results when a single point is chosen from the Pareto front and at the current low prices of ethane compared to propane. Pure ethane is the preferred feedstock of choice even although simulations show that co-cracking of ethane and propane increases the selectivity towards ethene and propene. Due to the low price of ethane the gross profit is higher as compared to the naphtha case. In addition the reactor studies for ethane cracking allowed higher hydrocarbon mass flow rates to be used and thus a higher production capacity was possible. However there is still a major gap between the profit made by cracking ethane and the profit made by cracking naphtha. The prices of ethane are becoming so low, due to the shale gas developments in the USA, that even in Europe the transportation of ethane and the conversion to ethene is becoming beneficial (Longden, 2013).

8.4 Conclusion

Multi-objective optimization of industrial steam crackers was carried out using the elitist non-dominating genetic algorithm with adapted jumping gene operator (NSGA-II-aJG) coupled for the first time to a first principles-based model called COILSIM1D. Several multi-objective optimizations were carried out by changing the objectives, reactor geometries, operating point and the feedstocks.

In the first part two sets of objective functions were studied. The first objective set consisted of the sum of ethene and propene yield, the maximum value of the initial coking rate at a certain axial position, and the heat duty while the second set contained the total production of ethene and propene, the maximum initial coking rate and the operating expenses. It was shown that the maximum initial coking rate was a good indicator to estimate the run length of the furnace regardless of the feedstock used in the furnace.

Both optimizations showed that the COT was limited to a maximum temperature. In both cases lower COP's were preferred. For dilution an opposite conclusion was drawn for both sets of objective functions. In case of the primary objective (ethene and propene yield, coking rate and heat duty) functions lower dilutions seem preferred while in case of the secondary objective (ethene and propene production, coking rate, operating expenses) functions higher dilutions seem to be preferred. This was caused by the fact that increasing the dilution with the secondary objective functions only had a limited influence on the operating expenses while in case of the primary objective functions the impact on the heat duty was significant. Furthermore it was shown that both objective sets were representative for a single-objective optimization towards profit per unit feedstock as the Pareto front of both sets included the maximum found by single-objective optimization. However only the secondary objective set was representative for a single-objective optimization towards the gross profit of the furnace as the Pareto front included the maximum found by single-objective optimization.

When comparing two naphtha's with different amounts of naphthenic and aromatic compounds it was clear that the naphtha with the higher amount had a lower production of ethene and propene but also lower operating expenses since only a limited reaction heat was required for the aromatics. At the current prices however the naphtha with the lower amount of aromatics is still

preferred as the increase in aromatics and the decrease in operating expenses can compensate the reduced ethene and propene production.

Depending on the feedstock the COT, corresponding to points of the Pareto front, was limited by a maximum value which was lower than the imposed limits. An exception was ethane were the maximum temperature lay outside the COT interval allowed for the optimization. This maximum COT varied from 1118 K for gasoil to 1171 K. Lower COP's and higher dilutions were preferred in case of all feedstocks while the hydrocarbon mass flow rate was scattered between its boundaries.

When comparing a unit at start of run with a unit nearing its end of run it was clear that a higher COT and thus more heat input and a higher maximum initial coking rate was needed to obtain the same production capacity for ethene and propene but similar conclusions were drawn for the other process variables: lower COP and higher dilution were preferred. The generated profit of the optimal point also decreased by 10% when the unit is nearing decoking operations.

In case of co-cracking of ethane and propane the ethane fraction also became an important process variable as it has a significant influence on both the total production capacity of ethene and propene but also the operating expenses of the unit as propane is significantly more expensive than ethane. The COT remained the most important process variable but a higher scatter was observed for the COT when compared to all other optimizations due to the additional influence of the changing feedstock. Although the ethene and propene selectivity increases when co-cracking ethane and propane due to high price of propane compared to ethane remains the preferred feedstock.

8.5 References

Berreni, M., & Wang, M. (2011). Modelling and dynamic optimization of thermal cracking of propane for ethylene manufacturing. Computers & Chemical Engineering, 35, 2876-2885.

Clean Cities. (2013). Alternative Fuel Price Report: January 2013: U.S. Department of energy.

Eckart, Z., Kalyanmoy, D., & Lothar, T. (2000). Comparison of Multiobjective Evolutionary Algorithms: Empirical Results. Evolutionary computation, 8, 173-195.

Edwin, E. H., & Balchen, J. G. (2001). Dynamic optimization and production planning of thermal cracking operation. Chemical Engineering Science, 56, 989-997.

EIA. (2013).   http://www.eia.gov

Fadaee, M., & Radzi, M. A. M. (2012). Multi-objective optimization of a stand-alone hybrid renewable energy system by using evolutionary algorithms: A review. Renewable and Sustainable Energy Reviews, 16, 3364-3369.

Gao, X. D., Chen, B. Z., He, X. R., Qiu, T., Li, J. C., Wang, C. M., & Zhang, L. J. (2008). Multi-objective optimization for the periodic operation of the naphtha pyrolysis process using a new parallel hybrid algorithm combining NSGA-II with SQP. Computers & Chemical Engineering, 32, 2801-2811.

Ghashghaee, M., & Karimzadeh, R. (2011). Multivariable optimization of thermal cracking severity. Chemical Engineering Research and Design, 89, 1067-1077.

Guria, C., Bhattacharya, P. K., & Gupta, S. K. (2005). Multi-objective optimization of reverse osmosis desalination units using different adaptations of the non-dominated sorting genetic algorithm (NSGA). Computers & Chemical Engineering, 29, 1977-1995.

Kasat, R. B., & Gupta, S. K. (2003). Multi-objective optimization of an industrial fluidized-bed catalytic cracking unit (FCCU) using genetic algorithm (GA) with the jumping genes operator. Computers & Chemical Engineering, 27, 1785-1800.

Keyvanloo, K., Sedighi, M., & Towfighi, J. (2012). Genetic algorithm model development for prediction of main products in thermal cracking of naphtha: Comparison with kinetic modeling. Chemical Engineering Journal, 209, 255-262.

Kumar, P., & Kunzru, D. (1985). Modeling of naphtha pyrolysis. Industrial & Engineering Chemistry Process Design and Development, 24, 774-782.

Lim, H., Choi, J., Realff, M., Lee, J. H., & Park, S. (2006). Development of optimal decoking scheduling strategies for an industrial naphtha cracking furnace system. Industrial & Engineering Chemistry Research, 45, 5738-5747.

Lim, H., Choi, J., Realff, M., Lee, J. H., & Park, S. (2009). Proactive Scheduling Strategy Applied to Decoking Operations of an Industrial Naphtha Cracking Furnace System. Industrial & Engineering Chemistry Research, 48, 3024-3032.

Liu, C. W., Zhang, J., Xu, Q., & Li, K. Y. (2010). Cyclic scheduling for best profitability of industrial cracking furnace system. Computers & Chemical Engineering, 34, 544-554.

Longden, R. (2013). INEOS Europe and Evergas enter into long-term shipping agreements. http://www.ineos.com/nl/News/Shared-News/INEOS-Europe-and-Evergas-enter-into-long-term-shipping-agreements/

Nabavi, S. R., Rangaiah, G. P., Niaei, A., & Salari, D. (2009). Multiobjective Optimization of an Industrial LPG Thermal Cracker using a First Principles Model. Industrial & Engineering Chemistry Research, 48, 9523-9533.

Nabavi, S. R., Rangaiah, G. P., Niaei, A., & Salari, D. (2011). Design Optimization of an LPG Thermal Cracker for Multiple Objectives. *International Journal of Chemical Reactor Engineering, 9,* 1-34.

Nakamura, D. N. (2007). Global ethylene capacity increases slightly in 2006. *Oil & Gas Journal, 105,* 46-52.

Platts. (2013). http://www.platts.com/

Rada-Vilela, J., Chica, M., Cordón, Ó., & Damas, S. (2013). A comparative study of Multi-Objective Ant Colony Optimization algorithms for the Time and Space Assembly Line Balancing Problem. *Applied Soft Computing, 13,* 4370-4382.

Ren, T., Patel, M., & Blok, K. (2006). Olefins from conventional and heavy feedstocks: Energy use in steam cracking and alternative processes. *Energy, 31,* 425-451.

Schaefer, K. (2013). A Different Way To Invest in Natural Gas Stocks.   http://oilandgas-investments.com/2013/investing/stocks-canada-producers-part2/

Singh, J., Kumar, M. M., Saxena, A. K., & Kumar, S. (2005). Reaction pathways and product yields in mild thermal cracking of vacuum residues: A multi-lump kinetic model. *Chemical Engineering Journal, 108,* 239-248.

Tan, F., & Peng, S. L. (2014). Exxon starts world's 1st crude-cracking petrochemical unit. http://uk.reuters.com/article/2014/01/08/exxon-singapore-petrochemical-idUKL3N0KH2VU20140108

Towfighi, J., Niaei, A., Karimzadeh, R., & Saedi, G. (2006). Systematics and modelling representations of LPG thermal cracking for olefin production. *Korean Journal of Chemical Engineering, 23,* 8-16.

van Goethem, M. W. M., Barendregt, S., Grievink, J., Moulijn, J. A., & Verheijen, P. J. T. (2010). Model-based, thermo-physical optimisation for high olefin yield in steam cracking reactors. *Chemical Engineering Research and Design, 88,* 1305-1319.

Wang, X., & Tang, L. (2013). Multi-objective Operation Optimization of Naphtha Pyrolysis Process using a Parallel Differential Evolution. *Industrial & Engineering Chemistry Research,* 14415–14428.

Yao, D., & Ionel, D. M. (2013). A Review of Recent Developments in Electrical Machine Design Optimization Methods With a Permanent-Magnet Synchronous Motor Benchmark Study. *Industry Applications, IEEE Transactions on, 49,* 1268-1275.

Zimmermann, H., & Walzl, R. (2000). Ethylene. *Ullmann's Encyclopedia of Industrial Chemistry* (pp. 465-529): Wiley.

Chapter 9: GPU based simulations of reactive mixtures

9.1 Abstract

Incorporating detailed chemistry in solvers still remains a daunting and intractable task due to the prohibitive computational cost. However the combination of advanced mathematical solution techniques such as tabulation and calculating the analytical Jacobian in combination with efficient computational techniques that use the graphical processing unit (GPU) to do calculations can drastically speedup the simulation. These techniques are not mutually exclusive as is demonstrated for an ordinary differential equation (ODE) problem describing the classical adiabatic, constant-volume ignition of an equimolar methane/air mixture. Acceleration with up to a factor 120 can be obtained with the new algorithm compared to the algorithm employed in the reference solver. Maximum speedup is obtained in the case where the analytical Jacobian and the rates are calculated using the GPU when using intrinsic compiler functions to calculate transcendental functions which are used to calculate thermodynamic and kinetic coefficients. This is because the GPU can calculate transcendental functions significantly more efficient than a central processing unit (CPU).

9.2 Introduction

Accurate chemical kinetic models that incorporate detailed chemistry are extremely powerful and valuable. The use of these comprehensive reaction mechanisms is important as only these mechanisms grasp the essential chemistry and are valid over a wide range of process conditions. Many significant public policy and business decisions are made on the basis of kinetic model predictions. For example, the Montreal Protocol, which imposed a worldwide ban on certain halocarbons, was based on a kinetic model of the ozone layer (Halligudi et al., 2002). Also in the chemical industry these models are widely applied, e.g. in steam cracking of hydrocarbons (Dente et al., 1979; van Goethem et al., 2001) or in refining (Jaffe et al., 2005; Klein et al., 2006). For the oxidation of a variety of fuels comprehensive mechanisms have significantly improved the insight in many combustion phenomena (Law, 2007). Furthermore there is an urgent need of incorporating such detailed reaction mechanisms in more complex multidimensional simulations (Lu & Law, 2009) to assess the effect of the three-dimensional geometry on product yields. However, detailed modeling of complex kinetic mechanisms still remains a daunting task. The computational cost of a single reactor simulation rises quickly with the kinetic mechanism's size. The latter is particularly true for combustion, oxidation and pyrolysis mechanisms where considering several thousands of species is no exception owing to improved understanding of reaction families and availability of rate coefficients (Vinu & Broadbelt, 2012) for these free-radical dominating chemistries. This improved knowledge combined with the automation of reaction network generation through computer codes (Ranzi et al., 1995; Côme et al., 1996; Pierucci & Ranzi, 2008; Rangarajan et al., 2012a, 2012b; Vandewiele et al., 2012; Magoon & Green, 2013) has enabled the generation of large, comprehensive reaction mechanisms. However the time of a reactor simulation including these comprehensive mechanisms increases

significantly with the growing size of the mechanism (see Figure 9.1). The computer codes used

for this simulation must of course be able to be processed in a reasonable amount of time and

require only a minimum amount of memory storage while maintaining an adequate accuracy.

Speed is especially important when a simulator is used for online optimization of a running plant

(Pierucci et al., 1996). To be able to simulate these ever growing kinetic mechanisms the

development of approaches for improving the computational efficiency without sacrificing

accuracy is a necessity.
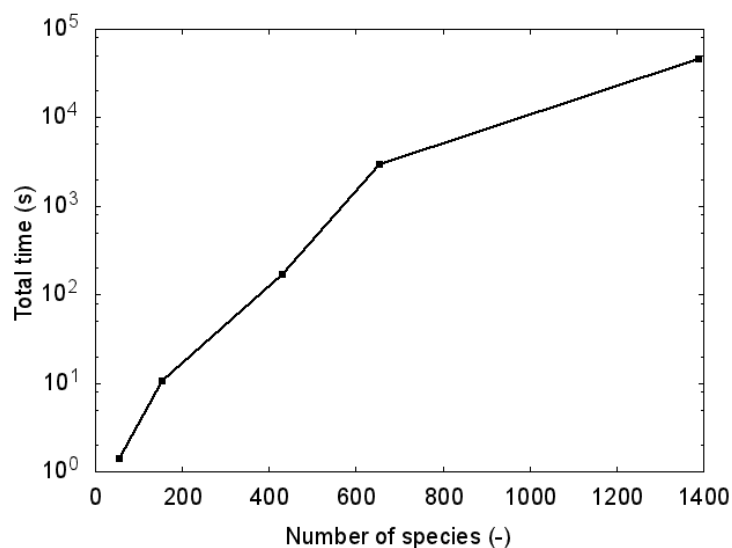
Figure 9.1: Total simulation time of an adiabatic, constant volume ignition of methane as function of the mechanism size using VODE.

A wide array of techniques for minimizing this computational cost is available in literature and

has been successfully applied (Pope, 1997; Shi et al., 2011; Perini et al., 2012). According to the

authors these techniques can be roughly divided into three different categories: chemical

techniques, mathematical techniques and computational techniques. The first category of

available techniques is the chemical technique. Here chemical knowledge about the mechanism is

used to simplify the kinetic mechanism. In a recent review regarding the state of combustion these techniques (Law, 2007) have been extensively discussed, and hence only a brief summary is presented below. Several skeletal reduction techniques have been developed to reduce the number of species and reactions by removing irrelevant species and reactions while keeping the error introduced by mechanism reduction under user defined values. Andreis et al. (2013) applied a reduction strategy on an ethanol combustion mechanism containing 56 species and 372 reactions and reduced it to a mechanism containing 11 species and 8 reactions. They reported a decrease in simulation time which is proportional to the number of elementary reactions removed from the full mechanism. Bhattacharjee et al. (2003) used mechanism reduction techniques on the GRImech 3.0 mechanism. They reported a reduction in solver time of a factor 3 when comparing the full mechanism with the reduced mechanism. Next to a-priori mechanism reduction it is also possible to do in-situ mechanism reduction, i.e. during simulation. He et al. (2011) applied an on-the-fly mechanism reduction approach to integrate a detailed n-heptane oxidation mechanism, with 653 species and 2827 elementary reactions, with a computational fluid dynamics (CFD) code and reported a speedup of a factor 18. Time-scale reduction techniques are also chemical techniques that comprise methods based on the quasi-steady-state assumption (QSSA) and methods using a partial equilibrium approach (PEA) (Bykov & Gol'dshtein, 2013). For example Zhang et al. (2013) applied the QSSA together with an on-the-fly reduction technique for the non-QSSA species and found a speedup of a factor 3 when appropriate QSS species were selected. Although several methods have been developed for the appropriate selection of QSS species (Turanyi & Toth, 1992; Turanyi et al., 1993; Lu et al., 2001), the selection of the QSS species remains largely dictated by a user-specified threshold value, and hence, expert user involvement .

The second category comprises the mathematical techniques focusing on speeding up both the integrator (e.g. different types of solvers) and/or function evaluations (e.g. by approximating computationally expensive functions) by improvement of the adopted algorithms. One of the most used mathematical techniques is in-situ adaptive tabulation (ISAT) (Pope, 1997). In ISAT, variables that are otherwise difficult to calculate, e.g. reaction rates, are tabulated in-situ and stored for later use. If the variable needs to be calculated again later in the same region of the mapping space, the value of the variable can be calculated using an interpolation technique. Pope (1997) used an adapted ISAT method to do perform reactive flow calculations and tested it for non-premixed methane–air combustion in a statistically homogeneous turbulent reactor, reporting a speedup of a factor 1000 compared to the reference simulation. However ISAT is usually limited by the mechanism size since mechanisms with more than 50 species tend to need a very large mapping space. As an example Ren et al. (2013) needed a mapping space of 500 Mbytes for a reaction mechanism containing only 31 species and 175 reactions. Therefore it is often combined with dimension and mechanism reduction techniques thus limiting the size of the mapping space. Hiremath and Pope (2013) combined ISAT with dimension reduction and reported a 40% reduction in simulation time compared to the algorithm which only uses ISAT. Ren et al. (2013) used a reduced version of the GRI-Mech 1.2 mechanism and combined it with ISAT to simulate a bluff-body-stabilized non-premixed flame with the eddy dissipation concept (EDC) and transported probability density function (PDF) combustion models. They reported a speed up factor of 3 compared to the full mechanism without using ISAT.

Both the chemical techniques and the mathematical described ISAT technique introduce small but acceptable errors to the integration procedure. However other techniques are available which do not introduce any additional error. One such mathematical technique is applied by Perini et al.

(2012) and uses an analytical Jacobian for the solvers instead of a Jacobian calculated by finite differences. They reported that the final code was 80% faster than the original code where the Jacobian was calculated using finite differences.

The third category of computational techniques maximizes the algorithm's efficiency on state-of-the-art computer hardware and doesn't introduce any error either. One such computational method was applied by Shi et al. (2011). Shi et al. applied CPU/GPU hybrid calculations where the GPU is used to calculate the reaction rates. They reported a speedup of up to a factor 16 compared to the pure CPU algorithm. Similarly Zhang et al. (2011) developed a parallel implementation of a CO_2 sequestration simulator. They reported a speedup of a factor 64 when modern GPU technology is used as compared to a single-core CPU. In Chapter 6 the use of the GPU for the calculations of the viscosity in COILSIM1D also falls under this category.

Combination of different types of techniques has been reported to a limited extend (Hiremath & Pope, 2013; Zhang et al., 2013). However, to the authors' knowledge no extensive study on the combination of computational and mathematical techniques has been carried out. It is clear that the combination of these techniques could further accelerate simulations for large size mechanisms. For this purpose first the a priori tabulation, using an analytical Jacobian and using the GPU for part of the calculations were separately studied. In this chapter no chemical techniques such as network reductions and QSSA have been studied. The chosen techniques do not require extensive knowledge about the chemical mechanisms and they are independent of the adopted mechanism. The mechanisms size varies from 56 to near 3000 species. Secondly, two by two combinations of these techniques are evaluated and compared with a combination in which all three are employed simultaneously. Before testing these different speedup approaches the most efficient stiff solver for our problem was selected among LSODA, LSODE, LSODES

(Hindmarsh, 1983), RADAU5 (Hairer, 2010), VODE (Brown et al., 1989), and DASPK (Brown et al., 1994) codes.

9.3 Methodology

The time evolution in a batch reactor of an adiabatic, constant volume ignition of an stoichiometric methane/air mixture is considered as demonstration case. The solution of this problem corresponds to the solution of a set of differential equations describing the conservation laws of mass and energy. The main dependent variables of the described set of ODE's are the concentrations (C) of the reacting species and the average temperature (T) of the system. The reaction mechanism consists of n_r reactions which involve n_s chemical species. Each reaction can be written as:

$$\sum_{i=1}^{n_s} v'_{k,i} R_i \; \rightleftharpoons \; \sum_{i=1}^{n_s} v''_{k,i} R_i \tag{9.1}$$

Where v' are the forward stoichiometric coefficients (negative) and v'' are the backward stoichiometric coefficients (positive) and R is the name of the species. Note that the applied methodology can be adjusted for other reactor geometries or multidimensional simulations.

9.3.1 Mass and energy balances

The reaction mechanism in Equation 9.1 leads to n_s mass balances. The latter can be described by the following set of ODE's:

$$\frac{dC_i}{dt} = \sum_{k=1}^{n_r} (v''_{k,i} + v'_{k,i}) r_k(\mathbf{C}, T) \tag{9.2}$$

with r_k the reaction rate of reaction k. The reaction rates are however dependent on both the temperature and the concentrations. Four different types of reaction formulations are studied in

order to account for temperature dependence, third body reactions and pressure dependence. All

of these reactions follow the law of mass action. For reaction k this can be written as:

$$r_k(\mathbf{C}, T) = k_{f,k} \prod_{i=1}^{n_S} (C_i)^{-v'_{k,i}} - k_{b,k} \prod_{i=1}^{n_S} (C_i)^{v''_{k,i}} \tag{9.3}$$

Both the forward and the backward rate coefficients can be expressed by a modified Arrhenius

law:

$$k_{f,k}(T) = A_k . T^{b_k} . exp\left(\frac{E_k}{R.T}\right) \tag{9.4}$$

On many occasions the backward rate coefficient is calculated using thermodynamic consistency:

$$k_{b,k}(T) = \left.k_{b,k}(T)\middle/ Kc_{eq,k}(T)\right. \tag{9.5}$$

$$Kc_{eq,k}(T) = \exp(-\Delta G_k^0(T)) . \left(\frac{p_{atm}}{R.T}\right)^{\sum_{i=1}^{n_S}(v''_{k,i}+v'_{k,i})} \tag{9.6}$$

$$\Delta G_k^0(T) = \sum_{i=1}^{n_S} (v''_{k,i} + v'_{k,i}) g_i^0(T) \tag{9.7}$$

$$g_i^0(T) = \frac{h_i^0(T)}{RT} - \frac{s_i^0(T)}{R} \tag{9.8}$$

The thermodynamic properties h_i^0 and s_i^0 can be calculated using JANAF polynomials (Chase et

al., 1982). In case of an irreversible reaction $k_{b,k}$ is set equal to zero. It is however possible that

for some reactions the presence of other molecules in the mixture enhances the reaction rate, e.g.

so called third-body reactions. In this case the expression for the reaction rate is extended to:

$$r_k^{TB}(\mathbf{C}, T) = M_{eff}(\mathbf{C}, T) . r_k(\mathbf{C}, T) \tag{9.9}$$

$$M_{eff}(\mathbf{C}, T) = \sum_{i=1}^{n_S} \alpha_i C_i \tag{9.10}$$

with α_i the enhanced molecular reaction coefficients.

The last type of reaction rate expressions is the one where the simple modified Arrhenius form is not sufficient to describe the changes in reaction rates with the pressure. In these cases two kinetic rate coefficients describe the low $(k_{f,k}^0)$ and high pressure limits $(k_{f,k}^\infty)$ for the forward reaction rates. The effective reaction rate can be calculated as:

$$k_{f,k}(\boldsymbol{C},T) = k_{f,k}^\infty(T).F_k(\boldsymbol{C},T) \tag{9.11}$$

Two distinct forms for F_k can be written. The first form is the Lindemann's kinetic law form:

$$F_k^{Lind}(\boldsymbol{C},T) = Pr_k(\boldsymbol{C},T)/(1 + Pr_k(\boldsymbol{C},T)) \tag{9.12}$$

With Pr_k is the reduced pressure:

$$Pr_k(\boldsymbol{C},T) = \frac{M_{eff}(\boldsymbol{C},T).k_{f,k}^0(T)}{k_{f,k}^\infty(T)} \tag{9.13}$$

The second form is Troe's kinetic law form (Gardiner & Troe, 1984; Berger & Marin, 1999):

$$F_k^{Troe}(\boldsymbol{C},T) = \frac{Pr_k(\boldsymbol{C},T)}{1 + Pr_k(\boldsymbol{C},T)}.10^{\log(F_k^{TROE}(\boldsymbol{C},T))} \tag{9.14}$$

$$log_{10}F_k^{TROE}(\boldsymbol{C},T) = \cfrac{log_{10}F_{cent}(T)}{1 + \left[\cfrac{log_{10}Pr_k(\boldsymbol{C},T) + c_k(T)}{N_k(T) - d_k\left(log_{10}F_{cent}(T) + c_k(T)\right)}\right]^2} \tag{9.15}$$

$$c_k(T) = -0.4 - 0.67.log_{10}F_{cent}(T) \tag{9.16}$$

$$N_k(T) = 0.75 - 1.27.log_{10}F_{cent}(T) \tag{9.17}$$

$$d_k(T) = 0.14 \tag{9.18}$$

$$F_{cent}(T) = (1-a).exp\left(\frac{-T}{T^{***}}\right) + a.exp\left(\frac{-T}{T^*}\right) + exp\left(\frac{-T}{T^{**}}\right) \tag{9.19}$$

Where a, T^*, T^{**}, T^{***} are specified in the kinetic input file. The last term of Equation 9.19 is optional and is omitted if T^{**} is equal to zero.

In addition to the mass balances the energy balance can be written as:

$$\frac{dT}{dt}(\boldsymbol{C},T) = -\frac{1}{\overline{c_v}(\boldsymbol{C},T)}\sum_{i=1}^{n_s}\left(\frac{u_i(T)}{M_i} - \frac{M_i}{\rho}\frac{dC_i}{dt}(\boldsymbol{C},T)\right) \tag{9.20}$$

With M_i the molar mass of the species and ρ the density of the system. Since the reactor is a batch reactor the density is constant and can be calculated at the beginning of the simulation. $\overline{c_v}$ is the mixture average constant volume heat capacity which can be calculated as:

$$\overline{c_v(\boldsymbol{Y},T)} = \sum_{i=1}^{n_s}\frac{C_i c_{v,i}}{\rho} \tag{9.21}$$

Both c_v and u can be calculated using JANAF polynomials (Chase et al., 1982).

9.3.2 Solvers and solution methods

Equations 9.2 to 9.21 describe a set of $n_s + 1$ ODE's that can be solved numerically when the initial conditions are given. It is well known that the ODE's for combustion, partial oxidation or pyrolysis result in a set of stiff ordinary differential equations (ODEs) due to the distinct reactivity of radicals and molecules leading to a large separation in time-scales. Obtaining the solution of these equations requires the use of so-called stiff solvers. Over the last three decades a wide variety of very efficient and reliable stiff ODE solvers has been developed. In this chapter six different solvers were evaluated: LSODA, LSODE, LSODES, RADAU5, VODE and DASPK. LSODE combines the capabilities of the former GEAR and GEARB solvers. It solves explicitly given stiff and non-stiff equations (decided a priori by the user) and for stiff equations it can treat the Jacobian matrix as both a full matrix or a banded matrix (Hindmarsh, 1983). LSODES is similar to LSODE but in case of stiff equations the Jacobian is treated as a general sparse matrix (Hindmarsh, 1983). LSODA is yet another variant of LSODE. LSODA switches automatically between non-stiff (Adams-Moulton) and stiff (backward differentiation) methods. The solver

always starts using non-stiff methods (Hindmarsh, 1983). The fourth solver is RADAU5 which uses a 5th order implicit Runge-Kutta method to integrate the problem (Hairer, 2010). The fifth solver is VODE. It uses variable-coefficient Adams-Moulton and backward differentiation methods in Nordsieck form (Brown et al., 1989). The last solver DASPK is a DAE solver which uses variable-order variable-stepsize backward differentiation to integrate the problem (Shengtai & Linda, 1999). So all solvers except RADAU5 are based on a similar method however there are small in implementation (e.g. the Jacobian update criteria) which can influence the efficiency of these solvers for the problem at hand. The used solvers are almost the same as those studied by Klein et al. (2006) except for VODE and DASPK.

For all solvers the relative and absolute tolerance was set to 10^{-4} and to 10^{-13} respectively for all integrated variable. In case of DASPK no preconditioning was used to make a fair comparison.

9.3.3 Jacobian formulation

The Jacobian J of the ODE's (H) is a $(n_s+1) \times (n_s+1)$ matrix where each element is calculated by:

$$J_{ij} = \frac{\partial H_i}{\partial Z_j}(\mathbf{Z}) \tag{9.22}$$

Two distinct types of derivatives can be written: one with respect to the concentration of a species i (C_i) and one with respect to the temperature (T). For the full derivation of each of the Jacobian elements see Perini et al. (2012). Only an overview of the used equations is given here.

Derivatives with respect to the concentrations

The upper left part of the Jacobian consists of the derivatives of rates of formation of the species to the concentration of the species:

$$J_{ij} = \sum_{k=1}^{n_r} \left(\nu_{k,i} \cdot \frac{\partial r_k}{\partial C_j} \right) \tag{9.23}$$

Since there are three different forms for the rate expression, three different derivatives for the rate with respect to the concentration need to be derived. For the modified Arrhenius the following equation is obtained:

$$\frac{\partial r_k}{\partial C_j} = \frac{-1}{C_j} \left(\nu'_{k,j} \cdot r_{f,k} + \nu''_{k,j} \cdot r_{b,k} \right) \tag{9.24}$$

This formulation can further be used in the more complex rate equations. The expression for a third body reaction can be written as:

$$\frac{\partial r_k^{TB}}{\partial C_j} = r_k \cdot \frac{\partial M_{eff}}{\partial C_j} + M_{eff} \cdot \frac{\partial r_k}{\partial C_j} \tag{9.25}$$

$$\frac{\partial M_{eff}}{\partial C_j} = \alpha_j \tag{9.26}$$

For a pressure dependent reaction a similar expression can be derived:

$$\frac{\partial r_k^{PD}}{\partial C_j} = r_k \cdot \frac{\partial F_k^{PD}}{\partial C_j} + F_k^{PD} \cdot \frac{\partial r_k}{\partial C_j} \tag{9.27}$$

For reactions which follow Lindemann's kinetic law the following equation can be written:

$$\frac{\partial F_k^{PD,Lind}}{\partial C_j} = \frac{\partial M_{eff,k}}{\partial C_j} \cdot \frac{k_{f,k,0} \cdot k_{f,k,\infty}}{\left(k_{f,k,0} \cdot M_{eff,k} + k_{f,k,\infty} \right)^2} \tag{9.28}$$

while for Troe's kinetic law Equation **9.29** is obtained.

$$\frac{\partial F_k^{PD,Troe}}{\partial C_j} = F_k^{Troe} \cdot \left(\frac{\partial M_{eff,k}}{\partial C_j} \cdot \frac{k_{f,k,0} \cdot k_{f,k,\infty}}{\left(k_{f,k,0} \cdot M_{eff,k} + k_{f,k,\infty} \right)^2} + \frac{Pr_k(\mathbf{C},T)}{1 + Pr_k(\mathbf{C},T)} \cdot \ln(10) \cdot \frac{\partial log_{10}(F_k^{PD,Troe})}{\partial C_j} \right) \tag{9.29}$$

The derivation of $\frac{\partial log_{10}(F_k^{PD,Troe})}{\partial C_j}$ is extensive and thoroughly described by Perini et al. (2012).

For the differentiation of the change in temperature with respect to the concentrations or the left side of last row of the Jacobian, Equation 9.30 is used.

$$J_{n_s+1,j} = \frac{-1}{\overline{c_v} \cdot \rho}\left(c_{v,j} \cdot \frac{dT}{dt} + \sum_{i=1}^{n_s} u_i \cdot J_{i,j}\right) \tag{9.30}$$

Derivatives with respect to the temperature

The right part of the last column consists of the derivatives of the rate of formation of the species to the temperature and is given by Equation 9.31.

$$J_{i,n_s+1} = \sum_{k=1}^{n_r} v_{k,i} \cdot \frac{\partial r_k}{\partial T} \tag{9.31}$$

$$\frac{\partial r_k}{\partial T} = \frac{\partial k_{f,k}}{\partial T} \cdot \prod_{r=1}^{n_s}(C_r)^{-v'_{k,r}} - \frac{\partial k_{b,k}}{\partial T} \cdot \prod_{r=1}^{n_s}(C_r)^{v''_{k,r}} \tag{9.32}$$

For the modified Arrhenius form the derivative of the rate coefficient can be written as:

$$\frac{\partial k_{f,k}}{\partial T} = \frac{k_{f,k}}{T} \cdot \left(b_k + \frac{E_k}{R \cdot T}\right) \tag{9.33}$$

If the backward rate coefficient is calculated by thermodynamic consistency the expression for the backward rate coefficient becomes:

$$\frac{\partial k_{b,k}}{\partial T} = \frac{1}{Kc_{eq,k}} \cdot \left(\frac{\partial k_{f,k}}{\partial T} + k_{f,k} \cdot \left[\frac{\sum_{j=1}^{n_s}(v''_{k,j} + v'_{k,j})}{T} + \frac{\partial \Delta G_k^0}{\partial T}\right]\right) \tag{9.34}$$

For third body reactions the effective molecularity is independent of the temperature and the following equation can be derived:

$$\frac{\partial r_k^{TB}}{\partial T} = \frac{\partial r_k}{\partial T} \cdot M_{eff,k} \tag{9.35}$$

For pressure dependent reactions the derivative can be written as:

$$\frac{\partial r_k^{PD}}{\partial T} = \frac{\partial r_k}{\partial T} \cdot F_k^{PD} + \frac{\partial F_k^{PD}}{\partial T} \cdot r_k \tag{9.36}$$

Where $\frac{\partial F_k^{PD}}{\partial T}$ can be calculated for Lindemann's rate expression by:

$$\frac{\partial F_k^{PD,Lind}}{\partial T} = \frac{M_{eff,k}}{\left(k_{f,k,\infty} + M_{eff,k} \cdot k_{f,k,0}\right)^2} \cdot \left(k_{f,k,\infty} \cdot \frac{\partial k_{f,k,0}}{\partial T} - k_{f,k,0} \cdot \frac{\partial k_{f,k,\infty}}{\partial T}\right) \tag{9.37}$$

and for Troe's rate expression:

$$\frac{\partial F_k^{PD,Troe}}{\partial T} = F_k^{Troe} \cdot \left(\frac{\partial F_k^{PD,Lind}}{\partial T} + \ln(10) \cdot \frac{\partial \log(F_k^{Troe})}{\partial T}\right) \tag{9.38}$$

For the extensive derivation of $\frac{\partial \log(F_k^{Troe})}{\partial T}$ reference is again made to Perini et al. (2012). The last

derivative is the bottom right element of the analytical Jacobian:

$$J_{n_s+1,n_s+1} = \frac{-1}{\bar{c}_v} \left[\frac{dT}{dt} \cdot \sum_{i=1}^{n_s} \left(\frac{C_i}{\rho} \cdot \frac{\partial C_{v,i}}{\partial T}\right) + \sum_{i=1}^{n_s} \left(\frac{1}{\rho} \cdot \left\{c_{v,i} \cdot \frac{dC_i}{dT} + U_i \cdot J_{i,n_s+1}\right\}\right)\right] \tag{9.39}$$

9.3.4 Tabulation

One of the approaches to increase the efficiency of the algorithms is tabulation of variables which are time consuming to calculate. Tabulation has been adopted for a long time (Magnuson, 1964; Bird, 1980; Pope, 1997; Ren et al., 2013) and it can be seen that tabulation for recursive functions, e.g. Fibonacci's function, where previously tabulated numbers can be used to calculate the following numbers can be quite efficient. However this can easily be extended to more complex functions which are tabulated at certain values of the independent variable(s). To get the function value between tabulated values a simple interpolation function is needed (Dorman et al., 1991). In our case a polynomial interpolation is used:

$$y = \sum_{i=1}^{n} y_i \cdot \prod_{\substack{j=1 \\ j \neq i}}^{n} \frac{(x - x_j)}{(x_i - x_j)} \tag{9.40}$$

Where y is the dependent variable, x is the independent variable and n is the order of interpolation. Three different orders of interpolation were studied: first order or linear interpolation, second order or parabolic interpolation and fourth order interpolation. Although many compilers nowadays have mathematical libraries that are efficient at solving some of these complex functions (e.g. the exponential function) tabulation remains more efficient but with a slight loss in accuracy (Yamamoto et al., 2004). The accuracy of the interpolated value is of course dependent on both the grid distance of the table as well as the used interpolation method. Tabulation is still used for different applications including the evaluation of the rate coefficients (Pope, 1997; Scheuer et al., 2012). In reaction engineering most temperature-dependent functions such as species thermodynamic properties and rate coefficients as well as their derivatives require these demanding analytical evaluations, e.g. the exponential function, using intrinsic compiler functions. To alleviate these demanding calculations an a priori tabulation method was tested (entire table was created at the start of the simulation) for these temperature-dependent functions (internal energy, heat capacity, high pressure rate coefficient, low pressure rate coefficient, ck, Fk, equilibrium coefficient, derivative of the heat capacity and the derivative of the equilibrium coefficient) using the described interpolation methods and different grid distances. Tabulation of functions which are only dependent on temperature decreases the mapping space needed as compared to mapping the reaction rates which are dependent on both temperature and concentration of the species as done by most authors using ISAT (Pope, 1997; Hiremath & Pope, 2013; Ren et al., 2013). The former reduced mapping space still allows tabulation to be used even for the larger sized mechanisms (more than 100 species).

9.3.5 Reformulation for GPU calculation

The time limiting factor when integrating a set of stiff ODE's is in most cases the evaluation of the rates of formation and the Jacobian (Manca et al., 2001). This is due to the fact that the evaluation of the rates and the Jacobian takes significant time and that these routines are called in the order of 100 times per simulation. Hence, decreasing the time spent in each subroutine can significantly speedup the calculations. It has been recently demonstrated that it is possible to rewrite the evaluation of the rates in such a way that they can be calculated on a GPU (Shi et al., 2011). In a similar way the evaluation of the analytical Jacobian can be done on a GPU. Running these calculations on a GPU can accelerate both subroutines significantly by exploiting the highly parallel structure of GPUs. However, the hardware used in a workstation by hybrid CPU/GPU calculations differs from the hardware used when doing classical CPU calculations.

Figure 9.2 shows a schematic overview of how the rate routine on the GPU works. In a first initialization step the parameters required to do the calculations (thermodynamic and kinetic parameters) are copied from the host memory (CPU) to the device memory (GPU) over a slow peripheral component interconnect (PCI) bus. Afterwards these parameters reside both in the host and device memory and are accessible to both CPU and GPU upon request. The GPU is used in each integration step for the rate of formation evaluation. Since the rate of formation evaluation requires both temperature and concentrations these are transferred from the host memory to the device memory in each integration step. The GPU can then use these variables together with the parameters to calculate the rates. The subroutine describing these calculations is called a kernel. The kernel writes the results, i.e. the rates of formation, back to the device memory. For the variables to be usable by the solver the rates of formation need to be transferred back from the device memory to the host memory. These steps are repeated for each integration step.
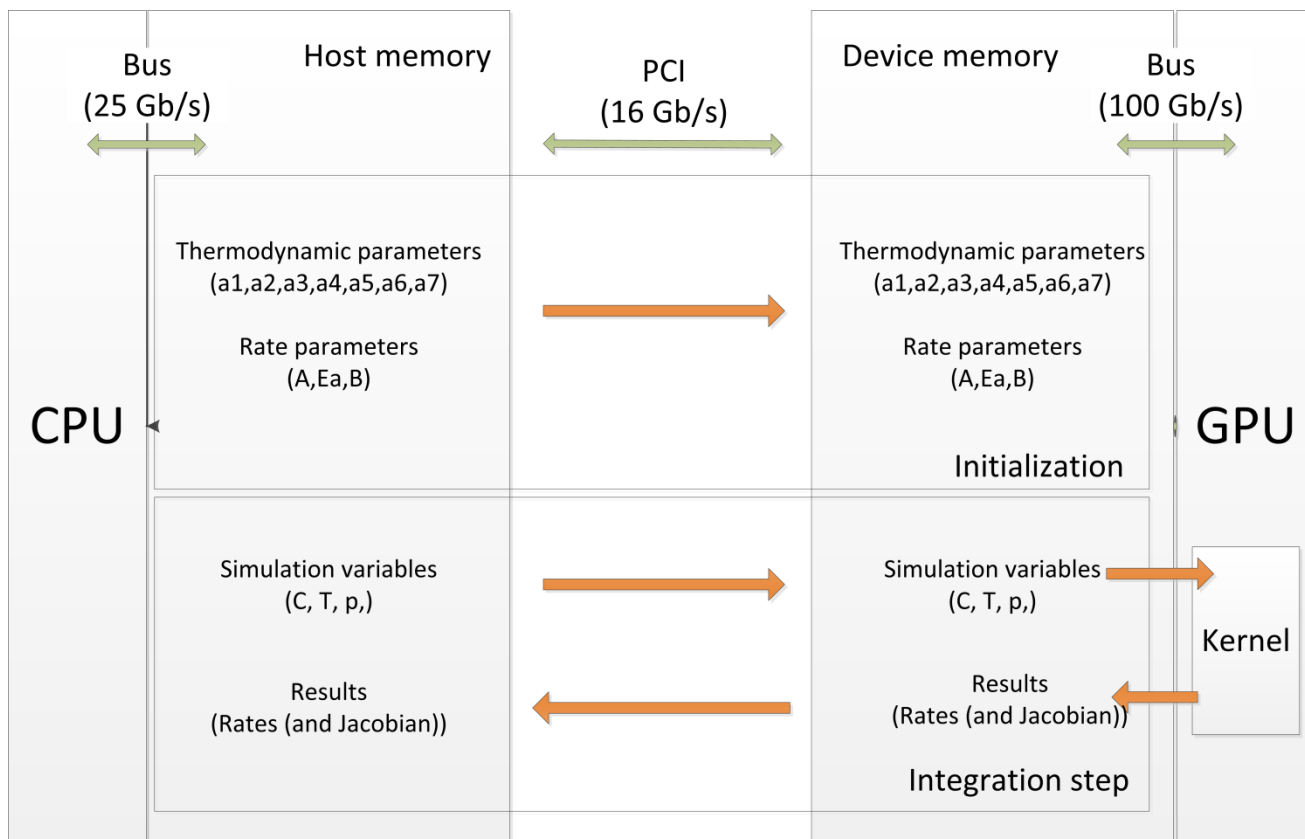
Figure 9.2: Schematic description of GPU rate of formation and Jacobian evaluation.

For the evaluation of the Jacobian there are theoretically two options. Either the Jacobian is evaluated on the CPU or the Jacobian is evaluated on the GPU. However if the Jacobian is calculated through finite differences by the solver it is approximated using $n_s + 1$ calls of the rate of formation evaluation subroutine which is already reformulated to run on the GPU. This approach is used by Shi et al. (2011) were SENKIN calculates the Jacobian by finite differences. If the Jacobian is calculated analytically it technically could be evaluated on the CPU separately. However this approach would need to transfer variables from the GPU to the CPU memory over a slow PCI connection because part of the variables used for the calculation of the Jacobian are already calculated in the rate of formation evaluation subroutine, e.g. reaction rates, thermodynamic coefficients, which is always called by the solver before the Jacobian subroutine.

Since the rate of formation evaluation subroutine is reformulated for the GPU these required variables would reside in the GPU memory and not in the CPU memory. Transferring these variables is a very slow process and thus undesirable. It is in addition very easy to parallelize the analytical evaluation of the Jacobian making it an ideal candidate for evaluation on the GPU. Taking both considerations into account the Jacobian subroutine was rewritten in a similar way as the rate subroutine, see Figure 9.2. To the authors' knowledge rewriting the evaluation of the Jacobian to be calculated on the GPU has never been done before.

Programming of these GPU kernels has become a lot easier since CUDA (Perini et al., 2012) from NVidia has been released. CUDA or Compute Unified Device Architecture is a parallel computing platform and programming model created by NVIDIA and implemented by the graphics processing units (GPUs) that they produce. Nowadays CUDA has language extensions for CUDA C/C++ and CUDA Fortran ("CUDA Fortran: Programming guide and reference," 2012).

In addition of running the evaluation of the rates and the Jacobian on the GPU the solvers themselves were also adapted to run the LU-decomposition of the Jacobian on the GPU as was done by Shi et al. (2011). The GPU version of the LU-decomposition algorithm was taken from CULA (CULA_dgetrf) and interfaced to the routines used by the solvers.

9.3.6 Reaction mechanisms

In this evaluation combustion mechanisms of different sizes available in literature were used. The first mechanism used is the ethanol mechanism. The ethanol mechanism is a kinetic model for the study of ethanol oxidation (Marinov, 1999). It consists of 56 species interacting in 351 reversible reactions. The second mechanism is the butane mechanism. It has been developed to investigate aromatic and polycyclic aromatic hydrocarbon (PAH) formation pathways in a premixed, rich,

sooting, n-butane–oxygen–argon burner stabilized flame (Marinov et al., 1998) . It consists of 156 species and 680 reactions. The third mechanism used is the butanol mechanism (Sarathy et al., 2012). It is a chemical kinetic model developed for the oxidation for all four butanol isomers. It consists of 436 species and 2335 reactions. The next two mechanisms describe the combustion of heptane and gasoline respectively (Mehl et al., 2011). The heptane mechanism consists of 654 species undergoing 5258 reactions. It is part of the gasoline mechanism which contains 1550 species undergoing 6000 reactions. The last mechanism used was the methyl decanoate mechanism. It is used to study the oxidation of methyl decanoate, a surrogate for biodiesel fuels. It contains 3012 species and 8820 reactions. Table 9.1 gives an overview of the mechanisms used. To make a fair comparison regardless of the mechanism size it was opted to study the same problem in all mechanisms. All mechanisms where thus used to study the stoichiometric combustion of methane with air was studied. Initial temperature and pressure were set at 1500 K and 20.10^5 Pa respectively.

Table 9.1: Overview of used kinetic mechanisms

Model	Number of species	Number of reactions	Reference
Ethanol	56	351	(Marinov, 1999)
Butane	156	680	(Marinov et al., 1998)
Butanol	426	2335	(Sarathy et al., 2012)
Heptane	654	5258	(Mehl et al., 2011)
Gasoline	1550	6000	(Mehl et al., 2011)
Methyldecanoate	3012	8820	(Herbinet et al., 2008)

9.3.7 Hardware and software

All simulations were carried out on a dedicated Window 7 (64 bit) workstation equipped with an Intel Xeon E5620 CPU and 6 GB or RAM memory. In addition an NVIDIA Tesla C2075 card was installed for the GPU calculations. All code was compiled with PGI visual FORTRAN (v11.10) for Windows with O3 optimization and the CUDA Fortran language extensions option enabled. The CUDA 4.0 toolkit was used.

9.4 Results and discussion

9.4.1 Solver selection

Figure 9.3 shows a comparison of the different solvers regarding total simulation time and the number of evaluations needed. As can be seen all the solvers follow the same trend when the mechanism size increases. Increasing mechanism size results into more rate of formation evaluations (Figure 9.3b) but a similar amount of Jacobian evaluations (Figure 9.3c). More rate of formation evaluations of course result into a larger simulation time (Figure 9.3a). The additional rate of formation evaluations seem to be mainly caused by the larger Jacobian that needs to be evaluated by finite differences. In Figure 9.3d only the rate of formation evaluations that are not used for the evaluation of the Jacobian are shown. This number remains almost unchanged. LSODA performs poorest of all tested solvers. The second to poorest solver is RADAU5 which is followed by LSODE and LSODES. The competition between LSODE and LSODES seems to be dependent on the mechanism used for the simulation, with a slightly better overall performance of LSODE. The two best solvers are VODE and DASPK with the better performance for the former. Figure 9.3c and d clearly show that the better performance of VODE is due to the lower number of rate of formation evaluations and Jacobian evaluations that are

required before convergence is reached. This difference can be attributed to the slightly different methods all of these solvers use. RADAU5 which does not use a backward differentiation method is with the exception of LSODA the worst solver. LSODA's lack of efficiency is most likely related to the fact that the problem is initially being solved with a non-stiff method while the problem at hand is stiff. The results are slightly different than those obtained by Klein et al. (2006) who established the following order: LSODES > LSODE > LSODA > DASSL (predecessor of DASPK). The extension of DASSL namely DASPK seems to have improved efficiency compared to the older DASSL code based on the present results. VODE was not studied by Klein et al. (2006).

For the VODE solver a power function can be fitted through the total simulation time (t) as function of the total number of species in the mechanism (n_s). Equation 9.41 describes the data with the square of the multiple correlation coefficient (R^2) equal to 0.98:

$$t = n_s^{3.29}.10^{-6}$$

<div align="right">**(9.41)**</div>

Equation 9.41 can be used to assess the efficiency gain when mechanism reduction techniques are applied using the VODE integration procedure. It is clear that depending on the number of species that can be eliminated efficiency gains can be significant.
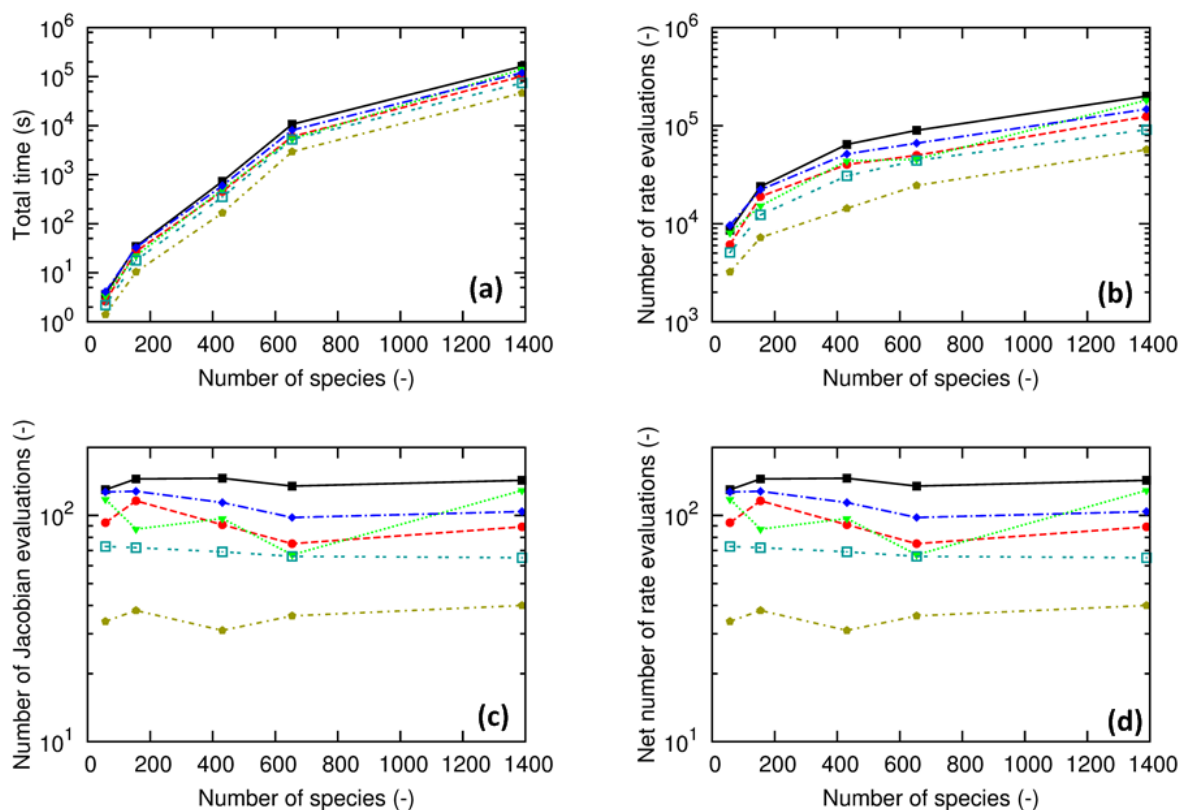
Figure 9.3: (a) total time, (b) number of rate of formation evaluations, (c) number of Jacobian evaluations and (d) Net number of rate of formation evaluations for different solvers.

LSODA; ■, LSODE; ●, LSODE; ▽, RADAU5; ◆, VODE; ⬠, DASPK; ⊟.

The same trends in solver efficiency improvement were observed even for all solvers when different speedup methodologies were evaluated. Therefore in the remainder of this work the discussion has been limited to the most efficient solver for our case, i.e. VODE. However, the results also hold for the other solvers. Note that all these solvers use the same routines for reaction rates, Jacobian and LU decompositions and therefore the time for rate of formation evaluations, Jacobian evaluations and LU decompositions is recalculated for a single evaluation.

9.4.2 Tabulation

Figure 9.4c shows the increased efficiency of a single function evaluation for a heat capacity, a rate coefficient and an equilibrium coefficient for different interpolation methods. This increased efficiency comes at a cost of accuracy. Figure 9.4a shows the relative error of using different interpolation methods and Figure 9.4b shows the error using different tabulation intervals. Higher order interpolation and smaller tabulation intervals typically yield more accurate results. Fourth order interpolation is used throughout the rest of the chapter since the increased accuracy only results in a slight increase in time compared to the first order interpolation. The tabulation interval was chosen to be 10 K because it yields accurate results and because smaller tabulation intervals (5 K and 1 K) result in visible errors due to machine precision.

Though the function evaluation using tabulation is significantly faster, it has to be kept in mind that intrinsic compiler function evaluations are still needed to construct the lookup table. If more or an equal number of intrinsic function evaluations are necessary to construct the table than those that are needed for the integration procedure the program could still slow down. For this reason the table was kept as narrow as possible. Figure 9.5 shows the effect of the improved efficiency when using tabulated functions instead of intrinsic functions of the compiler. The total simulation time is broken down in to the time needed for integration, rate of formation evaluation, Jacobian evaluation and LU decomposition. The acceleration by using tabulation seems to be slightly increasing with the mechanism size, i.e. a factor 1.5 for the smallest mechanism (Figure 9.5b) up to a factor 2.5 for the largest mechanism (Figure 9.5d). The time for the LU decomposition remains unchanged since no tabulated functions are used in this subroutine.
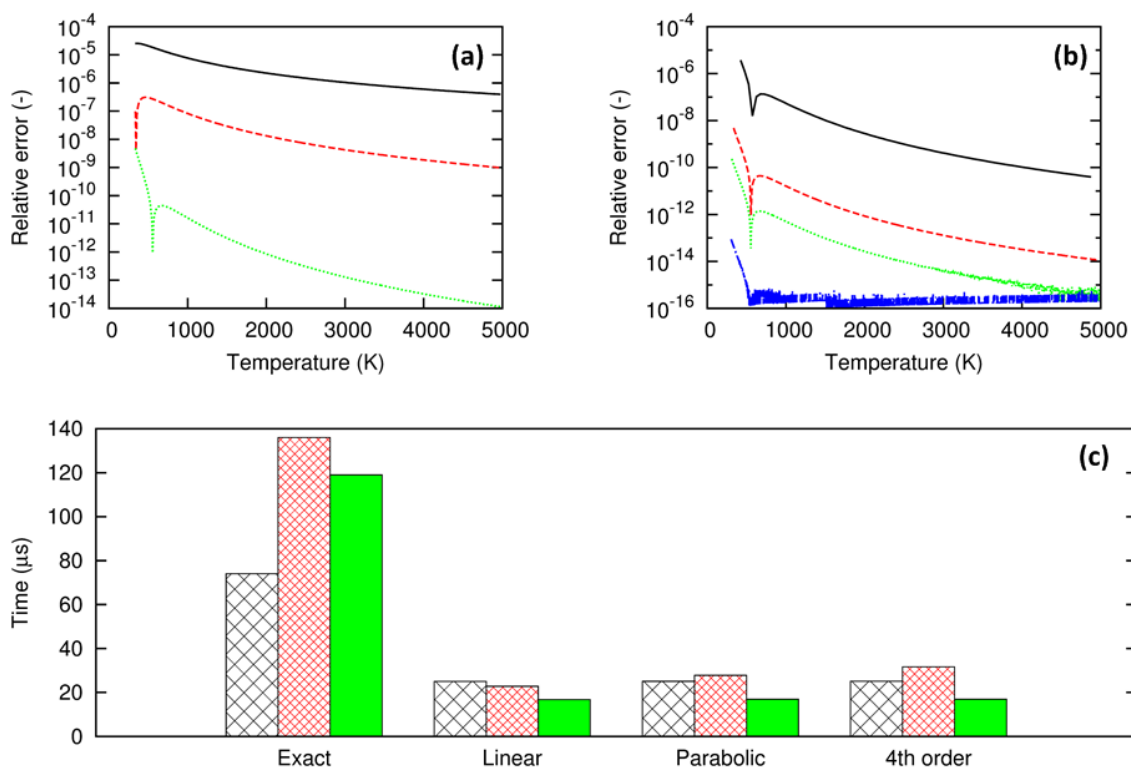
Figure 9.4: (a) Relative error of the tabulated function for different degrees of interpolation: Linear interpolation;━━━, Parabolic interpolation;━ ━, Fourth order interpolation;▪▪▪▪▪ at a tabulation interval of 10K; (b) Relative error for the tabulated function for different tabulation intervals: 50K;━━━, 10K;━ ━, 5K;▪▪▪▪▪, 1K;━▪ for 4th order interpolation; (c) Time of a single function evaluation for an exact function and tabulated functions for different temperature dependent coefficients: Forward rate coefficient k_f; ⨂⨂⨂, Equilibrium coefficient K_{eq}; ⨉⨉⨉⨉⨉⨉, Constant pressure heat capacity c_p; ▧ at a tabulation interval of 10K using a 4th order interpolation method.
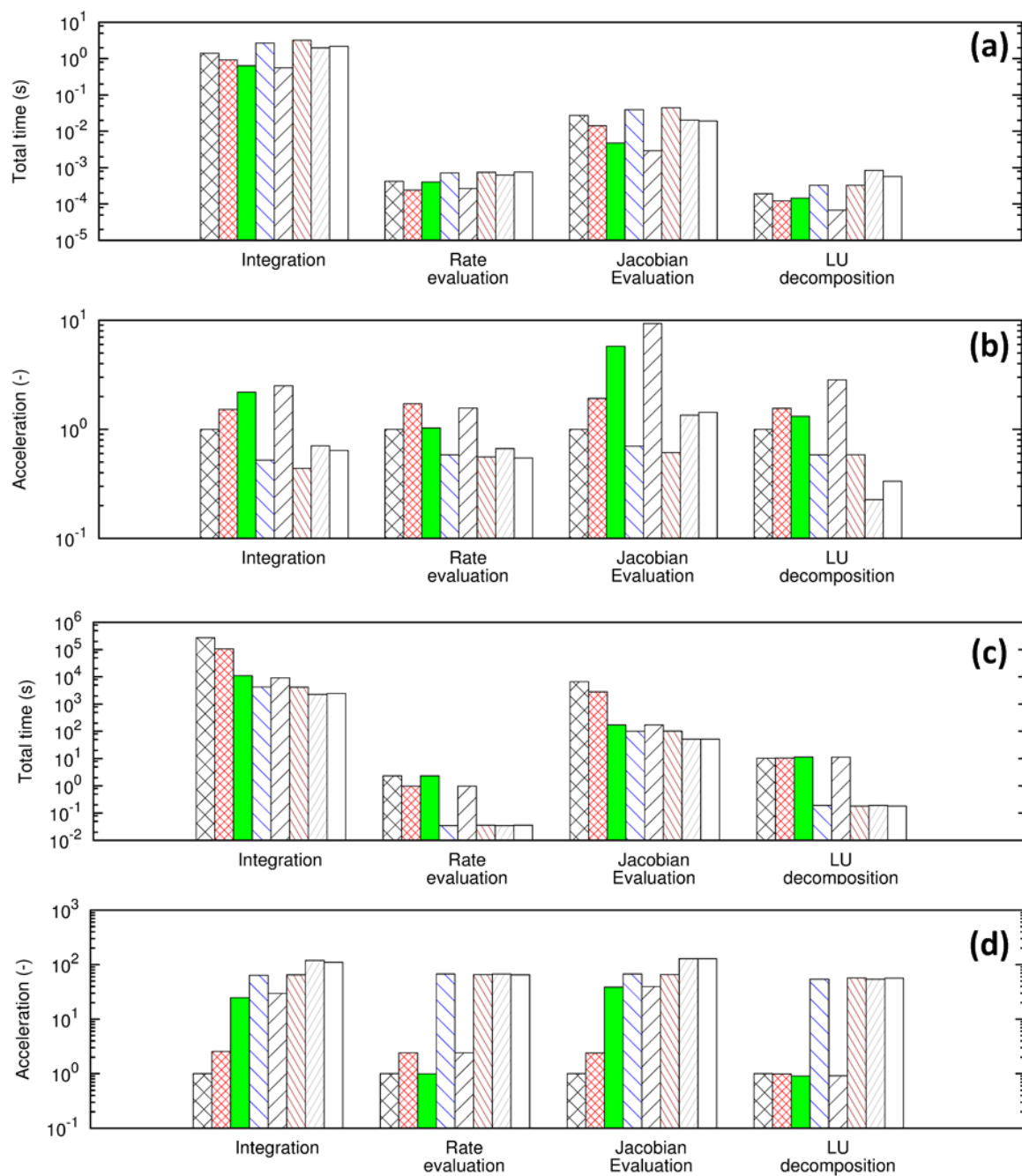
Figure 9.5: (a) Total time and (b) acceleration factor for different optimization techniques for the ethanol mechanism consisting of 56 species and 351 reactions; (c) total time and (d) acceleration factor for different optimization techniques for the methyldecanoate mechanism consisting of 3012 species and 8820 reactions. Base case; ⊠, Tabulation; ⊠, Analytical Jacobian; ▮, GPU; ⊠, Analytical Jacobian + tabulation; ⊿, GPU + Tabulation; ⊿, Analytical Jacobian + GPU; ⊿, Analytical Jacobian + GPU + Tabulation; ⬚.

9.4.3 Analytical Jacobian

Figure 9.5 also shows a comparison of the evaluation of the Jacobian by finite differences and calculated analytically. The analytical Jacobian evaluation offers an acceleration of the code with a factor 2 and 25 for the smallest (Figure 9.5b) and largest mechanism (Figure 9.5d) respectively. Obviously, this acceleration is accomplished by a significant speedup in the evaluation of the Jacobian while the time for a single rate evaluation and LU-decomposition stays the same. The evaluation of an analytical Jacobian can be a factor 5 (for the smallest mechanism) to 25 (for the largest mechanisms) faster than the evaluation by finite differences which is done by calling the rate evaluation function n_s+1 times.

9.4.4 Evaluation of the rates on the GPU

Figure 9.5 also shows a comparison of solver and evaluation times between the CPU and the GPU algorithm. It can be seen that for the smallest mechanism the GPU code is significantly slower than the CPU code, Figure 9.5 a-b, while for the largest mechanism, Figure 9.5 c-d, an acceleration factor of 60 is obtained. The GPU version is slower for the smaller mechanisms due to the time losses during transfer of simulation variables from the host to the device memory and vice versa. This loss of time becomes relatively more important when it's compared to the calculation time on the GPU. The time for transferring variables is influenced by two factors: bandwidth and latency. The first factor is latency. Latency is the time between when the instruction to transfer data is given and when the actual data-transfer commences. The latency is independent of the data size. The second factor is bandwidth or the amount of data that can be transferred per time unit. Since bandwidth is limited and more data needs to be transferred to the device memory for larger mechanisms this increases the transfer time for larger mechanisms. However the time spent during calculations (on the GPU) also increases when the mechanism

size increases and thus compensates the increased transfer time. It can be seen that the influence of latency thus becomes less important when the mechanism size increases. However for the smallest mechanisms latency is one of the most important delays and thus results in a slower code. The acceleration of the evaluation of the rates also has repercussions on the calculation of the Jacobian. Since the Jacobian is calculated by finite differences and thus requires n_s rate of formation evaluations the acceleration of the Jacobian is about the same as the acceleration of the calculation of the rates.

9.4.5 Combination of different methods

None of the described methods above is mutually exclusive so they can be combined and a further gain in efficiency of the solver is possible. However practically it will not always result in the expected efficiency gain because each implemented method will influence the potential speed up factor of the other methods. As three methods are used, four different combinations are evaluated. The first combination uses tabulation and the analytical Jacobian. The second combination uses tabulation and CPU/GPU hybrid calculations. The third method uses the GPU to not only calculate the reaction rates but also to evaluate the analytical Jacobian. Finally all three methods, i.e. tabulation, CPU/GPU hybrid calculations and an analytical Jacobian are combined.

Tabulation and an analytical Jacobian

When combining the tabulation method with an analytical Jacobian only a limited acceleration is obtained in comparison with the analytical Jacobian using intrinsic compiler functions (see Figure 9.5). An acceleration of around two is obtained for the rates routine. This acceleration does not yield a significant reduction of the total integration time as the rates routine is not

needed anymore for the calculation of the Jacobian by finite differences resulting in fewer calls to the rates routine. Hence, acceleration of the rates routine only accelerates the total integration procedure in a limited way: around a factor of 1.2 for both the smallest and the largest mechanism. The acceleration of the calculation of the analytical Jacobian by tabulation is very limited.as only a limited fraction of all calculations in the Jacobian calculations can be replaced by lookup of temperature dependent tabulated values. The net result is that tabulation only results in a limited acceleration of the integration procedure when combined with an analytical Jacobian evaluation.

Tabulation on the GPU

Figure 9.5 show the effect when using tabulated functions on a GPU. It is clear that no significant speedup is gained when using tabulated functions instead of intrinsic functions on the GPU. On the contrary, using tabulated functions results in a very small decrease in efficiency of the rate of formation evaluation and since the Jacobian is calculated by finite differences also the Jacobian evaluation. This is caused by each multiprocessor of the GPU being equipped with a shared special function unit (SFU) which specializes in the evaluation of transcendental functions (e.g. sine, cosine, exponential) causing the evaluation of the most used intrinsic functions to be much faster on an GPU than on a CPU (Victor et al., 2010). For example the GTX280, due to the presence of fast transcendental hardware, achieves a factor of 5.7 performance gain compared to Core i7 processor for the evaluation of these transcendental functions. Since this acceleration is similar to the one obtained by tabulation on the CPU no significant difference between the intrinsic GPU version and the tabulated GPU version is expected which is confirmed by our results.

Evaluation of the rates and the analytical Jacobian on the GPU

The combination of the rate of formation evaluation and the calculation of the analytical Jacobian is a logical choice because both procedures are highly parallelizable and have a significant influence on the total simulation time. Figure 9.5 show that the combination of the analytical Jacobian with the evaluation of both the rates and this analytical Jacobian on the GPU is very powerful. For the smallest mechanism the acceleration is minimal (Figure 9.5b) but for the largest mechanism it is significant yielding an acceleration factor of 120 (Figure 9.5d). The evaluation of the analytical Jacobian on the GPU is about 3 times faster than the evaluation of the same Jacobian on the CPU. This results in a significant reduced solver time. The solver time is even further reduced by the evaluation of the rates being faster on the GPU. As will be discussed further this combination proved to be the most efficient combination of all the studied methods. Figure 9.6 shows the results for all sizes of the studied mechanisms; with the following power function for the total simulation time as function of the number species given by:

$$t = 4n_s^{1.90}.10^{-4}$$
(9.42)

Equation 9.42 describes the data with a multiple correlation coefficient of 0.91. Using Equation 9.41 and Equation 9.42 an expression for the total acceleration (A) as function of the mechanism size can be obtained:

$$Ac = 2.5n_s^{1.39}.10^{-3}$$
(9.43)

Equation 9.43 can be used to assess the possible speedup for mechanisms of difference sizes using the most optimal method. Equation 9.43 predicts that even more acceleration can be obtained than the factor 120 when a larger mechanism would be considered, e.g. acceleration factor of 340 for a mechanism size of 5000. However, Equation 9.43 has to be used with care because other limitations such as memory limitations could come into play when the network

sizes increases. Additionally the ratio of the number of reactions to the number of species can also have its influence on the total simulation time (Shi et al., 2011). Increasing this ratio results in more reaction rate evaluations needed to calculate the rate of formation of each species. This thus influences the acceleration factor which is not taken into account by Equation 9.43.
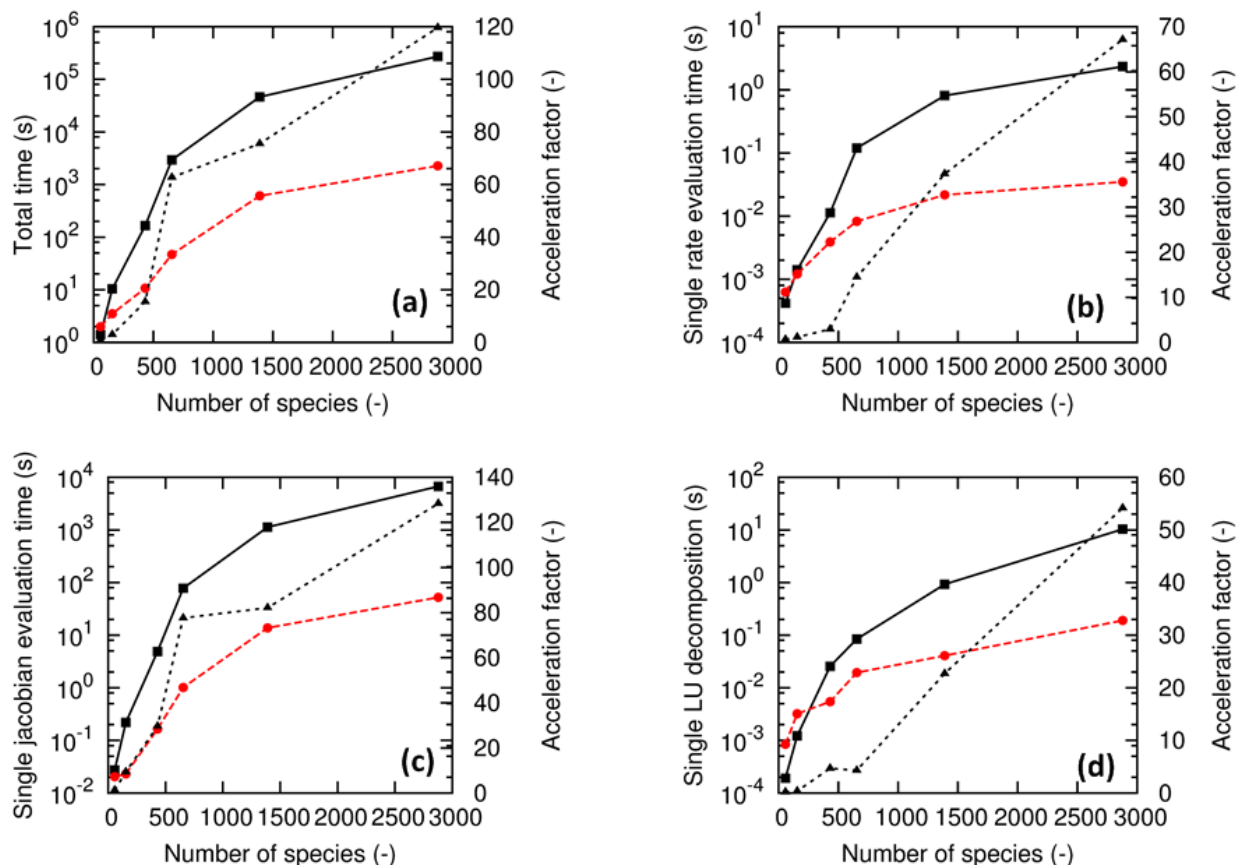
Figure 9.6: (a) Total time, (b) Time for a single rate of formation evaluation, (c) Time for a single Jacobian evaluation, (d) Time for a single LU decomposition for the finite differences Jacobian on CPU method and the method that evaluates both the Jacobian and the rates on GPU.

Finite differences;━■━, Analytical Jacobian on GPU;━●━, Acceleration factor;- - -▲- - -.

Evaluation of the rates and the analytical Jacobian on the GPU using tabulation

The last combination is the combination of all the three techniques. As mentioned previously the special function unit on the GPU makes tabulation less efficient than using intrinsic functions and limiting the number of these intrinsic function evaluations by using a Jacobian makes the tabulation even more costly. This can be clearly seen in Figure 9.5 where adding tabulation to the analytical Jacobian calculated on the GPU slows down the code by around 10% for both the smallest and the largest mechanism as compared to the previous case.

9.5 Conclusions

Different speedup methods have been evaluated for mechanisms of different sizes either in standalone mode or in combination with others for the VODE solver. The latter performed significantly better than the other solvers LSODA, LSODE, LSODES, RADAU5 and DASPK and therefore was used as reference. Depending on the mechanism size an important acceleration is possible by calculating the analytical Jacobian rather than using the finite difference based Jacobian, using tabulated functions for the temperature dependent variables rather than using exact function evaluations and using the GPU to do part of the calculations, e.g. calculations of the rates and the Jacobian. However, the combination of two-by-two or all three of these speedup methods allows to additionally accelerate reactive mixture simulations with up to factor 120. This acceleration is not obtained by combining all three methods but rather combining the calculation of the analytical Jacobian with calculations on the GPU and not using the tabulation method. Combining it additionally with tabulation results in a reduction of the overall speedup because the GPU is equipped with a Special Function Unit (SFU) which allows for an efficient calculation

of transcendental functions such as the exponential. This SFU can calculate these transcendental functions much faster than a CPU and as fast as the calculation of a tabulated function.

Applying the above mentioned methods to COILSIM1D described in Chapter 6 is not useful. COILSIM1D uses a specialized solver which does not require the evaluation of the Jacobian. In addition the structure of the kinetic model CRACKSIM only allows the β network to be calculated on the GPU. Due to the tabulated PRC values in the μ network data transfer between the CPU and GPU memory would be too large to do calculations on the GPU. The number of the species in the β network is however limited to 94 species and thus calculations on the GPU would be slower. Tabulation could be useful as it could speed up the calculations of the rate coefficient and other temperature related values. As mentioned in Chapter 6 tabulation of the Wilke coefficients every 20 K has the same acceleration as evaluating these Wilke coefficients on the GPU.

9.6 References

Andreis, G. S. L., Vaz, F. A., & De Bortoli, A. L. (2013). Bioethanol combustion based on a reduced kinetic mechanism. Journal of Mathematical Chemistry, 51, 1584-1598.
Berger, R. J., & Marin, G. B. (1999). Investigation of Gas-Phase Reactions and Ignition Delay Occurring at Conditions Typical for Partial Oxidation of Methane to Synthesis Gas. Industrial & Engineering Chemistry Research, 38, 2582-2592.
Bhattacharjee, B., Schwer, D. A., Barton, P. I., & Green, W. H. (2003). Optimally-reduced kinetic models: reaction elimination in large-scale kinetic mechanisms. Combustion and Flame, 135, 191-208.
Bird, R. S. (1980). Tabulation techniques for recursive-programs. Computing Surveys, 12, 403-417.
Brown, P., Byrne, G., & Hindmarsh, A. (1989). VODE: A Variable-Coefficient ODE Solver. SIAM Journal on Scientific and Statistical Computing, 10, 1038-1051.
Brown, P., Hindmarsh, A., & Petzold, L. (1994). Using Krylov Methods in the Solution of Large-Scale Differential-Algebraic Systems. Siam Journal on Scientific Computing, 15, 1467-1488.
Bykov, V., & Gol'dshtein, V. (2013). Fast and slow invariant manifolds in chemical kinetics. Computers & Mathematics with Applications, 65, 1502-1515.

Chase, M. W., Curnutt, J. L., Downey, J. R., McDonald, R. A., Syverud, A. N., & Valenzuela, E. A. (1982). Janaf thermchemical tables, 1982 supplement. *Journal of Physical and Chemical Reference Data, 11*, 695-940.

Côme, G. M., Warth, V., Glaude, P. A., Fournet, R., Battin-Leclerc, F., & Scacchi, G. (1996). Computer-aided design of gas-phase oxidation mechanisms—Application to the modeling of n-heptane and iso-octane oxidation. *Symposium (International) on Combustion, 26*, 755-762.

CUDA Fortran: Programming guide and reference. (2012). The Portland Group.

Dente, M., Ranzi, E., & Goossens, A. G. (1979). Detailed prediction of olefin yields from hydrocarbon pyrolysis through a fundamental simulation model (SPYRO). *Computers & Chemical Engineering, 3*, 61-75.

Dorman, B., Irwin, A. W., & Pedersen, B. B. (1991). On equation of state interpolation errors in stellar interior calculations. *Astrophysical Journal, 381*, 228-233.

Gardiner, W. C., & Troe, J. (1984). Rate Coefficients of Thermal Dissociation, Isomerization and Recombination Reactions. In Combustion Chemistry (pp. 173-196): Springer.

Hairer, G. W. E. (2010). Solving Ordinary Differential Equations II: Springer Berlin Heidelberg.

Halligudi, S. B., Devassay, B. M., Ghosh, A., & Ravikumar, V. (2002). Kinetic study of vapor phase hydrodechlorination of halons by Pd supported catalysts. *Journal of Molecular Catalysis a-Chemical, 184*, 175-181.

He, K. Y., Androulakis, I. P., & Ierapetritou, M. G. (2011). Numerical Investigation of Homogeneous Charge Compression Ignition (HCCI) Combustion with Detailed Chemical Kinetics Using On-the-Fly Reduction. *Energy & Fuels, 25*, 3369-3376.

Herbinet, O., Pitz, W. J., & Westbrook, C. K. (2008). Detailed chemical kinetic oxidation mechanism for a biodiesel surrogate. *Combustion and Flame, 154*, 507-528.

Hindmarsh, A. C. (1983). ODEPACK, A Systematized Collection of ODE Solvers, R. S. Stepleman et al. (eds.), North-Holland, Amsterdam, (vol. 1 of), pp. 55-64. IMACS Transactions on Scientific Computation, 1, 55-64.

Hiremath, V., & Pope, S. B. (2013). A study of the rate-controlled constrained-equilibrium dimension reduction method and its different implementations. *Combustion Theory and Modelling, 17*, 260-293.

Jaffe, S. B., Freund, H., & Olmstead, W. N. (2005). Extension of structure-oriented lumping to vacuum residua. *Industrial & Engineering Chemistry Research, 44*, 9840-9852.

Klein, M. T., Hou, G., Bertolacini, R. J., Broadbeld, L. J., & Kumar, A. (2006). Molecular modeling in heavy hydrocarbon conversions: CRC Press.

Law, C. K. (2007). Combustion at a crossroads: Status and prospects. *Proceedings of the Combustion Institute, 31*, 1-29.

Lu, T. F., Ju, Y. G., & Law, C. K. (2001). Complex CSP for chemistry reduction and analysis. *Combustion and Flame, 126*, 1445-1455.

Lu, T. F., & Law, C. K. (2009). Toward accommodating realistic fuel chemistry in large-scale computations. *Progress in Energy and Combustion Science, 35*, 192-215.

Magnuson, J. A. (1964). Tabulation for Deriving Procedural Rate Constants from Dynamic Thermograms. *Analytical Chemistry, 36*, 1807-1810.

Magoon, G. R., & Green, W. H. (2013). Design and implementation of a next-generation software interface for on-the-fly quantum and force field calculations in automated reaction mechanism generation. *Computers & Chemical Engineering, 52*, 35-45.

Manca, D., Buzzi-Ferraris, G., Faravelli, T., & Ranzi, E. (2001). Numerical problems in the solution of oxidation and combustion models. Combustion Theory and Modelling, 5, 185-199.

Marinov, N. M. (1999). A detailed chemical kinetic model for high temperature ethanol oxidation. International Journal of Chemical Kinetics, 31, 183-220.

Marinov, N. M., Pitz, W. J., Westbrook, C. K., Vincitore, A. M., Castaldi, M. J., Senkan, S. M., & Melius, C. F. (1998). Aromatic and Polycyclic Aromatic Hydrocarbon Formation in a Laminar Premixed n-Butane Flame. Combustion and Flame, 114, 192-213.

Mehl, M., Pitz, W. J., Westbrook, C. K., & Curran, H. J. (2011). Kinetic modeling of gasoline surrogate components and mixtures under engine conditions. Proceedings of the Combustion Institute, 33, 193-200.

Perini, F., Galligani, E., & Reitz, R. D. (2012). An Analytical Jacobian Approach to Sparse Reaction Kinetics for Computationally Efficient Combustion Modeling with Large Reaction Mechanisms. Energy & Fuels, 26, 4804-4822.

Pierucci, S., Brandani, P., Ranzi, E., & Sogaro, A. (1996). An industrial application of an on-line data reconciliation and optimization problem. Computers & Chemical Engineering, 20, 1539-1544.

Pierucci, S., & Ranzi, E. (2008). A review of features in current automatic generation software for hydrocarbon oxidation mechanisms. Computers & Chemical Engineering, 32, 805-826.

Pope, S. B. (1997). Computationally efficient implementation of combustion chemistry using in situ adaptive tabulation. Combustion Theory and Modelling, 1, 41-63.

Rangarajan, S., Bhan, A., & Daoutidis, P. (2012a). Language-oriented rule-based reaction network generation and analysis: Applications of RING. Computers & Chemical Engineering, 46, 141-152.

Rangarajan, S., Bhan, A., & Daoutidis, P. (2012b). Language-oriented rule-based reaction network generation and analysis: Description of RING. Computers & Chemical Engineering, 45, 114-123.

Ranzi, E., Faravelli, T., Gaffuri, P., & Sogaro, A. (1995). Low-temperature combustion: Automatic generation of primary oxidation reactions and lumping procedures. Combustion and Flame, 102, 179-192.

Ren, Z. Y., Goldin, G. M., Hiremath, V., & Pope, S. B. (2013). Simulations of a turbulent non-premixed flame using combined dimension reduction and tabulation for combustion chemistry. Fuel, 105, 636-644.

Sarathy, S. M., Vranckx, S., Yasunaga, K., Mehl, M., Oßwald, P., Metcalfe, W. K., Westbrook, C. K., Pitz, W. J., Kohse-Höinghaus, K., Fernandes, R. X., & Curran, H. J. (2012). A comprehensive chemical kinetic combustion model for the four butanol isomers. Combustion and Flame, 159, 2028-2055.

Scheuer, A., Drochner, A., Gieshoff, J., Vogel, H., & Votsmeier, M. (2012). Runtime efficient simulation of monolith catalysts with a dual-layer washcoat. Catalysis Today, 188, 70-79.

Shengtai, L., & Linda, P. (1999). Design of new Daspk for Sensitivity Analysis. University of California at Santa Barbara.

Shi, Y., Green Jr, W. H., Wong, H.-W., & Oluwole, O. O. (2011). Redesigning combustion modeling algorithms for the Graphics Processing Unit (GPU): Chemical kinetic rate evaluation and ordinary differential equation integration. Combustion and Flame, 158, 836-847.

Turanyi, T., Tomlin, A. S., & Pilling, M. J. (1993). On the error of the quasi-steady-state approximation. Journal of Physical Chemistry, 97, 163-172.

Turanyi, T., & Toth, J. (1992). Classics revisited - comments to an article of Frank Kamenetskii on the quasi-steady-state approximation. Acta Chimica Hungarica-Models in Chemistry, 129, 903-907.

van Goethem, M. W. M., Kleinendorst, F. I., van Leeuwen, C., & van Velzen, N. (2001). Equation-based SPYRO® model and solver for the simulation of the steam cracking process. Computers & Chemical Engineering, 25, 905-911.

Vandewiele, N. M., Van Geem, K. M., Reyniers, M. F., & Marin, G. B. (2012). Genesys: Kinetic model construction using chemo-informatics. Chemical Engineering Journal, 207, 526-538.

Victor, W. L., Changkyu, K., Jatin, C., Michael, D., Daehyun, K., Anthony, D. N., Nadathur, S., Mikhail, S., Srinivas, C., Per, H., Ronak, S., & Pradeep, D. (2010). Debunking the 100X GPU vs. CPU myth: an evaluation of throughput computing on CPU and GPU. In Proceedings of the 37th annual international symposium on Computer architecture. Saint-Malo, France: ACM.

Vinu, R., & Broadbelt, L. J. (2012). Unraveling Reaction Pathways and Specifying Reaction Kinetics for Complex Systems. In Annual Review of Chemical and Biomolecular Engineering (Vol. 3, pp. 29-54).

Yamamoto, A., Kitamura, Y., & Yamane, Y. (2004). Computational efficiencies of approximated exponential functions for transport calculations of the characteristics method. Annals of Nuclear Energy, 31, 1027-1037.

Zhang, S. L., Androulakis, I. P., & Ierapetritou, M. G. (2013). A hybrid kinetic mechanism reduction scheme based on the on-the-fly reduction and quasi-steady-state approximation. Chemical Engineering Science, 93, 150-162.

Zhang, Y., Vouzis, P., & Sahinidis, N. V. (2011). GPU simulations for risk assessment in CO2 geologic sequestration. Computers & Chemical Engineering, 35, 1631-1644.

Chapter 10: Conclusions and perspectives

10.1   Conclusions

The focus of this work was on the one hand on developing a fundamental model which is able to simulate the steam cracking process itself for a wide variety of feedstocks. On the other hand it should allow to optimize the operating variables of the steam cracking process while keeping the total simulation time limited.

The use and development of this model required the combination of a wide variety of experimental and computational techniques.

The model first of all needs to allow to simulate a wide range of process conditions for a variety of feedstocks. This proved to be only possible if a detailed microkinetic model was used and if a detailed composition of the feedstock is specified. The latter should be of a similar level of detail or even higher than the one used in the microkinetic model. It was shown that comprehensive 2D GC (GC × GC) is one of those techniques that can be provide the level of detail needed. Therefore GC × GC needs to be coupled to different (selective) detectors such as an FID, SCD, NCD and TOF-MS. By combination of the information supplied by these detectors a quantitative analysis by group type and carbon number was made possible. Twenty different classes can be differentiated namely paraffins, isoparaffins, mononaphthenes, dinaphthenes, monoaromatics, naphthenoaromatics, diaromatics, naphthenodiaromatics, triaromatics, naphthenotriaromatics, tetra-aromatics, thiols/sulfides, benzothiophenes, dibenzothiophenes, pyridines, anilines, quinolines, indoles, acridines and carbazoles. Quantification of these groups was shown to be possible up to a carbon number of 46 by using GC columns which were stable up to oven

temperatures of 643 K. The use of selective NCD and SCD detector allows for the inclusion of nitrogen- and sulfur containing compounds. In addition to the 20 groups the developed analytical technique also allows for the quantification of a limited number of phenolic compounds using mass selective detection.

In Chapter 5 a reconstruction method based on Shannon entropy maximization was shown to allow the reconstruction of a the detailed composition of feedstocks obtained by the above described application of GC × GC. Feedstocks up to vacuum gas oils and including sulfur containing hydrocarbons can accurately be reconstructed. There is however, still room for improvement in the reconstruction of different subgroups within the same parent group, e.g. mono-aromatics within the aromatics group. For the reconstruction of sulfur containing hydrocarbons the importance of additional commercial indices such as total sulfur and aromatic sulfur was shown. Adding the elemental sulfur and the aromatic sulfur content as commercial index allows to drastically improve the reconstruction of sulfur containing compounds without influencing the accuracy of the reconstruction for the hydrocarbon compounds. Nitrogen containing compounds were not yet included but an extension towards nitrogen could be implemented in a similar way as sulfur containing compounds were implemented.

The detailed composition either obtained via GC × GC or via feedstock reconstruction can be used in a fundamental model (COILSIM1D) for steam cracking of hydrocarbons. The model combines a single event microkinetic model (CRACKSIM) with a one-dimensional plug flow reactor model. The microkinetic model is based on the free radical mechanism and was divided in two sub models: the β network and the monomolecular μ network. In the latter monomolecular

reactions dominate for radical species with more than 5 carbon atoms (μ radicals). The number of differential equations that needs to be integrated is further reduced by applying the QSSA on the μ radicals. QSSA allows deriving analytical expressions for the concentration of these radical reaction intermediates. In Chapter 7 the model is further extended with a comprehensive model for a transfer line exchanger. It was shown that reactions can still occur in the (beginning) of the TLE. The model could also calculate the outer tube convection coefficient which is often assumed to be infinite in literature. The final model is able to accurately predict the yields of the major products (ethene and propene) as well as the by-products for a wide range of feedstocks (from ethane up to gas oils) in a matter of seconds of CPU time. Due to the accurate and fast prediction of the yields at the outlet of COILSIM1D could be implemented in more complex simulation types such as multi-objective optimization.

Chapter 8 implemented the developed fundamental simulation model in a multi-objective optimization algorithm, i.e. the elitist non-dominant sorting genetic algorithm with adapted jumping gene operator (NSGA-II-aJG). Several multi-objective optimizations were tested by changing the objectives, operating variables and the feedstocks (including the corresponding reactors). It was shown that using objectives such as the total production of ethene and propene, the maximum initial coking rate and the operating expenses could represent single-objective optimizations towards gross profit and gross profit per unit as the final Pareto front included the optimal process variables for these solutions together with a broad range of alternative solutions. The algorithm was also able to differentiate between naphtha's of a different quality. Naphtha's with higher amount of aromatics resulted in a lower production of ethene and propene but also lower operating expenses since the reaction heat is proportionally reduced. Differences were also

observed for different feedstock types. The maximum temperature of the Pareto front decreased from 1171 K for propane to 1118 K for gas oil. A higher average boiling point of the feedstock resulted into a lower maximum COT present in the Pareto front. A similar comparison was made between a bare tube and a coked tube. Higher temperatures, heat input and coking rates were reached for the coked tube due to the lower volume and the lower space time. Conclusions regarding the process variables were similar as in the other cases.

In Chapter 9 different speedup methods were evaluated for mechanisms of different sizes to see if further computational efficiency improvements were possible. Methods that were tested included tabulation, evaluation of an analytical Jacobian and using the graphical processing unit to handle part of the calculations. In first instance VODE was chosen as the most efficient ODE solver as it performed significantly better than the other solvers LSODA, LSODE, LSODES, RADUA5 and DASPK. Depending on the mechanism size an important acceleration is possible by implementing an analytical Jacobian, tabulation and performing calculations on the GPU. The combination the analytical Jacobian and the rates being calculated using the GPU while no tabulation is used proved to be the most efficient solution with acceleration factors up to 120. However applying the developed methods to COILSIM1D is not useful as the specifically developed solver does not require the evaluation of the Jacobian. In addition the structure of the kinetic model CRACKSIM only allows the β network to be calculated on the GPU. Due to the tabulated PRC values in the μ network data transfer between the CPU and GPU memory would be too large to do calculations for the μ on the GPU while the limited number of species in the β network discourages the GPU calculations for the β network.

10.2 Perspectives

This work tries to develop a fundamental model which is able to simulate the steam cracking process ranging from molecular scale all the way up to plant scale. However continuous improvement of all of the techniques is needed to be able to deal with the relative fast changes that are occurring in industrial steam cracking plants, e.g. shale oil developments, lower quality crude oil, etc.

Both in shale oil and in low-quality crude oil the quantity of hetero-elements, e.g. nitrogen, sulfur and oxygen, keeps increasing and an accurate analysis is required not only for pure, sulfur and nitrogen containing hydrocarbons but also oxygen containing hydrocarbons. GC × GC currently cannot deal with high amounts of oxygen containing hydrocarbons in addition to pure, sulfur and nitrogen containing hydrocarbons. Selective detection of oxygen, either by using an oxygen selective FID (O-FID) or an atom emission detector could help solve this problem. The acquisition rate of the latter should however drastically be increased to be able to be used with GC × GC. Hyphenation of GC × GC with other techniques such as liquid chromatography or supercritical fluid chromatography, either online or offline, could also help separate these oxygen containing but also nitrogen and sulfur containing compounds prior to injection on GC × GC.

The detection of these hetero-elements at trace amounts is also becoming increasingly important since restrictions on these impurities are becoming stricter, e.g. arsine and phosphine. Gas chromatographic methods fail at these ultralow concentrations (ppb and ppt levels). New techniques will need to be developed. A recent and sensitive technique is Selected Ion Flow Tube Mass Spectrometry or SIFT-MS. SIFT-MS is a sensitive mass spectrometry technique for trace level gas analysis using soft chemical ionization of sample trace gases. Currently it is used for air

analysis but extensions towards the analysis of hydrocarbon mixtures should be looked into for the analysis of these trace impurities.

Furthermore the cracking behavior of the sulfur, nitrogen and oxygen containing compounds is not well understood and both experimental studies, using these state-of-the-art selective techniques, and modeling studies are needed to gain more insight in the cracking behavior of these compounds.

To use these new models in industry not only the analytical techniques but also the numerical techniques should be upgraded to take into account these oxygen-, nitrogen- and sulfur containing compounds. In this work a first step was taken to include the sulfur-containing compounds in the reconstruction but more work is needed for the oxygen- and nitrogen containing compounds.

These higher amounts of hetero-elements not only influences the yields of a steam cracker but also cokes formation. For example sulfur-containing compounds inhibit CO production and influence the coking rates and product distribution. Models that grasp the interplay of the sulfur-containing compounds with those of the feed and also account for their influence on coke formation can assist olefin producers in selecting the proper pretreatment/addition/blending strategy in order to obtain optimal operating condition

In addition to the higher amount of hetero-elements these heavy fossil fractions have a higher average boiling point and a higher tendency to deposit at lower temperatures. This leads to (more) coke formation in the convection section but also in the transfer line exchanger. Research will need to be performed in order to optimize the design and operating conditions of the different heat exchangers in the steam cracker convection and cooling section to understand and limit fouling in these sections. Finally coke formation inside the TLE is not well understood and

is attributed to a combination of three coke formation mechanisms: a catalytic mechanism, a free-radical mechanism, and a droplets condensation/tar deposition mechanism. To better understand the contribution of each of these mechanisms significant experimental data is needed to assess the effect of operating variables and feedstock composition.

Appendix A: Detailed composition of VGO B and VGO C

Table A. 1: Detailed group type analysis of VGO B in wt%: P=n-paraffins, I=isoparaffins, MN=mononaphthenes, DN=dinaphthenes, MA=monoaromatics, NA=naphthenoaromatics, DA=diaromatics, NDA=naphthenodiaromatics, TrA=Triaromatics, NTrA=naphthenotriaromatics, TeA=Tetraaromatics

#C	P	I	MN	DN	MA	NA	DA	NDA	TrA	NTrA	TeA	Total
8	n.d.	n.d.	n.d.	n.d.	0.01	n.d.	n.d.	n.d.	n.d.	n.d.	n.d.	0.02
9	0.01	n.d.	0.01	n.d.	0.02	n.d.	n.d.	n.d.	n.d.	n.d.	n.d.	0.04
10	0.01	0.01	0.02	n.d.	0.02	0.01	0.06	n.d.	n.d.	n.d.	n.d.	0.15
11	0.03	0.02	0.03	0.02	0.04	0.11	0.07	n.d.	n.d.	n.d.	n.d.	0.32
12	0.04	0.03	0.06	0.08	0.07	0.17	0.29	n.d.	n.d.	n.d.	n.d.	0.76
13	0.09	0.08	0.18	0.08	0.10	0.25	0.44	0.07	n.d.	n.d.	n.d.	1.28
14	0.17	0.15	0.27	0.09	0.23	0.39	0.45	0.25	0.07	n.d.	n.d.	2.07
15	0.38	0.23	0.32	0.19	0.53	0.45	0.51	0.53	0.28	n.d.	n.d.	3.41
16	0.42	0.29	0.54	0.28	0.51	0.54	0.63	0.62	0.63	0.02	n.d.	4.48
17	0.59	0.56	0.83	0.23	0.57	0.55	0.57	0.93	0.82	0.08	0.04	5.78
18	0.82	0.81	0.94	0.15	0.77	0.67	0.45	0.79	0.80	0.16	0.04	6.41
19	1.30	1.17	0.54	0.13	1.30	0.41	0.42	0.73	0.63	n.d.	0.06	6.68
20	1.46	1.18	1.72	0.10	1.36	0.38	0.41	0.72	0.59	0.35	0.07	8.36
21	1.41	1.59	0.85	0.08	1.48	0.32	0.16	0.55	n.d.	0.37	0.05	6.87
22	1.48	1.91	0.69	n.d.	1.50	0.18	0.04	0.33	n.d.	0.35	0.02	6.50
23	1.50	1.92	0.46	n.d.	1.77	n.d.	n.d.	0.11	n.d.	0.18	n.d.	5.93
24	1.55	2.07	0.30	n.d.	1.90	n.d.	n.d.	0.09	0.11	n.d.	n.d.	6.02
25	1.61	2.86	0.13	n.d.	1.18	n.d.	n.d.	n.d.	n.d.	n.d.	n.d.	5.79
26	1.65	2.29	0.05	n.d.	0.76	n.d.	n.d.	n.d.	n.d.	n.d.	n.d.	4.74
27	1.30	2.02	n.d.	n.d.	0.62	n.d.	n.d.	n.d.	n.d.	n.d.	n.d.	3.94
28	1.33	1.92	n.d.	n.d.	0.50	n.d.	n.d.	n.d.	n.d.	n.d.	n.d.	3.74
29	1.09	1.72	n.d.	n.d.	0.28	n.d.	n.d.	n.d.	n.d.	n.d.	n.d.	3.09
30	1.00	1.75	n.d.	n.d.	0.20	n.d.	n.d.	n.d.	n.d.	n.d.	n.d.	2.95
31	0.93	1.31	n.d.	n.d.	0.13	n.d.	n.d.	n.d.	n.d.	n.d.	n.d.	2.36
32	0.61	0.88	n.d.	n.d.	0.07	n.d.	n.d.	n.d.	n.d.	n.d.	n.d.	1.55
33	0.63	0.86	n.d.	n.d.	n.d.	n.d.	n.d.	n.d.	n.d.	n.d.	n.d.	1.49
34	0.74	0.74	n.d.	n.d.	n.d.	n.d.	n.d.	n.d.	n.d.	n.d.	n.d.	1.48
35	0.38	0.60	n.d.	n.d.	n.d.	n.d.	n.d.	n.d.	n.d.	n.d.	n.d.	0.97
36	0.37	0.37	n.d.	n.d.	n.d.	n.d.	n.d.	n.d.	n.d.	n.d.	n.d.	0.74
37	0.31	0.17	n.d.	n.d.	n.d.	n.d.	n.d.	n.d.	n.d.	n.d.	n.d.	0.49
38	0.29	0.14	n.d.	n.d.	n.d.	n.d.	n.d.	n.d.	n.d.	n.d.	n.d.	0.43
39	0.25	0.16	n.d.	n.d.	n.d.	n.d.	n.d.	n.d.	n.d.	n.d.	n.d.	0.41
40	0.23	n.d.	n.d.	n.d.	n.d.	n.d.	n.d.	n.d.	n.d.	n.d.	n.d.	0.23
41	0.19	n.d.	n.d.	n.d.	n.d.	n.d.	n.d.	n.d.	n.d.	n.d.	n.d.	0.19
42	0.15	n.d.	n.d.	n.d.	n.d.	n.d.	n.d.	n.d.	n.d.	n.d.	n.d.	0.15
43	0.13	n.d.	n.d.	n.d.	n.d.	n.d.	n.d.	n.d.	n.d.	n.d.	n.d.	0.13
44	0.05	n.d.	n.d.	n.d.	n.d.	n.d.	n.d.	n.d.	n.d.	n.d.	n.d.	0.05
Total	24.49	29.81	7.95	1.45	15.93	4.43	4.49	5.72	3.93	1.52	0.28	100.0

Table A. 2: Detailed group type analysis of VGO C in wt%: P=n-paraffins, I=isoparaffins,

MN=mononaphthenes, DN=dinaphthenes, MA=monoaromatics, NA=naphthenoaromatics, DA=diaromatics,

NDA=naphthenodiaromatics, TrA=Triaromatics, NTrA=naphthenotriaromatics, TeA=Tetraaromatics

#C	P	I	MN	DN	MA	NA	DA	NDA	TrA	NTrA	TeA	Total
10	n.d.	n.d.	n.d.	n.d.	n.d.	n.d.	0.02	n.d.	n.d.	n.d.	n.d.	0.02
11	n.d.	n.d.	n.d.	n.d.	n.d.	n.d.	0.02	n.d.	n.d.	n.d.	n.d.	0.02
12	0.01	n.d.	0.02	0.01	n.d.	n.d.	0.09	0.01	n.d.	n.d.	n.d.	0.13
13	0.03	0.02	0.05	0.02	0.04	0.01	0.16	0.06	n.d.	n.d.	n.d.	0.39
14	0.06	0.05	0.09	0.03	0.08	0.05	0.17	0.17	0.03	n.d.	n.d.	0.73
15	0.12	0.09	0.13	0.06	0.19	0.10	0.18	0.27	0.14	n.d.	n.d.	1.27
16	0.16	0.10	0.19	0.07	0.20	0.12	0.19	0.30	0.35	0.04	0.02	1.74
17	0.25	0.18	0.26	0.07	0.24	0.13	0.25	0.34	0.42	0.14	0.08	2.37
18	0.33	0.34	0.33	0.15	0.21	0.13	0.26	0.24	0.46	0.21	0.21	2.87
19	0.53	0.36	0.38	0.14	0.36	0.19	0.41	0.16	0.64	0.32	0.34	3.83
20	0.58	0.40	0.57	0.01	0.50	0.35	0.42	0.11	0.39	0.30	0.24	3.87
21	0.61	0.49	0.62	0.05	0.53	0.34	0.44	0.07	n.d.	0.27	0.26	3.68
22	0.78	0.55	0.49	0.04	0.74	0.33	0.45	n.d.	0.32	0.22	0.23	4.15
23	0.83	0.91	0.55	0.05	0.82	0.06	0.39	n.d.	0.24	0.05	0.08	3.98
24	0.98	1.01	0.66	0.01	0.91	0.03	0.16	n.d.	0.46	n.d.	0.06	4.26
25	1.01	1.13	0.62	n.d.	1.01	n.d.	0.04	n.d.	n.d.	n.d.	0.03	3.84
26	1.06	1.26	0.65	n.d.	0.94	n.d.	n.d.	n.d.	n.d.	n.d.	n.d.	3.90
27	1.24	1.47	0.55	n.d.	0.82	n.d.	n.d.	n.d.	n.d.	n.d.	n.d.	4.08
28	1.22	1.51	0.40	n.d.	0.69	n.d.	n.d.	n.d.	n.d.	n.d.	n.d.	3.81
29	1.19	1.69	0.02	n.d.	0.53	n.d.	n.d.	n.d.	n.d.	n.d.	n.d.	3.42
30	1.38	2.16	n.d.	n.d.	0.40	n.d.	n.d.	n.d.	n.d.	n.d.	n.d.	3.94
31	1.61	2.17	n.d.	n.d.	0.32	n.d.	n.d.	n.d.	n.d.	n.d.	n.d.	4.10
32	2.08	2.26	n.d.	n.d.	0.13	n.d.	n.d.	n.d.	n.d.	n.d.	n.d.	4.47
33	2.19	2.64	n.d.	n.d.	n.d.	n.d.	n.d.	n.d.	n.d.	n.d.	n.d.	4.84
34	2.45	2.78	n.d.	n.d.	n.d.	n.d.	n.d.	n.d.	n.d.	n.d.	n.d.	5.23
35	1.72	2.50	n.d.	n.d.	n.d.	n.d.	n.d.	n.d.	n.d.	n.d.	n.d.	4.21
36	1.26	2.81	n.d.	n.d.	n.d.	n.d.	n.d.	n.d.	n.d.	n.d.	n.d.	4.07
37	1.43	3.30	n.d.	n.d.	n.d.	n.d.	n.d.	n.d.	n.d.	n.d.	n.d.	4.73
38	0.57	2.38	n.d.	n.d.	n.d.	n.d.	n.d.	n.d.	n.d.	n.d.	n.d.	2.95
39	0.48	1.63	n.d.	n.d.	n.d.	n.d.	n.d.	n.d.	n.d.	n.d.	n.d.	2.11
40	0.43	1.55	n.d.	n.d.	n.d.	n.d.	n.d.	n.d.	n.d.	n.d.	n.d.	1.99
41	0.38	1.58	n.d.	n.d.	n.d.	n.d.	n.d.	n.d.	n.d.	n.d.	n.d.	1.96
42	0.29	1.40	n.d.	n.d.	n.d.	n.d.	n.d.	n.d.	n.d.	n.d.	n.d.	1.69
43	0.21	0.69	n.d.	n.d.	n.d.	n.d.	n.d.	n.d.	n.d.	n.d.	n.d.	0.90
44	0.16	0.28	n.d.	n.d.	n.d.	n.d.	n.d.	n.d.	n.d.	n.d.	n.d.	0.43
Total	27.63	41.68	6.56	0.71	9.64	1.84	3.65	1.73	3.44	1.56	1.55	100.0

Appendix B: Detailed composition of gas oil A,B and C

Table B. 1: Detailed group type analysis of Gas oil A in wt%: P=n-paraffins, I=isoparaffins, MN=mononaphthenes, DN=dinaphthenes, MA=monoaromatics, NA=naphthenoaromatics, DA=diaromatics, NDA=naphthenodiaromatics, TrA=Triaromatics, T=Thiols/Sulfides, BT=Benzothiophenes, NBT=Naphthenobenzothiophenes, DBT=Dibenzothiophenes

#C	P	I	MN	DN	MA	NA	DA	NDA	TrA	T	BT	NBT	DBT	Total
9	0.03	0.06	0.02	n.d.	0.06	n.d.	n.d.	n.d.	n.d.	n.d.	n.d.	n.d.	n.d.	0.18
10	0.09	0.04	0.12	0.01	0.10	n.d.	0.01	n.d.	n.d.	n.d.	0.06	n.d.	n.d.	0.43
11	0.19	0.13	0.17	0.08	0.24	0.15	0.13	n.d.	n.d.	0.01	0.20	n.d.	n.d.	1.30
12	0.37	0.28	0.82	0.15	0.30	0.25	0.39	n.d.	n.d.	0.11	0.35	n.d.	0.09	3.11
13	0.64	0.61	1.05	0.19	0.56	0.23	0.67	n.d.	n.d.	0.16	0.37	0.05	0.40	4.92
14	1.15	0.97	1.12	0.23	0.47	0.22	0.45	0.08	0.03	0.22	0.48	0.30	0.77	6.49
15	1.50	1.23	1.32	0.15	0.75	0.51	0.52	0.39	n.d.	0.29	0.57	0.21	0.63	8.08
16	1.87	1.81	1.18	n.d.	1.11	0.62	0.63	0.44	0.03	0.27	0.65	0.17	0.52	9.29
17	2.31	2.28	1.71	n.d.	1.57	0.27	0.22	0.51	0.15	0.23	0.64	0.03	0.22	10.13
18	2.89	3.18	1.75	n.d.	1.83	0.05	0.52	0.32	n.d.	0.34	0.60	n.d.	n.d.	11.48
19	3.24	4.68	1.15	n.d.	2.21	n.d.	0.26	0.17	n.d.	0.05	0.30	n.d.	n.d.	12.06
20	2.92	3.35	1.04	n.d.	1.93	n.d.	0.36	n.d.	n.d.	n.d.	0.05	n.d.	n.d.	9.64
21	2.28	3.20	0.93	n.d.	1.86	n.d.	0.10	n.d.	n.d.	n.d.	n.d.	n.d.	n.d.	8.35
22	1.90	2.69	0.81	n.d.	0.92	n.d.	n.d.	n.d.	n.d.	n.d.	n.d.	n.d.	n.d.	6.33
23	1.30	1.86	0.41	n.d.	0.91	n.d.	n.d.	n.d.	n.d.	n.d.	n.d.	n.d.	n.d.	4.48
24	0.71	1.34	0.17	n.d.	0.20	n.d.	n.d.	n.d.	n.d.	n.d.	n.d.	n.d.	n.d.	2.42
25	0.24	0.64	0.05	n.d.	0.12	n.d.	n.d.	n.d.	n.d.	n.d.	n.d.	n.d.	n.d.	1.05
26	0.05	0.15	0.01	n.d.	n.d.	n.d.	n.d.	n.d.	n.d.	n.d.	n.d.	n.d.	n.d.	0.22
27	0.01	0.03	n.d.	n.d.	n.d.	n.d.	n.d.	n.d.	n.d.	n.d.	n.d.	n.d.	n.d.	0.04
28	n.d.	n.d.	n.d.	n.d.	n.d.	n.d.	n.d.	n.d.	n.d.	n.d.	n.d.	n.d.	n.d.	n.d.
Total	23.69	28.53	13.83	0.81	15.14	2.30	4.25	1.91	0.21	1.68	4.26	0.76	2.63	100.00

Table B. 2: Detailed group type analysis of Gas oil B in wt%: P=n-paraffins, I=isoparaffins,

MN=mononaphthenes, DN=dinaphthenes, MA=monoaromatics, NA=naphthenoaromatics, DA=diaromatics,

NDA=naphthenodiaromatics, TrA=Triaromatics, T=Thiols/Sulfides, BT=Benzothiophenes,

NBT=Naphthenobenzothiophenes, DBT=Dibenzothiophenes

#C	P	I	MN	DN	MA	NA	DA	NDA	TrA	T	BT	NBT	DBT	Total
7	0.05	0.05	n.d.	n.d.	0.02	n.d.	n.d.	n.d.	n.d.	n.d.	n.d.	n.d.	n.d.	0.11
8	0.12	0.16	0.05	n.d.	0.10	n.d.	n.d.	n.d.	n.d.	n.d.	n.d.	n.d.	n.d.	0.42
9	0.19	0.13	0.18	n.d.	0.23	0.04	n.d.	n.d.	n.d.	0.01	0.01	n.d.	n.d.	0.80
10	0.34	0.31	0.15	0.02	0.31	n.d.	0.03	n.d.	n.d.	0.02	0.17	n.d.	n.d.	1.37
11	0.65	0.47	0.53	0.07	0.47	0.35	0.38	n.d.	n.d.	0.12	0.47	n.d.	n.d.	3.50
12	1.39	1.10	0.95	0.50	1.07	0.67	1.01	n.d.	n.d.	0.12	0.53	n.d.	0.08	7.42
13	2.66	2.63	1.77	0.42	1.84	0.45	1.06	0.05	n.d.	0.17	0.41	0.02	0.28	11.76
14	3.58	4.23	1.64	0.44	1.84	0.28	0.80	0.08	0.02	0.21	0.35	0.06	0.41	13.93
15	3.67	4.54	1.42	0.21	1.67	0.02	0.35	0.21	n.d.	0.11	0.39	0.06	0.35	12.99
16	3.23	3.83	1.09	0.03	1.83	0.05	0.36	0.12	n.d.	0.09	0.34	n.d.	0.16	11.14
17	2.73	3.79	0.87	n.d.	1.44	0.13	n.d.	0.09	n.d.	0.03	0.22	n.d.	n.d.	9.31
18	2.43	3.59	0.34	n.d.	1.25	0.08	n.d.	n.d.	n.d.	0.03	0.15	n.d.	n.d.	7.87
19	1.76	3.14	0.48	n.d.	0.93	n.d.	n.d.	n.d.	n.d.	n.d.	0.08	n.d.	n.d.	6.40
20	1.25	1.77	0.36	n.d.	0.86	n.d.	n.d.	n.d.	n.d.	n.d.	0.02	n.d.	n.d.	4.26
21	0.89	1.57	0.26	n.d.	0.71	n.d.	n.d.	n.d.	n.d.	n.d.	n.d.	n.d.	n.d.	3.43
22	0.63	1.01	0.18	n.d.	0.31	n.d.	n.d.	n.d.	n.d.	n.d.	n.d.	n.d.	n.d.	2.14
23	0.42	0.83	0.14	n.d.	0.15	n.d.	n.d.	n.d.	n.d.	n.d.	n.d.	n.d.	n.d.	1.54
24	0.29	0.79	0.06	n.d.	0.03	n.d.	n.d.	n.d.	n.d.	n.d.	n.d.	n.d.	n.d.	1.17
25	0.15	0.16	0.02	n.d.	n.d.	n.d.	n.d.	n.d.	n.d.	n.d.	n.d.	n.d.	n.d.	0.33
26	0.09	n.d.	n.d.	n.d.	n.d.	n.d.	n.d.	n.d.	n.d.	n.d.	n.d.	n.d.	n.d.	0.09
27	0.02	n.d.	n.d.	n.d.	n.d.	n.d.	n.d.	n.d.	n.d.	n.d.	n.d.	n.d.	n.d.	0.02
Total	26.55	34.09	10.48	1.68	15.07	2.09	3.98	0.55	0.02	0.91	3.16	0.13	1.28	100.00

Table B. 3: Detailed group type analysis of Gas oil C in wt%: P=n-paraffins, I=isoparaffins,

MN=mononaphthenes, DN=dinaphthenes, MA=monoaromatics, NA=naphthenoaromatics, DA=diaromatics,

NDA=naphthenodiaromatics, TrA=Triaromatics, T=Thiols/Sulfides, BT=Benzothiophenes,

NBT=Naphthenobenzothiophenes, DBT=Dibenzothiophenes

#C	P	I	MN	DN	MA	NA	DA	NDA	TrA	T	BT	NBT	DBT	Total
7	0.11	0.23	0.01	n.d.	0.04	n.d.	n.d.	n.d.	n.d.	n.d.	n.d.	n.d.	n.d.	0.40
8	0.07	0.14	0.11	n.d.	0.13	n.d.	n.d.	n.d.	n.d.	n.d.	n.d.	n.d.	n.d.	0.45
9	0.11	0.10	0.26	n.d.	0.18	n.d.	n.d.	n.d.	n.d.	n.d.	n.d.	n.d.	n.d.	0.64
10	0.16	0.16	0.27	0.05	0.26	n.d.	0.04	n.d.	n.d.	n.d.	n.d.	0.01	n.d.	0.95
11	0.21	0.20	0.36	0.10	0.15	0.06	0.24	n.d.	n.d.	n.d.	n.d.	0.04	n.d.	1.36
12	0.31	0.24	0.50	0.06	0.30	0.23	0.75	n.d.	n.d.	0.01	0.04	0.06	n.d.	2.50
13	0.49	0.47	1.34	n.d.	0.45	0.41	1.08	0.24	n.d.	0.05	0.10	0.07	n.d.	4.70
14	0.83	0.77	1.53	n.d.	0.45	0.57	1.22	0.40	0.08	0.03	0.14	0.07	0.01	6.10
15	1.77	1.61	1.94	n.d.	0.56	0.94	0.84	0.55	0.15	0.02	0.12	0.08	0.02	8.60
16	2.79	2.91	2.88	n.d.	1.81	0.73	0.65	0.68	0.21	0.01	0.08	0.07	n.d.	12.81
17	2.76	3.69	3.14	n.d.	2.45	0.72	0.57	0.60	0.18	n.d.	0.01	0.04	n.d.	14.17
18	2.81	4.27	1.07	n.d.	1.52	0.57	0.53	0.50	0.15	n.d.	n.d.	0.03	n.d.	11.44
19	2.71	4.08	1.54	n.d.	1.27	0.16	0.41	0.37	0.15	n.d.	n.d.	0.01	n.d.	10.70
20	1.71	1.74	1.29	n.d.	0.75	n.d.	0.08	0.12	n.d.	n.d.	n.d.	n.d.	n.d.	5.69
21	1.39	1.74	1.29	n.d.	0.47	n.d.	n.d.	n.d.	n.d.	n.d.	n.d.	n.d.	n.d.	4.88
22	1.14	1.41	1.00	n.d.	0.25	n.d.	n.d.	n.d.	n.d.	n.d.	n.d.	n.d.	n.d.	3.80
23	0.79	0.91	1.11	n.d.	0.28	n.d.	n.d.	n.d.	n.d.	n.d.	n.d.	n.d.	n.d.	3.10
24	0.57	0.63	0.74	n.d.	0.13	n.d.	n.d.	n.d.	n.d.	n.d.	n.d.	n.d.	n.d.	2.07
25	0.58	0.60	0.17	n.d.	0.25	n.d.	n.d.	n.d.	n.d.	n.d.	n.d.	n.d.	n.d.	1.61
26	0.42	0.53	0.20	n.d.	0.28	n.d.	n.d.	n.d.	n.d.	n.d.	n.d.	n.d.	n.d.	1.43
27	0.23	0.37	0.10	n.d.	n.d.	n.d.	n.d.	n.d.	n.d.	0.73	n.d.	n.d.	n.d.	1.43
28	0.15	0.30	n.d.	n.d.	n.d.	n.d.	n.d.	n.d.	n.d.	n.d.	n.d.	n.d.	n.d.	0.45
29	0.10	0.28	n.d.	n.d.	n.d.	n.d.	n.d.	n.d.	n.d.	n.d.	n.d.	n.d.	n.d.	0.38
30	0.09	0.15	n.d.	n.d.	n.d.	n.d.	n.d.	n.d.	n.d.	n.d.	n.d.	n.d.	n.d.	0.24
31	0.05	0.06	n.d.	n.d.	n.d.	n.d.	n.d.	n.d.	n.d.	n.d.	n.d.	n.d.	n.d.	0.11
Total	22.36	27.58	20.83	0.22	11.97	4.40	6.41	3.47	0.91	0.84	0.48	0.48	0.04	100.00